Boundary shear stress distribution and flow structures in trapezoidal channels

by

KAMRAN ANSARI

Thesis submitted to The University of Nottingham for
the degree of Doctor of Philosophy

April 2011

ABSTRACT

The commercially available Computational Fluid Dynamics (CFD) software ANSYS-CFX version 11 (2008) is employed to predict the distribution of the bed and sidewall shear stresses in trapezoidal open channels. The investigation includes computation of wall shear stress (1) directly, using CFD for a range of channels layouts (straight, turning, with ridges), and (2), building on the division line concept initially formulated by Leighly in 1932 and later by Einstein in 1942, through the evaluation of the Guo and Julien (2005) equations, as proposed by Cacqueray *et al.* (2009). These equations include the two complex integral terms II and III, pertaining to viscous and secondary current effects, have been analysed for each cross section, for straight channels.

The CFD predictions are validated first against the experimental results of Tominaga *et al.* (1989) to ensure that the models used are appropriate. Once this is done, the impact of (1) the variation of the slant angle of the sidewalls, (2) the channel aspect ratio and (3) the composite roughness on the shear stress distribution in straight prismatic channels is analysed directly based on the CFD predictions.

In wide open channels the lines of boil, consisting of low speed streaks, periodically in the transverse direction, is believed to be due to the initiation of sand ridges on the bed; in other words due to the coupled interaction between moving bed and flow. A numerical analysis on the flow structures created and the distribution of shear stresses on the bed and sidewalls of channel sections having ridges on its bed is therefore carried out to clarify this point and assess the potential consequences on our predictions.

Finally, because of obvious practical relevance, as most rivers follow a winding course, numerical simulations on the distribution of shear on the boundaries inside a channel bend is also presented.

PUBLICATIONS

Ansari, K., Morvan, H. P. and Hargreaves, D. M. (2011)."A numerical investigation into secondary currents and wall shear in trapezoidal channels." *Journal of Hydraulic Engineering, ASCE*, accepted (scheduled to appear in April 2011 issue).

Ansari, K., Morvan, H. P. and Hargreaves, D. M. (2011)."A numerical study of artificial bed ridges in wide, open channels and their effects on secondary currents and wall shear." *Journal of Hydraulic Engineering, ASCE*, submitted (in review).

Ansari, K., Morvan, H. P. and Hargreaves, D. M. (2010)."A numerical analysis on the distribution of shear stress in curved trapezoidal channels." *First IAHR European Division Congress*, $4^{th} - 6^{th}$ May, 2010, Edinburgh, UK.

Ansari, K., Morvan, H. P. and Hargreaves, D. M. (2010)."Distribution of shear stress and flow structures in trapezoidal channels with ridges on bed." *First IAHR European Division Congress*, $4^{th} - 6^{th}$ May, 2010, Edinburgh, UK.

Ansari, K., Morvan, H. P. and Hargreaves, D. M. (2011)."Effect of numerical approach on the prediction of shear stress and flow structures inside a bend." In preparation.

ACKNOWLEDGEMENTS

First and foremost, I wish to express my deep gratitude to my supervisors Dr Hervé Morvan and Dr David Hargreaves for their constant encouragement, guidance and support throughout my PhD study.

I would also like to thank Mehran University and the Government of Pakistan for awarding me the scholarship to make this PhD possible.

My sincere appreciation goes to my family and friends for their love and prayers during my study.

Last but not the least, deepest thanks to my wife and children for their ever-lasting love, care and support in life. Without them, I would not have been able to complete this project.

TABLE OF CONTENTS

LIST OF FIGURES

LIST OF TABLES

CHAPTER 1

INTRODUCTION

1.1 Introduction

Water flowing in an open channel exerts a longitudinal shear force on the wetted perimeter of the flow cross section, which tends to erode the channel walls (Kartha & Leutheusser, 1970). The boundary shear stress is one of the most important parameters in open channel flow but at the same time also one of the most difficult to analyze from a purely theoretical point of view. The influence of secondary flow, cross sectional shape, and non-uniform roughness distribution around the wetted perimeter all combine to make the prediction of the boundary shear stress distribution impossible even for simple cases (Knight, 1981). Also the interrelationship of these factors makes the prediction of the boundary shear stress distribution a difficult task (Yang & Lim, 1998). The pattern and the number of secondary flow cells as well as the channel cross-sectional shape influence the lateral distribution of the boundary shear stress (Mohammadi & Knight, 2004).

Turbulent structures and the boundary shear stress in steady and uniform flows have been studied by many researchers such as Tracy (1965), Knight and Patel (1985) and Yang (2002). Some empirical equations for the boundary shear on the bed and walls have been proposed by many such as Knight (1981), Zheng and Jin (1998) and Guo and Julien (2005). Yang (1996), and Yang and Lim (1997, 1998) have used the hypothesis that mechanical energy of the turbulent flow is transferred towards the boundary via the shortest relative distance. A lot of work has also been done on the distribution of shear in smooth rectangular ducts such as Rhodes and Knight (1994), Jin *et al.* (2004). Mohammadi and Knight (2004) also worked on the distribution of shear stress in a V-shaped channel whereas Knight and Sterling (2000) have worked on the boundary shear in partially full pipes. Unfortunately, little work has been done on the distribution of boundary shear in trapezoidal channel sections thus far, except for some contributions by Flintham and Carling (1988), Tominaga *et al.* (1989) and Yuen (1989). This despite the fact

that trapezoidal channels are the most commonly used manmade irrigation and drainage channels.

1.2 Problem Statement

In open channel flows, the boundary shear stress and its distribution along the wetted perimeter is of great importance. A knowledge of this variable, be it local or mean values, is required in many hydraulic problems related to the computation of flow resistance, side wall correction, sediment transport rate, channel erosion or deposition and designs of the channels for the long term stability (Yang & Lim, 1998).

The problem of separating the bed shear stress and the sidewall shear stress is very important in almost all studies of open channel flows particularly for sediment transport and channel stability issues. One must separate the bed shear stress from the total shear stress for the estimation of bed load transport in open channel flows; similarly, for the study of channel migration or prevention of bank erosion, one must know the sidewall shear stress.

Recent progress in the field of Computational Fluid Dynamics (CFD) and the more traditional division line has allowed some detailed and practical knowledge to be gained for smooth rectangular channels (Cacqueray *et al.*, 2009). Most stability channels are designed as trapezoidal channels in Pakistan but have shown great problems of sediment deposition and sidewall scouring (Bakker *et al.*, 1989), which are costly for a country with such a large network of irrigation and drainage channels.

The present work aims to investigate the distribution of bed shear in trapezoidal channels using CFD and to check it against traditional design formulations (Einstein, 1942) and recent analytical developments (Guo and Julien, 2005) in order to be able to compute both mean wall and bed shear stress values accurately and quickly. The development of cellular secondary currents due to the initiation of sand ridges on bed of wide-open channels has also been investigated. Finally, the distribution of wall shear on the wetted perimeter inside a bend is also looked into.

1.3 Aim and Objectives

The main aim of the research is to understand the trapezoidal channel flow mechanics, in particular to distribution of shear on the wetted perimeter, with a view the investigate the channel stability keeping in mind the irrigation and drainage channels in Pakistan.

The above aim is achieved through the following objectives;

- To setup and validate a CFD methodology for open channel flow and shear stress simulations.
- To evaluate and investigate the distribution of shear stress on the channel boundaries to add to the body of the work as in Knight (1981) and Knight *et al.* (1984).
- To evaluate and investigate the effects of the roughness, secondary currents, aspect ratios and slant angles on the shear stress distribution in prismatic trapezoidal channels.
- To expand to and validate the old Division Line concept of Leighly (1932) and Einstein (1942) in in-bank trapezoidal channels as recently started by Cacqueray *et al.* (2009).
- To investigate the distribution of shear stress in trapezoidal channel bends.
- To have a better understanding of the channel dynamics concerning bed forms and bank stability because of the above.

Following the achievements of the above objectives, a better understanding of the distribution of the shear stress on the wetted perimeter in trapezoidal open channels would be developed which would be helpful in the design and management of irrigation and drainage channels, especially in Pakistan.

1.4 Outline of the thesis

This thesis consists of eight chapters, which are briefly discussed below.

Chapter 2 focuses on the basic concepts of open channel hydraulics. Some definitions related to the flow in open channels are given and issues such as open

channel equilibrium and regime concepts for design of stable open channels are discussed.

In Chapter 3, a literature review is presented. The experimental work done on the subject of distribution of shear stress is reviewed. The various hypotheses given by different researchers on the concept of division line are discussed. It also includes some research done on the development of bed forms in open channels flumes.

Chapter 4 provides details on the numerical modelling including an introduction to the governing equations and associated turbulence models. It also discusses the boundary conditions and numerical strategy in the models used in this work.

Chapter 5 focuses on the results generated through the CFD simulations on straight prismatic trapezoidal channels. It is divided into two parts, the first part provides the validation of the CFD model by comparison of CFD results with experimental ones found in the literature such as Knight *et al.* (1984) and Flintham and Carling (1988). In the second part, a parametric analysis is done on the variation of shear stress on the wetted perimeter of some 256 channels. Variations in aspect ratio, slant angle and roughness on the boundaries are made to see their effects on the shear stress distribution. Leighly's (1932) type division lines are also constructed, and using Guo and Julien (2005) equations, an analysis is also carried out separately on the distribution of shear stress on the bed and sidewalls with a focus on the effects of secondary currents and fluid internal shear on the overall shear stress distribution.

In Chapter 6 an in depth analysis is carried out on the distribution of secondary currents and shear stresses in straight prismatic open channels with artificial bed forms. The ridges were planted on the bed of wide channels as the secondary currents observed in high aspect ratio channels during the study of prismatic channels (Chapter 5) did not match the counter rotating cells found throughout the width of the channel as reported in the previous studies e.g. Knight and Patel (1985). Simulations were run on channel sections having varying numbers of ridges on the bed as well as size of the ridges to study the effect of these

variations on the flow structures and shear stress distribution in wide-open channels.

In Chapter 7, an extensive analysis is carried out on the development of flow structures and variation of shear stress inside an open channel bend. Various approaches were used here to model the free surface. In most simulations, a symmetry (lid) condition was used to fix the position of the free surface. However, simulations using a multiphase model were run to show the errors introduced using the symmetry condition were not excessive. A comparison is also done on the effects of using different turbulence models.

In Chapter 8, the main conclusions of the research are presented. This chapter also provides recommendations for further research.

CHAPTER 2

OPEN CHANNEL HYDRAULICS

2.1 Introduction

This chapter presents a brief overview of the key open channel hydraulic concepts and definitions. Open channels are natural or manmade conveyance structures which have a free surface, i.e. a boundary exposed to the atmosphere. The free surface is essentially an interface between two fluids of different density i.e. air above and a liquid such as water below it. In addition, it has a constant pressure, which is called the atmospheric pressure. In the case of flowing fluids, the gravitational effects usually cause the motion, and the pressure distribution with the fluid is generally hydrostatic. Open channel flows are usually turbulent and unaffected by surface tension, (French, 1985).

2.2 Classification of open channel flow

It is possible to classify flow occurring in an open channel on the basis of many different criteria and one of the primary criteria of classification is the variation of depth of flow, y, in time, t, and space, x. If time is the criterion, then flow may be classified as either "steady", which implies that depth of flow does not change with time, $\partial y/\partial t = 0$, or "unsteady" which implies that the depth does not change with time, $\partial y/\partial t \neq 0$. Similarly if space is used as the criterion, then flow may be classified as "uniform", if the depth of flow does not vary with distance, $\partial y/\partial x = 0$, or as "non-uniform", if the depth varies with distance, $\partial y/\partial x \neq 0$. The terminology uniform and non-uniform usually implies that the flow is also steady. Non-uniform flow also termed as varied flow, can further be classified as either "gradually varied", where the depth of flow changes slowly as compared to distance e.g. in a reservoir behind a dam, or as "rapidly varied", where the depth of flow changes quickly as compared to distance e.g. hydraulic jump. For the present study channel sections with steady uniform flow have been considered.

2.3 Specific energy

A central principle in the hydraulics of open channel flow is the law of conservation of energy. The total energy of a parcel of water travelling on a streamline is given by Bernoulli equation as,

$$H = z + \frac{p}{\gamma} + \frac{u^2}{2g} \tag{2.1}$$

where,

H = total energy

z = elevation of streamline above datum

p = pressure

γ = fluid specific weight

p/γ =pressure head

u = streamline velocity

g = local acceleration of gravity

$u^2/2g$ = velocity head

The sum $z + (p/\gamma)$ defines the elevation of the hydraulic grade line above the datum, which in general varies from point to point along the streamline. To examine the variation of this sum under different circumstances, consider a particle of cross-sectional area, δA, length, δs, density, ρ, and mass $\rho\, \delta A\, \delta s$, moving along an arbitrary streamline in the $+S$ direction as shown in Figure 2.1.

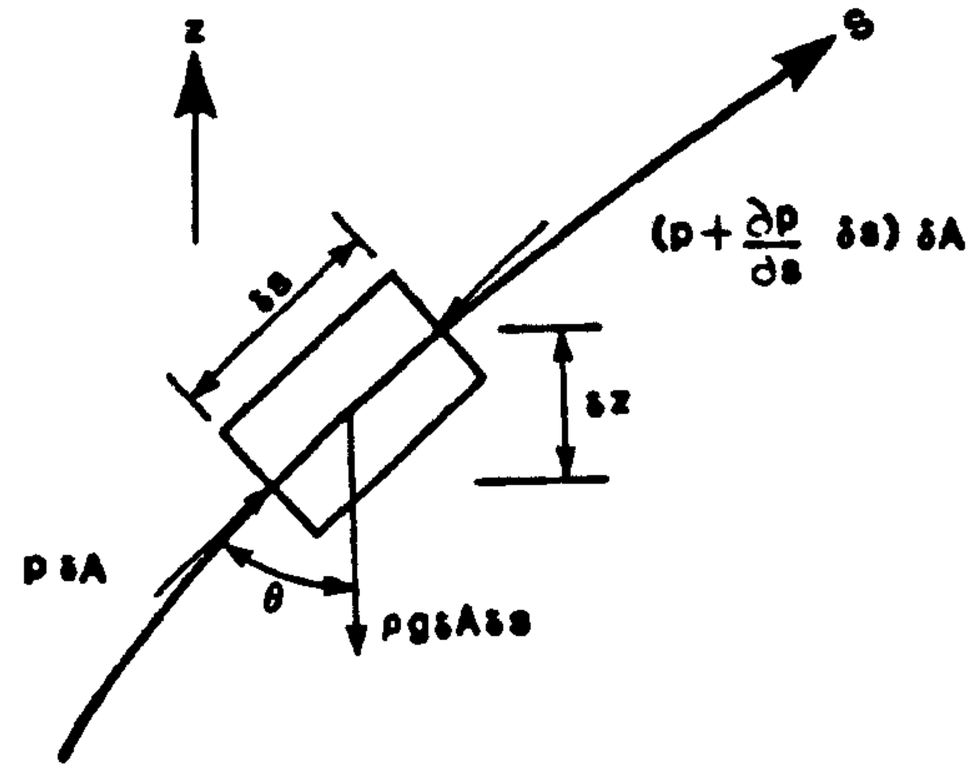

Figure 2.1 Component forces acting on a particle moving along a streamline after French, (1985).

If it is assumed that the fluid is frictionless, then there are no shear forces, and only the gravitational body forces and the surface forces on the ends of the particle must be considered. The gravitational force is $\rho g \delta A \delta s$ the pressure force on the upstream face is $p\delta A$ and the pressure on the downstream face is $[p + (\partial p/\partial s)\delta s]\delta A$. Applying Newton's second law of motion in the direction of the flow gives,

$$F = \delta m\ a \tag{2.2}$$

$$\rho\ \delta A\ \delta s\ a = p\ \delta A - \left(p + \frac{\partial p}{\partial s}\delta s\right)\delta A - \rho g\ \delta A\ \delta s \cos\theta \tag{2.3}$$

where, a is the acceleration of the fluid particle along the streamline.

Simplifying the above equation, we get,

$$\frac{\partial p}{\partial s} + \rho g \frac{\partial z}{\partial s} + \rho a = 0$$

and since,

$$\frac{\partial z}{\partial s} = \cos\theta$$

therefore,

$$\frac{\partial}{\partial s}(p + \gamma z) + \rho a = 0 \tag{2.4}$$

The above equation is also known as the Euler equation for motion along a streamline. If $a = 0$, the above equation can be integrated to yield the hydrostatic law i.e. pressure varies linearly with depth.

The implications of equation (2.4) are significant in open channel flow. If minor fluctuations due to turbulence are ignored and the streamlines have no acceleration component in the plane of the cross-section, i.e., the streamlines have neither substantial curvature nor divergence, then the flow is termed parallel and a hydrostatic pressure distribution exists. In practice, most uniform flows and gradually varied flows may be regarded as parallel flows. In a parallel flow, the sum $z + p/\gamma$ is a constant and is equal to depth of flow, y, if the channel bottom is taken as datum. Then, by definition, the specific energy of an open channel flow relative to the bottom of the channel is,

$$E = y + \alpha \frac{u^2}{2g} \tag{2.5}$$

where, α is the kinetic energy correction factor which is used to correct the non-uniformity of the velocity profile and u is the average velocity of flow and is, $u = \frac{Q}{A}$ where, Q is the flow rate and A is the flow area.

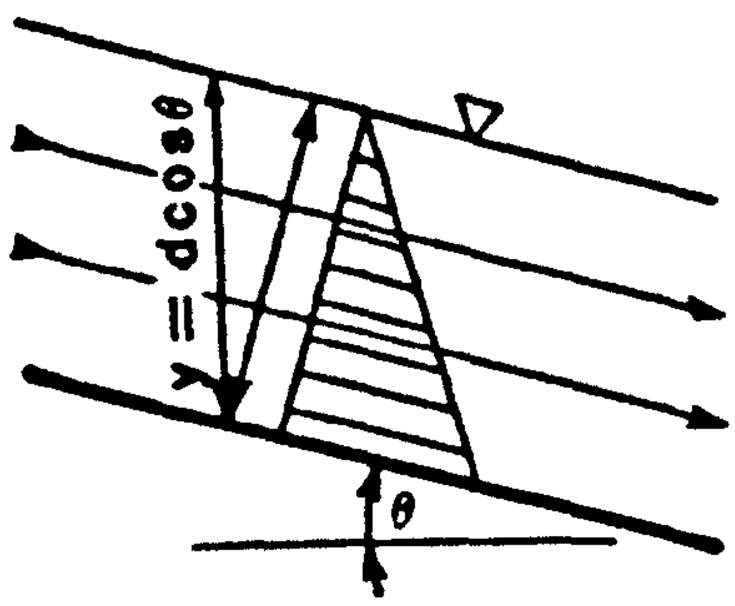

Figure 2.2 Pressure distribution in parallel flow with $\cos\theta \cong 1$ after Chow, (1959).

The assumption in equation (2.5) is that the slope of the channel is very small, or $cos\theta \approx 1$ and $y \approx d\ cos\theta$, where θ is the inclination of the channel with respect to horizontal axis, as shown in Figure 2.2.

In general the equation is valid if $\theta < 10^o$ or $S < 0.18$, where S is the slope of the channel. If θ is not small then the pressure distribution is not hydrostatic since the vertical depth of flow is significantly different from the depth measured perpendicular to the channel bed.

2.4 Critical flow

Equation (2.5) shows that if $cos\theta \approx 1$, $\alpha = 1$ and the channel section and discharge are specified, then the specific energy is only a function of the depth of flow. If y is plotted against E, a curve with two branches results as shown in Figure 2.3.

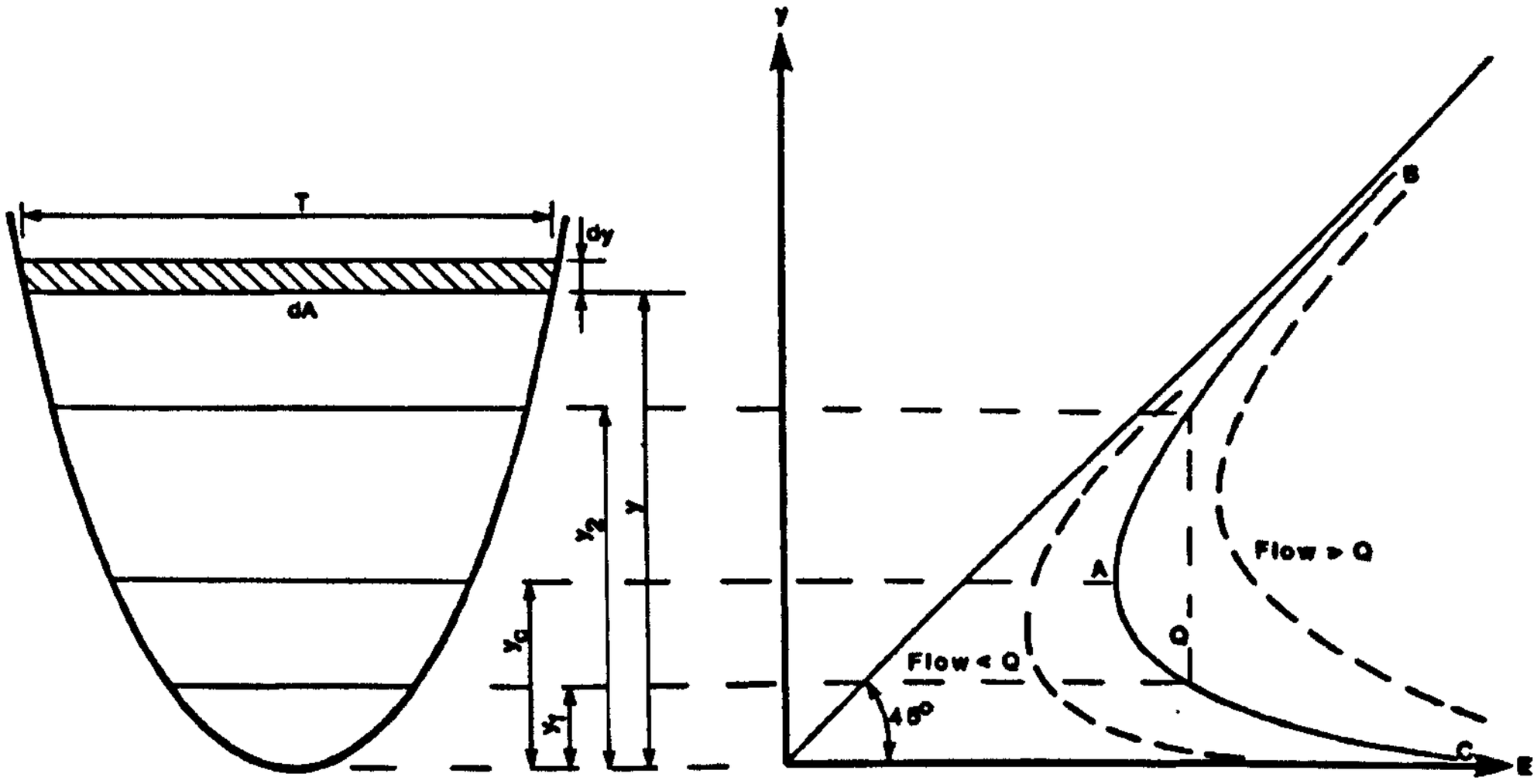

Figure 2.3 Specific energy curve after French, (1985).

The limb AC approaches the E axis asymptotically and the limb AB approaches the line $y = E$ asymptotically. For all the points on the E axis greater than A, there are two possible depths of flow, known as the alternate depths of flow. Since A represents the minimum specific energy, the co-ordinates of this point can be found by taking the first derivative of equation (2.5) with respect to y and equating the results to zero,

$$E = y + \alpha\frac{u^2}{2g} = y + \alpha\frac{Q^2}{2gA^2} \tag{2.6}$$

$$\frac{dE}{dy} = 1 - \alpha \frac{Q^2}{gA^3} \frac{dA}{dy} = 0 \tag{2.7}$$

where, A is the flow area.

The differential water area, dA, near the free surface is equal to Tdy, where T is the top width. By definition the hydraulic depth, D, is

$$D = \frac{A}{T} \tag{2.8}$$

Substituting $\alpha = 1$ and equation (2.8) in equation (2.7) gives,

$$1 - \frac{Q^2}{gA^3} \frac{dA}{dy} = 1 - \frac{Q^2}{gA^2} \frac{T}{A} = 1 - \frac{u^2}{gD} = 0 \tag{2.9}$$

$$\frac{u^2}{2g} = \frac{D}{2} \tag{2.10}$$

$$\frac{u}{\sqrt{gD}} = 1 \tag{2.11}$$

which is the definition of the critical flow.

Thus, minimum specific energy occurs at the critical hydraulic depth. Hence the branch AC can be interpreted as representing supercritical flows and branch AB as subcritical flows.

2.5 Froude Number

The ratio of the inertial forces to the gravitational forces acting on the flow is termed as dimensionless Froude number denoted by 'F_r' defined as,

$$F_r = \frac{U_m}{\sqrt{gD}} = \frac{U_m}{\sqrt{g(A/T)}} = \frac{Q}{\sqrt{g(A^3/T)}} \tag{2.12}$$

where, F_r is the Froude number, U_m is the mean velocity in the channel, Q is the discharge, g is the gravitational acceleration, D is the hydraulic depth, A is the cross-sectional flow area, and T is the top width of the channel. Here the

denominator, $\sqrt{gD}$, represents the speed with which the gravity waves propagate in open channels. This is also referred to as wave celerity.

The Froude number is also a criterion of the type of flow present in an open channel. The flow is said to be at critical state when F_r is equal 1.0 with inertial and gravitational forces in equilibrium. It is classified as, subcritical, tranquil or streaming when F_r is less than 1.0 with gravitational forces dominant and as, supercritical, rapid or shooting when F_r is greater than 1.0 with inertial forces dominant. The hydraulic behaviour of open channel flow varies significantly depending on whether the flow is subcritical, critical, or supercritical. In the present study the channel sections with subcritical flow are considered.

2.6 Open channel flow kinematics

Flow kinematics describes fluid motion in terms of velocity and acceleration. In open channels, two orthogonal coordinate systems are common; (1) global right hand Cartesian (x, y, z) systems, with x in the main downstream direction, y in the lateral direction to the left bank, and z upward; and (2) local cylindrical (r , θ, z) systems, in which r is the channel radius of curvature in a horizontal plane, as shown in Figure 2.4.

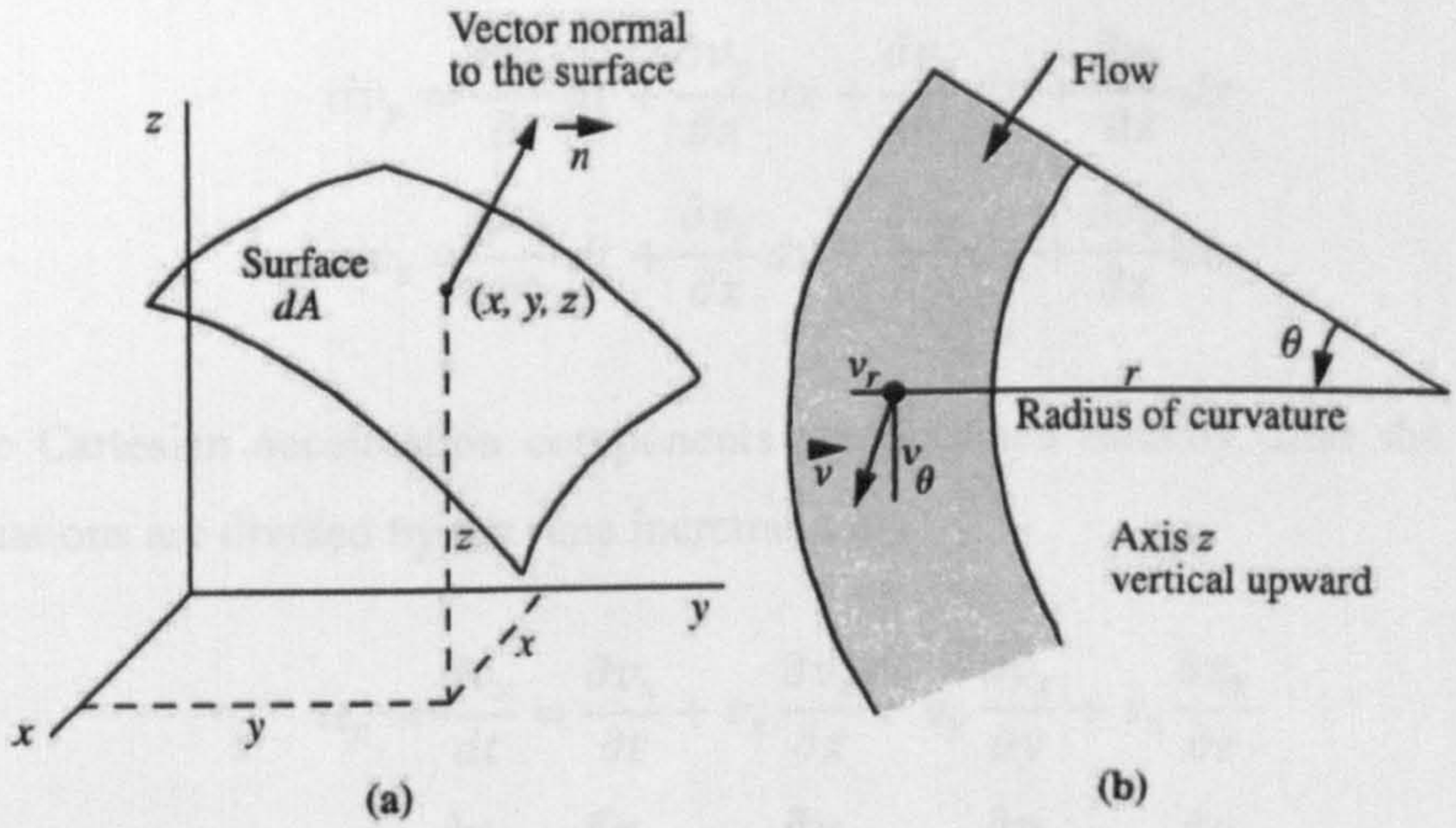

Figure 2.4 Cartesian and cylindrical coordinates after Julien, (2002).

The rate of change in the position of a fluid element is a measure of its velocity. Velocity is defined as the ratio between the displacement *ds* and the corresponding increment of time *dt*. Velocity, *v*, is a vector quantity that varies in both space (*x*, *y*, *z*) and time *t*. Its magnitude *v* at a given time equals the square root of the sum of squares of its orthogonal components,

$$v = \sqrt{v_x^2 + v_y^2 + v_z^2} \tag{2.13}$$

where, $v_x = dx/dt$, $v_y = dy/dt$ and $v_z = dz/dt$.

A line tangent to the velocity vector at every point at a given instant is known as a streamline. The path line of a fluid element is the locus of the element through time, e.g., the path followed by a single buoy on a channel. A streak line is defined as the line connecting all fluid elements that have passed successively at a given point in space, e.g., instantaneous position of all buoys released over time from a single point on a channel.

The differential velocity components over an infinitesimal distance *ds* (*dx*, *dy*, *dz*) and time increment *dt* at a point (*x*, *y*, *z*) are,

$$dv_x = \frac{\partial v_x}{\partial t}dt + \frac{\partial v_x}{\partial x}dx + \frac{\partial v_x}{\partial y}dy + \frac{\partial v_x}{\partial z}dz \tag{2.14}$$

$$dv_y = \frac{\partial v_y}{\partial t}dt + \frac{\partial v_y}{\partial x}dx + \frac{\partial v_y}{\partial y}dy + \frac{\partial v_y}{\partial z}dz \tag{2.15}$$

$$dv_z = \frac{\partial v_z}{\partial t}dt + \frac{\partial v_z}{\partial x}dx + \frac{\partial v_z}{\partial y}dy + \frac{\partial v_z}{\partial z}dz \tag{2.16}$$

The Cartesian acceleration components are obtained directly after the velocity equations are divided by the time increment *dt*,

$$a_x = \frac{\partial v_x}{dt} = \frac{\partial v_x}{\partial t} + v_x\frac{\partial v_x}{\partial x} + v_y\frac{\partial v_x}{\partial y} + v_z\frac{\partial v_x}{\partial z} \tag{2.17}$$

$$a_y = \frac{\partial v_y}{dt} = \frac{\partial v_y}{\partial t} + v_x\frac{\partial v_y}{\partial x} + v_y\frac{\partial v_y}{\partial y} + v_z\frac{\partial v_y}{\partial z} \tag{2.18}$$

$$a_z = \frac{\partial v_z}{dt} = \frac{\partial v_z}{\partial t} + v_x\frac{\partial v_z}{\partial x} + v_y\frac{\partial v_z}{\partial y} + v_z\frac{\partial v_z}{\partial z} \tag{2.19}$$

It is shown in above equations that the total acceleration can be separated into local and convective acceleration terms. Flows in which local acceleration terms vanish at any point are called steady flows and flows in which convective acceleration terms vanish are called uniform flows. Steady-uniform flows are thus flows which do not have any acceleration components.

2.7 Conservation of mass

The equation of continuity or the law of conservation of mass, states that mass can neither be created nor be destroyed. The continuity equation can be written in differential form as well as integral form. For differential form, consider the infinitesimal control volume as shown in Figure 2.5 filled with a fluid.

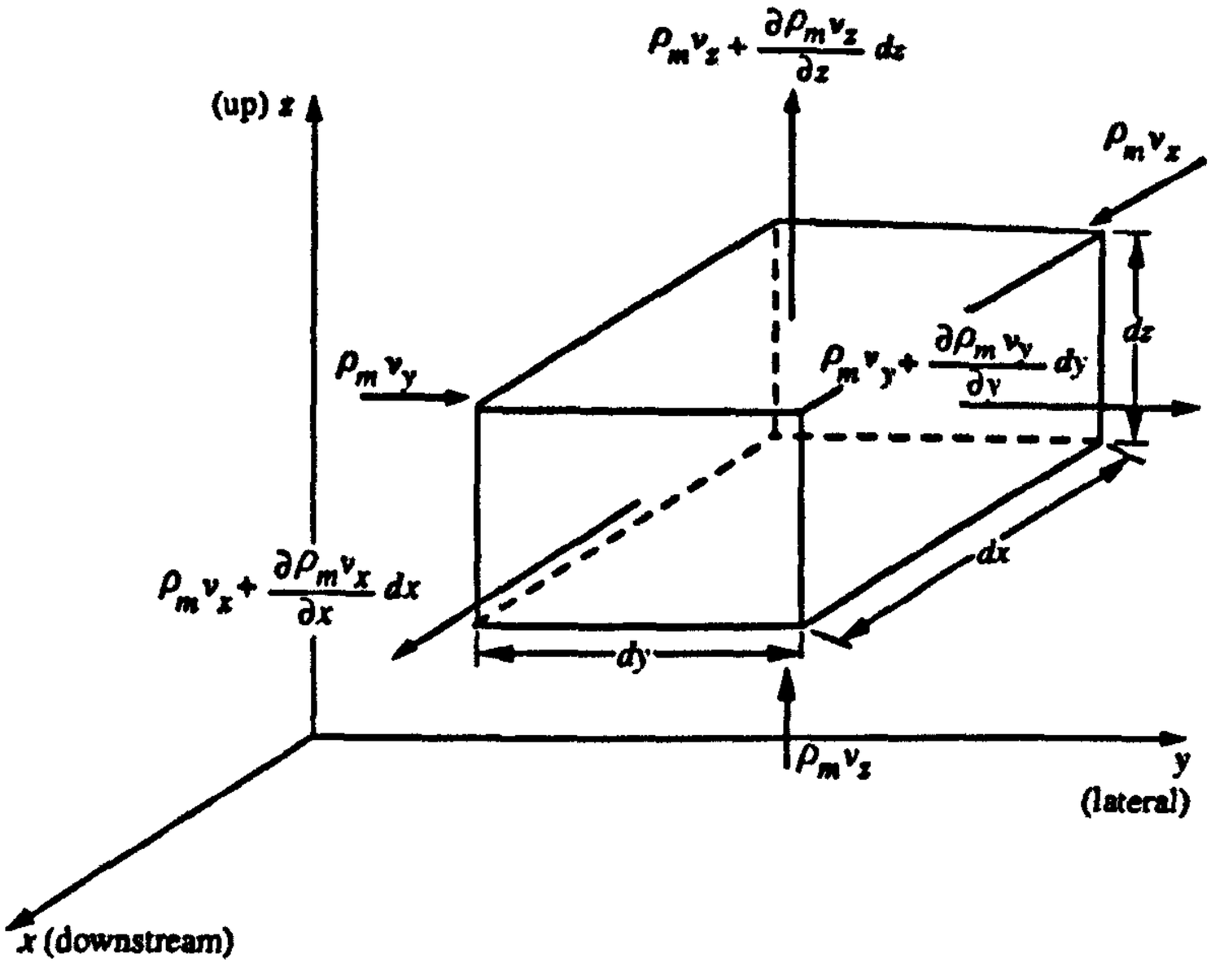

Figure 2.5 Infinitesimal element of a fluid after Julien, (2002).

The difference between the mass fluxes entering and leaving the differential control volume equals the rate of increase of internal mass. For instance, in the x direction, the net mass flux leaving the control volume is $[(\partial \rho_m v_x)/\partial x]dx$ times the area $dydz$. The change in internal mass is $(\partial \rho_m/\partial t)\ dxdydz$. Repeating the procedure in the y and the z directions yields the following differential relationship in Cartesian coordinates (x, y, z),

$$\frac{\partial \rho_m}{\partial t} + \frac{\partial}{\partial x}(\rho_m v_x) + \frac{\partial}{\partial y}(\rho_m v_y) + \frac{\partial}{\partial z}(\rho_m v_z) = 0 \tag{2.20}$$

For homogeneous incompressible suspensions without settling, the mass density is independent of space and time, consequently $\partial \rho_m / \partial t = 0$ and the divergence of the velocity vector in the Cartesian coordinates must be zero,

$$\frac{\partial v_x}{\partial x} + \frac{\partial v_y}{\partial y} + \frac{\partial v_z}{\partial z} = 0 \tag{2.21}$$

When dealing with open channel flows at low sediment concentrations and neglecting compressibility effects, equation (2.21) can be used.

2.8 Equations of motion

The analysis of the fluid motion results from the application of forces on a fixed control volume. From second law of motion, force F equals the product of mass m and acceleration a. If ρ is the mass density of the fluid then $a = F/m = F/\rho$. The forces acting on a Cartesian element of fluid and sediment (dx, dy, dz) are classified as either internal forces or external forces. The internal accelerations or body forces per unit mass, acting at the centre of mass of the element are denoted by g_x, g_y, g_z. The external forces per unit area applied on each face of the element are subdivided into normal and tangential stress components. The normal stresses σ_x, σ_y, σ_z are designated as positive for tension. The shear stresses, τ_{xy}, τ_{yx}, τ_{xz}, τ_{zx}, τ_{yz}, and τ_{zy} with two orthogonal components are applied on each face as shown in Figure 2.6.

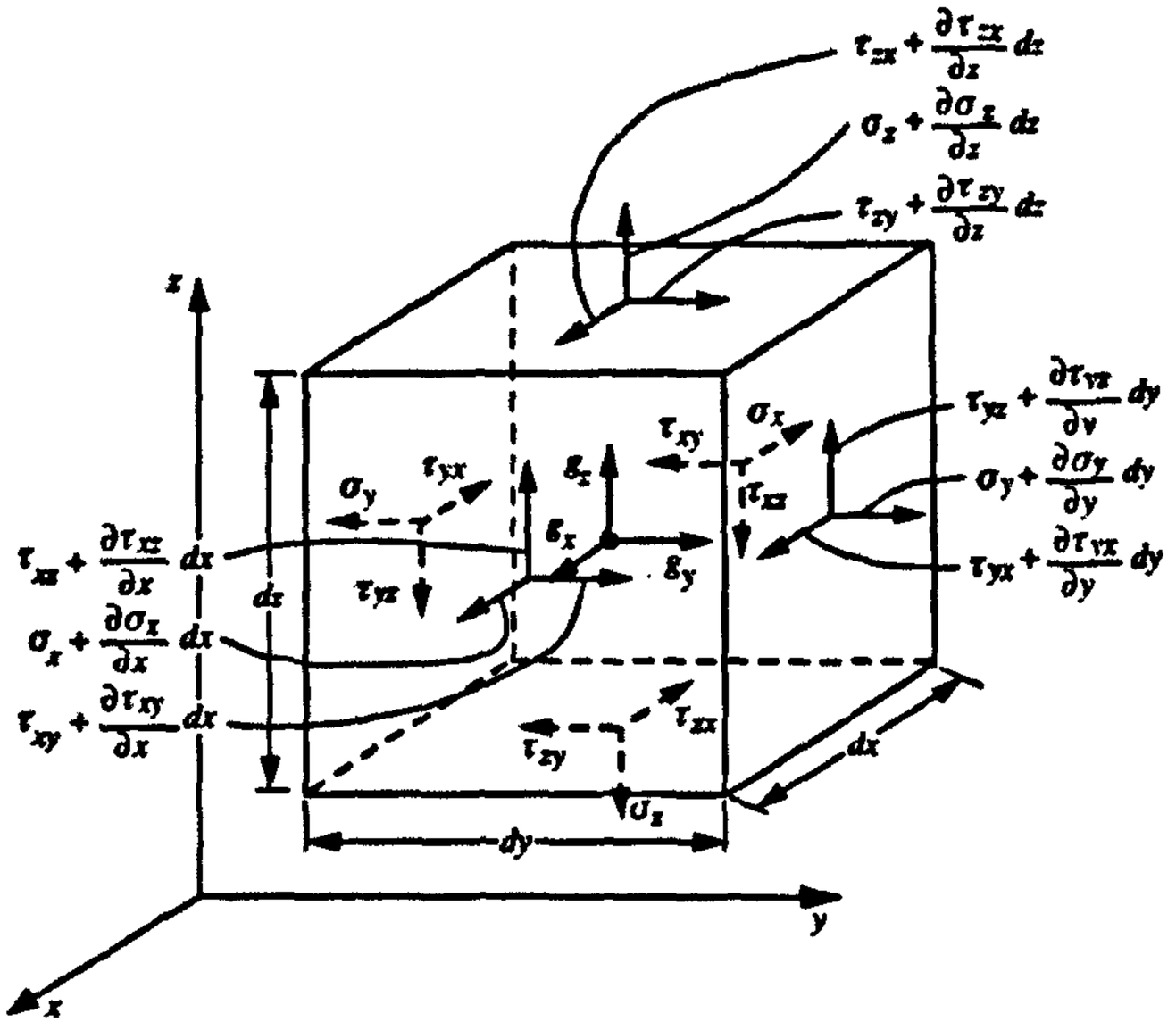

Figure 2.6 Surface stresses on a fluid element after Julien, (2002).

The first subscript indicates the direction normal to the face and the second subscript indicates the direction in which the stress is applied. The identities $\tau_{xy} = \tau_{yx}$, $\tau_{xz} = \tau_{zx}$ and $\tau_{yz} = \tau_{zy}$ result from the sum of the moments of shear stresses around the centroid. The cubic element in Figure 2.6 is considered in equilibrium when the sum of the forces per unit mass in each direction, x, y and z, equals the corresponding Cartesian acceleration components, a_x, a_y and a_z,

$$a_x = g_x + \frac{1}{\rho_m}\frac{\partial \sigma_x}{\partial x} + \frac{1}{\rho_m}\frac{\partial \tau_{yx}}{\partial y} + \frac{1}{\rho_m}\frac{\partial \tau_{zx}}{\partial z} \tag{2.22}$$

$$a_y = g_y + \frac{1}{\rho_m}\frac{\partial \sigma_y}{\partial y} + \frac{1}{\rho_m}\frac{\partial \tau_{xy}}{\partial x} + \frac{1}{\rho_m}\frac{\partial \tau_{zy}}{\partial z} \tag{2.23}$$

$$a_z = g_z + \frac{1}{\rho_m}\frac{\partial \sigma_z}{\partial z} + \frac{1}{\rho_m}\frac{\partial \tau_{xz}}{\partial x} + \frac{1}{\rho_m}\frac{\partial \tau_{yz}}{\partial y} \tag{2.24}$$

where, ρ_m is the density of mass-sediment mixture.

These equations of motion are general, without any restriction to compressibility, viscous shear, turbulence or other effects. The normal stresses can be rewritten as a function of pressure, p and additional normal stresses, τ_{xx}, τ_{yy} and τ_{zz} as,

$$\sigma_x = -p + \tau_{xx} \tag{2.25}$$

$$\sigma_y = -p + \tau_{yy} \tag{2.26}$$

$$\sigma_z = -p + \tau_{zz} \tag{2.27}$$

After the acceleration components a_x, a_y and a_z from equations (2.17) to (2.19) are considered, the equations of motion in the Cartesian coordinates can be written as,

$$a_x = \frac{\partial v_x}{\partial t} + v_x\frac{\partial v_x}{\partial x} + v_y\frac{\partial v_x}{\partial y} + v_z\frac{\partial v_x}{\partial z}$$
$$= g_x - \frac{1}{\rho_m}\frac{\partial p}{\partial x} + \frac{1}{\rho_m}\left(\frac{\partial \tau_{xx}}{\partial x} + \frac{\partial \tau_{yx}}{\partial y} + \frac{\partial \tau_{zx}}{\partial z}\right) \tag{2.28}$$

$$a_y = \frac{\partial v_y}{\partial t} + v_x\frac{\partial v_y}{\partial x} + v_y\frac{\partial v_y}{\partial y} + v_z\frac{\partial v_y}{\partial z}$$
$$= g_y - \frac{1}{\rho_m}\frac{\partial p}{\partial y} + \frac{1}{\rho_m}\left(\frac{\partial \tau_{xy}}{\partial x} + \frac{\partial \tau_{yy}}{\partial y} + \frac{\partial \tau_{zy}}{\partial z}\right) \tag{2.29}$$

$$a_z = \frac{\partial v_z}{\partial t} + v_x\frac{\partial v_z}{\partial x} + v_y\frac{\partial v_z}{\partial y} + v_z\frac{\partial v_z}{\partial z}$$
$$= g_z - \frac{1}{\rho_m}\frac{\partial p}{\partial x} + \frac{1}{\rho_m}\left(\frac{\partial \tau_{xz}}{\partial x} + \frac{\partial \tau_{yz}}{\partial y} + \frac{\partial \tau_{zz}}{\partial z}\right) \tag{2.30}$$

2.9 Hydraulic and energy grade lines

Consider a small element of fluid in a wide rectangular channel at a bed slope of S_o as shown in Figure 2.7. The flow is 1D and in x- direction; thus $v = v_x$ and $v_y = v_z = 0$. The shear stress that is due to the element stretching is $\tau_{xx} = 0$. The effects of the bank shear τ_{yx} can be neglected but the bed shear stress, τ_{zx}, is significant. At small bed slope angles, $\sin\theta \approx \tan\theta$ and $g_x = g\sin\theta \cong gS_o$, the equation of motion in the x-direction can be written as,

$$\frac{\partial v_x}{\partial t} + v_x \frac{\partial v_x}{\partial x} \cong g S_o - \frac{1}{\rho}\frac{\partial p}{\partial x} + \frac{1}{\rho}\frac{\partial \tau_{zx}}{\partial z} \tag{2.31}$$

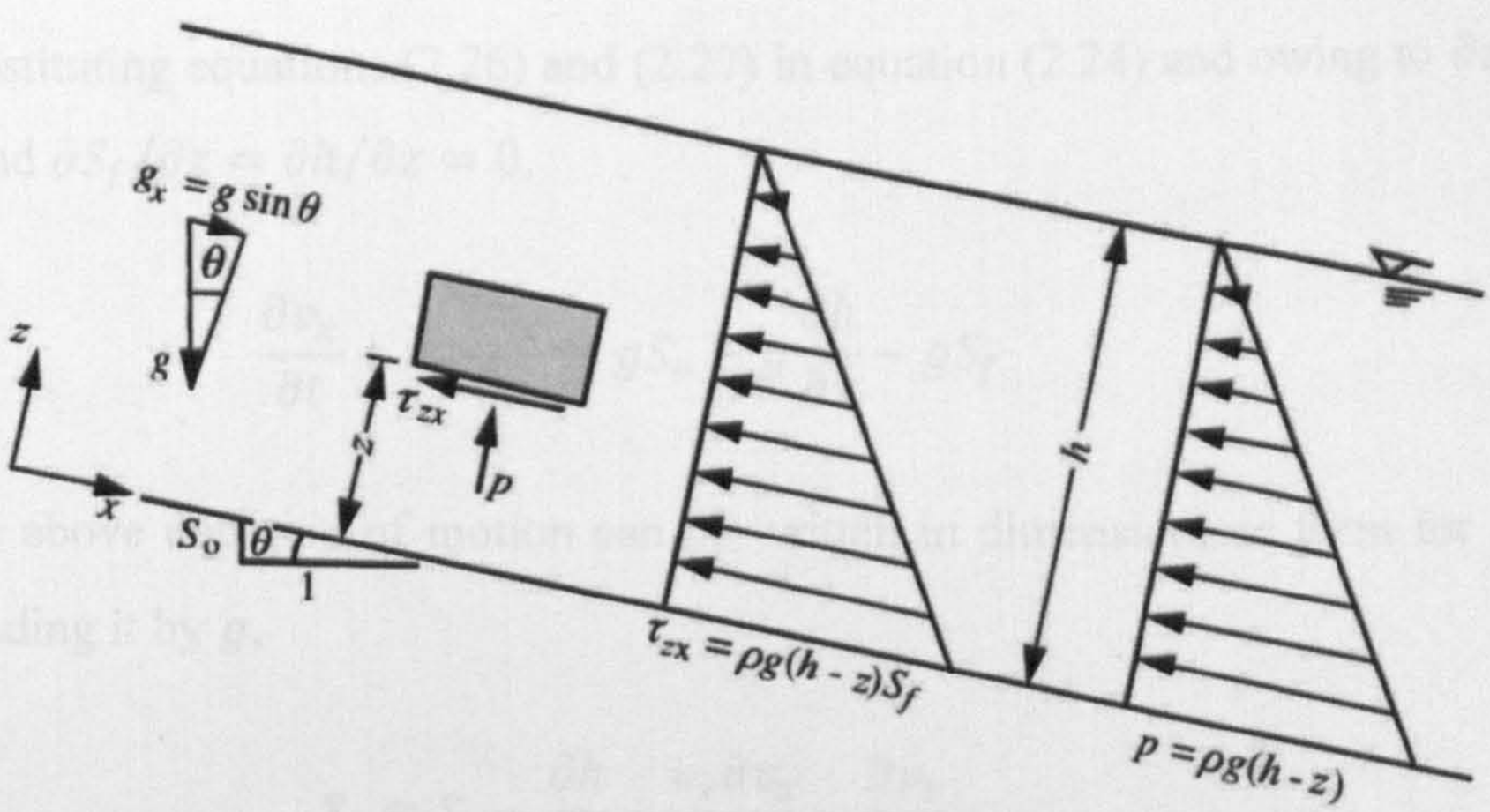

Figure 2.7 Pressure and shear stress distribution in a fluid column after Julien, (2002).

The pressure distribution can be obtained by integrating equation (2.23), given that $a_z = 0$ and that shear stress variation is small. The resulting hydrostatic pressure approximation that may be defined by $g_z = g\cos\theta \approx -g$ from the bed elevation is,

$$\int_p^0 dp = \rho \int_z^h -g dz$$

$$p = \rho g(h - z) \tag{2.32}$$

at the bed, $z = 0$, the pressure is $p_o = \rho g h$ and the relative pressure vanishes at the free surface, $p = 0$ when $z = h$.

The bed shear stress, τ_o, is obtained from the definition of the friction slope, S_f, for steady uniform flow as,

$$\tau_o = \rho g h S_f \tag{2.33}$$

Like pressure, the shear stress vanishes at the free surface and varies linearly over the depth. The shear stress distribution is thus,

$$\tau_{zx} = \rho g(h - z)S_f \tag{2.34}$$

Substituting equations (2.26) and (2.27) in equation (2.24) and owing to $\partial z/\partial x = 0$ and $\partial S_f/\partial z = \partial h/\partial z = 0$,

$$\frac{\partial v_x}{\partial t} + v_x \frac{\partial v_x}{\partial x} \cong gS_o - g\frac{\partial h}{\partial x} - gS_f \tag{2.35}$$

The above equation of motion can be written in dimensionless form for S_f after dividing it by g,

$$S_f \cong S_o - \frac{\partial h}{\partial x} - \frac{v_x \partial v_x}{g\partial x} - \frac{\partial v_x}{g\partial t} \tag{2.36}$$

The point velocity, v_x, can be replaced by mean flow velocity, V, considering that the correction factor is close to unity,

$$S_f \cong S_o - \frac{\partial h}{\partial x} - \frac{V}{g}\frac{\partial V}{\partial x} - \frac{1}{g}\frac{\partial V}{\partial t} \tag{2.37}$$

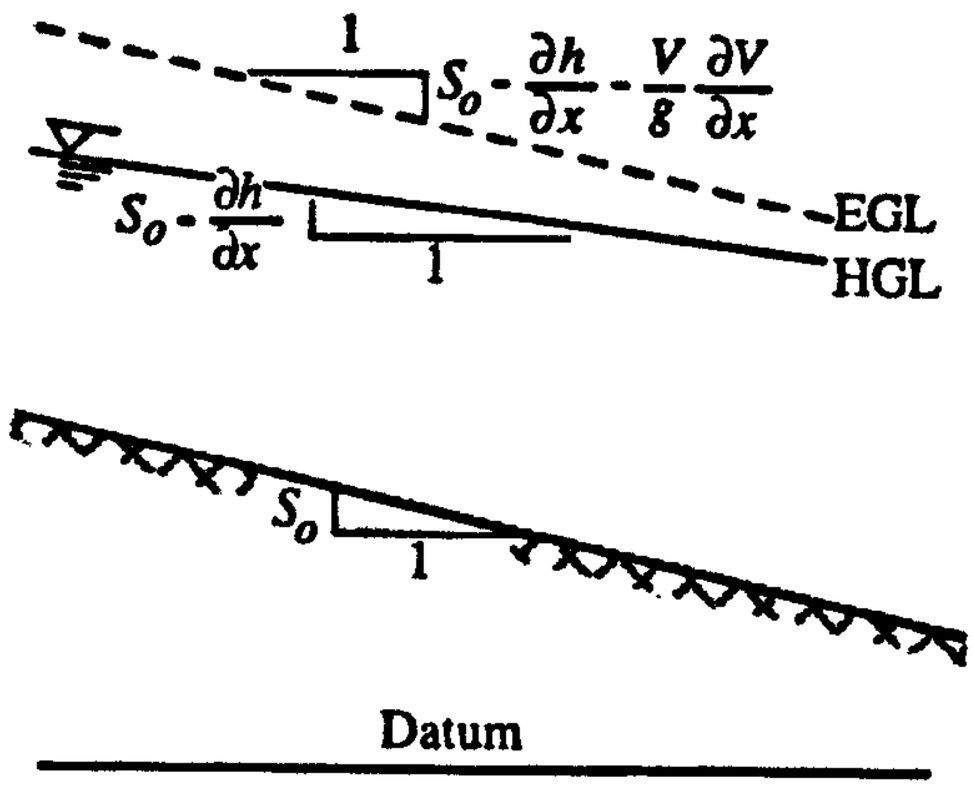

Figure 2.8 Energy grade line (EGL) and hydraulic grade line (HGL) after Julien, (2002).

Figure 2.8 shows the graphical representation of the three slopes considering that $S_o = -(\partial z/\partial x)$. Thus the first term on the right hand side of equation (2.30)

physically describes the bed slope, the first two terms describe the free surface slope and the first three terms describe the slope of the energy grade line.

2.10 Open channel equilibrium

An open channel is stable when all the particles along its wetted perimeter are not moving. This implies that, without transport of bed material, a cross sectional geometry cannot change with time. Consider the cross-sectional geometry of a straight channel for which all particles of weight F_s along the wetted perimeter are at incipient motion. The critical shear stress τ_{sc} on a side slope θ is determined in analogy to the critical shear stress τ_c that corresponds to the angle of repose, φ. A very simplified but elegant equilibrium relationship was proposed by Lane (1953) who, after assuming that $\tau_c \sim F_s tan\varphi$ and the resultant on the side slope $R/F_s cos\theta = tan\varphi$ obtained,

$$\frac{\tau_{sc}}{\tau_c} = \sqrt{1 - \frac{sin^2\theta}{sin^2\varphi}} = cos\theta \sqrt{1 - \frac{tan^2\theta}{tan^2\varphi}} \tag{2.38}$$

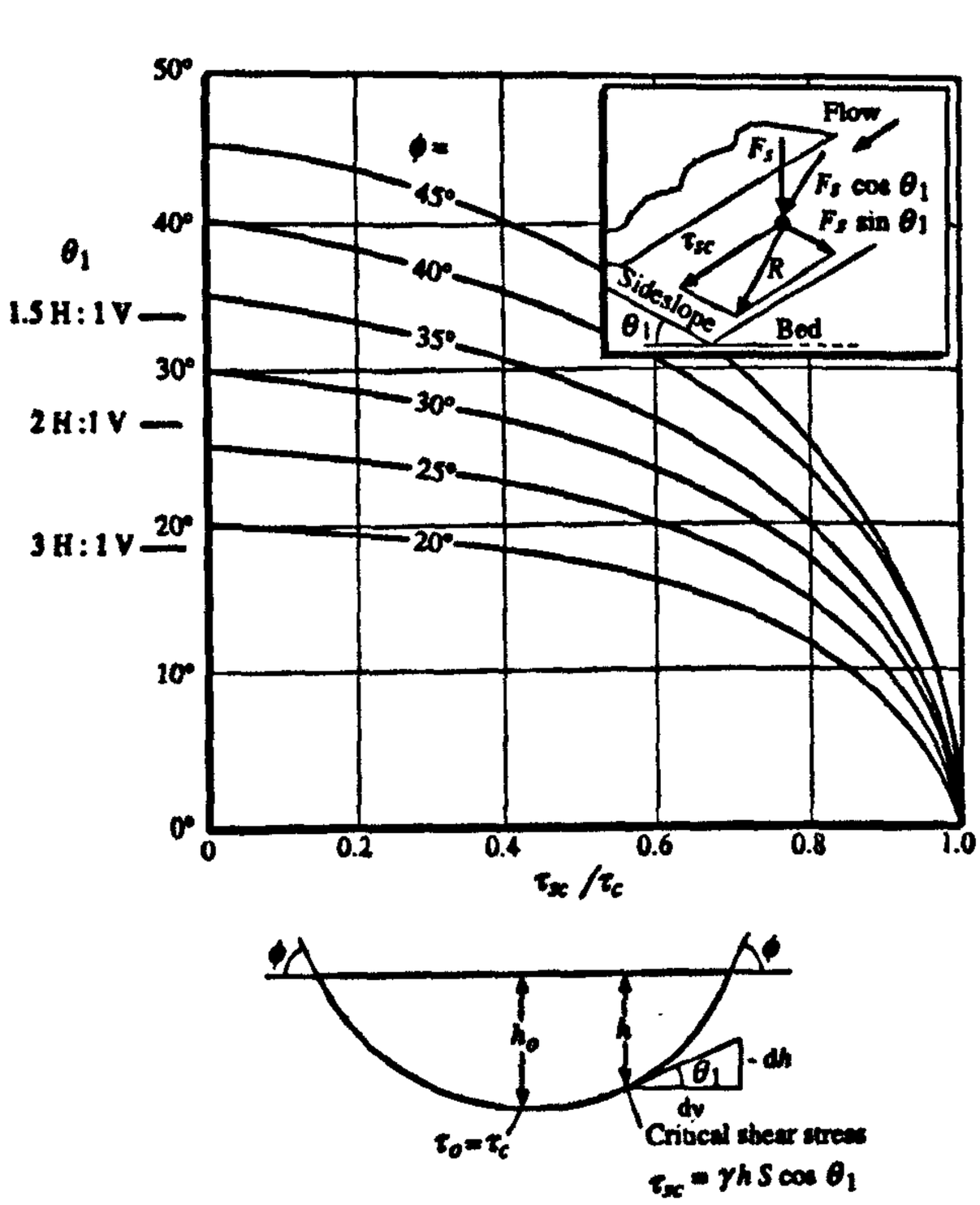

Figure 2.9 Ideal cross sectional geometry after Julien, (2002).

As shown in Figure 2.9, the shear stress along the deepest point in the channel is $\tau_c = \gamma h_o S$ and on the side slope is $\tau_o = \gamma h S cos\theta$. Equating both equations for γS gives,

$$\gamma S = \frac{\tau_c}{h_o} = \frac{\tau_o}{h cos\theta}$$

$$\tau_o h_o = \tau_c h cos\theta \tag{2.39}$$

The differential equation for the ideal cross section geometry is obtained from $\theta = -dh/dx$ after τ_o/τ_c is cancelled from equations (2.31) and (2.32), thus,

$$\left(\frac{dh}{dy}\right)^2 + \left(\frac{h}{h_o}\right)^2 tan^2\varphi = tan^2\varphi \tag{2.40}$$

where, h_o is the flow depth at the centre line of the channel.

The ideal cross sectional geometry in which all particles are at incipient motion has a co-sinusoidal shape, with y measured laterally from the centre line,

$$\frac{h}{h_o} = cos\left(\frac{y tan\varphi}{h_o}\right) \tag{2.41}$$

The flow depth corresponds to incipient motion on a plane surface, $0.047(G - 1)d_s/S$, where G is the relative density of sediment and d_s is the particle size. The surface width can be obtained from equation (2.34) by calculating the value of y at $h = 0$, as $h_o\pi/tan\varphi$. The width depth ratio is constant and equal to $\pi\, cot\varphi$. The cross sectional area is $2h_o^2 cot\varphi$ and the hydraulic radius is,

$$R = \frac{8h_o cos\varphi}{\pi(4 - sin^2\varphi)} \tag{2.42}$$

The mean flow velocity, V, is then obtained from the resistance relationship, the Manning equation.

2.11 Regime relationships

The construction of irrigation canals in Pakistan and India fostered investigation of the design of canals under regime conditions i.e. canal that is non-silting and non-scouring or in other words canal having no net change in its sediment content over a length (Julien, 2002). Empirical relationships have been proposed by Kennedy (1895) and Lacey (1930). The Lacey silt factor f_e was defined to designate the properties of "Kennedy's standard silt" of the Upper Bari Doab canal. The geometry of canals with different bed materials were compared in terms of different values of f_e. The silt factor, f_l, was shown to increase with grain size, the approximate relationship $f_l = 1.59 d_{mm}^{1/2}$ can be used. The key relationships from Lacey determined the mean flow velocity, V, in feet per second, the hydraulic radius, R, in feet, the cross-section area, A, in square feet, the wetted perimeter, P, in feet, and the dimensionless slope as a function of the design discharge, Q, in cubic feet per second, and the Lacey silt factor,

$$V = 0.794\, Q^{1/6}\, f_l^{1/3} \tag{2.43}$$

$$R = 0.47\, Q^{1/3}\, f_l^{-1/3} \tag{2.44}$$

$$A = 1.26\, Q^{5/6}\, f_l^{-1/3} \tag{2.45}$$

$$P = 2.66\, Q^{1/2} \tag{2.46}$$

$$S = 0.00053\, Q^{-1/6}\, f_l^{5/3} \tag{2.47}$$

In wide-shallow channels, the hydraulic radius is approximately equal to the flow depth, and the channel width can often be approximated by the wetted perimeter. The width–depth ratio thus increases slightly with discharge and decreases slightly with grain size. Another characteristic of the regime equation is that once the discharge and grain size are determined a unique value of bed slope is calculated from equation (2.47). Note that the method does not allow changes in slope at a given discharge and grain size. Consequently, the velocity in Eq. (6.43) does not depend on slope.

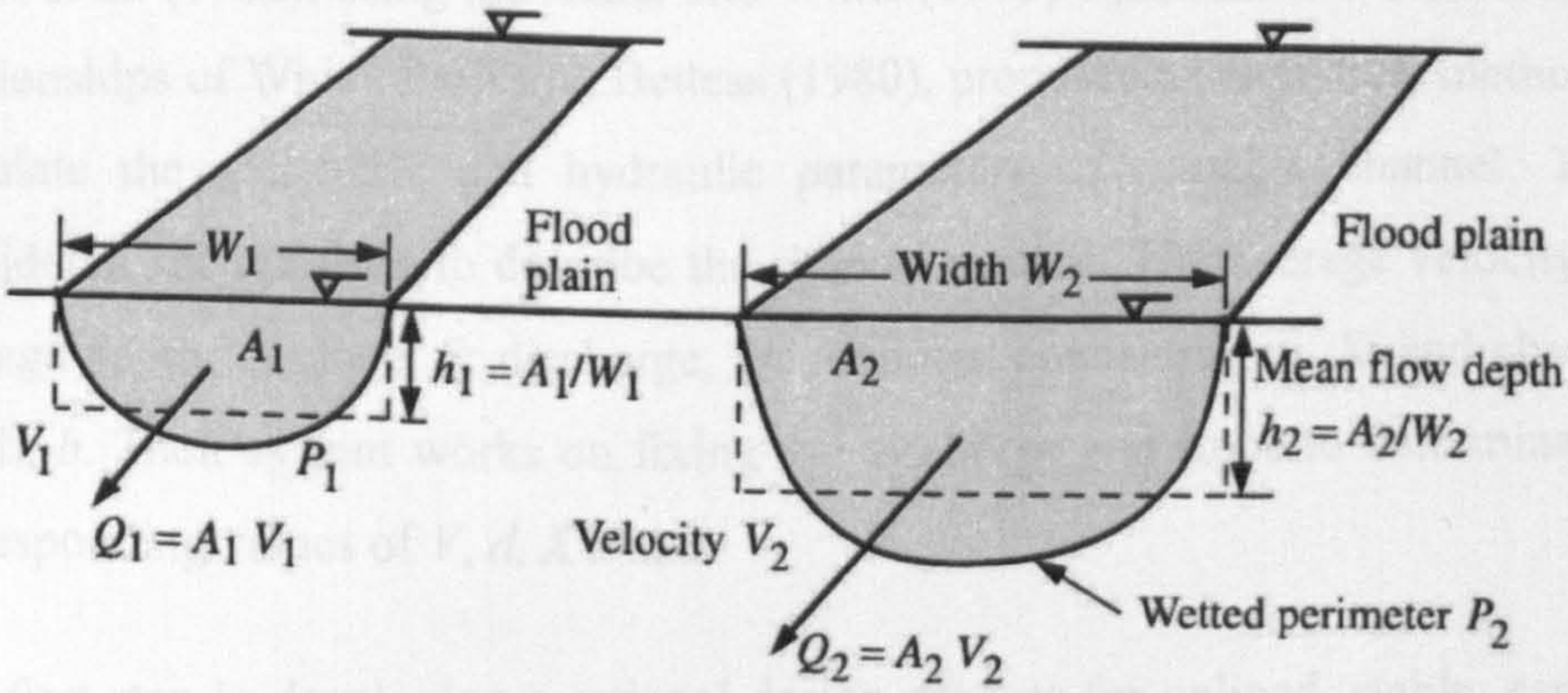

Figure 2.10 Downstream hydraulic geometry after Julien, (2002).

The regime equations refer to downstream channel geometry at a given bankfull discharge. As shown in Figure 2.10, different discharges in equations (2.43) to (2.47) correspond to bankfull conditions in different channels. Because these channels can be located at different positions in the same fluvial system, channel properties are referred to as downstream hydraulic geometry. Downstream hydraulic geometry describes bankfull conditions for different cross sections, as opposed to the at-a-station hydraulic geometry that describes channel properties at different discharges at a given cross section.

2.12 Design of stable, unlined, earthen open-channels

A stable channel section is one in which neither objectionable scour nor deposition occurs. The design of such stable channels is complex as in such channels the stability not only depends on the hydraulic parameters but also on the properties of the materials, which composes the bed and sides of the channel (French, 1985). Fortier and Scobey (1926) published the results of a survey taken by The American Society of Civil Engineers' Special Committee on Irrigation Hydraulics. These results went on to become the theoretical basis for the channel design method known as the "Method of maximum permissible velocity". This pioneering work of Fortier and Scobey (1926) was the basis of channel design for many years but it is design methodology based on experience and observation rather than physical principles (French, 1985).

White *et al.* (1982), using the Acker and White (1973) equations and the frictional relationships of White, Paris and Bettess (1980), proposed an analytical method to calculate the geometric and hydraulic parameters of a stable channel. They considered six variables to describe the channel system: The average velocity, V; average depth, d; slope, S; discharge, Q; sediment concentration, X; and channel width, b. Their system works on fixing the discharge and slope to determine the corresponding values of V, d, X and b.

The first step in developing a rational design process for unlined, stable, earthen channels is to examine the forces, which cause scour. When a particle rests on the bottom of a channel, the force acting to cause movement is the result of the flow of water past the particle. Similarly, a particle resting on the side slope is acted on not only the flow-generated force, but also by the gravitational component, which tends to make the particle roll or slide down the slope. If the resultant of these two forces is greater than the forces resisting movement, gravity and cohesion, then erosion of the channel perimeter occurs. By definition, a tractive force or shear force is the force acting the particles composing the perimeter of the channel and is result of the flow of water past these particles. In practice, this tractive force or shear force is not the force acting on a single particle but over a certain area of the channel perimeter (Lane, 1955).

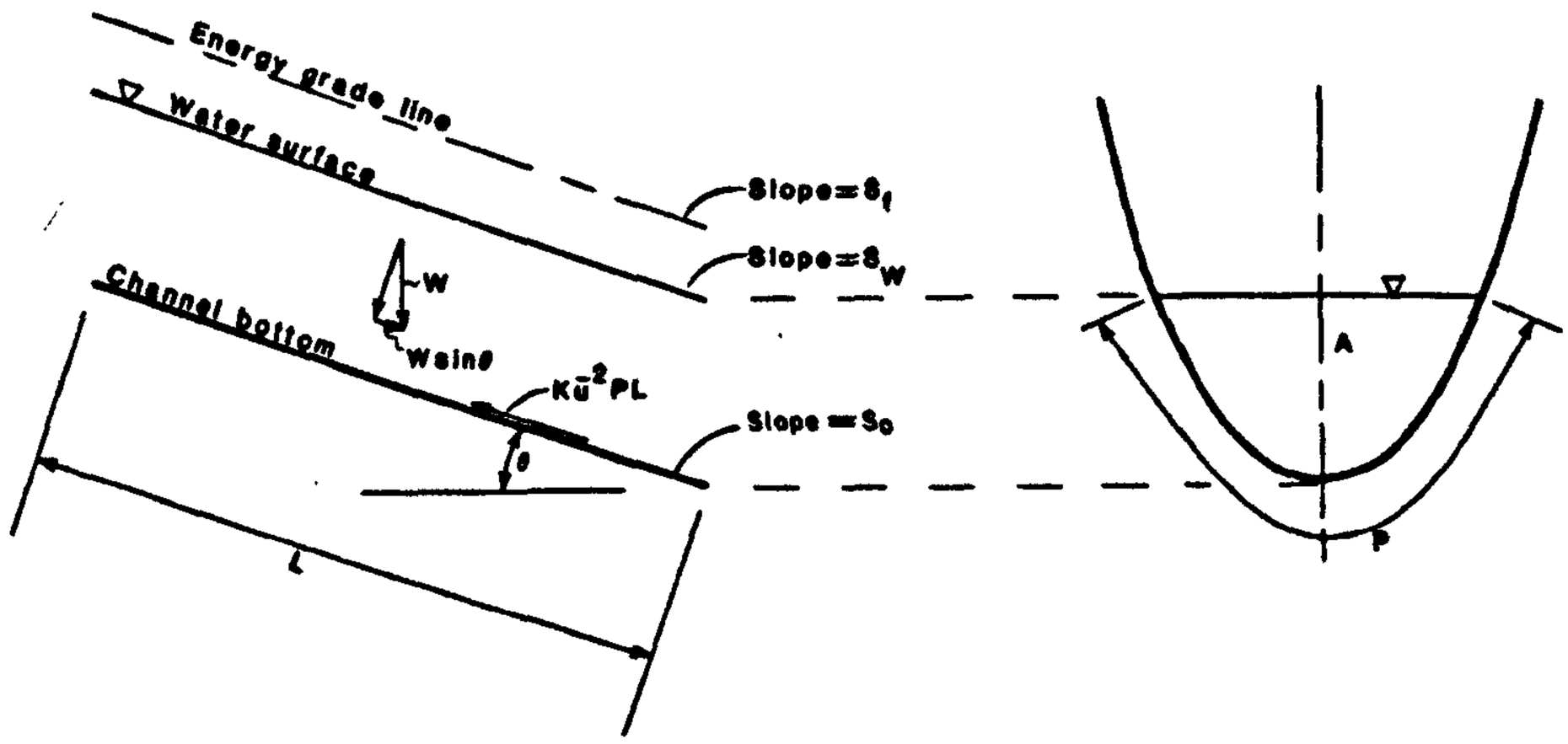

Figure 2.11 Schematic definition of variables in open channel uniform flow after French, (1985).

Figure 2.11 shows the schematic definition of the variables in open channel uniform flow. The shear force in uniform flow should be approximated by the effective gravitational force acting on the water within control volume and parallel to the channel bottom,

$$F_t = \gamma ALS \tag{2.48}$$

where, A is the channel cross sectional area, L is the length of the control volume and S is the longitudinal slope of the channel.

The unit shear force is,

$$\tau_o = \frac{\gamma ALS}{PL} = \gamma RS \tag{2.49}$$

where, τ_o is the average value of the shear force per unit of the wetted area, γ is the specific weight or unit weight of water, P is the wetted perimeter of the channel and R is the hydraulic radius.

In most channels, shear force is not uniformly distributed over the perimeter, and, therefore, for an accurate design methodology to be developed, the distribution of the shear force on the perimeter of the channel must be estimated (French, 1985).

2.13 Shear Stress in a Moving Fluid

There can be no shear stress in a fluid at rest and it is developed when the fluid is in motion or in other words, when the particles of the fluid move relative to each other having different velocities.

The fluid in contact with the boundary adheres to it and therefore will have the same velocity as the boundary. Considering successive layers parallel to the boundary, the velocity of the fluid will vary from layer to layer as its distance varies from the boundary.

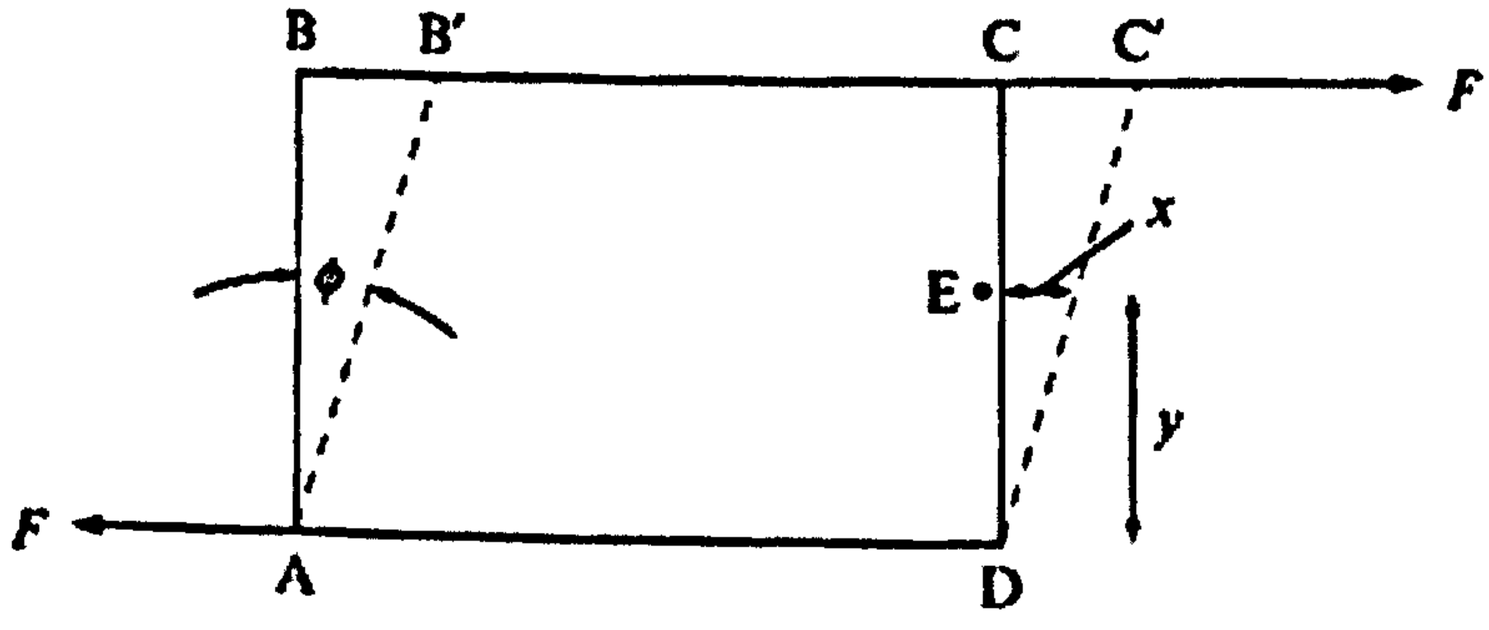

Figure 2.12 Development of shear in a fluid after Douglas *et al.* (2005).

Consider an element *ABCD* in a fluid with the thickness '*s*' perpendicular to the diagram as shown in the Figure 2.1. The force '*F*' will act over an area '*A*' equal to *BC* x *s*. Hence the shear stress τ is,

$$\tau = \frac{F}{A} \tag{2.50}$$

and the shear strain/deformation will be measured by angle 'ϕ'. In a fluid contrary to solids the shear strain will continue to increase with time and the fluid will flow. It has been found experimentally that the rate of shear strain is directly proportional to the shear stress (Douglas *et al.*, 2005).

Consider a particle '*E*' at a distance '*y*' from *AD*, and suppose it moves through a distance '*x*' in time '*t*', then for small angles,

$$shear\ strain = \emptyset = \frac{y}{x} \tag{2.51}$$

and

$$rate\ of\ shear\ strain\ \frac{x}{yt} = \frac{\left(\frac{x}{t}\right)}{y} = \frac{u}{y} \tag{2.52}$$

where, '*u*' is the velocity of the particle *E*.

Since shear stress is proportional to the shear strain,

$$\tau \propto \frac{u}{y} \tag{2.53}$$

$$\tau = constant \frac{u}{y} \tag{2.54}$$

Here the constant of proportionality is the dynamic viscosity of the fluid and is usually denoted by 'μ'.

$$\tau = \mu \frac{u}{y} \tag{2.55}$$

The term u/y is the change of velocity with 'y' and in differential form may be written as du/dy and may be substituted in equation (2.55) as,

$$\tau = \mu \frac{du}{dy} \tag{2.56}$$

This is also called the Newton's law of viscosity.

2.14 Shear Stress Distribution

We know that shear stress is the force per unit area in the flow direction. Consider a control volume, with its surface defined by *ABCD*, and a unit width perpendicular to the surface as shown in the Figure 2.13. The internal shear 'τ' at any level 'z' above the channel bed can be obtained. The x-coordinate is in the flow direction along the channel slope S, and the z-coordinate is perpendicular to the flow. The forces acting on the element having a length 'dx' will be as follows:

The hydrostatic pressure forces on *AB* and *CD*.

The shear stress 'τ' acting on *BC*.

The x-component of the fluid weight 'W_x' for the control volume.

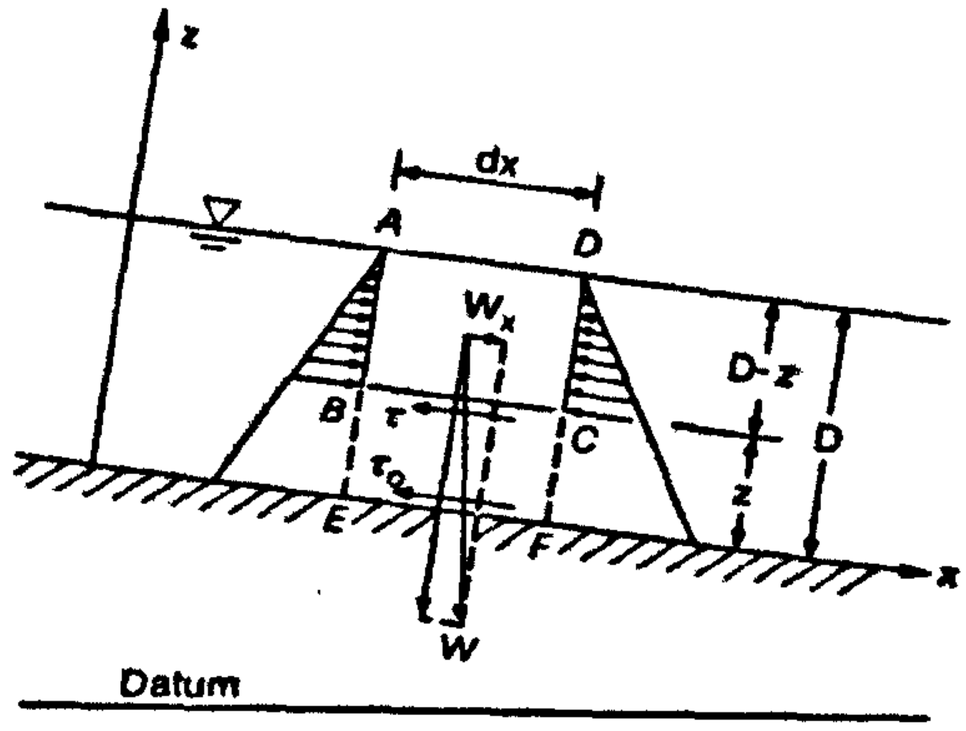

Figure 2.13 Schematic of forces on control volume after Chang (1988).

For uniform flow conditions, the hydrostatic forces are in balance and therefore 'W_x' must be counterbalanced by the shear force.

$$W_x = \tau dx \tag{2.57}$$

$$W.S - \tau.dx = 0 \tag{2.58}$$

Replacing the weight 'W' by '$\gamma\ (D\text{-}z)\ dx$' in equation (2.58)

$$\gamma(D-z)dx.S - \tau.dx = 0 \tag{2.59}$$

where, 'γ' is the specific weight of the fluid and is equal to 'ρg' and 'D' is the depth of flow,

$$\text{or } \tau = \gamma(D-z)S \tag{2.60}$$

Hence from equation (2.60), we can say that the shear stress varies linearly with the depth.

If the channel flow is three-dimensional, the average shear on the channel boundary τ_o can be obtained by considering a control volume *AEFD*, as shown in the previous Figure 2.13, with a differential reach length 'dx' and a cross sectional area of the channel 'A'. The weight of the fluid in the volume would be $\gamma A dx$. We know that the x-component of 'W' is counter balanced by the boundary shear force, therefore,

$$\gamma A dx.S = \tau_o P dx \tag{2.61}$$

where, 'P' is the wetted perimeter.

$$\tau_o = \frac{\gamma AS}{P} \tag{2.62}$$

therefore,

$$\tau_o = \gamma RS \tag{2.63}$$

where, 'R' is the hydraulic radius which is equal to A/P.

2.15 Reynolds Number

It is defined as the ratio of inertial force to the friction force. We know that several type of forces usually act on the volume of an element, the frictional forces proportional to the viscosity 'μ', the inertial forces proportional to the density 'ρ', the pressure forces and the volume forces e.g. gravitational force 'g'.

For motion, which is mainly in the x-direction, the inertial force per unit volume is,

$$\rho \frac{du}{dt} \tag{2.64}$$

where 'u' is the velocity component in the x-direction and d/dt is the substantial derivative. For steady flow this can be written as,

$$\rho \frac{du}{dx}\frac{dx}{dt} \tag{2.65}$$

which is equal to,

$$\rho u \frac{du}{dx} \tag{2.66}$$

where, du/dx is the change in velocity with position.

The inertial force per unit volume is therefore,

$$\rho u \frac{du}{dx} \tag{2.67}$$

From Newton's law of friction, we know that,

$$\tau = \mu \frac{du}{dx} \tag{2.68}$$

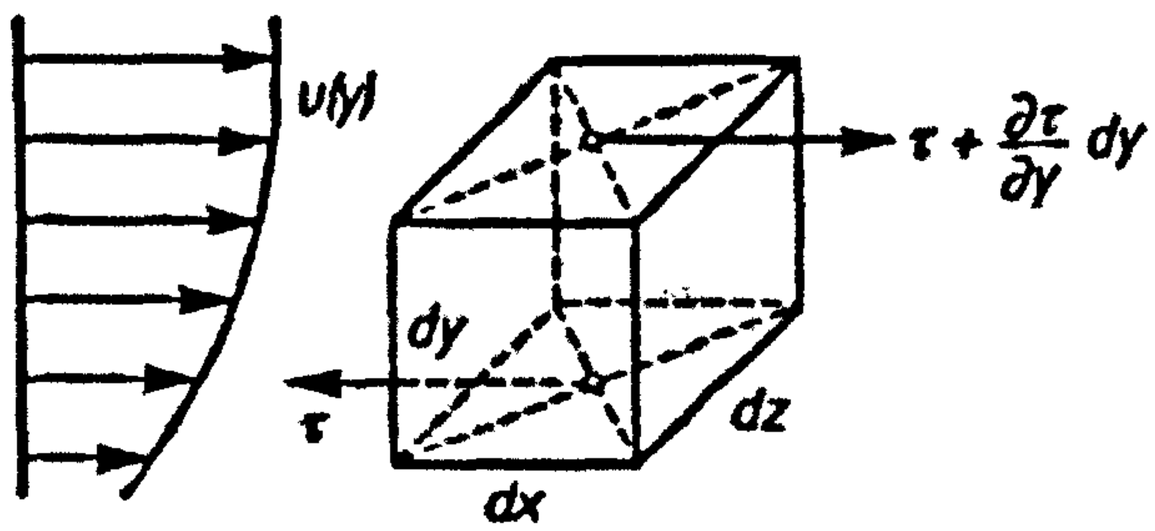

Figure 2.14 Friction forces on a volume element after Schlichting, (2000).

For a volume element whose x-direction is in the direction of motion, gives rise to the following expression for the shear forces,

$$\left(\tau + \frac{\partial \tau}{\partial y}\partial y\right) dxdz - \tau dxdz = \frac{\partial t}{\partial y} dxdydz \tag{2.69}$$

The frictional force per unit volume is thus $\partial\tau/\partial y$, which according to Newton's law of friction becomes, $\mu \frac{\partial^2 u}{\partial y^2}$

Hence the ratio of inertial force to friction force, which is nothing but Reynolds Number, becomes

$$R_e = \frac{inertial\ force}{friction\ force} = \frac{\rho u\, \partial u/\partial x}{\mu\, \partial^2 u/\partial y^2} \approx \frac{\rho(V^2/d)}{\mu(V/d^2)} \tag{2.70}$$

Since the velocity at any point in the flow field 'u' is proportional to the free stream velocity 'V', the velocity gradient $\partial u/\partial x$ is proportional to the V/d ratio and $\partial^2 u/\partial y^2$ is proportional to the V/d^2 ratio, where, d is the characteristic length dimension of the body such as sphere's diameter.

Therefore,

$$R_e = \frac{\rho V d}{\mu} \tag{2.71}$$

Since Kinematic Viscosity $\nu = \mu/\rho$, therefore the above expression may also be written as,

$$R_e = \frac{V d}{\nu} \tag{2.72}$$

The Reynolds number is also a criterion for the classification of flow into laminar flow, transitional flow, or turbulent flow and may be defined as below:

2.15.1 Laminar Flow

A flow in which the viscous forces are so large relative to the inertial forces that the flow is dominated by the viscous forces then it is called a laminar flow. In such a flow, the fluid particles move along definite, smooth paths in a coherent fashion. Laminar flow is usually occurs when Reynolds number is less than or equal to 500.

2.15.2 Transitional Flow

A flow, which can be, classified neither as laminar flow nor is turbulent flow called transitional flow. Transitional flow usually occurs for Reynolds number ranging from 500 to 12500.

2.15.3 Turbulent Flow

A flow in which the inertial forces are large as relative to the viscous forces such that the inertial forces dominate the situation then it is called a turbulent flow. Turbulent flow usually occurs when Reynolds number is greater than 12500.

For the present study all the flows have Reynolds number greater than 12500 and are therefore turbulent flows.

2.16 The Darcy – Weisbach Formula

The Darcy – Weisbach formula was originally developed for pipe flow (Chow, 1959). It defines the friction factor 'f' as a dimensionless number,

$$f = \frac{4\tau_o}{\frac{1}{2}\rho U_m^2} \tag{2.73}$$

where, τ_o is the average shear stress at the boundary, ρ is the mass density of the fluid and U_m is the mean velocity of flow. We know that shear stress τ_o is equal to γRS and hence the above equation becomes,

$$f = \frac{4\gamma RS}{\frac{1}{2}\rho U_m^2} \tag{2.74}$$

$$f = \frac{8\gamma RS}{\rho U_m^2} \tag{2.75}$$

$$U_m = \sqrt{\frac{8gRS}{f}} \tag{2.76}$$

$$\frac{U_m}{U_*} = \left(\frac{8}{f}\right)^{1/2} \tag{2.77}$$

where, $U_* = \sqrt{gRS}$ is the friction or shear velocity.

Yen (2002) gives for steady uniform flow in open channels with rigid impervious boundary, having Reynolds number greater than 25000, a Colebrook-White type formula as,

$$\frac{1}{\sqrt{f}} = -K_1 \log\left(\frac{k_s}{K_2 R} + \frac{K_3}{4R_e\sqrt{f}}\right) \tag{2.78}$$

where, 'k_s' is the Nikuradse sand roughness height, K_1, K_2 and K_3 are coefficients or constants.

2.17 Nikuradse sand roughness

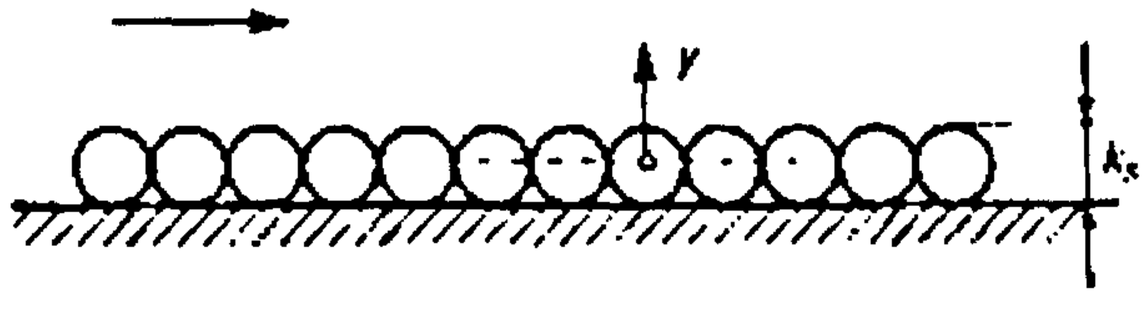

Figure 2.15 Nikuradse sand roughness height k_s (Schlichting, 2000).

The wall surfaces always exhibits some roughness in reality. Since there can be infinite number of possible surface states, a standard roughness has been introduced to describe the effect of roughness on a flow (Schlichting, 2000). Here it is assumed as shown in the Figure 2.15 that the wall is covered with a layer of spheres packed together as densely as possible. The diameter of the sphere is called the sand roughness height 'k_s' and is a measure of the surface roughness of the wall. For the present study the roughness height is taken in Nikuradse sand roughness height and is specified wherever necessary.

2.18 Composite or Compound Channel Roughness

In many of the designed artificial channels and most natural channels, the roughness varies along the perimeter of the channel, and in such cases it is some times necessary to calculate an equivalent value of the roughness coefficient for the entire perimeter. Yen (2002) says that composite/compound resistance coefficient of a cross section can be expressed in the Manning's 'n' form, with the cross sectional value of 'n_c', being a weighted sum of the local resistance factors so that the open channel flow computations can be kept in the *1-D* analysis. He has compiled a list of formulas proposed by different researchers for computing 'n_c' based on different assumptions about the relationships of the discharges, velocities, forces or shear stress between the component sub-sections and the total cross-section. He has also compiled a list of different methods, which have been proposed to divide the cross-section into sub-sections for the application of these formulas. In dividing the section into sub-sections the internal water lines have

never been used in the computations of wetted perimeters or Hydraulic radii assuming that the dividing water lines have a zero internal shear stress.

2.19 Sidewall Correction

Laboratory streams inevitably always have a smaller width to depth ratio than natural streams. The results of the flume experiments therefore cannot be expected to correspond to field experiments unless a correction for the shear on the wall is made (Vanoni & Brooks, 1957). In most of the Laboratory flumes experiments the walls are not as rough as the bed because of sand beds and hence the distribution of shear is not uniform. As the bed becomes rougher, the shear on the bed increases and the shear on the wall decreases relative to the bed since the bed offer more resistance to the flow. Because of the variable effect of the wall caused by the changing bed roughness, a wall correction is needed to unify the results. Vanoni & Brooks (1957) divided the channel cross section into two sub-sections, one corresponding to the channel bed and the other to the channel walls assuming the boundaries between the channel bed and walls to have zero shear and therefore were not considered in calculations for wetted perimeter and hydraulic radii.

2.20 Conclusions

Some basic definitions used in the open channel flow kinematics related to the research were discussed in this chapter. The effect of flowing water on the boundaries and the design of stable unlined earthen channels was also looked into.

The next chapter gives a brief literature review on the subject of boundary shear stress distribution by different researchers and also discusses various hypotheses of dividing the channel cross section into three parts for accurate prediction of wall shear stress.

CHAPTER 3

LITERATURE REVIEW

3.1 Introduction

This review intends to present some selected significant contributions to measurements of shear stress in open channels. Some of the earliest experimental works as well as some hypotheses on the separation of shear stress on the wetted perimeter on the subject are looked into. It should be noted that a considerable amount of open channel flow research has been undertaken in this field and the present review does not pretend to be exhaustive.

The concept of dividing the channel cross section into different parts corresponding to the bed and sidewalls for the calculation of boundary shear stress has been very old and different researchers from time to time have brought about some new concepts based on different hypotheses. The contributions of different researchers on the subject have also been briefly described here in this chapter.

3.2 Shear stress measurement

Several methods are known for determining the intensity of shear stress on a portion of the fixed boundary of a fluid flow. These include both direct and indirect measurements. A standard indirect technique employed in boundary layer investigation involves the measurement of velocity and pressure profiles normal to the boundary at successive cross sections and then solving for shear. The results are less satisfactory if the shear is small or varies in a complex fashion (Ghosh and Roy, 1970).

Ludweig (1949) developed an indirect method that relates shear force to the loss of heat from a hot spot on the boundary to the flow medium. A method developed by Murphy and Smith (1956) relates shear force to the evaporation of a liquid film from the boundary. In both these cases the insulation between the boundary and its surrounding must be excellent or considerable error may result.

Preston (1954) successfully developed a simple technique for estimating the local shear on smooth boundaries using a pitot tube in contact with the surface. The method is based on the assumption of an inner law,

$$\frac{u}{u_*} = 8.67\left(\frac{u_* y}{\nu}\right)^{1/7} \tag{3.1}$$

where, u is the velocity at a distance y from the boundary, u_* is the shear velocity and ν is the kinematic viscosity relating the local wall shear to the velocity distribution near the wall.

After the availability of the Preston tube (Preston, 1954), Ippen *et al.* (1960) and Ippen and Drinker (1962) were among the first to demonstrate the applicability of this technique to the open channel work. Another good work on the distribution of boundary shear stress in smooth rectangular open channels with the help of Preston tube is by Kartha and Leutheusser (1970). They used laboratory flumes of various aspect ratios from 1 to 12.5 for their study.

Hsu (1955) using a similar velocity distribution equation as Preston's established the analytical relationship between the dynamic pressure reading and the local shear. Hwang and Laursen (1963) also extended the Preston's technique for estimating the local shear for rough boundaries. They developed an analytical relationship between the dynamic pressures acting on the pitot tube in contact with the rough surface and the local shear.

Another indirect method commonly used is based on the logarithmic velocity distribution after Prandtl-Karman, which involves the measurement of velocity profiles along lines normal to the boundary. From the semi-log plot of the closely spaced velocity profiles observed near the boundary, the distribution of M of the velocity distribution law along the boundary can be determined which when divided by a constant factor and κ, Karman's turbulent coefficient, yields the local shear distribution. This is expressed as,

$$u = M \log\frac{y}{y_o} \tag{3.2}$$

where, $M = 2.303\frac{\sqrt{\tau_o}}{\rho}$, τ_o is the local shear stress, ρ is the fluid density, and y_o is the distance at which the velocity distribution indicates zero velocity.

Liepman and Dhawan (1952) have done direct measurement of the boundary shear in air by measuring the shear force on a small isolated floating element of the surface. However, maintaining a small distance around the element, keeping it in line and recording small shear force are indeed very difficult.

Lane (1955) has analyzed several analytical techniques developed for predicting the shear stress distribution over the wetted perimeter of the channel cross section.

Ghosh and Roy (1970) employed a new direct measurement technique, which in essence consists of isolating a certain length from a long channel and suspending it in line, leaving a gap at the side and bottom. They measured local boundary shear on both rough and smooth rectangular and trapezoidal channel sections and compared the results with indirect estimates like pitot tube technique and wall shear given by Karman-Prandtl logarithmic velocity distribution law. Of the two indirect estimates, the surface pitot tube technique was found to be more reliable.

3.3 Experimental work on Boundary shear stress distribution

Since 1970s several experimental studies have been reported like Ghosh and Roy (1970), Kartha and Leutheusser (1970), Myers (1978), Knight and Macdonald (1979), Knight (1981), Noutsopoulos and Hadjipanos (1982), Knight *et al.* (1984), Knight and Patel (1985), Flintham and Carling (1988), Tominaga *et al.* (1989), Knight and Sterling (2000), Mohammadi and Knight (2004) etc. on the smooth and rough open channels as well as closed conduits. Some of these findings are discussed below.

Ghosh and Roy (1970) obtained the boundary shear stress distribution in smooth and rough open channels of both rectangular and trapezoidal sections by direct measurement of shear drag on an isolated length of a test channel utilizing the technique of three point suspension system. They compared their results with other indirect estimates from isovels and Preston tube measurements. They found

that the shear stress distribution along the wetted perimeter is nonuniform in character.

Kartha and Leutheusser (1970) carried out experiments on smooth laboratory flumes of rectangular cross section to calculate wall shear stress. They were of the opinion that none of the analytical techniques available at that time for calculation of shear stress was good enough to be counted upon for the design of alluvial channels.

Myers (1978) again used the Preston tube to measure the shear stress distribution around the periphery of a complex channel consisting of a deep section and a flood plain. He concluded that there was strong momentum transfer due to interaction between the channel flow and that over its flood plain, which causes significant magnitude of shear force. Failure to take account of this phenomenon results in serious overestimation of channel section's carrying capacity for any depth of flow.

Knight and Macdonald (1979b) carried out experiments in rectangular flumes to calculate the distribution of velocity and boundary shear stress. They varied the bed roughness and aspect ratios of the channels to find their influence on the results. They found that the ratio between the mean sidewall and bed shear stress varied between 0.2 to 1.2 depending upon the boundary roughness distribution and aspect ratio. They also found that for channels with high bed roughness the 100% and 95% two-dimensional flow occurs at b/h equal to 25 and 10 respectively and hence defined concept of wide channels.

Knight (1981) presents a method whereby the mean wall or bed shear stress may be calculated for flows in rectangular channels over a wide range of differential roughness and breadth to depth ratios. He provided empirical equations for the boundary shear on the wall and the bed. The systematic reduction in the shear force carried by the sidewalls with increase in aspect ratio b/h and the bed roughness was illustrated. He has combined the data already published by himself and some other researchers and has asked the others to follow his steps and try to improve his work.

Noutsopoulos and Hadjipanos (1982) did similar work as done by Knight (1981) on simple and compound channels of rectangular cross section using Preston tube and velocity profiles method for measuring boundary shear stress. Their results were some what similar to those of Knight (1981) and they give the value for aspect ratio of 2.34 where the average shear on the sidewall and bed become equal and for Knight (1981) it was 2.4.

Knight *et al.* (1984) worked on the boundary shear stress and boundary shear force distribution in smooth rectangular channels. They did a wonderful job of compiling the data of previous researchers on the subject and then derived empirical equations that give the percentage of the total shear force carried by the sidewalls as a function of aspect ratio *b/h*. They also made some comparisons between boundary shear stress distribution in open channels and closed conduits. They noticed certain differences in the distribution due to the different secondary flow structure.

Knight and Patel (1985) carried out laboratory experiments on the smooth closed ducts of rectangular cross section from aspect ratios of 1 to 10 to calculate the boundary shear stress distribution. They found that the number and shape of the secondary flow cells, which, in turn, depend upon the aspect ratio, influence the distributions. Multiple pairs of contra-rotating secondary flow cells were identified. They also presented for maximum, centre line and mean boundary shear stress on the duct sidewalls in terms of aspect ratio.

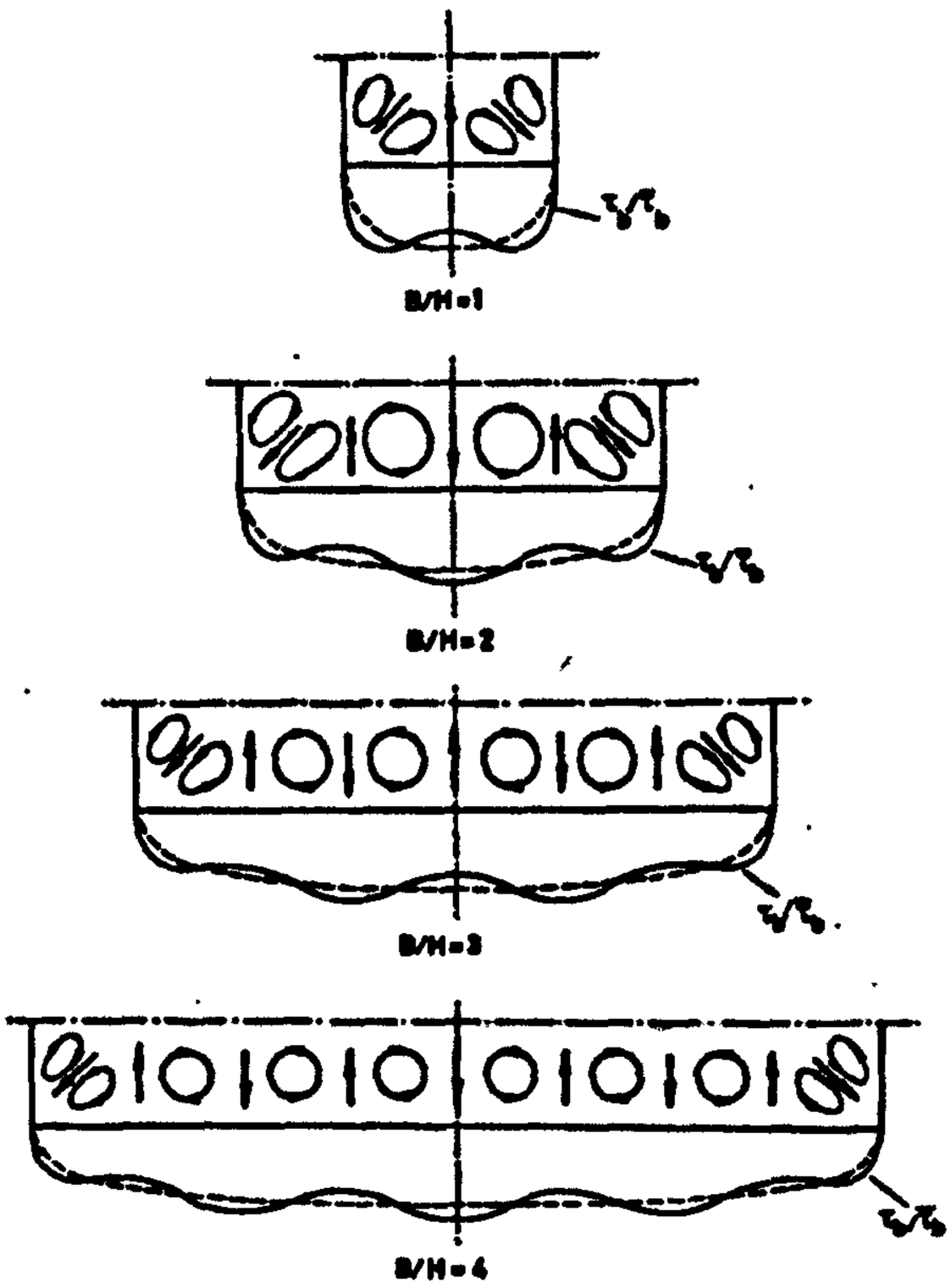

Figure 3.1 Interaction between secondary currents and boundary shear stress distribution as suggested by Knight and Patel (1985).

Flintham and Carling (1988) worked on uniform and differentially roughened rectangular as well as trapezoidal channels to see the effect of roughness on the boundary shear. They provided some equations for the determination of mean bed and sidewall shear stress in straight symmetrical rectangular and trapezoidal channels in which bed roughness is equal to or greater than the sidewall roughness.

Tominaga *et al.* (1989) studied the three dimensional secondary flows and their effects on the boundary shear stress distribution in open channels. The effects of the free surface, channel shape and the boundary roughness on the secondary current structures were investigated experimentally and numerically. They found that the secondary current structure in trapezoidal open channels were different from those in the rectangular channels. They saw that in trapezoidal channels a vortex with reverse rotation of the free surface vortex got generated in the region between sidewall and free surface and consequently the dip in the maximum velocity position does not appear in trapezoidal open channels.

Knight *et al.* (1992) undertook experiments on homogeneously and heterogeneously roughened channels and presented equations for the percentage of the total shear force which acts on the walls and the associated mean and maximum boundary shear stress on both bed and sidewall. These equations include the effects of aspect ratio, wall slant angle and the relative roughness. Their main findings include the general reduction in $\%SF_w$ with the increase in P_b/P_w and k_{sb}/k_{sw} values.

Knight *et al.* (1994) have presented a very comprehensive review of some of the studies on the distribution of boundary shear stress in prismatic and non-prismatic open channels. Knight and co-workers undertook these studies at the University of Birmingham between 1978 and 1992. Design equations are given for quantifying the mean and maximum boundary shear stresses on the bed and sidewalls. The effects of the variations of the Froude number on the results are also analysed.

Knight and Sterling (2000) carried experiments on the boundary shear stress distribution on circular conduits running partially full using the Preston tube technique. The results for the percentage of total shear force carried by the sidewalls have been shown to agree well with the Knight's (1984) empirical formula for prismatic channels.

Mohammadi and Knight (2004) studied the boundary shear stress distribution in V-shaped bottom channels for five flow discharges and four different bed slopes. They found that the percentage shear force carried by the sidewalls was favourably correlated with the perimeter ratio, P_b/P_w rather than aspect ratio, b/h. They compared the results of percentage shear force carried by the sidewalls with other channels of rectangular, trapezoidal and part full circular cross sections and found significant differences and came to the conclusion that the channel shape plays an important part in the distribution of boundary shear stress on the wetted perimeter.

Knight *et al.* (2007), using the so-called Shiono and Knight Method (SKM), presented a simple model for the prediction of depth-averaged velocity and boundary shear in trapezoidal channels with secondary flows. They have used a wide range of boundary shear stress data from various sources to validate their

model. The values for the transverse velocity, v, is shown to be consistent with the observations, whereas the local boundary shear stress distributions do not always match the experimental data despite accurate depth averaged streamwise velocity.

Knight and Tang (2008) give analytical stage-discharge formulae for both zonal and total discharges in straight prismatic channels of simple and compound trapezoidal shapes based on the combination of area method and Shiono and Knight method. Their formulae also permit the boundary shear force to be determined for every linear element on the wetted perimeter. They have shown their predicted results to be in good agreement with the experimental data.

Sharifi *et al.* (2009) present a multi-objective evolutionary algorithm to study the lateral variation of friction factor, f, dimensionless eddy viscosity, λ, and effects of the secondary flow, Γ, the knowledge of which is very essential for calculations under Shiono and Knight method. They provide guidance for choosing appropriate values for the three parameters for modelling flow in smooth homogeneous trapezoidal channels.

Knight *et al.* (2010) give a simple lateral distribution model based on the Shiono and Knight Method of analysis for prediction of lateral distributions of depth-averaged velocity, stage discharge relationships and boundary shear stress. It has the limitation of only being appropriate for steady flow analyses in straight prismatic channels.

3.4 Concept of division line

The concept of dividing the cross section into three parts one corresponding to the bed and two corresponding to the two sidewalls for the determination of boundary shear stress separately on the wetted perimeter has been advancing on different approaches some of which are discussed below.

3.4.1 Division by isovel pattern (Curvilinear approach)

Professor J. B. Leighly in 1932 (Leighly, 1932) was probably the first one to graphically obtain the shear stress distribution for natural channels in the absence of secondary currents. He suggested the idea of indirect determination of the shear

stress distribution with the help of velocity distribution by first determining the isovel pattern and then finding its orthogonal. According to him the mass of water in the section of the stream, of unit length, may be divided into a number of prisms, whose bases are units of area on the bed. After calculating the mass of water in each prism the force exerted on the unit area forming the base may be computed, which is nothing but the shear stress exerted by the water on the bed, by the equation,

$$F = mgS \tag{3.3}$$

where, 'm' is the mass of water, 'g' is the acceleration due to gravity and 'S' is the slope of the channel.

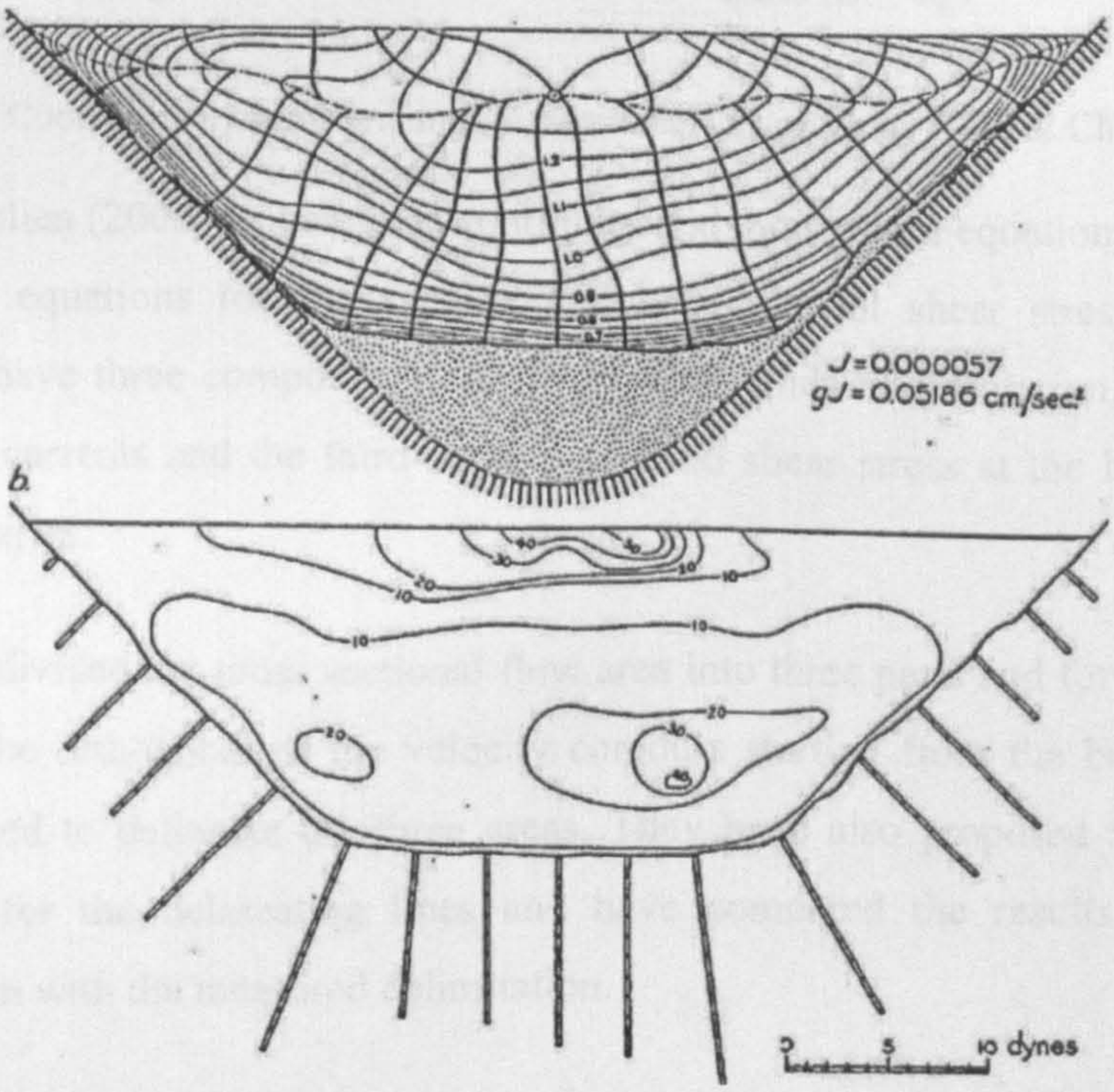

Figure 3.2 Cross sectional velocity distribution and the the forces exerted on the unit areas of bed after Leighly (1932).

Chiu & Chiou (1986) later suggested a mathematical model based on the concept of isovel patterns permitting the application of the Leighly's idea. They developed a parameter estimation method for a 3-dimensional mathematical method, which does not require primary flow velocity data. The method was applied to study a 3-

dimensional structure of flow in rectangular open channels. The interaction among the primary and secondary flows and the shear stress distribution was investigated under various values of Manning's *n*, width to depth ratios and slope of the channels.

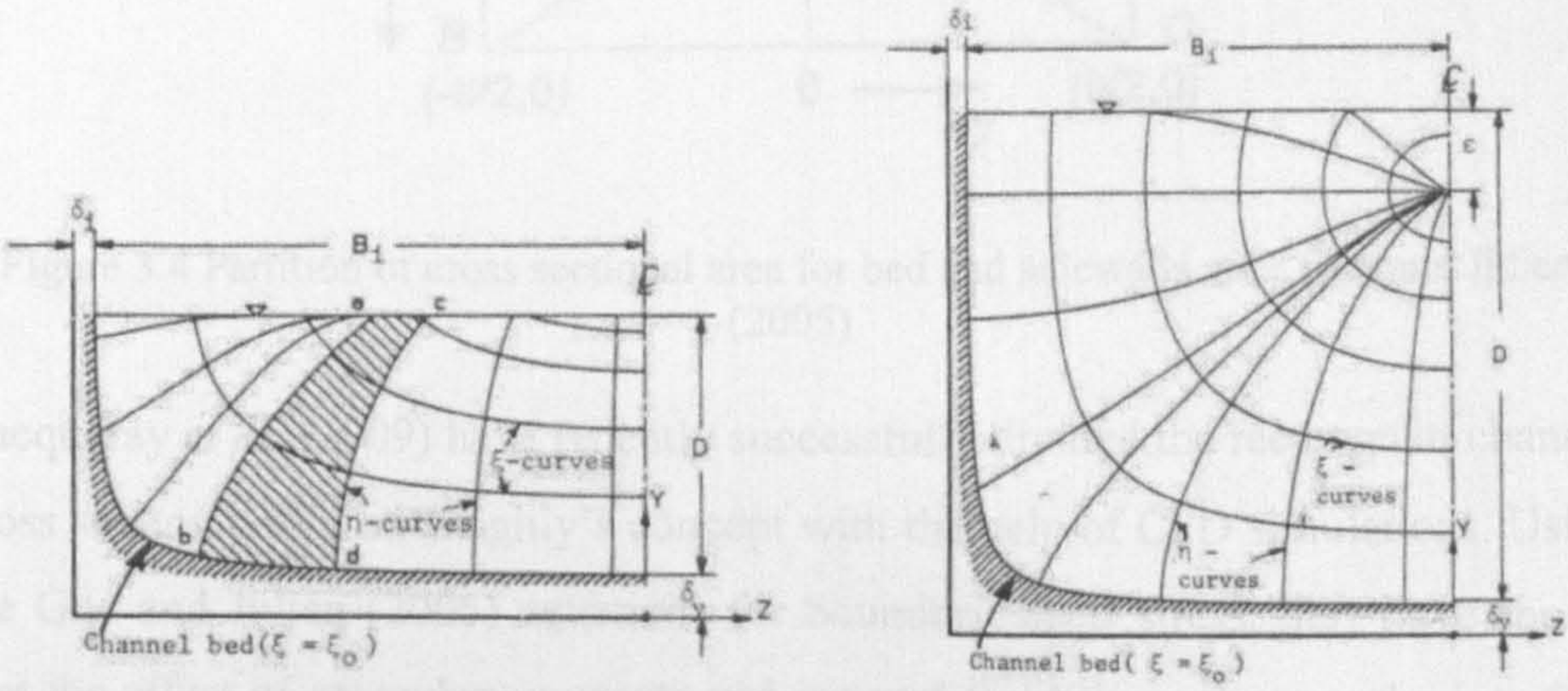

Figure 3.3 Coordinate systems and model parameters as given by Chiu & Chiou (1986)

Guo and Julien (2005) by using the continuity and momentum equations found the theoretical equations for the average bed and sidewall shear stresses. These equations have three components; the first corresponds to gravitation, second to secondary currents and the third to internal fluid shear stress at the interface of two boundaries.

They also divided the cross sectional flow area into three parts and forwarded the idea that the orthogonal of the velocity contours starting from the base corners may be used to delineate the three areas. They have also proposed some basic equations for the delineating lines and have compared the results of model delimitation with the measured delimitation.

Although their proposed mathematical equations consist of three parts but for simplification they have ignored the effects of the secondary currents and the also the eddy viscosity to be constant and hence propose the first term of their equations to be the dominant term for the calculation of average shear stress on the bed and sidewalls.

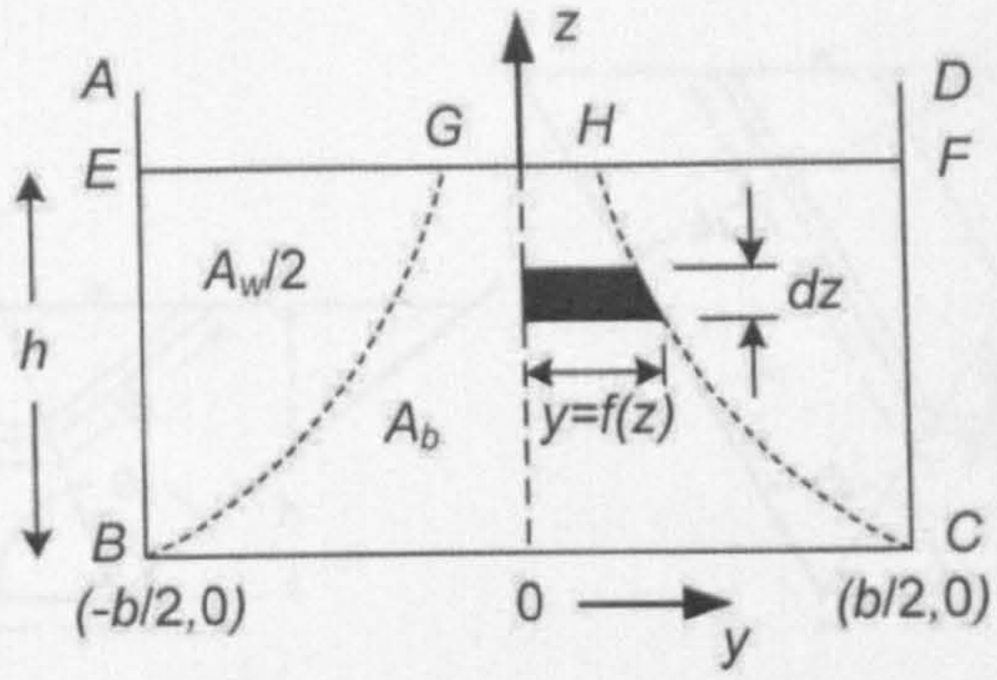

Figure 3.4 Partition of cross sectional area for bed and sidewalls after Guo and Julien (2005)

Cacqueray *et al*. (2009) have recently successfully divided the rectangular channel cross section based on Leighly's concept with the help of CFD simulations. Using the Guo and Julien (2005) equations for boundary shear stress, they have shown that the effect of secondary currents and internal fluid shear stress at the interface is not negligible and contribute significantly on the shear stress development at the boundaries. The shifts of the line due to changes in the channel aspect ratios have also been analysed. After calculating the boundary shear stress with the help of CFD the results have been compared with the experimental results given by Knight *et al.* (1984) which show good agreement. The present study also aims to extend the findings of Cacqueray *et al*. (2009) to trapezoidal channel sections and also compound channels.

3.4.2 Division by straight line approach

After Leighly, Keulegan (1938) proposed that for polygonal channels the flow region can be divided into three parts corresponding to both sidewalls and the bed. He used a straight division line, which is in fact the bisector of the base angle for this purpose.

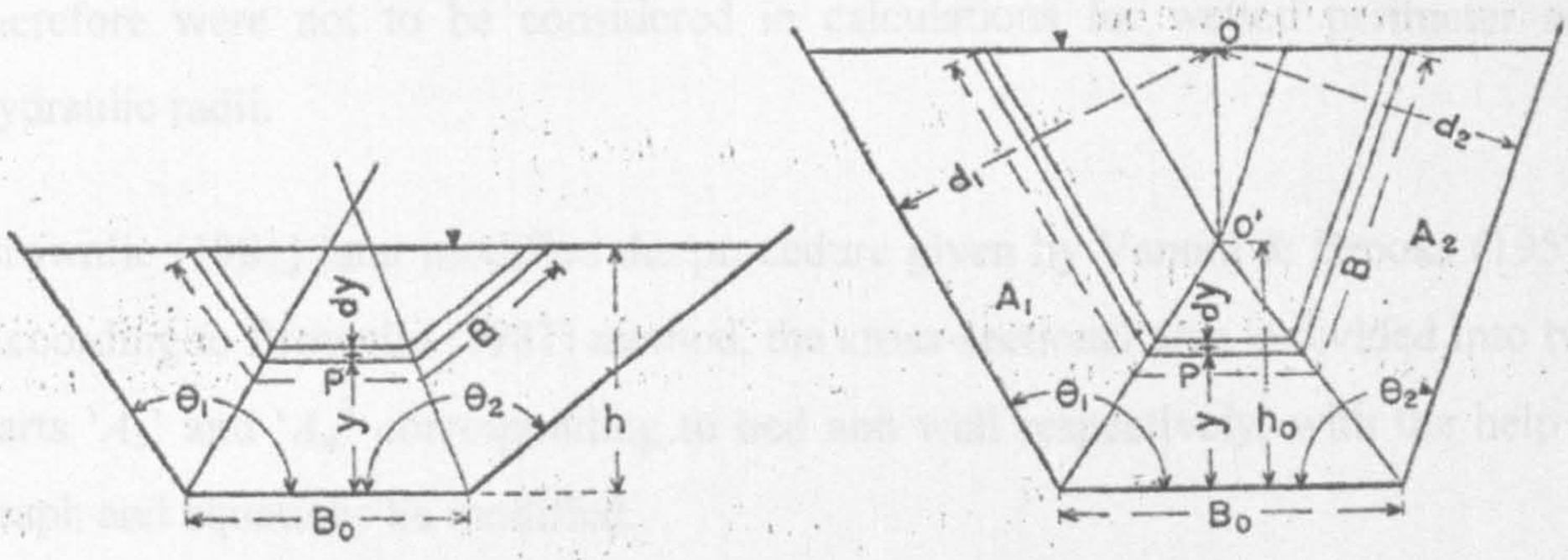

Figure 3.5 Division of Channel cross section into three parts after Keulegan (1938)

For turbulent flow in prismatic channels, Einstein and Haywood (1942) proposed that the shear force exerted on the bed should be separated from that exerted on the lateral boundaries. They divided the flow cross section area into three sub-sections, two that corresponds to the sidewalls, and one that corresponds to the channel bed. Einstein defined two hydraulic radii, one for the wall R_w and one for the bed R_b, and proposed the separation of the channel cross section into two regions as well, each based on local hydraulic radius and roughness coefficient based on the Manning's equation. Einstein does not show any sketch for the division lines but Haywood show straight lines, which are obtained iteratively so that there is zero friction along the lines and the weight of the fluid matches the wall shear force.

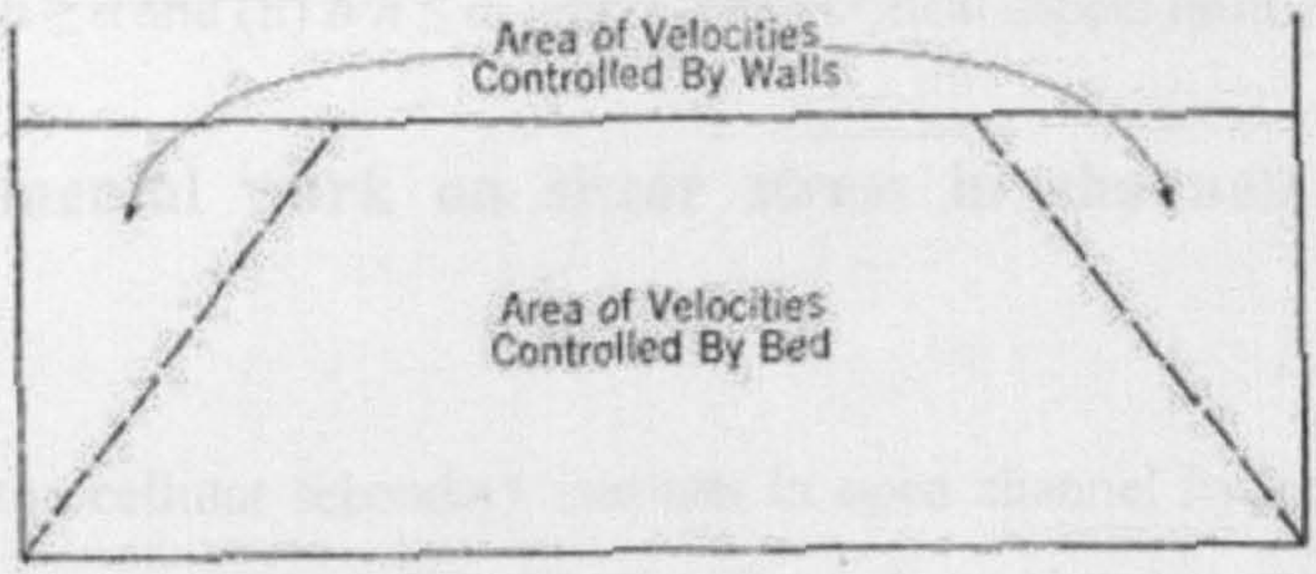

Figure 3.6 Schematic of flume cross section after Einstein and Haywood (1942)

3.4.3 Division by assumption of zero shear on the dividing boundary

Vanoni & Brooks (1957) divided the channel cross section into two sub-sections, one corresponding to the channel bed and the other to the channel walls assuming the boundaries between the channel bed and walls to have zero shear and

therefore were not to be considered in calculations for wetted perimeter and hydraulic radii.

Brownlie (1981) later modified the procedure given by Vanoni & Brooks (1957). According to Brownlie (1981) method, the cross-sectional area is divided into two parts 'A_b' and 'A_w' corresponding to bed and wall respectively, with the help of graph and equations he modified.

3.4.4 Division by concept of dissipation of surplus energy

Yang & Lim (1997 & 1998) proposed the concept that the surplus energy of a unit volume of fluid in a 3-dimensional flow channel will be transported towards and dissipated at a boundary in a direction, which defined a minimum relative distance 'φ' between the source concerned and the boundary. This relative distance depends upon the roughness of the boundary as the rough boundary has a larger capacity to energy dissipation as compared to a smooth boundary.

Based on this concept a generalized criterion for the partitioning of the flow cross sectional area into various parts corresponding to the channel shape and roughness composition on the wetted perimeter is developed. It is a straight line, based on the concept given by Einstein (1942), which is actually the line of zero Reynolds shear stress within the flow cross sectional area. They have worked on both the cases i.e. (i) $b/h \geq \alpha$ and (ii) $b/h \leq \alpha$, where α is a critical aspect ratio.

3.5 Experimental work on shear stress in channels with bed forms

The study of the cellular secondary currents in open channel hydraulics is very important as they are responsible for the three dimensional variation of flow patterns, wall shear stress, sediment transport and bed forms (Nezu and Rodi, 1985). Open channel flows are mostly three dimensional and the primary flow, along the channel main direction, is greatly affected by the secondary flow in the cross stream and vertical directions. Prandtl (1952) classified secondary flows into two categories. Secondary flow of first kind is usually seen in curved or meandering channels in which the flow may circulate in the cross-sectional plane

either driven by centrifugal or transverse pressure gradients. Secondary flow of the second kind is related to the non-homogeneity and anisotropy of the turbulence and may be caused due to number of reasons such as asymmetry of the channel boundaries, free surface effects or variation in bed conditions (Wang & Cheng, 2006).

So-called lines of boil, consisting of low speed streaks and high in sediment concentration have been reported in the literature. These boiling streets, as they are usually known, are formed periodically in the transverse direction and the distance between any two neighbouring boiling lines is around twice the flow depth (Nezu, 2005). Some experimental research work has been carried out after these observations on the fluid motion in conduits with longitudinal bed forms. Nezu and Nakagawa (1984) carried out some experimental preliminary work on cellular secondary currents to assess the interaction between secondary currents and the bed forms. Using Laser Doppler Anemometer (LDA) and ultra sonic bed form instrument Nezu *et al.* (1988) and Nezu and Nakagawa (1989) found that some organized fluid motions and the associated sediment transport occurred side by side on a moveable plane sand bed.

Nezu and Nakagawa (1984 & 1993) proposed that the evolution process of longitudinal bed forms starts with the presence of the corner vortex, which is created due to the sidewall effect. This corner vortex creates lateral variations in bed shear stress and ultimately leads to the formation of the sand ridges near the walls. This further induces and/or modifies the bed shear stress in the lateral direction, generating new vortices. This process carries on until the cellular secondary currents and the sand ridges occur across the entire section. Colombini (1993) however argues that the initiation of cellular secondary flows is an instability-related process. Small disturbances either from the bed surface or the flow itself are responsible for the stream-wise vortices which then produce lateral sediment transport and sorting. Nezu and Rodi (1985) also point out that when aspect ratio b/h is greater than or equal to 5, i.e. in wide open channels, time averaged secondary currents are not readily identified, but instantaneous patterns do exist. They fluctuate in time and space and might not be captured in a long time-averaged analysis. These instantaneous secondary currents may be

responsible for the formation of smooth and rough strips on the bed and, ultimately, sand ribbons, which in turn stabilize secondary currents in space.

Ikeda (1981) studied the size and shape of the self-formed strips with uniform non-cohesive sands and found that longitudinal sand ridges were formed over the entire movable bed. The crests of the ridges were several millimetres high and the distance between adjacent crests was roughly twice the flow depth.

Nezu *et al.* (1985) mention that the bed shear stress attains a mild peak in the side-wall zone and would be scoured first to become a trough. This sand thus scoured would be carried both downstream because of the downstream velocity component, u, and sideways because of the lateral velocity component, v, (corner cellular currents) and then gather to form the first ridge.

Grass *et al.* (1991) describe the results of physical experiments which demonstrate the presence of powerful vortical structures with a general horseshoe-type configuration in the turbulent boundary layers over rough walls. These horseshoe-type vortical structures, usually combined an asymmetrical or partly rolled-up motion, represent the dominant dynamic element in the smooth wall boundary layer turbulence. They extract energy from the mean shear flow by vortex stretching mechanism and act as pumps transporting mass, momentum, vorticity and contaminants across the boundary layer.

Ansari *et al.* (2011) studied the wall shear and secondary current variation in trapezoidal channels and also found that no secondary currents were generated in the central portion of the wide channels ($b/h > 5$) with rigid beds. They were initially concerned that their model was incomplete, though it agreed with Nezu and Rodi (1985) but decided to investigate this issue further. The detailed mechanisms that control the generation and maintenance of cellular secondary currents (and the resulting bed forms) have not yet been explained (Choi *et al.*, 2007). It is the mutual interaction between morpho-dynamics and hydrodynamics that is responsible for the bed ridges and the boiling streets.

3.6 Shear stress distribution in bends

Natural alluvial channels are very rarely straight along reaches of more than a few channel widths (Chang, 1988). Curvature affects the flow of water in an open channel in several ways. These include super-elevation on the outer bank, development of secondary flow (cross-stream circulation) also called the helical flow driven by a centrifugal force, the redistribution of the longitudinal velocities and scouring along the outer banks and depositing along the inner bank in mobile boundaries (Jin & Steffler, 1993). In spite of its practical importance, the mechanisms responsible for the redistribution of velocities and the boundary shear stress in open channel bends are not yet fully understood (Blanckaert & Graf, 2004). It is thus very important to be able to evaluate these effects in a channel during their design for the stability.

Ippen and Drinker (1962) investigated the distribution of boundary shear stress in curved reaches of smooth trapezoidal channels under the condition of subcritical flow. They conducted series of tests to determine the effects of variation in discharge and bend geometry on the shear pattern. Their channels varied in aspect ratio, b/h, of 7 and 12. They found that the local shear stress was as high as twice the mean shear stress computed from uniform flow.

Some more work on the subject has recently been done e.g. Blanckaert and Graf (2001) and Blanckaert and De Vriend (2005) but it is still an area which needs to be developed further.

3.7 Conclusions

In this chapter an extensive review of the work done on shear stress distribution was presented. Different techniques available for the measurement of shear stress were listed. Many of the experimental findings on the subject discussed. Although a lot of experimental work has been done on the distribution of shear stress and flow structures in open channels and closed conduits but not enough has been reported on the numerical analysis on the subject.

The next chapter gives an insight into the various numerical techniques available and discusses the steps involved in constructing a model in computational fluid dynamics (CFD) generally. The commercially available CFD software used is also looked into.

CHAPTER 4

NUMERICAL MODELLING

4.1 Introduction

This chapter contains a brief description of the numerical methods used within this research and also the description of the software used. The boundary conditions, which are required to define a specific situation under investigation, are also discussed.

4.2 Introduction to computational fluid dynamics (CFD)

Computational Fluid Dynamics, (CFD), is a computer-based tool for simulating and analysing systems involving fluid flow, heat transfer and other associated phenomena. It works by numerically solving the equations of fluid flow over a region of interest, with specified or known conditions at the boundaries of that region. Modern CFD techniques emerged between the late 1960s and early 1970s when fluid flow investigations were largely experiment based and only very simple fluid flow problems could be accurately numerically solved. With the rapid development of modern computational techniques and numerical solution methodologies over the last few decades, CFD has now been widely used in various industrial applications for investigating a vast range of industrial and environmental problems. However, compared to industrial applications, using CFD to model morphology and hydrology problems is relatively new, research on channel flow CFD modelling has been very active, particularly in recent years (e.g. Nezu and Nakagawa, 1993; Lane, 1998; Ma *et al.*, 2002; Cao *et al.*, 2003, etc.). This can be largely attributed to the availability of adequate computational resources at a reasonably low cost. CFD has increasingly acted as a supplementary tool to the more traditional methods in the systematic investigations of various controls in river morphology, flow structure and sediment transport, and it has increasingly played an important role in river management and flood prediction. Issues such as spatial and geometry resolution, grid resolution, grid dependence, representation of wall roughness, appropriate

turbulence models, etc., are all currently under intensive discussion (e.g. Hardy *et al.*, 1999, Morvan *et al.*, 2008). Nevertheless, with a numerical model and boundary conditions that provide adequate representations of the key processes of the fluid flow investigated, CFD simulations may provide considerable insight into, and clear explanations of, the structure of the flow and the interactions of the key components of the processes than do the traditional field or laboratory measurements. Practically, there are several unique advantages of CFD over experiment based approaches in fluid system designs e.g. substantial reduction of lead times and costs of new designs, ability to study systems where controlled experiments are difficult or impossible to perform as in the case of very large systems, ability to study systems under hazardous conditions at and beyond their normal performance limits as in the cases of safety studies and accident scenarios, or practically unlimited level of detail of results (Versteeg & Malalasekera, 2007). Thus CFD provides a cost-effective and accurate alternative to scale model testing, with variations being performed on the simulations very quickly. As a result of these factors, CFD is now an established industrial design tool, helping to reduce design time scales and improve processes throughout the engineering world.

4.3 The Navier Stokes equations

The constituent equations for fluid flows are well established and they are basically in the form of a coupled set of partial differential equations, known as the Navier–Stokes equations. CFD techniques simulate physical fluid flow by numerically solving these coupled partial differential equations. Different ways of numerically solving these equations give rise to different CFD techniques in which various forms of these equations may be employed. In the framework of the finite difference/volume technique, the most fundamental solution method is referred to as the Direct Numerical Simulation (DNS). In the DNS method, the transient form of the Navier–Stokes equations is solved numerically by means of spectral and pseudo spectral techniques. However, because of the complexity of general industrial, as well as environmental, problems and the limitation in the capabilities of present computer systems, DNS is nowadays still primarily limited in its use to the study of some of the very simple but fundamental flow problems.

When DNS is employed for simulations of high Reynolds number turbulence flows, a prohibitively large number of computational cells must be employed in order to resolve the smallest turbulence vortices, and usually this is not practical. However it is possible to model the effects of turbulence on the flow without considering every single eddy, by considering time averaged effects. This is encompassed by defining mean values which when substituted into the full Navier-Stokes equations, give rise to the Reynolds Averaged Navier-Stokes (RANS) equations which are used in the CFD simulations. Due to the averaging operation, the resulting system of equations, i.e. RANS, is not a closed system as it contains six more unknowns than equations. The unknowns are the so-called Reynolds stresses, which involve time-averaged products of fluctuating velocity components and need to be modelled for closure. This system can only be closed by incorporating an appropriate turbulence model. This has the advantage that a relatively coarse computational grid may be employed.

4.4 Reynolds averaged Navier Stokes (RANS) equations

The numerical modelling involves the solution of the Navier-Stokes Equations, which are based on the assumptions of the conservation of mass and momentum within a moving fluid. The conservation of mass in the absence of any sources of mass and momentum would be,

$$\frac{\partial \rho}{\partial t} + \frac{\partial}{\partial x_i} \rho u_i = 0 \tag{4.1}$$

where, u_i is the velocity and ρ is the density of the fluid.

The conservation of momentum in the absence of any sources of mass and momentum is also described as,

$$\frac{\partial}{\partial t}(\rho u_i) + \frac{\partial}{\partial x_k}(\rho u_k u_i) = -\frac{\partial p}{\partial x_i} + \frac{\partial \tau_{ik}}{\partial x_k} \tag{4.2}$$

where, p is the pressure and τ_{ik} is the stress tensor.

These equations are then time averaged to eliminate the small turbulent fluctuations and solve for the mean flow. Each main variable such as u_i is treated as a sum of mean, $\overline{u_i}$ and a fluctuating quantity u_i', as a part of Reynolds-Averaging process. All this leads to the introduction of an extra term in the momentum equation as a consequence of the non-linearity of its advection term, i.e. the second term in the above equation. This term, which is called the Reynolds Stress, is to be modelled. This means that a mathematical closure model is needed, which usually involves the solution of additional transport equations as part of so-called turbulence models. The turbulence model provides one equation for each Reynolds Stress as well as one equation for the dissipation of the turbulence energy. These equations are obtained by manipulating the Navier-Stokes Equations and modelling some of the resulting terms (Tennekes and Lumley, 1972).

The fundamental parameters required to describe a channel flow are the pressure and the velocity of the fluid flow. If the flow is assumed to be incompressible and Newtonian, then these parameters are solely governed by the constitutional Navier–Stokes equations which are based on the basic physical principles of conservation of mass and momentum. For an incompressible and turbulent fluid flow, the Reynolds-averaged form of the Navier–Stokes equations may be written in a Cartesian coordinate system as follows:

$$\rho\frac{\partial u_i}{\partial t}+\rho u_j\frac{\partial u_i}{\partial x_j} = -\frac{\partial p}{\partial x_i}+\frac{\partial}{\partial x_j}\left[\mu\left(\frac{\partial u_i}{\partial x_j}+\frac{\partial u_j}{\partial x_i}\right)\right]+\frac{\partial \tau_{ij}}{\partial x_j}+\rho g_i \tag{4.3}$$

Continuity equation

$$\frac{\partial u_i}{\partial x_i}=0 \tag{4.4}$$

where x_i represents the components of the Cartesian coordinate system (i = 1, 2, 3); t represents the time; u_i, p, ρ and μ are the mean fluid velocity components, pressure, density and molecular viscosity, respectively; and g_i represents the gravitational acceleration. The first term on the left side of equation (4.3)

represents the rate of change of momentum per unit volume with respect to time, the second term represents the change of momentum resulting from advective motion. On the right side of the equation, the first term is the force resulting from the pressure differences in the fluid flow, the second term combines the viscous shear forces resulting from the motion of the fluid and the third term is the force produced by the turbulent fluctuations of the fluid particles. This third term is a result of the Reynolds-averaging of the original Navier–Stokes equations, known as the Reynolds stress tensor and defined as

$$\tau_{ij} = -\rho\overline{u_i' u_j'} \tag{4.5}$$

and, in practice, it represents the effects of the turbulence on the fluid flow. Here the over bar denotes a Reynolds-average and the dash represents the fluctuating part of the turbulent velocity. Since the Reynolds stress is not known a priori, the Reynolds averaged Navier–Stokes equations (4.3) – (4.4) are not closed, unless a model is provided that relates the Reynolds stress tensor τ_{ij} to the global mean property of the fluid flow in a physically consistent fashion. In principle, with an appropriate turbulence model and a set of properly defined boundary conditions for the fluid flow, the fluid flow can be modelled numerically by solving the Reynolds-averaged Navier–Stokes equations (4.3) – (4.4) in all three directions of the coordinate system. Therefore, it is the turbulence model and the boundary conditions that define the output of the CFD model.

4.5 Turbulence modelling for RANS equations

As said earlier, that the use of an appropriate turbulence model in a particular application for the fluid flow simulation is very important, and the model used may vary from one application to another. Some of the turbulence models commonly used are described here.

4.5.1 Two equation models

Two-equation models, such as the k- ε model, the k-ω model and their variations, are the most popularly used models in various engineering and environmental applications. This is largely due to their ease in implementation and being able to

obtain reasonably accurate solutions with the available computer power. A few of the two equation models are discussed below.

4.5.1.1 The standard k-ε turbulence model

Launder and Spalding (1974) first proposed the k-ε model in the early 1970s and it has enjoyed reasonable success in many engineering and scientific applications. One of the main reasons is the fact that it has been widely used and is therefore well documented. The standard k-ε model is also an eddy-viscosity-type turbulence model and it represents the eddy viscosity by the turbulent kinetic energy k and the dissipation rate ε as follows:

$$\mu_t = c_\mu \rho \frac{k^2}{\varepsilon} \tag{4.6}$$

where c_μ is an empirically derived constant and it usually takes the value of 0.09 in the standard k-ε model (e.g. Launder and Spalding, 1974). The turbulent kinetic energy k and the dissipation rate ε in the k-ε model have to be obtained in order to estimate the turbulent viscosity and this is achieved by solving two transport equations for k and ε. At high values of the Reynolds numbers, which is nearly always the case for natural river flows, they are given by

Kinetic energy equation

$$\rho \frac{\partial k}{\partial t} + \rho u_j \frac{\partial k}{\partial x_j} = \frac{\partial}{\partial x_i}\left[\left(\frac{\mu + \mu_t}{\sigma_k}\right)\frac{\partial k}{\partial x_i}\right] + P - \rho\varepsilon \tag{4.7}$$

where

$$P = (\mu + \mu_t)\left(\frac{\partial u_i}{\partial x_j} + \frac{\partial u_j}{\partial x_i}\right)\frac{\partial u_i}{\partial x_j} \tag{4.8}$$

is the term which represents the production of turbulence.

And dissipation rate equation

$$\rho\frac{\partial\varepsilon}{\partial t}+\rho u_j\frac{\partial\varepsilon}{\partial x_j}=\frac{\partial}{\partial x_i}\left[\left(\frac{\mu+\mu_t}{\sigma_\varepsilon}\right)\frac{\partial\varepsilon}{\partial x_i}\right]+c_{\varepsilon1}\frac{\varepsilon}{k}P-c_{\varepsilon2}\frac{\varepsilon}{k}\rho\varepsilon \qquad (4.9)$$

where $c_{\varepsilon1}$, $c_{\varepsilon2}$, σ_k and σ_ε are constants that are typically assumed to take the values of 1.44, 1.92, 1.0 and 1.3, respectively (e.g. Launder and Spalding, 1974).

However, the main shortcoming of the standard k-ε model is its assumption of isotropy in the turbulence fluctuations when modelling the Reynolds stresses and this can result in a large turbulent viscosity. Therefore this model frequently produces inaccurate predictions in some turbulent fluid flows (e.g. Mohammadi and Pironneau, 1994; Ingham *et al.*, 1997).

4.5.1.2 The renormalization group (RNG) k-ε turbulence model

The RNG model is obtained theoretically through a process of statistical eliminations and it is a significant improvement over the standard k-ε turbulence model in simulating 3D fluid flows with a large degree of strain in the fluid and for boundaries with a large curvature. For high Reynolds number fluid flows, the RNG k-ε model employs the same expressions for the turbulence viscosity as in the standard k-ε model, namely equation (4.6), and a similar set of transport equations to the standard k-ε model for k and ε, namely

Kinetic energy equation

$$\rho\frac{\partial k}{\partial t}+\rho u_j\frac{\partial k}{\partial x_j}=\alpha\frac{\partial}{\partial x_i}\left[(\mu+\mu_t)\frac{\partial k}{\partial x_i}\right]+P-\rho\varepsilon \qquad (4.10)$$

and dissipation rate equation

$$\rho\frac{\partial\varepsilon}{\partial t}+\rho u_j\frac{\partial\varepsilon}{\partial x_j}=\alpha\frac{\partial}{\partial x_i}\left[(\mu+\mu_t)\frac{\partial\varepsilon}{\partial x_i}\right]+c_{\varepsilon1}\frac{\varepsilon}{k}P-c_{\varepsilon2}\frac{\varepsilon}{k}\rho\varepsilon-R \qquad (4.11)$$

where R is a parameter which includes the rate-of-strain and plays an important role in anisotropic large-scale eddies, and it can be expressed as follows:

$$R=\rho\frac{c_\mu\eta^3\left(\frac{1-\eta}{\eta_0}\right)}{1+\beta\eta^3}\frac{\varepsilon^2}{k}$$

$$\eta = \frac{k}{\varepsilon}\sqrt{2S_{ij}S_{ij}}$$

$$S_{ij} = \frac{1}{2}\left(\frac{\partial u_i}{\partial x_j} + \frac{\partial u_j}{\partial x_i}\right)$$

The values of the constants which appear in the RNG theory usually take the values $c_\mu = 0.0845$, $c_{\varepsilon 1} = 1.42$, $c_{\varepsilon 2} = 1.68$, $\alpha = 1.3$, $\beta = 0.011 - 0.015$ and $\eta_0 = 4.38$ (e.g. Yakhot and Orszag, 1986; Boysan, 1995). These values should be compared with the values as found in the standard k-ε model (e.g. Launder and Spalding, 1974), where $c_\mu = 0.09$, $c_{\varepsilon 1} = 1.44$, and $c_{\varepsilon 2} = 1.92$. It should be noted that although the values of the two sets of constants are very similar, the constants employed in the RNG model are basically obtained theoretically whereas those employed in the standard k-ε model have been found from experimental data and thus determined experimentally. Further, it should be noted that the standard empirical constants in all the k-ε models should not be expected to be universal constants and modifications may be required to suit specific physical situations.

The equation (4.6) for the eddy viscosity μ_t holds for high Reynolds number fluid flow in the RNG k-ε model, but with $c_\mu = 0.0845$. In addition to this expression, the RNG theory also gives a more general form for the expression for the eddy viscosity (e.g. Boysan, 1995),

$$\mu_t = \mu\left[1 + \sqrt{\frac{c_\mu \rho}{\mu}}\frac{k}{\sqrt{\varepsilon}}\right]^2 \qquad (4.12)$$

which is valid across the full range of turbulent fluid flow conditions from low to high Reynolds numbers.

4.5.2 Reynolds-stress models (RSMs)

The Reynolds Stress Models (RSMs) are based on transport equations for all components of the Reynolds stress tensor and the dissipation rate. They individually solve a transport equation for each of Reynolds stress component. The Reynolds averaged momentum equations for mean velocity are,

$$\frac{\partial \rho U_i}{\partial t} + \frac{\partial}{\partial x_j}(\rho U_i U_j) - \frac{\partial}{\partial x_j}\left[\mu\left(\frac{\partial U_i}{\partial x_j} + \frac{\partial U_j}{\partial x_i}\right)\right] = \frac{\partial p''}{\partial x_i} - \frac{\partial}{\partial x_j}(\rho\overline{u_i u_j}) + S_{M_i} \tag{4.13}$$

where, p'' is the modified pressure, S_{M_i} is the sum of the body forces and the fluctuating Reynolds stress contribution is $\rho\overline{u_i u_j}$. The modified pressure has no turbulence contribution and is related to the static pressure as,

$$p'' = p + \frac{2}{3}\mu\frac{\partial U_k}{\partial x_k} \tag{4.14}$$

The standard Reynolds Stress model in ANSYS CFX solves the following equation for the transport of Reynolds stresses,

$$\frac{\partial \rho\overline{u_i u_j}}{\partial t} + \frac{\partial}{\partial x_k}(U_k\rho\overline{u_i u_j}) - \frac{\partial}{\partial x_k}\left(\left(\mu + \frac{2}{3}C_S\rho\frac{k^2}{\varepsilon}\right)\frac{\partial \overline{u_i u_j}}{\partial x_k}\right) = P_{ij} - \frac{2}{3}\delta_{ij}\rho\varepsilon + \Phi_{ij} + P_{ij,b} \tag{4.15}$$

where, Φ_{ij} is the pressure-strain tensor and P_{ij} and $P_{ij,b}$ are the shear and buoyancy turbulence production terms of the Reynolds stresses respectively and are given by,

$$P_{ij} = -\rho\overline{u_i u_k}\frac{\partial U_j}{\partial x_k} - \rho\overline{u_j u_k}\frac{\partial U_i}{\partial x_k} \tag{4.16}$$

$$P_{ij,b} = B_{ij} - C_{buo}\left(B_{ij} - \frac{1}{3}B_{kk}\delta_{ij}\right) \tag{4.17}$$

$$B_{ij} = g_i b_j + g_j b_i \tag{4.18}$$

For full buoyancy model based on density differences, b_i is modelled as,

$$b_i = -\frac{\mu_t}{\rho\sigma_\rho}\frac{\partial \rho}{\partial x_i} \tag{4.19}$$

As the turbulence dissipation appears in the individual equations, an equation for ε is still required, which, now has the form,

$$\frac{\partial(\rho\varepsilon)}{\partial t}+\frac{\partial}{\partial x_k}(\rho U_k\varepsilon)=\frac{\varepsilon}{k}(c_{\varepsilon 1}P-c_{\varepsilon 2}\rho\varepsilon)+\frac{\partial}{\partial x_k}\left[\left(\mu+\frac{\mu_t}{\sigma_{\varepsilon RS}}\right)\frac{\partial\varepsilon}{\partial x_k}\right] \tag{4.20}$$

The Reynolds Stress model is also available with anisotropic diffusion coefficients. In this case the ANSYS CFX solves the following equations for the transport of Reynolds stresses.

$$\begin{aligned}\frac{\partial\rho\overline{u_iu_j}}{\partial t}+\frac{\partial}{\partial x_k}(U_k\rho\overline{u_iu_j})-\frac{\partial}{\partial x_k}\left(\left(\delta_{kl}\mu+\rho C_S\frac{k}{\varepsilon}\overline{u_ku_l}\right)\frac{\partial\overline{u_iu_j}}{\partial x_l}\right)\\ =P_{ij}-\frac{2}{3}\delta_{ij}\rho\varepsilon+\Phi_{ij}+P_{ij,b}\end{aligned} \tag{4.21}$$

In this case the production due to buoyancy due to density difference is modelled as,

$$b_i=C_s\frac{k}{\varepsilon\sigma_\rho}\overline{u_iu_k}\frac{\partial\rho}{\partial x_k} \tag{4.22}$$

The equation for ε is,

$$\begin{aligned}\frac{\partial(\rho\varepsilon)}{\partial t}+\frac{\partial}{\partial x_k}(\rho U_k\varepsilon)\\ =\frac{\varepsilon}{k}(c_{\varepsilon 1}P-c_{\varepsilon 2}\rho\varepsilon)\\ +\frac{\partial}{\partial x_k}\left[\left(\mu\delta_{kl}+c_\varepsilon\rho\frac{k}{\varepsilon}\overline{u_ku_l}\right)\frac{\partial\varepsilon}{\partial x_l}\right]\end{aligned} \tag{4.23}$$

4.5.2.1 Pressure-strain terms

One of the most important terms in Reynolds stress models is the pressure-strain correlation, Φ_{ij}. It acts to drive the turbulence towards an isotropic state by redistributing the Reynolds stresses. It can be split into two parts,

$$\Phi_{ij}=\Phi_{ij,1}+\Phi_{ij,2} \tag{4.24}$$

where, $\Phi_{ij,1}$ is the slow term also known as return to isotropy term and $\Phi_{ij,2}$ is called the rapid term.

There are three varieties of standard Reynolds stress models available based on ε-equation. These are commonly known as LRR-IP, LRR-QI and SSG. The LRR-IP and LRR-QI models were developed by Launder, Reece and Rodi (1975). In both the models, the pressure-strain correlation is linear. The extension IP stands for Isotropization of Production and QI stands for Quasi-Isotropic. These models only differ in the formulation of rapid term, $\Phi_{ij,2}$. The slow term in both the models is,

$$\Phi_{ij,1} = -C_1\rho\frac{\varepsilon}{k}\left(\overline{u_i u_j} - \frac{2}{3}\delta_{ij}k\right) \tag{4.25}$$

where constant $C_1 = 1.8$.

The rapid term in LRR-IP is,

$$\Phi_{ij,2} = -C_2\left(P_{ij} - \frac{2}{3}P\delta_{ij}\right) \tag{4.26}$$

where, $C_2 = 0.6$ and $P = 0.5P_{ii}$.

The rapid term in LRR-QI is,

$$\begin{aligned}\Phi_{ij,2} = &-\frac{C_2+8}{11}\left(P_{ij} - \frac{2}{3}P\delta_{ij}\right) - \frac{30C_2+8}{11}\rho k\left(\frac{\partial U_i}{\partial x_j} + \frac{\partial U_j}{\partial x_i}\right)\\ &-\frac{8C_2-2}{11}\left(D_{ij} - \frac{2}{3}P\delta_{ij}\right)\end{aligned} \tag{4.27}$$

where D_{ij} is given by,

$$D_{ij} = -\rho\overline{u_i u_k}\frac{\partial U_k}{\partial x_j} - \rho\overline{u_j u_k}\frac{\partial U_k}{\partial x_i} \tag{4.28}$$

The SSG model was developed by Speziale, Sarkar and Gatski (1991) and uses quadratic relation for the pressure-strain correlation and has the transport equation for the Reynolds Stress as,

$$\frac{\partial}{\partial t}\left(\rho\overline{u_i' u_j'}\right) + \frac{\partial}{\partial x_k}\left(\rho u_k\overline{u_i' u_j'}\right) = -\rho\left(\overline{u_i' u_k'}\frac{\partial u_j}{\partial x_k} + \overline{u_j' u_k'}\frac{\partial u_i}{\partial x_k}\right)$$

$$-\frac{\partial}{\partial x_k}\left[\left(\mu+\frac{\mu_t}{\sigma_k}\right)\frac{\partial}{\partial x_k}\left(\overline{u_i'u_j'}\right)\right]+\mathrm{p}\left(\overline{\frac{\partial \mathrm{u_i'}}{\partial \mathrm{u_j}}+\frac{\partial \mathrm{u_j'}}{\partial \mathrm{x_i}}}\right)-\frac{2}{3}\delta_{\mathrm{ij}}\rho\varepsilon \qquad (4.29)$$

where, the terms on the RHS of the equation are Stress Production P_{ij}, Diffusion, Pressure-Strain and the Dissipation respectively and μ and μ_t are the dynamic and eddy viscosity.

In order to compare the pressure-strain correlation for the three models, a general form can be derived based on the anisotropy tensor, α_{ij}, the mean strain rate tensor, S_{ij} and the vorticity tensor, Ω_{ij}. The general form can be written as,

$$\Phi_{ij,1}=-\rho\varepsilon\left[C_{s1}\alpha_{ij}+C_{s2}\left(\alpha_{ik}\alpha_{kj}-\frac{1}{3}\alpha_{mn}\alpha_{mn}\delta_{ij}\right)\right] \qquad (4.30)$$

$$\begin{aligned}\Phi_{ij,2}=&-C_{r1}P\alpha_{ij}+C_{r2}\rho kS_{ij}-C_{r3}\rho kS_{ij}\sqrt{\alpha_{mn}\alpha_{mn}}\\&+C_{r4}\rho k\left(\alpha_{ik}S_{jk}+\alpha_{jk}S_{ik}-\frac{2}{3}\alpha_{kl}S_{kl}\delta_{ij}\right)\\&+C_{r5}\rho k\left(\alpha_{ik}\Omega_{jk}+\alpha_{jk}\Omega_{ik}\right)\end{aligned} \qquad (4.31)$$

where,

$$a_{ij}=\frac{\overline{u_iu_j}}{k}-\frac{2}{3}\delta_{ij} \qquad (4.32)$$

$$S_{ij}=\frac{1}{2}\left(\frac{\partial U_i}{\partial x_j}+\frac{\partial U_j}{\partial x_i}\right) \qquad (4.33)$$

$$\Omega_{ij}=\frac{1}{2}\left(\frac{\partial U_i}{\partial x_j}+\frac{\partial U_j}{\partial x_i}\right) \qquad (4.34)$$

This general form can be used to model linear and quadratic correlations by using appropriate values of constants which are given in Table 4.1.

Table 4.1 Model constants for the three Reynolds stress models.

Constant	Model		
	LRR-IP	LRR-QI	SSG
$\sigma_{\varepsilon RS}$	1.10	1.10	1.36
C_{ε}	0.18	0.18	0.18
$C_{\varepsilon 1}$	1.45	1.45	1.45
$C_{\varepsilon 2}$	1.9	1.9	1.83
C_{s1}	1.8	1.8	1.7
C_{s2}	0.0	0.0	-1.05
C_{r1}	0.0	0.0	0.9
C_{r2}	0.8	0.8	0.8
C_{r3}	0.0	0.0	0.65
C_{r4}	0.6	0.873	0.625
C_{r5}	0.6	0.655	0.2

The Reynolds Stress Models (RSMs) have emerged as strong candidates for use in industrial turbulent flow calculations as well as in environmental flow modelling and are now incorporated in commercial codes. As the RSMs are second-order closure models, they are potentially superior to the simpler eddy-viscosity models, such as the k-ε models. They potentially require excessive amount of computational effort for the simulation of 3D fluid flows. However, it should be noted that the use of the RSMs is the way forward when the anisotropic Reynolds stress has a large effect on the fluid flow structures, such as those that occur when simulating the secondary fluid flow in an open channel.

As discussed earlier a Reynolds stress model is very necessary for modelling the effects of the secondary currents which are due to the anisotropy in the normal Reynolds Stresses (Cokljat, 1993). These effects are not predicted by simple two equation isotropic models, as they do not model the individual stresses, therefore the SSG model was selected. It may be noted that the SSG model has an advantage over other such models like LRR as it uses a quadratic relation for the pressure redistribution and does not require any additional term to account for the

wall effects, which are difficult to implement numerically. It has also been successfully used over the years by the Nottingham team (Morvan *et al.*, 2002, Morvan, 2005, Morvan *et al.*, 2005, Cacqueray *et al.*, 2009, Morvan and Hargreaves, 2009 and Ansari *et al.*, 2011). For this reason SSG model has been mostly used in the present study.

4.6 Discretisation

The Navier Stokes Equations are non-linear partial differential equations (PDEs), which treat the whole fluid domain as a continuum. Unfortunately the PDEs cannot be solved analytically. They need to be solved numerically i.e. algebraically which means discretising. Discretisation is done in different forms, which are discussed below:

4.6.1 Numerical discretisation

The numerical discretisation allows the continuum to be replaced by a finite set of nodes. There are three main grid based numerical methods of discretisation namely, finite difference method (FDM), finite element method (FEM) and the finite volume method (FVM). The FVM is the most popular with in the commercial CFD codes, in which the domain of interest is divided into finite volumes called the control volumes (CV). At the centre of each volume called nodes the values of the quantities like density, pressure and velocity are to be stored and solved by the governing equations. These cell values are the cell-averaged representative values and not (only) nodal values.

4.6.2 Spatial discretisation or Mesh generation

Spatial discretisation is done through mesh generation of the given domain. Special care needs to be taken during generation of the mesh, a mesh with very few nodes may lead to quick solution yet not very accurate one and similarly a dense mesh might waste computational time and memory. The best approach would be to develop such a mesh which is dense in the areas of interest such as at the walls where large variation of fluid properties is expected and be coarse in other areas where there is not be change expected in the fluid properties.

4.6.3 Temporal discretisation

For the transient problems an appropriate time step needs to be defined. The time step should be sufficiently small as to capture the required features of the flow but, like cell size, not too small to waste the computational power and also not too large that does not capture the important features of the flow.

4.6.3.1 Courant number

The criterion which is often used to determine the time step size is Courant number. The Courant number stops the time step from being large enough for a fluid particle to travel entirely through one cell during one iteration. This number should not ideally be greater than unity. It may be defined as follows,

$$C_r = \frac{\bar{u}\Delta t}{\Delta l} \tag{4.35}$$

where C_r is the Courant number, $\bar{u}$ is the average velocity, Δt is the maximum time step size and Δl is the largest grid cell size parallel to the direction of flow.

4.7 Boundary conditions

The boundary conditions need to be defined for the behaviour of the variables at the edges of the domain. For transient flow modelling, initial conditions representing the state of the fluid flow at the time when the computation starts must also be specified. It should be stressed that the boundary conditions imposed must reflect the real situation of the river flow that is being modelled, although this is not always an easy task. For open channel flows there are usually five types of boundary conditions to be considered namely, inlet, outlet, walls, free surface and periodic. Some of the boundary conditions are defined below.

4.7.1 Inlet

An inlet boundary condition is used where the flow is predominantly directed into the domain. The distribution of all flow variables needs to be specified at the inlet boundary. One way of specifying the inlet and outlet conditions is using the mass

flow rate type conditions, where a normal mean velocity is specified at the inlet and coupled with a mass flow boundary at the downstream end of the reach, which ensures that the fluid leaves the downstream boundary at the same mass flow as it entered. There is one drawback for the mass flow boundary condition that significant channel lengths are required to allow the flow to develop which in turn require large meshes in the stream wise direction.

4.7.2 Outlet

If the location of the outlet is selected far away from geometrical disturbances then the flow eventually reaches a fully developed state where no change occurs in the flow direction. In such a region we can place an outlet and state that the gradient of all variables except pressure is zero in the flow direction.

4.7.3 Walls

The wall is the most common boundary condition encountered in confined fluid flow problems. No slip condition is the appropriate condition for the velocity components at the solid walls in which $u = v = 0$, which describes that the fluid next to the wall assumes the velocity at the wall equal to zero. The implementation of the wall boundary condition in turbulent flows start with the evaluation of,

$$y^+ = \frac{\Delta y_P}{\nu}\sqrt{\frac{\tau_w}{\rho}} \tag{4.36}$$

where Δy_P is the distance of the near wall node P to the solid surface.

A near wall flow is taken to be laminar if $y^+ \leq 11.63$ and turbulent is $y^+ > 11.63$ and then the wall function approach is used.

4.7.4 Symmetry

The conditions at the symmetry boundary are that number one there no flow across the boundary and number two there is no scalar flux across the boundary. The normal velocities are set to zero at the symmetry boundary and the values of

all other properties just outside the solution domain are equal to their values at the nearest node just outside the domain.

4.7.5 Periodic or cyclic

A periodic or cyclic boundary condition applies the output of the downstream boundary of the channel into that of the input of the upstream boundary so that the channel appears infinitely long. In order to reduce the large meshes the use of periodic boundary condition has become popular. This allows much smaller cells in the stream wise direction. As a consequence of employing the periodic boundary condition it is necessary to drive the flow via a body force representing the slope of the channel and the effects of the gravity, rather than the mass flow rate boundary condition. If the channel geometry is created flat the effects of the gravity and channel slope are implemented via a resolved gravity vector,

$$\rho g = (\rho g \sin\theta, 0, -\rho g \cos\theta) \tag{4.37}$$

where, θ is the angle between the channel slope and the horizontal, ρ is the fluid density and g is the gravitational acceleration.

The x-component causes the water to flow along the channel and the z-component is responsible for creating the hydrostatic pressure.

4.7.6 Constant pressure boundary condition

This type of boundary condition is used in situations where exact details of the flow distribution are unknown but the boundary values of the pressure are known. In applying the fixed pressure boundary, the pressure correction is set to zero at the nodes.

4.8 Free surface flows

Most of the current CFD investigations on river flows employ a so-called fixed lid surface approach where, for steady fluid flows, an approximate fixed lid may be specified to represent the water surface. Unfortunately, for unsteady flow

situations, the instantaneous water surface is not known a priori and it may have to be numerically predicted at each time interval as any incorrect specification of the water surface will affect the distribution of the mass and momentum of the fluid flow in the computational domain. This may result in the fluid velocity being overestimated or underestimated and thus this leads to errors in the prediction of the bed shear stress and consequently bed load transport.

4.8.1 Fixed lid schemes

For steady state river flows, for which the water surface is known, the shape of the free surface may be specified as a fixed lid boundary of the computational domain. On this fixed lid, frictionless conditions are enforced which allow the water to slip, but not to pass through the free surface. In such a situation the water flow may be solved in the usual manner, subject to the other appropriate boundary conditions being specified. It is clear that when a prescribed water surface is used, any incorrect specification of the water surface position may result in over-under-predictions of the fluid velocity and this leads to inaccuracies in the bed shear stress calculations.

4.8.2 The volume of fluid (VOF) model

In flood seasons, the water discharge, and thus the water level, changes rapidly, and the water surface must be free to change instantaneously in the computational domain and also as part of the numerical solution in order to simulate the flood flow. In this case, the unsteady solution procedures of the Volume of Fluid (VOF) technique may be employed. It should be noted that although the VOF technique was designed for solving unsteady fluid flow problems, it may also be used to predict a steady flow when the water surface is not known a priori.

The VOF model (e.g. Hirt and Nichols, 1981), can be employed to track the position of the water surface in the computational domain when the control volume method is employed. In each control volume in the computational domain, a water volume fraction, VF, can be defined as follows:

$$VF = \frac{\delta\Omega_{water}}{\delta\Omega_{cell}} \tag{4.38}$$

where, $\delta\Omega_{cell}$ is the volume of the computational cell and $\delta\Omega_{water}$ is the fraction of the volume of the cell filled with water. Therefore, we have

The volume fraction equation

VF = 1; cell is full of water

VF = 0; cell is full of air

0 < VF < 1; cell contains a free surface

Thus, according to the law of mass conservation of air and water, the volume fraction of the water satisfies the partial differential equation,

$$\frac{\partial VF}{\partial t} + u_i \frac{\partial VF}{\partial x_i} = 0 \tag{4.39}$$

There are different ways of solving equation (4.39) for the water volume fraction VF in a cell. The most original way is to use the so-called donor–acceptor scheme (e.g. Hirt and Nichols, 1981), by solving the equation explicitly. Once the location of the water surface has been obtained, the appropriate boundary conditions may be enforced on the free surface.

However, it should be stressed that implementing boundary conditions on a free surface is not always an easy task, in particular when the free surface is constantly changing its position. In order to avoid the complexity of implementing boundary conditions on the free surface, a multi-flow approach can be employed where some airflow can be introduced into the computation domain above the water cells. Then the water surface is transformed into an interface between the air and the water, and the 'donor–acceptor' scheme may be used to solve equation (4.39) and predict the location of the interface. In this case, the effect of the possible airflow on the water surface may also easily be taken into account if so desired. It should be noted that because the viscosity of air is approximately 50 times smaller than that of water, the airflow above the water has little effect on the water flow

unless a large airflow rate is imposed, such as when modelling the effects of a strong wind on the water surface.

In addition to the use of the 'donor–acceptor' scheme, equation (4.39) can also be solved implicitly in the same manner as that used to solve other transport equations. However, due to the interpolation being employed in the solution process of the volume fraction equation, the numerical diffusion occurs near to the interface between the air and the water and this may result in difficulties in accurately defining the location of the water surface. To reduce this numerical diffusivity, which is caused by the discreteness of the volume fraction equation, a second-order discreteness scheme, such as the second-order upwind scheme, may be used.

It should be stressed that the use of VOF is computationally expensive. Therefore, the fixed lid approach may be used with some confidence for most fluid flow simulations where no large water surface elevations occur.

4.9 The Methodology of CFD

The process of performing a CFD simulation can be divided into four components, which are briefly described below:

4.9.1 Creating the Geometry and Mesh

This is the first process in which the geometry of the region of interest is defined. The objective is to produce a mesh for the input to the physics pre-processor. The regions of the fluid flow, solid regions and surface boundary names are also set here. There are several commercial softwares available to build geometries and then mesh them like CAD2Mesh, GAMBIT etc.

4.9.2 Defining the Physics of the model

This is the second process, which is used to create input, which is later used by the solver. After the mesh files are loaded into the physics pre-processor, the physical models that are to be included in the simulation are selected and the fluid properties as well as the boundary conditions are specified here.

4.9.3 Solving the CFD Problem

In this process, the partial differential equations are integrated over all the control volumes in the region of interest, which is nothing but the application of the basic conservation laws over each control volume. These integral equations are then converted to a system of algebraic equations by generating a set of approximations for the terms in the integral equations. The algebraic equations are then solved iteratively. The iterative approach is needed because of the non-linear nature of the equations. At the end of iteration, an error or residual is reported as a measure of the overall conservation of the flow properties. As the solution approaches the exact solution, it is said to be converging. At the end of this solver process a results file is created and then passed on to the post processor for analysis.

4.9.4 Visualizing results in post-processor

In this process, the results are analyzed and visualised interactively. Here many graphical representations of different variables can be seen and analysed.

4.10 CFD model construction in CFX

A brief description of the construction of the model in commercial software used is given below:

4.10.1 Software used

The commercially available CFD software ANSYS-CFX version 10/11/12 has been used. The software relies on the finite element based finite volume method of operating.

The Reynolds Averaged Navier Stokes (RANS) equations have been used to represent the fully developed flow in a prismatic channel. These equations are obtained by applying time averaging to the full Navier – Stokes equations, which result in the six new terms known as Reynolds stresses (Versteeg & Malalasekera, 2007). To account for these Reynolds stresses and to close the system a turbulence model is needed. A large number of turbulence models are available for use in the

commercial CFD software used like k-ε model, k-ω model, LRR-IP model, and LRR-QI model but SSG turbulence model was preferred due to its accuracy in predicting the secondary currents over the others.

The periodic domain interface boundary condition was used to save the time as only one cell was taken in the stream wise direction and the bed of the channel was kept horizontal. A driving force equal to ρgS, where ρ is the density of water taken as 997 kg/m^3, g is the acceleration due to gravity taken as 9.81 m/s and S is the slope of the channel in m/m, was introduced as a momentum source in the stream wise x-direction.

4.10.2 Creating the geometry

A consistent frame of reference for the coordinate axes is taken, x-axis corresponds to the stream wise direction, y-axis corresponds to the lateral direction and the z-axis corresponds to the vertical direction. The origin is placed at the upstream boundary and coincides with the base of the centre line of the channel and the water is taken to be flowing in the negative x-direction. Due to the channel's symmetric geometry, only half of the geometry is modelled taking a symmetrical plane at the central z-axis. The approach, which is adopted in creating the geometry, is to first create the upstream cross-section and then extend it in the stream wise direction as the channels are prismatic. The tool, which is used in creating all the geometries, is GAMBIT. As the geometry has six faces so each one is given a separate name, which would be utilized during specifying the boundary conditions during the model construction in the CFX –Pre. The six faces are named as periodic high x, periodic low x, symmetry centre, symmetry top, wall side and wall top which represent the faces upstream of channel, downstream of channel, centre of channel, free surface, side wall of channel and the bed of the channel respectively.

4.10.3 Creating the mesh

The construction of the grid or mesh involves the sub-division of the geometry into smaller sections known as cells or elements. Throughout the meshing process hexahedral cells have been created, where by the domain is represented by a series

of six sided poly-hedra with oblong faces. The basis of the construction has been to produce a mesh of uniform cell size i.e. uniform cell height (z-direction) and uniform width (y-direction). Keeping the mesh uniform helps in reducing the variations obtained in the values of $y+$. As periodic boundary conditions have been implemented so only one cell is taken in the stream flow direction (x-axis). The meshes are first created on the upstream face of the channel cross-section and then the face is swept with the mesh by unit thickness in the negative x-direction. Coarse meshes were created and then were refined and the results were compared so as to make the results mesh independent. The $y+$ values were also checked at the boundaries bed and sidewall to check if they lied within the specified values.

4.10.4 Defining the physics of the problem

After building the geometry and the mesh, the next stage is to define the physics of the problem. All the simulations are solved as steady state problems and a single phase of water, which is already available, as a library material in CFX has been chosen. As a library, material water is taken to be at room temperature of 25°C and so having all its properties at that temperature. As we know that in steady state condition free surface is always parallel to the bed of the channel so here also it is taken to be fixed and parallel to the bed. As the bed is taken to be horizontal so there need to be driving force to make the water flow in the channel, which is taken to be equal to ρgS, which is nothing but the weight component of water in the slope direction due to gravity. This is implemented as an additional source in the momentum equations in the stream flow direction (x-axis). Due to periodic boundary condition, a cycle is created which drives the flow of water repeatedly until it reaches a steady state condition. This means that the flow entering the inlet during the iteration $i+1$ is the flow leaving the outlet during the iteration i.

The next step is to define the boundary conditions. As stated earlier as only half of the channel geometry is taken so a symmetrical boundary condition is given to the channel centre face. Both the walls i.e. bed and sidewalls are taken as non-slip walls with some roughness induced in them by specifying roughness equivalent height ks. The free surface is also given a symmetrical boundary condition.

The next step is to select a turbulence model which has to be coupled with the RANS model. The turbulence model selected here was SSG (Speziale, Sarkar and Gatski, 1991) turbulence model as it is able to model the secondary currents more accurately as compared to other available models such as LRR-IP, LRR-QI (Launder, Reed and Rodi, 1975), etc. This model also employs a law of the wall function at the channel boundaries which connects the flow in the near wall region to the main flow which otherwise would require a very fine mesh at the boundaries which in turn would be very expensive with respect to computational cost and computational power.

4.10.5 Convergence criteria

The next step would be to define the convergence control criteria, which is in these cases taken to be physical time scale with a value of 0.1 second and the maximum number of iterations as 4000. All the residual targets are set at 10^{-9} value. It is very necessary to monitor the residuals as the solution progresses to get an indication of the convergence of the solution. The shear force on the bed and the walls was also monitored and the run was continued until the shear force remained stable for a sufficient number of iterations.

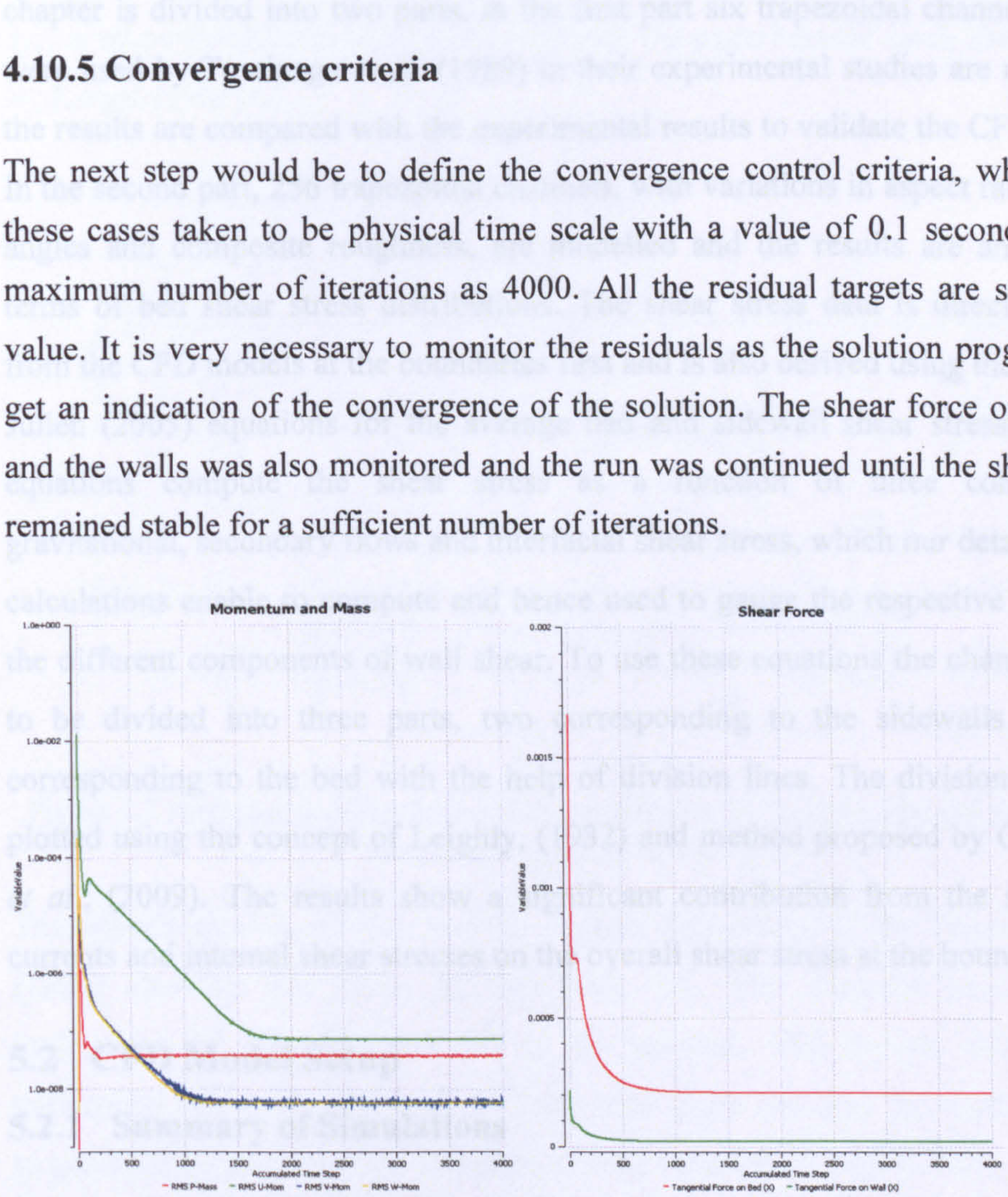

Figure 4.1 The monitoring of the momentum and mass residuals and the shear force on the bed and walls.

CHAPTER 5

STRAIGHT PRISMATIC TRAPEZOIDAL CHANNELS

5.1 Introduction

In this chapter an in depth, analysis is carried out on the distribution of shear stresses and flow structures in straight prismatic trapezoidal channels. This chapter is divided into two parts, in the first part six trapezoidal channels which were used by Tominaga *et al.* (1989) in their experimental studies are modelled, the results are compared with the experimental results to validate the CFD model. In the second part, 256 trapezoidal channels, with variations in aspect ratios, slant angles and composite roughness, are modelled and the results are analysed in terms of bed shear stress distributions. The shear stress data is directly output from the CFD models at the boundaries first and is also derived using the Guo and Julien (2005) equations for the average bed and sidewall shear stresses. These equations compute the shear stress as a function of three components; gravitational, secondary flows and interfacial shear stress, which our detailed CFD calculations enable to compute and hence used to gauge the respective merits of the different components of wall shear. To use these equations the channels have to be divided into three parts, two corresponding to the sidewalls and one corresponding to the bed with the help of division lines. The division lines are plotted using the concept of Leighly, (1932) and method proposed by Cacqueray *et al.*, (2009). The results show a significant contribution from the secondary currents and internal shear stresses on the overall shear stress at the boundaries.

5.2 CFD Model Setup

5.2.1 Summary of Simulations

This study is conducted on two sets of simulations. The first set consists of six trapezoidal channels, replicating the ones used by Tominaga *et al.* (1989) in their experimental work. The main purpose of this exercise was to validate the CFD model by comparing the CFD predictions with results available in the literature.

The second set consists of a large number of trapezoidal channels. With reference to Figure 5.1, variations of aspect ratio, b/h, slant angle, θ, and bed roughness, k_{sb}, were used to create a matrix of test cases. The actual values used were:

- Aspect ratio: 2, 4, 8, 12, 18, 24, 36 and 48.
- Slant angle: 0°, 10°, 20°, 30°, 40°, 45°, 50° and 60°.
- Bed roughness: 0.0015, 0.1, 0.2, and 0.4 mm.

The eight aspect ratios, eight slant angles and four bed roughness values give 256 cases. The water depth, h, is kept constant at 50 mm and the sidewall roughness, k_{sw}, is set to 0.0015 mm to be consistent with the experimental conditions adopted by Knight (1981).

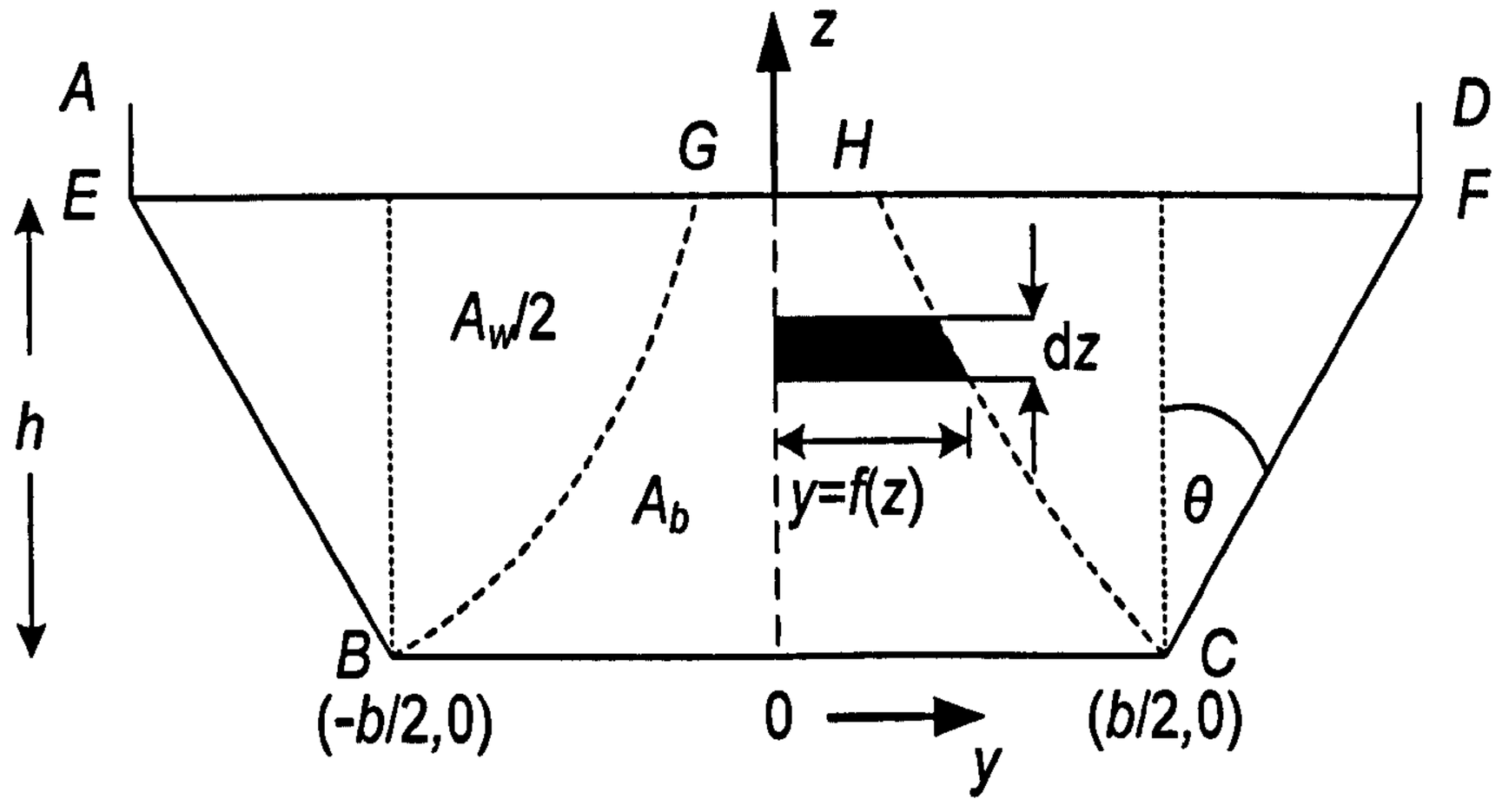

Figure 5.1 Partitioning of the flow cross sectional area for bed and sidewall shear stress (adapted from Guo & Julien, 2005).

The experimental conditions and the channel dimensions of the Tominaga *et al.* (1989) channels are given in the Table 5.1. The channels have sidewall inclinations of 30°, 46° and 58° to the vertical. The bottom width of the trapezoidal channels is constant for each slant angle and only the depth is varied to get different aspect ratios. The aspect ratios varied from 2.13 to 5.95.

Table 5.1 Experimental conditions for trapezoidal channels (Tominaga *et al.*, 1989).

Channel	Flow depth h (cm)	Bottom width b (cm)	Surface width T (cm)	Aspect ratio b/h	Sidewall angle θ (degrees)	Energy gradient S (x10^{-3})
T12	06.36	24.80	32.20	3.90	30	0.670
T13	11.00	24.80	37.50	2.25	30	0.389
T01	03.36	20.00	27.00	5.95	46	1.381
T02	05.01	20.00	30.40	3.99	46	1.000
T03	09.05	20.00	38.90	2.21	46	0.594
T23	07.12	15.20	39.80	2.13	58	0.594

The flow characteristics as given by Tominaga *et al.* (1989) are given in Table 5.2. The discharge, mean velocity, maximum velocity, Reynolds number, and Froude number for each flow condition are given. All the channels operate under turbulent flow conditions as the Reynolds number, R_e, vary from 35,900 to 87,600. The flow in each channel was also found to be sub-critical as the Froude number, F_r, varied between 0.32 and 0.61.

Table 5.2 Flow characteristics for trapezoidal channels (Tominaga *et al.*, 1989).

Channel	Discharge Q (l/s)	Mean velocity U_m (cm/s)	Max. velocity U_{max} (cm/s)	Reynolds number R_e (x10^4)	Froude number F_r
T12	06.33	34.90	45.16	5.74	0.47
T13	10.55	30.09	39.36	6.48	0.32
T01	02.72	35.21	42.72	3.59	0.61
T02	04.59	36.92	44.36	5.59	0.53
T03	09.95	37.33	45.36	8.76	0.40
T23	06.22	32.98	38.01	5.34	0.47

In the first instance the channels were run, using a source term commensurate with channel energy gradient, by keeping the bed and the sidewalls smooth during the simulations and the mass flow rate was compared with that in the experimental data. It was however found that the CFD results were showing a flow rate larger than the one observed during the experiments. Consequently, a uniform roughness height k_s was initially introduced on the bed and sidewalls and the mass flow rate was hence adjusted to match the experimental discharge.

Table 5.3 Roughness height k_s introduced for each channel and the comparison of discharge.

Channel	Roughness height k_s (mm)	Discharge		Difference [a] (%)
		Experimental Q (lit/s)	(CFD) Q (lit/s)	
T12	0.08	06.33	06.33	0.00
T13	0.37	10.55	10.55	0.00
T01	0.20	02.72	02.71	0.37
T02	0.15	04.59	04.59	0.00
T03	0.13	09.95	09.94	0.10
T23	0.17	06.22	06.22	0.00

[a] difference in discharge of experimental and CFD results in percentage.

Table 5.3 shows the final roughness height that achieved the same flow rate and the comparative flow rates for experimental and CFD simulations. The difference in the experimental and observed discharges is less than 0.37% for all the cases.

Laboratory streams have almost inevitably smaller aspect ratio, b/h, than natural streams. The results of the flume experiments cannot be expected to correspond to the field experiments (Vanoni and Brooks, 1957). In order to minimise the effect of the walls on the distribution of the shear on the bed, in experimental setup, the sidewalls are often smoother than the bed and this is certainly the case in the present experiments as well. The simulations were again run iteratively and the mass flow rates were compared by keeping the sidewalls smooth and bed rough as in the experimental set up, glass was used as sidewalls and painted iron plate was

used as bed by Tominaga *et al.* (1989). The roughness height for sidewalls k_{sw} was taken as 0.0015 mm which is the same roughness height taken by Knight (1981) for smooth walls during his experiments to keep it in line with previous researchers. The bed roughness height k_{sb} was changed for each simulation and the mass flow rate compared until both matched as was done previously. It may be noted here that Tominaga *et al.* have not mentioned the equivalent roughness height for bed and sidewalls of their channels. Therefore, it was necessary to find these equivalent roughness heights iteratively. Table 5.4 shows the final equivalent roughness height that achieved the same flow rate and the comparative flow rates for experimental and CFD simulations for each channel. The difference in the discharges was less than 0.16 % for all the cases.

Table 5.4 Roughness height k_s introduced for each channel and the comparison of discharge for smooth walled and rough bed channels.

Channel	Roughness (mm)		Discharge (lit/s)		Difference [a]
	Walls	Bed	Experimental	(CFD)	
	k_{sw}	k_{sb}	Q	Q	%
T12	0.0015	0.13	06.33	06.33	0.00
T13	0.0015	1.01	10.55	10.55	0.00
T01	0.0015	0.29	02.72	02.72	0.00
T02	0.0015	0.27	04.59	04.59	0.00
T03	0.0015	0.34	09.95	09.94	0.10
T23	0.0015	0.61	06.22	06.21	0.16

[a] difference in discharge of experimental and CFD results in percentage.

The difference between roughness height of bed and walls plays an important part on the shear stress distribution on the wetted perimeter (Flintham & Carling, 1988). It is measured through k_{sb}/k_{sw} ratio which is a dimensionless roughness parameter expressed in terms of Nikuradse's equivalent sand roughness height. The results with both types of simulations i.e. with uniform roughness on the bed and sidewalls and different roughness on the bed and sidewalls are compared with the results given by Tominaga *et al.* (1989) for validation of the CFD model in Section 5.4.

5.2.2 Domain and Boundary Conditions

A consistent frame of reference for the coordinate axes is with the x-axis corresponding to the stream-wise direction, the y-axis to the cross-stream direction and the z-axis to the vertical direction. The origin is placed midway between the upstream and downstream boundaries and coincides with the base of the centre line of the channel and the water is taken to be flowing in the positive x-direction. Taking advantage of channel symmetry, only half of the geometry is modelled and to facilitate this, a vertical symmetry boundary condition at the centre of the channel cross-section was used. Both the walls (bed and side) were taken as non-slip walls with roughness heights, k_{sb} and k_{sw} for the bed and sidewalls respectively. The free surface was modelled using a symmetry boundary condition. All the simulations were solved as single phase, steady state problems with water used as the fluid. In a uniform steady state condition, the free surface is always parallel to the bed of the channel so here also it was taken to be fixed and parallel to the bed. Periodic boundary condition was used on the up- and downstream faces, hence a momentum source in the stream-wise equal to ρgS, where ρ is the density of water (997 kg/m3), g is the acceleration due to gravity (9.81 m /s), and S is the slope of the channel in m/m, was applied. The value of slope, S, for the first set of simulations is given in Table 5.1 and that for the second set of simulations was kept constant as 0.001.

5.2.3 Mesh Generation

The domain is meshed entirely using hexahedral cells. A mesh of uniform cell size i.e. uniform cell height (z-direction) and uniform width (y-direction) was built. Keeping the mesh uniform helps in reducing the variations obtained in the values of y^+. The number of cells for the smallest section i.e. when b/h was 2 and slant angle was 0° were 2,500 Whereas for the largest section i.e. when b/h was 48 and slant angle was 60° were 56,000. As periodic boundary conditions have been used in the stream-wise direction, only one cell is taken in the stream flow direction (x-axis), a very high node distribution in the cross section can be afforded. Coarse meshes were created and then were refined in turn until the results for average velocity, maximum velocity, average shear on the bed and

sidewalls became stable. The cell size was kept at 1 mm by 1 mm as reducing it below that would have not produced acceptable results because the roughness height was increased up to 0.4 mm. The y^+ values were also checked at the bed and sidewall boundaries to ensure that they fell within the values required by the turbulence model.

5.2.4 Convergence Criteria

For steady-state problems in CFX, a time step is used as an "acceleration parameter" to guide the solution process. Here the time step was 0.1 second. All the residual targets were set at 10^{-9} value. It was found necessary to use such low targets to ensure that the shear forces on the bed and sidewall had reached steady values and matched the applied body force. Such tight convergence criteria were also required because the secondary currents took a great number of iterations to establish themselves.

5.3 CFD model verification

The verification of the CFD model is done by carrying out an analysis for the conservation of momentum for each case. This is a simple test in which the force balances are checked to ensure that the driving gravitational forces and resisting shear forces match precisely.

The average shear stress, $\overline{\tau_o}$, is calculated as,

$$\begin{aligned}\overline{\tau_o} = \frac{1}{P}\int_P \tau dl &= \frac{1}{P}\left[2\int_{wall}\tau dl + \int_{bed}\tau dl\right] \\ &= \frac{1}{P}\left[\frac{2h}{\cos\theta}\overline{\tau_w} + b\overline{\tau_b}\right]\end{aligned} \tag{5.1}$$

where $\overline{\tau_w}$ and $\overline{\tau_b}$ are the average sidewall and bed shear stress as computed by CFD, P is the wetted perimeter of the channel, h is the depth of water in the channel and b is the bed width of the channel section and θ is the sidewall inclination with vertical axis.

Under the uniform flow condition the mean shear stress at the boundaries can be given by,

$$\overline{\tau_o} = \rho g S R \tag{5.2}$$

where, R is the hydraulic radius and is the ratio of the cross sectional area of the channel sections, A, and the wetted perimeter, P. Therefore the following equality should hold well,

$$\frac{2h}{\cos\theta}\overline{\tau_w} + b\overline{\tau_b} = \rho g S A \tag{5.3}$$

or

$$2h'\overline{\tau_w} + b\overline{\tau_b} = \rho g S A \tag{5.4}$$

The results are tabulated in Table 5.5 and it can be seen that the overall conservation of momentum is satisfied by the CFD model for all the cases.

Table 5.5 Conservation of momentum analysis for CFD simulations.

Channel	$\overline{\tau_b}$ (Pa)	$\overline{\tau_w}$ (Pa)	$b\overline{\tau_b}$ (N/m)	$2h'\overline{\tau_w}$ (N/m)	$b\overline{\tau_b} + 2h'\overline{\tau_w}$ (N/m)	ρgSA (N/m)	Difference[a] (%)
Same roughness on the bed and sidewall							
T12	0.30677	0.28946	0.07608	0.04252	0.11860	0.11878	0.16
T13	0.25701	0.26178	0.06374	0.06650	0.13024	0.13037	0.10
T01	0.37860	0.31610	0.07572	0.03058	0.10630	0.10665	0.33
T02	0.37586	0.33258	0.07517	0.04797	0.12314	0.12348	0.27
T03	0.34820	0.32549	0.06964	0.08481	0.15445	0.15484	0.25
T23	0.28817	0.24389	0.04380	0.06554	0.10934	0.11375	3.88
Different roughness on the bed and sidewall							
T12	0.30677	0.28946	0.07608	0.04252	0.11860	0.11878	0.16
T13	0.25701	0.26178	0.06374	0.06650	0.13024	0.13037	0.10
T01	0.37860	0.31610	0.07572	0.03058	0.10630	0.10665	0.33
T02	0.40072	0.29947	0.08014	0.04320	0.12334	0.12348	0.11
T03	0.38736	0.29510	0.07747	0.07689	0.15436	0.15484	0.31
T23	0.33837	0.21909	0.05143	0.05887	0.11030	0.11375	3.03

[a] Difference in percentage between CFD results and direct analytical calculations.

5.4 CFD model validation

The validation of the CFD model is done by comparing the CFD predictions first with the results given by Tominaga *et al.* (1989) and then with some other results found in the literature and is discussed below.

5.4.1 Isovel pattern analysis

First of all, isovel patterns for the three cases T13, T03 and T23 are plotted and the graphs are compared with those given by Tominaga *et al.* (1989). Figure 5.2 shows the isovels of primary velocity U normalized by U_{max}.

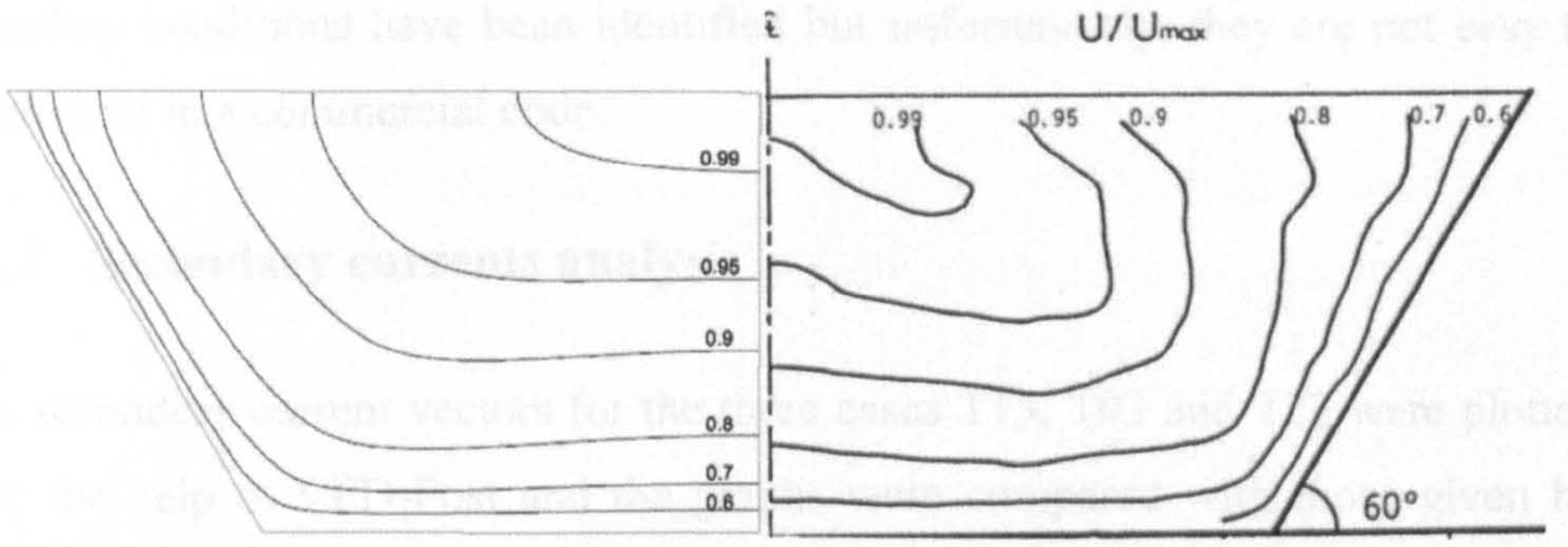

(a)

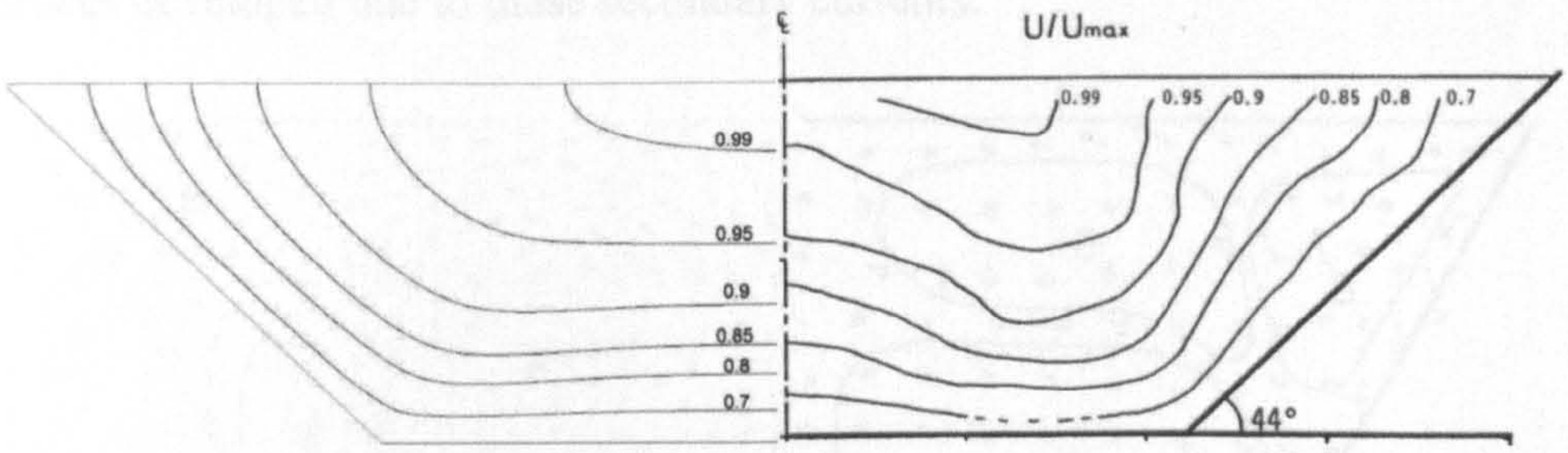

(b)

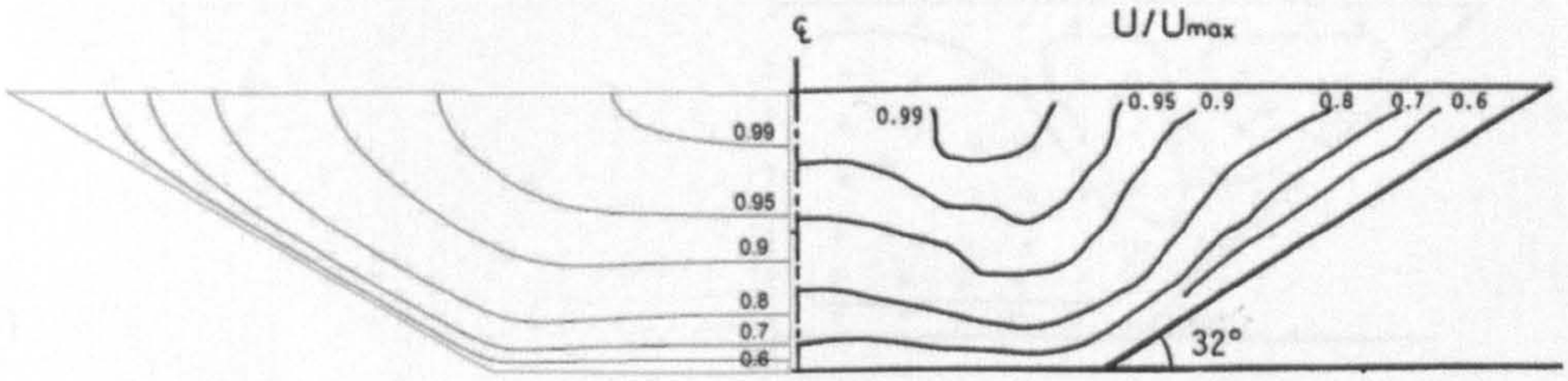

(c)

Figure 5.2 Comparison of the isovel patterns between CFD predictions (left) and Tominaga *et al.* (1989) (right) for the three cases (a) T13, (b) T03 and (c) T23.

The comparisons of the graphs show good agreement between the CFD predictions and the experimental results. However, a shift of the velocity is seen near the free surface especially as the sidewalls are opened and the velocity dip as observed in the experimental results is not seen. This is most probably due to the free surface boundary condition, a symmetry plane here, which does not account for free surface effects on turbulence. This condition is known and described by Celik and Rodi (1984) and also by Nezu and Nakagawa (1993). Although the

boundary conditions have been identified but unfortunately, they are not easy to implement in a commercial code.

5.4.2 Secondary currents analysis

The secondary current vectors for the three cases T13, T03 and T23 were plotted with the help of CFD-Post and the graphs were compared with those given by Tominaga *et al.* (1989) as shown in Figure 5.3. The vectors have been normalized to show the direction only and not the magnitudes just to see the longitudinal vortices developed due to these secondary currents.

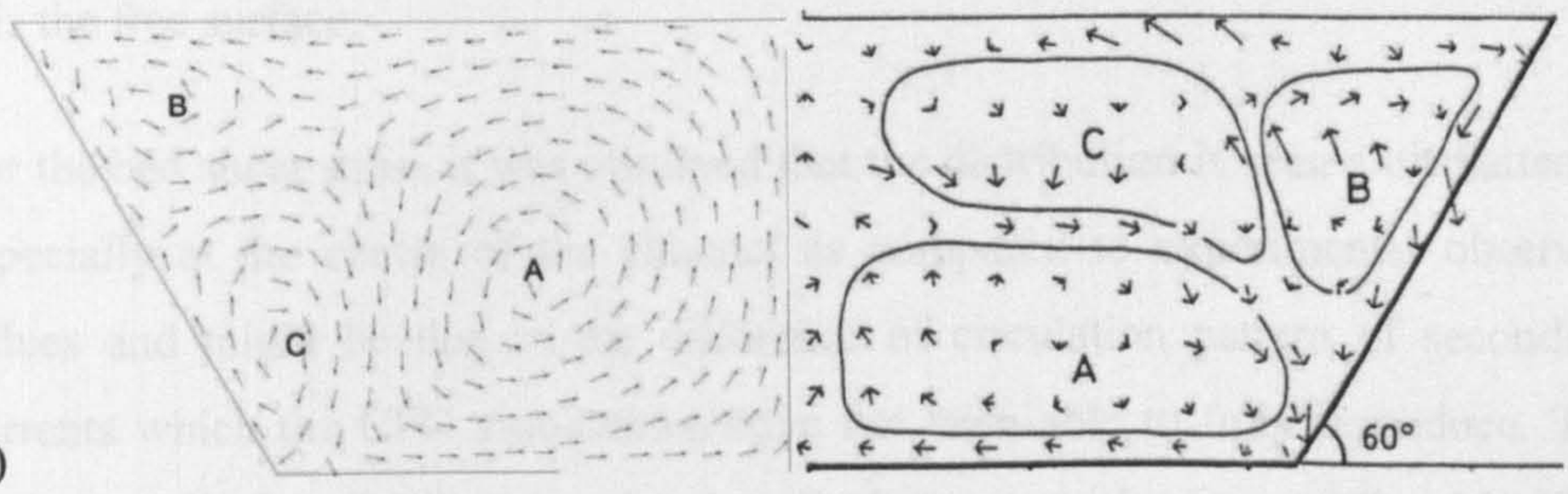

Figure 5.3 Comparison of the secondary current vectors between CFD predictions (left) and Tominaga *et al.* (1989) (right) for the three cases (a) T13, (b) T03 and (c) T23.

It was observed that the three vortices of secondary currents as seen by Tominaga *et al.* for trapezoidal channels were also visible but a shift towards the corner is seen in the case of Vortex C. This vortex as described by Tominaga *et al.* (1989) corresponds to the free surface vortex and the shift is most probably due to the same reason of capping of the free surface with the symmetry boundary condition.

5.4.3 Distribution of boundary shear

The distribution of the boundary shear on the bed and sidewalls is plotted next. The results are compared with the experimental ones given by Tominaga *et al.* (1989) and shown in Figure 5.4. The shear on the bed is plotted for the half width of the channel section due to symmetry along the centre line of the channel. Whereas, on the sidewalls it is plotted along the whole length. The distance along the bed and sidewall has been non- dimensionalized by dividing with half width of the channel and length of the sidewall respectively. Zero is the corner of the bed and sidewall and one for bed is the centre of the channel, whereas for sidewall it is the free surface.

For the bed shear stress it was observed that the distribution is seen a bit flattened especially at the centre of the channel as compared to experimental observed values and might be due to the difference of circulation pattern of secondary currents which the CFD simulations have not been able to fully reproduce. The difference in the distribution of sidewall shear stress is more noticeable. The variations of shear stress seen in the experiments especially at the corner joining the bed and sidewall and near the free surface are not found in the CFD simulations. Weaker or ill-positioned secondary cells are the obvious culprits here. At the free surface, the use of a symmetry plane is clearly not sufficient it would appear.

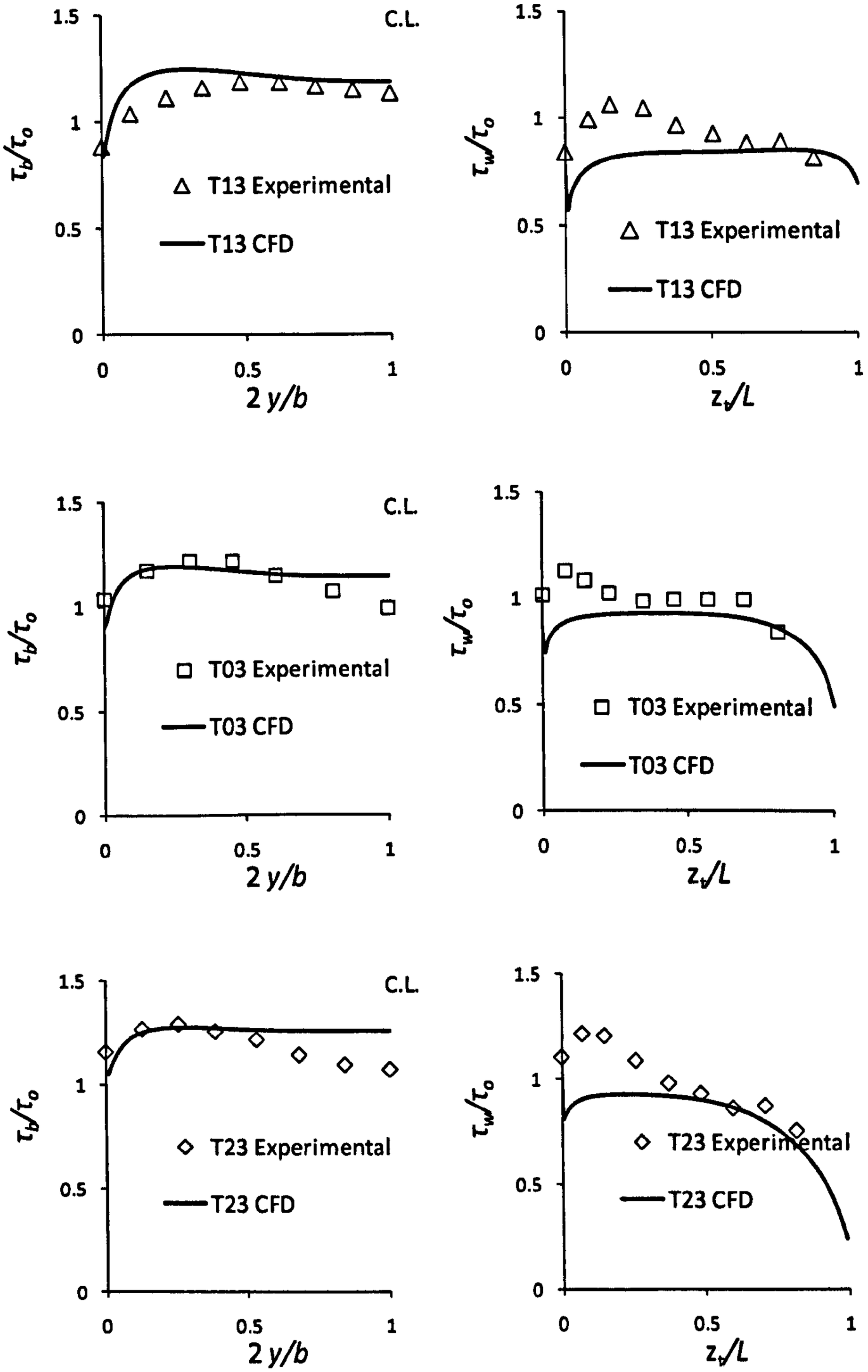

Figure 5.4 Comparisons of local non-dimensionalized wall shear on bed (τ_b/τ_o) and sidewalls (τ_w/τ_o) between CFD predictions and Tominaga *et al.* (1989).

5.4.4 Longitudinal vortices and the secondary currents

For trapezoidal channels, three longitudinal vortices are generally developed due to the effect of the secondary currents (Tominaga *et al.*, 1989). These vortices correspond to the bed, sidewall, and the corner connecting the bed and the sidewall and may be given the symbols of B, S and C respectively for future reference.

Figure 5.5 shows the change in secondary current vortices for a constant slant angle in this case 46°. Figures (a), (c) and (e) are achieved with uniform roughness on the bed and sidewalls Whereas figures (b), (d) and (f) have smooth sidewalls and rough beds. Figures (a) and (b) have an aspect ratio of 2, (c) and (d) have an aspect ratio of 4 whereas (e) and (f) have an aspect ratio of 6 approximately. It is observed that for a constant sidewall inclination, when the bed and the sidewalls have the uniform roughness, the vortex C becomes weaker as the aspect ratio increases and the vortices B and S merge as a single vortex. Whereas, if the sidewalls are smoother as compared to the bed, the vortex C tries to prolong its presence and therefore vortices B and S remain separated.

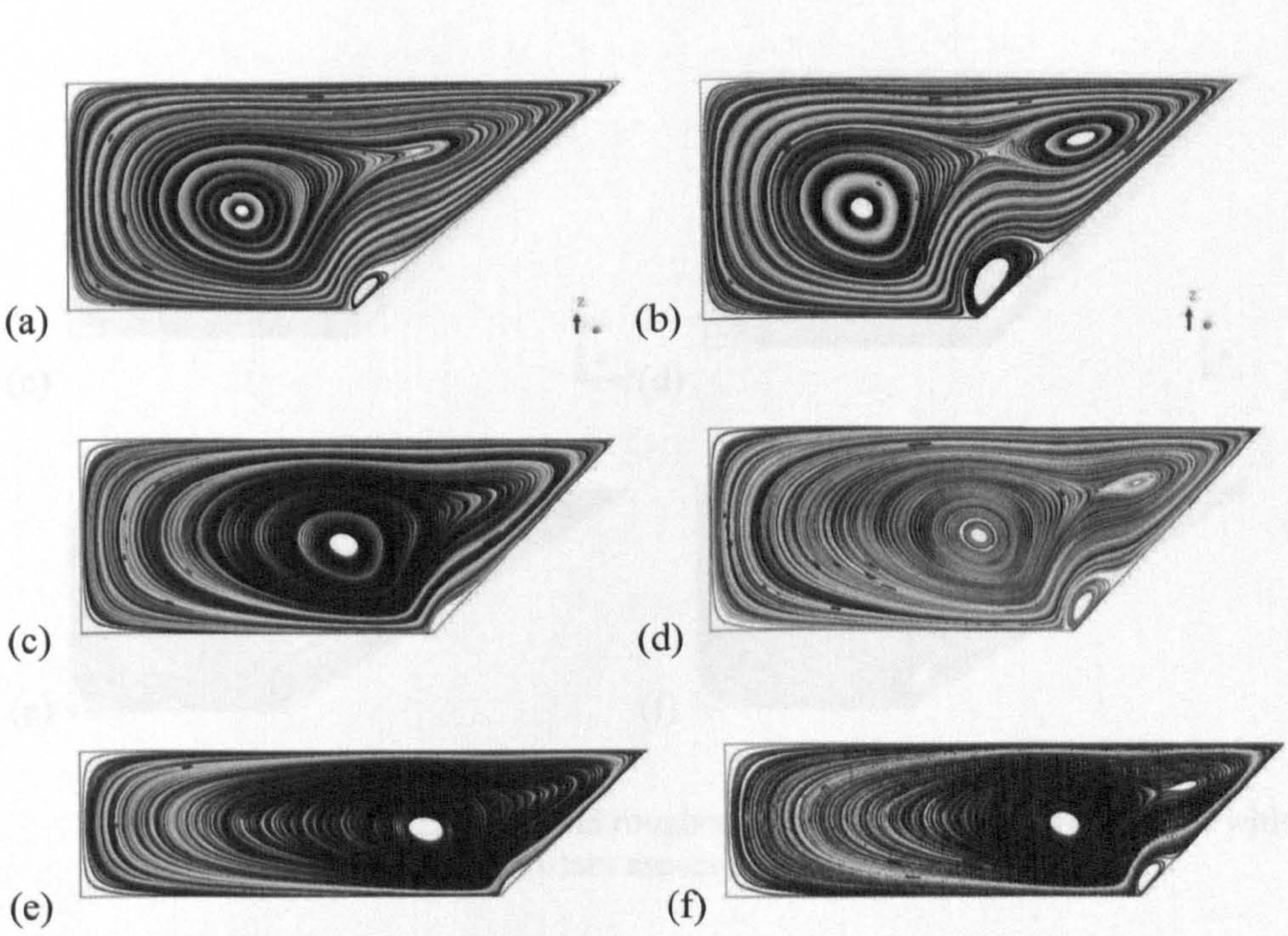

Figure 5.5 Effect of aspect ratio and roughness on secondary current vortices with constant slant angle of 46°.

Figure 5.6 shows the change in secondary current vortices for a constant aspect ratio in this case 2. Figures (a), (c) and (e) are achieved with uniform roughness on the bed and sidewalls whereas figures (b), (d) and (f) have smooth sidewalls and rough beds. Figures (a) and (b) have a slant angle of 30°, (c) and (d) have a slant angle of 46° whereas (e) and (f) have a slant angle of 58°. It is also observed that for a constant aspect ratio, in this case 2, when the bed and sidewalls have same roughness, as the angle between the bed and the sidewall increases beyond 0° the vortices B and S become separated and independent of each other, the vortex C also becomes weaker with the increase in the angle. Whereas, if the bed is rougher as compared to sidewalls again the vortex C tries to maintain its influence and tries to separate the other two vortices B and S as much as possible.

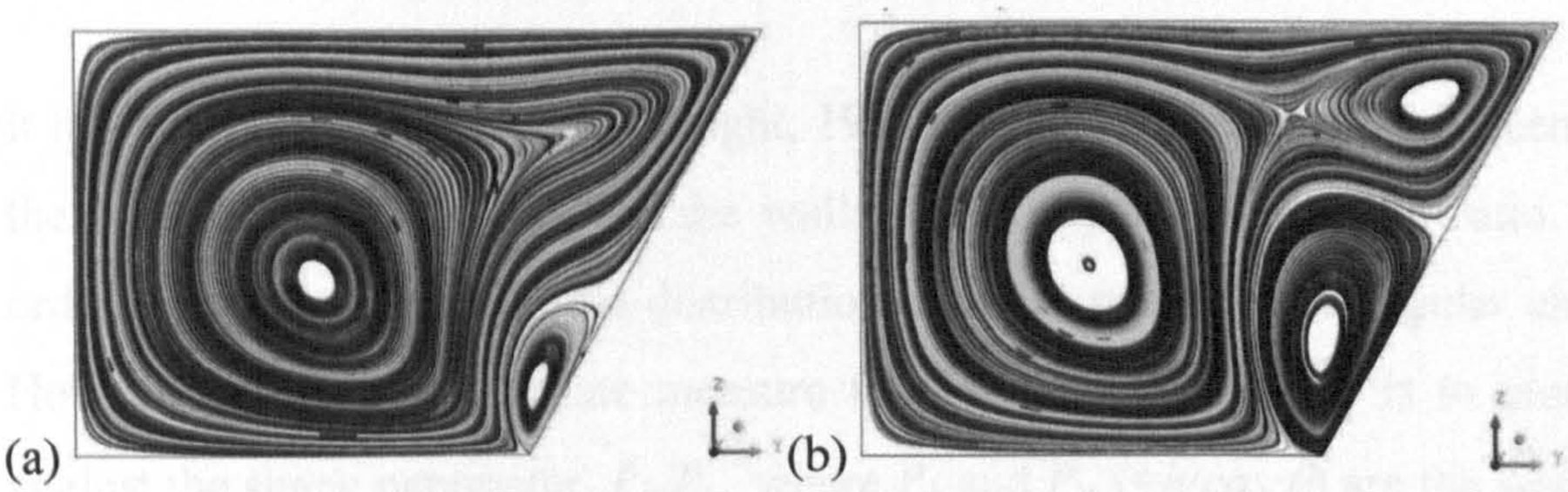

Figure 5.6 Effect of slant angle and roughness on secondary current vortices with constant aspect ratio of 2.

5.5 Results and analysis

The results of the second set of simulations and their corresponding analysis are given in detail in the following sections.

5.5.1 Direct CFD predictions of shear stress

In this section, a number of standard methods of presenting the data for wall shear stresses are reported. Where possible, comparison with the experimental data is used, to demonstrate the ability of the CFD simulations to represent the phenomena of interest here accurately.

5.5.1.1 Percentage shear force on wall versus shape parameter

It has been accepted practice (Knight, 1981) to provide plots of the percentage of the total shear force acting on the walls, $\%SF_w$ against the aspect ratio, b/h, in order to gain insights into the distribution of shear stress in rectangular channels. However, a more appropriate measure for trapezoidal channels is to plot $\%SF_w$ against the shape parameter, P_b/P_w, where P_b and P_w ($=h/\cos\theta$) are the wetted bed and wall perimeters respectively (Flintham and Carling, 1988; Mohammadi and Knight, 2004). This better accounts for the increase in side wall surface area as the slant angle increases.

Figure 5.7 shows a comparison between those CFD simulations where $k_{sb}=k_{sw}$ =0.0015 mm; (Knight, 1981) and a variety of experimental results with smooth channels or equal side and bed wall roughness. The data is taken from reference listed in the legend of the figure. This figure shows that the CFD results follow the expected pattern, across the range of shape parameters and slant angles considered.

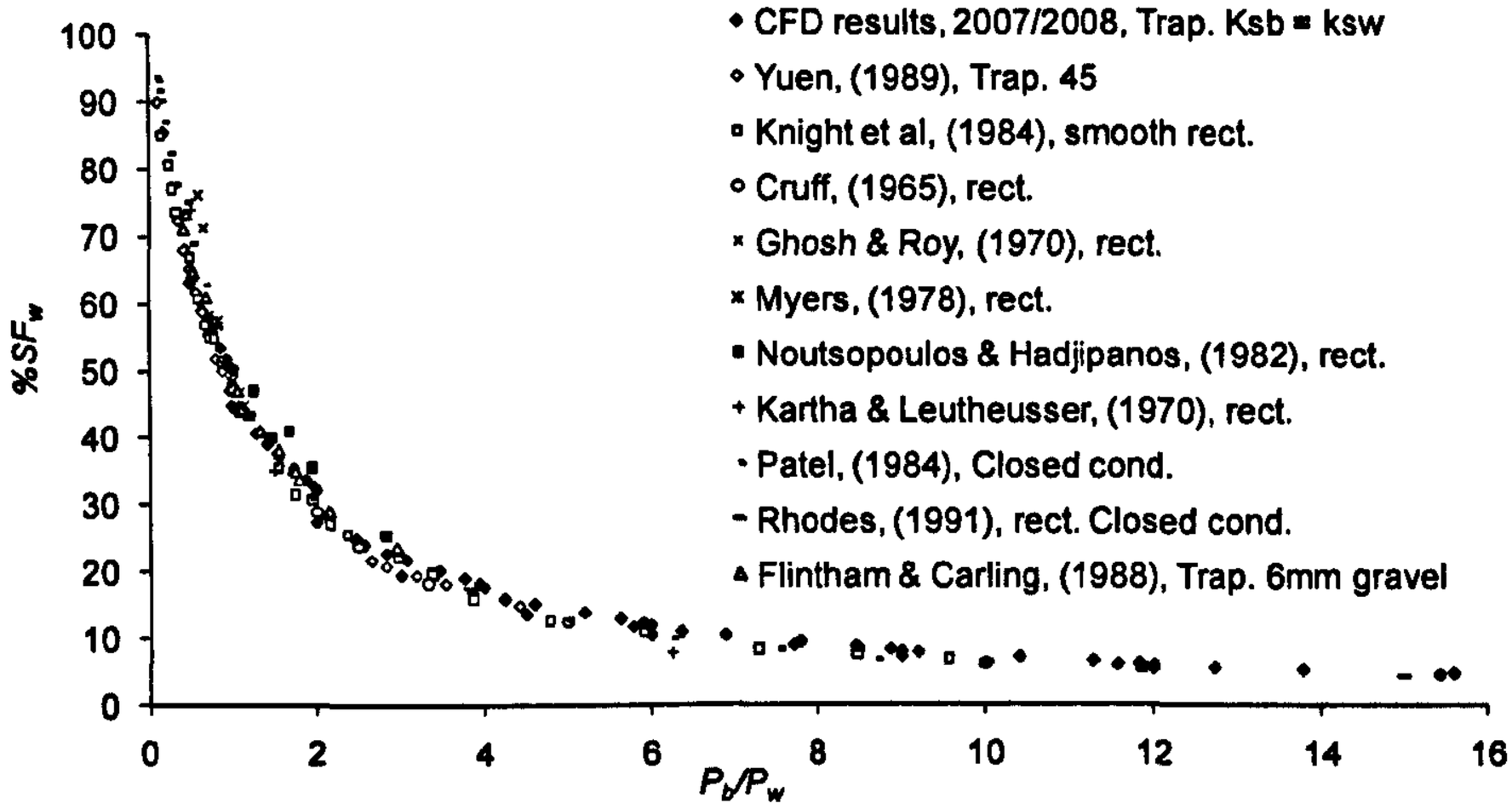

Figure 5.7 Percentage wall shear force versus shape parameter for CFD simulations and experimental data with smooth walls or equal bed/wall roughness.

5.5.1.2 Differentially roughened channels

The difference between roughness height of the bed and walls plays an important role in determining the shear stress distribution on the wetted perimeter (Flintham & Carling, 1988). It is measured through the k_{sb}/k_{sw} ratio which is a dimensionless roughness parameter expressed in terms of Nikuradse's equivalent sand roughness height. When considering different roughness on the bed and walls, a different effect manifests itself in the plot of $\%SF_w$ against P_b/P_w. As can be seen in Figure 5.8, there is a downward shift in $\%SF_w$ as the bed is roughened, both in the CFD simulations but also in Flintham and Carling's (1988) data. This corresponds to the physical effect of a rough wall producing more shear force on the water than a smooth wall. Clearly, the roughness heights used in the CFD simulations do not get close to those used by Flintham and Carling in their experiments, but the trend is nonetheless clear to see.

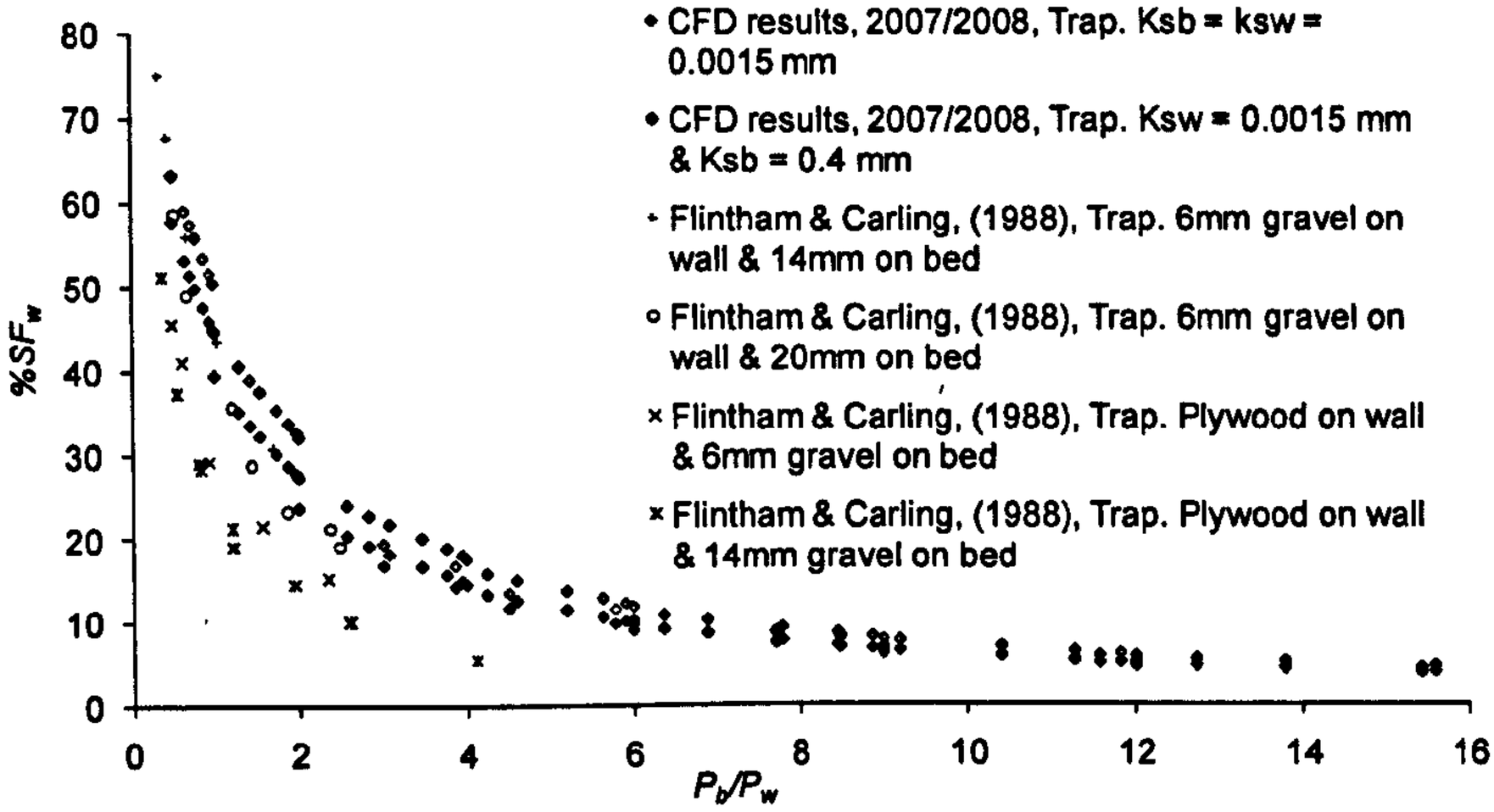

Figure 5.8 Percentage wall shear force versus shape parameter for CFD simulations and Flintham and Carling's (1988) experimental data with unequal bed/wall roughness.

An analysis was also carried out for the influence of the difference in the roughness of the bed and side walls. As mentioned in Section 5.2.1, the walls were kept "smooth" with a k_{sw} value of 0.0015 mm as the channels which were used in many of the original experiments had glass sidewalls for which a roughness height of 0.0015 mm (Knight, 1981) is an acceptable approximation. Adopting the idea of Knight (1981), Figure 5.9 shows the percentage shear force on the wall against the k_{sb}/k_{sw} ratio for both the CFD simulations and the data presented in Knight (1981). Only the results from simulations of rectangular channels have been used in the figure, to ensure a like-for-like comparison. The CFD results follow the same trend as Knight, although they appear to slightly over-predict the values from Knight's best fit curves.

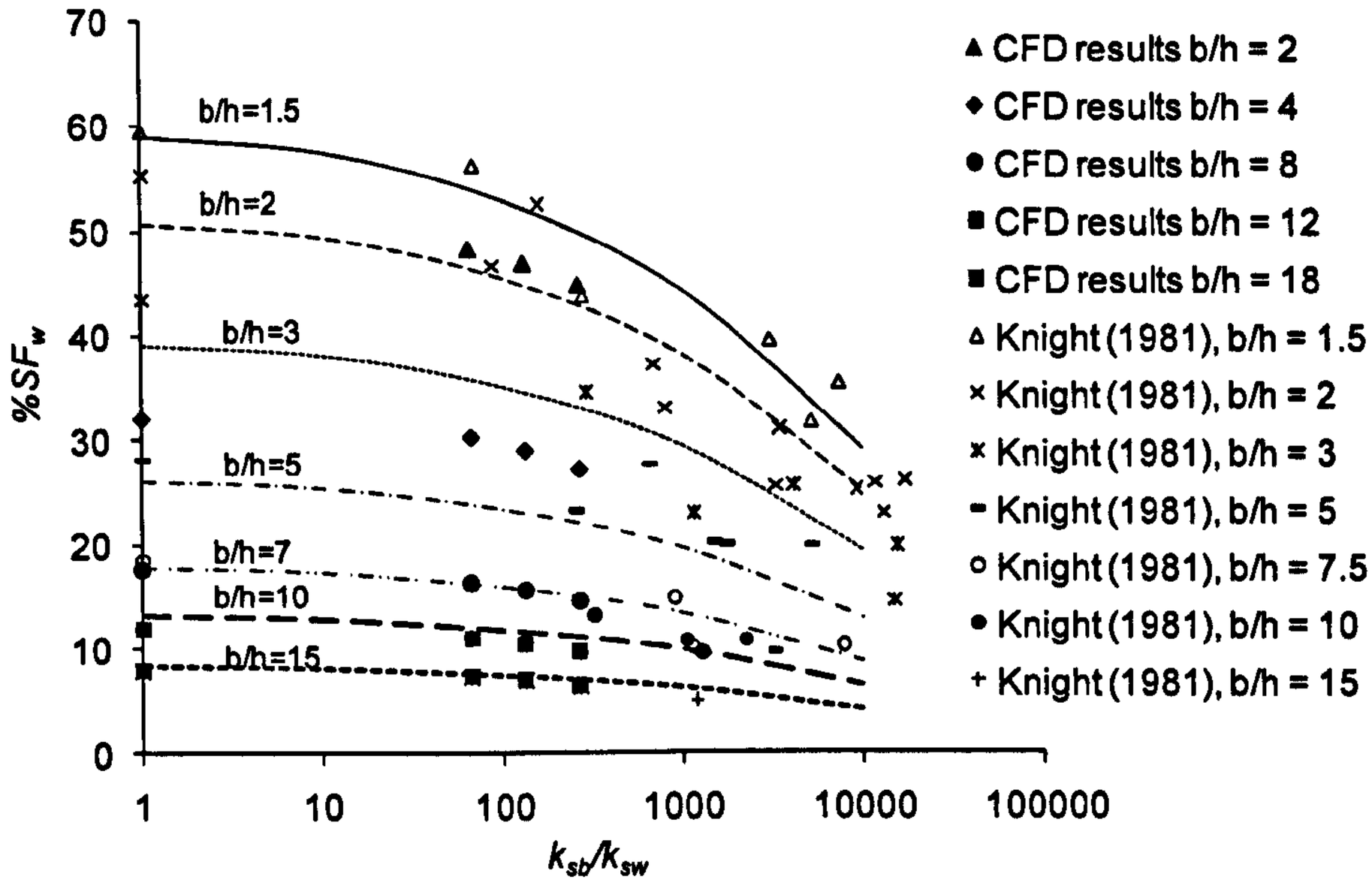

Figure 5.9: Percentage wall shear force versus the roughness ratio, k_{sb}/k_{sw}, for rectangular channels of various aspect ratios. The CFD simulations are compared with the data of Knight (1981).

5.5.1.3 Non-dimensionalised mean bed and sidewall shear stress

Another useful way of analysing the data is to plot the mean bed and side wall shear stresses non-dimensionalised by the two dimensional bed shear stress, ρghS, as per the suggestion of Knight *et al.* (1984). Figure 5.10 shows the results for the non-dimensionalised mean bed shear stress $\bar{\tau}_b/\rho ghS$ against aspect ratio b/h for CFD simulations and Knight *et al.* (1984) experimental data. Similarly, Figure 5.11 shows the results for non-dimensionalised mean bed shear stress $\bar{\tau}_b/\rho ghS$ against aspect ratio b/h for CFD simulations and Yuen (1989) experimental data. The CFD data is taken from the same type of channels as were used during the experiments so as to have a like for like comparison. In addition, the comparison is done for the sidewalls against the same set of experimental data as shown in Figure 5.12 and Figure 5.13. For the bed, the results are encouraging but there is an over-prediction for the sidewall. This may be due to the fact that the side walls make up such a small percentage of the wetted perimeter (certainly for the higher aspect ratios) that any errors inherent in the CFD simulations are exacerbated here.

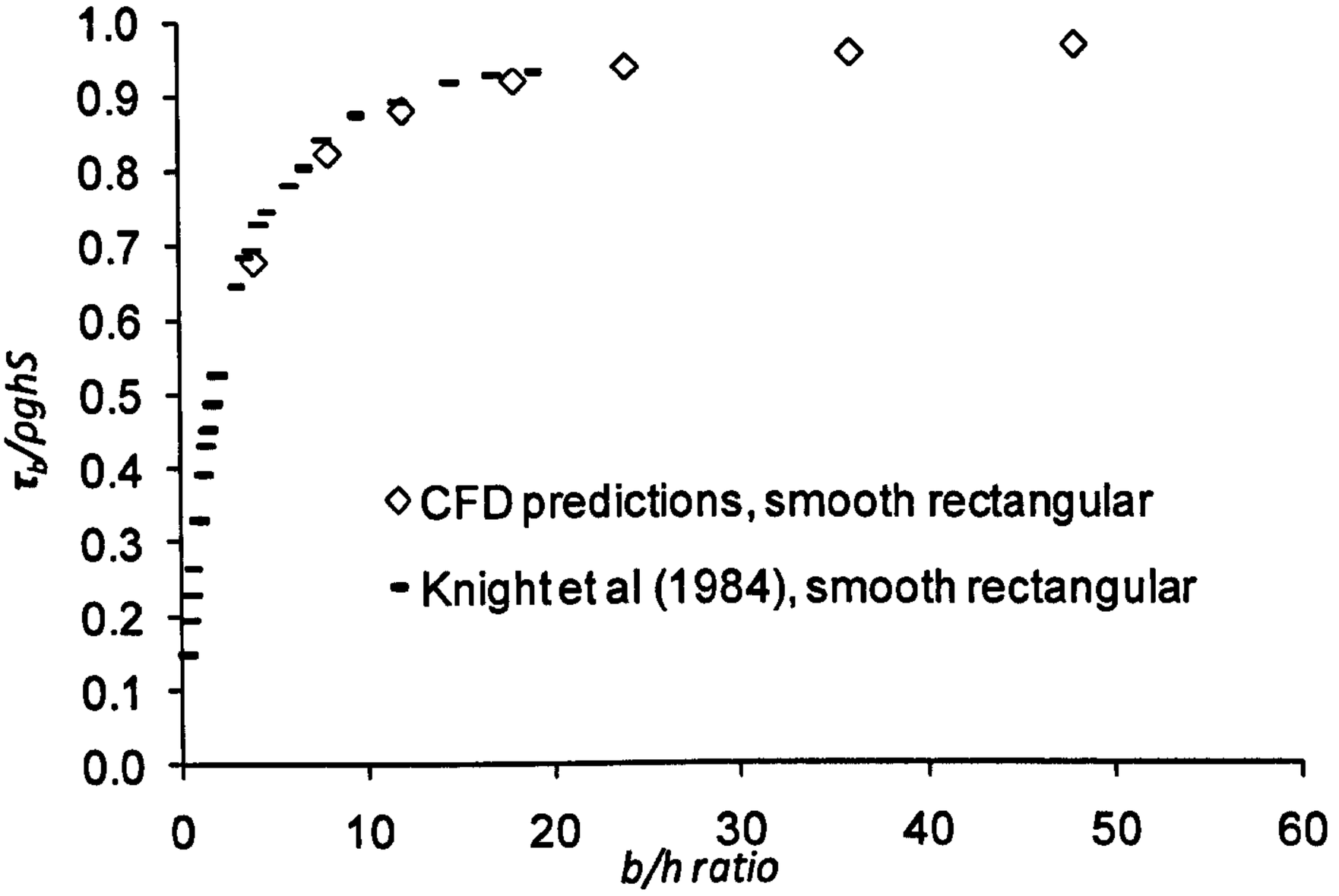

Figure 5.10 Non-dimensionalised mean bed shear stress $\overline{\tau_b}/\rho ghS$ against aspect ratio b/h for CFD simulations and Knight *et al.* (1984) experimental data.

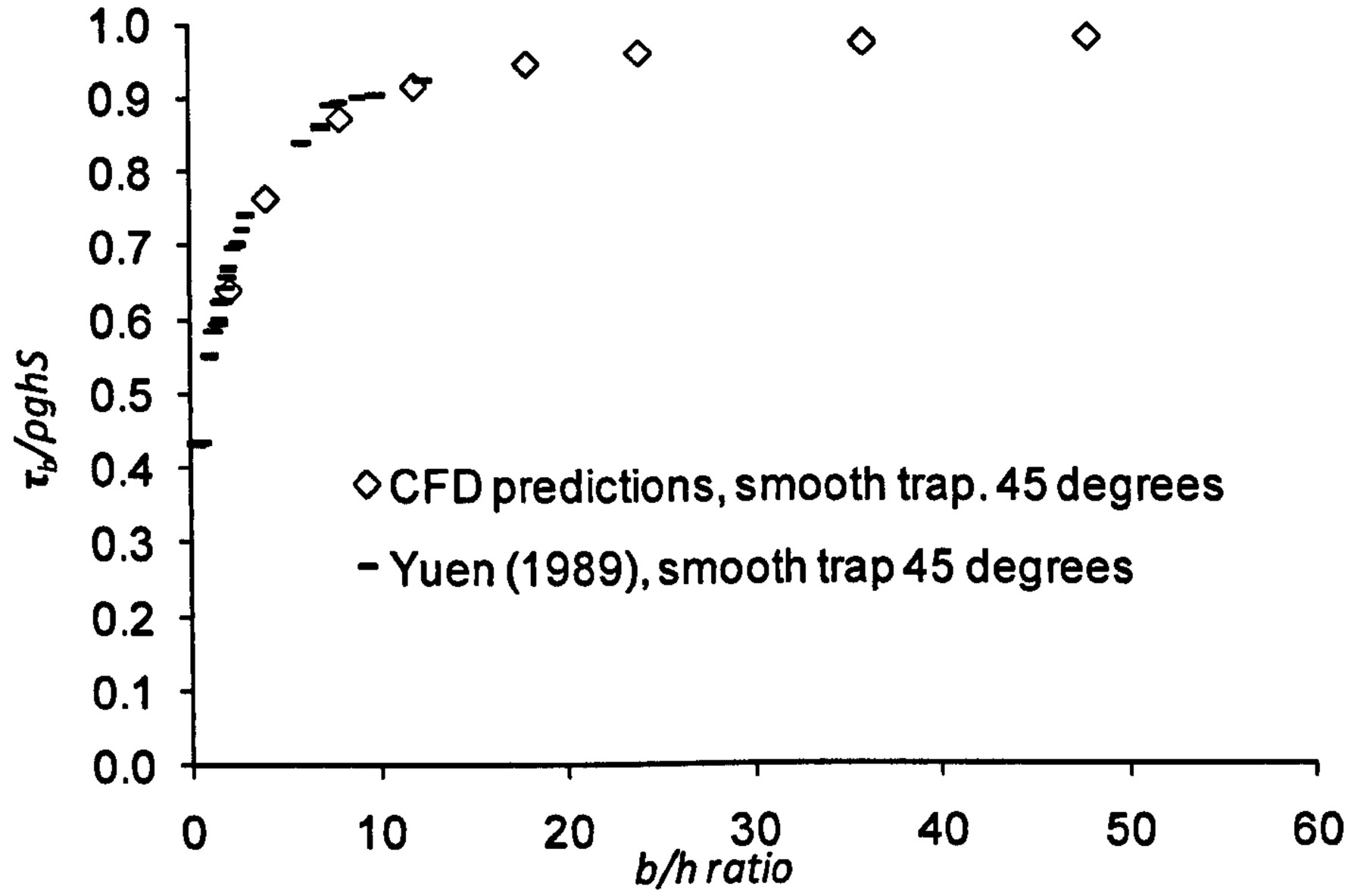

Figure 5.11 Non-dimensionalised mean bed shear stress $\overline{\tau_b}/\rho ghS$ against aspect ratio b/h for CFD simulations and Yuen (1989) experimental data.

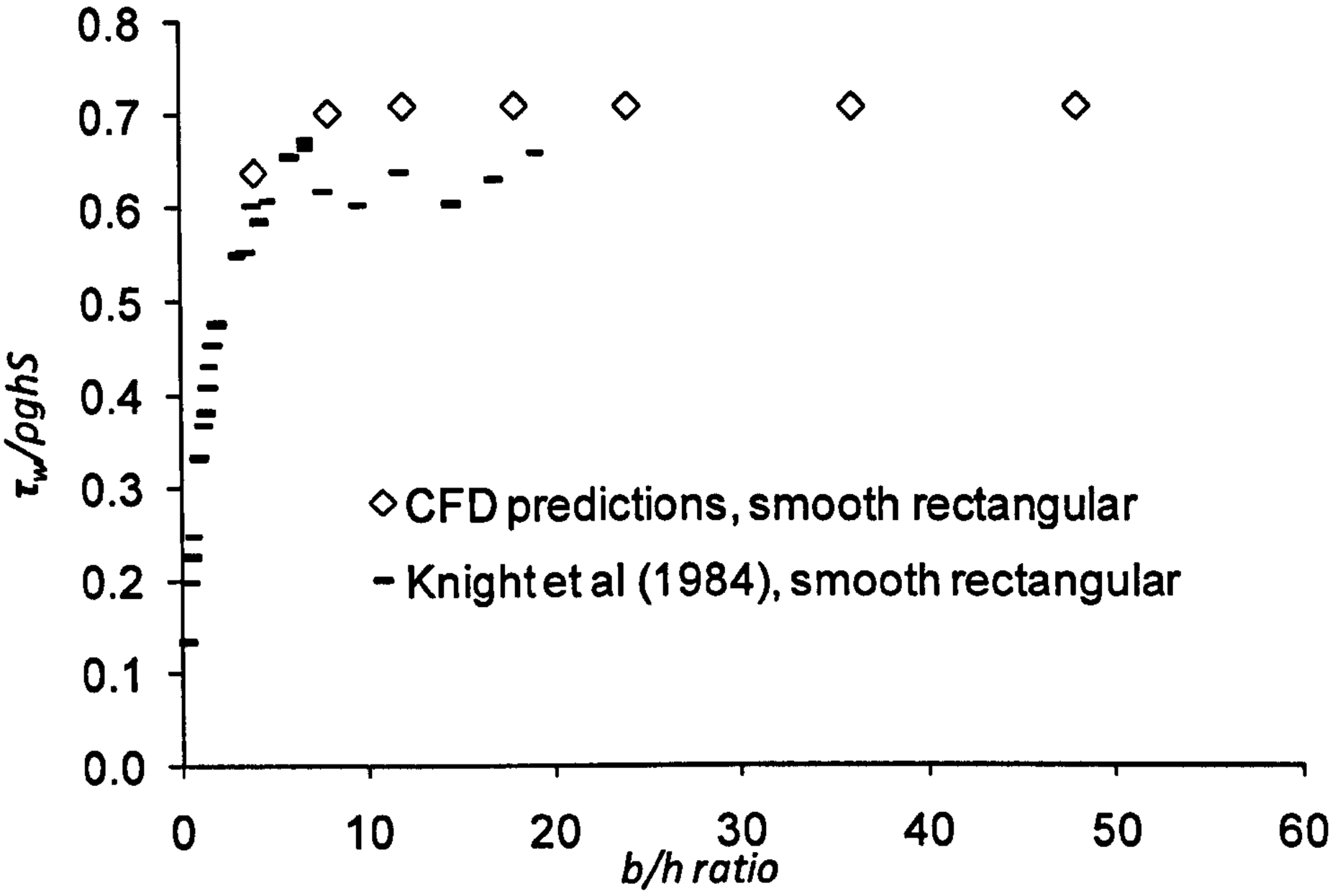

Figure 5.12 Non-dimensionalised mean sidewall shear stress $\overline{\tau_w}/\rho ghS$ against aspect ratio b/h for CFD simulations and Knight *et al.* (1984) experimental data.

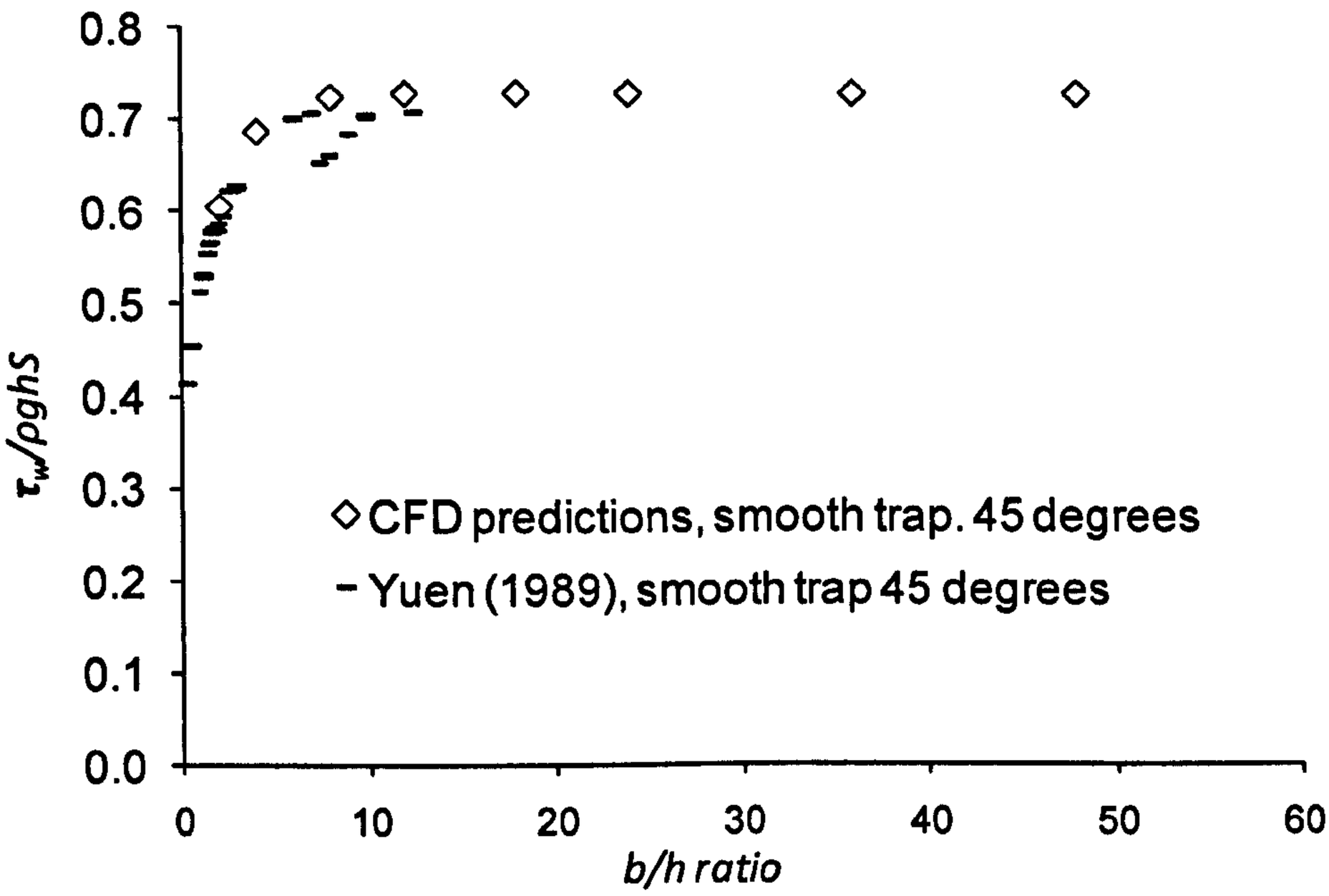

Figure 5.13 Non-dimensionalised mean sidewall shear stress $\overline{\tau_w}/\rho ghS$ against aspect ratio b/h for CFD simulations and Yuen (1989) experimental data.

After comparing the CFD results with experimental data graphs are also plotted for non-dimensionalised mean bed shear stress $\overline{\tau_b}/\rho ghS$, and mean sidewall shear stress $\overline{\tau_w}/\rho ghS$ against aspect ratio b/h with variation in slant angle for CFD

simulations. Figure 5.14 shows the plots for the non-dimensionalised mean bed shear stress $\overline{\tau_b}/\rho ghS$ against aspect ratio b/h for CFD simulations having bed roughness of 0.1 mm. The graph shows that for small aspect ratios the mean shear on the bed increases with the slant angle for a given b/h ratio. This variation in the shear stress goes on decreasing with the increase in the b/h ratio and for large aspect ratios not much variation is observed with the variation in slant angle for a given aspect ratio. Similarly Figure 5.15 shows the plots for the non-dimensionalised mean sidewall shear stress $\overline{\tau_w}/\rho ghS$ against aspect ratio b/h for CFD simulations having bed roughness of 0.1 mm. The graph shows that the shear stress on the sidewall increases with the aspect ratio until around $b/h = 8$ and then remains constant. This shows that the shear stress on the sidewalls for wide channels remains constant irrespective of the aspect ratio. For a given aspect ratio in narrow channels the shear stress on the sidewalls increases with the increase in slant angle but for wide channels it is seen to increase first until slant angle reaches 30° and then is seen to decrease with the increase in slant angle.

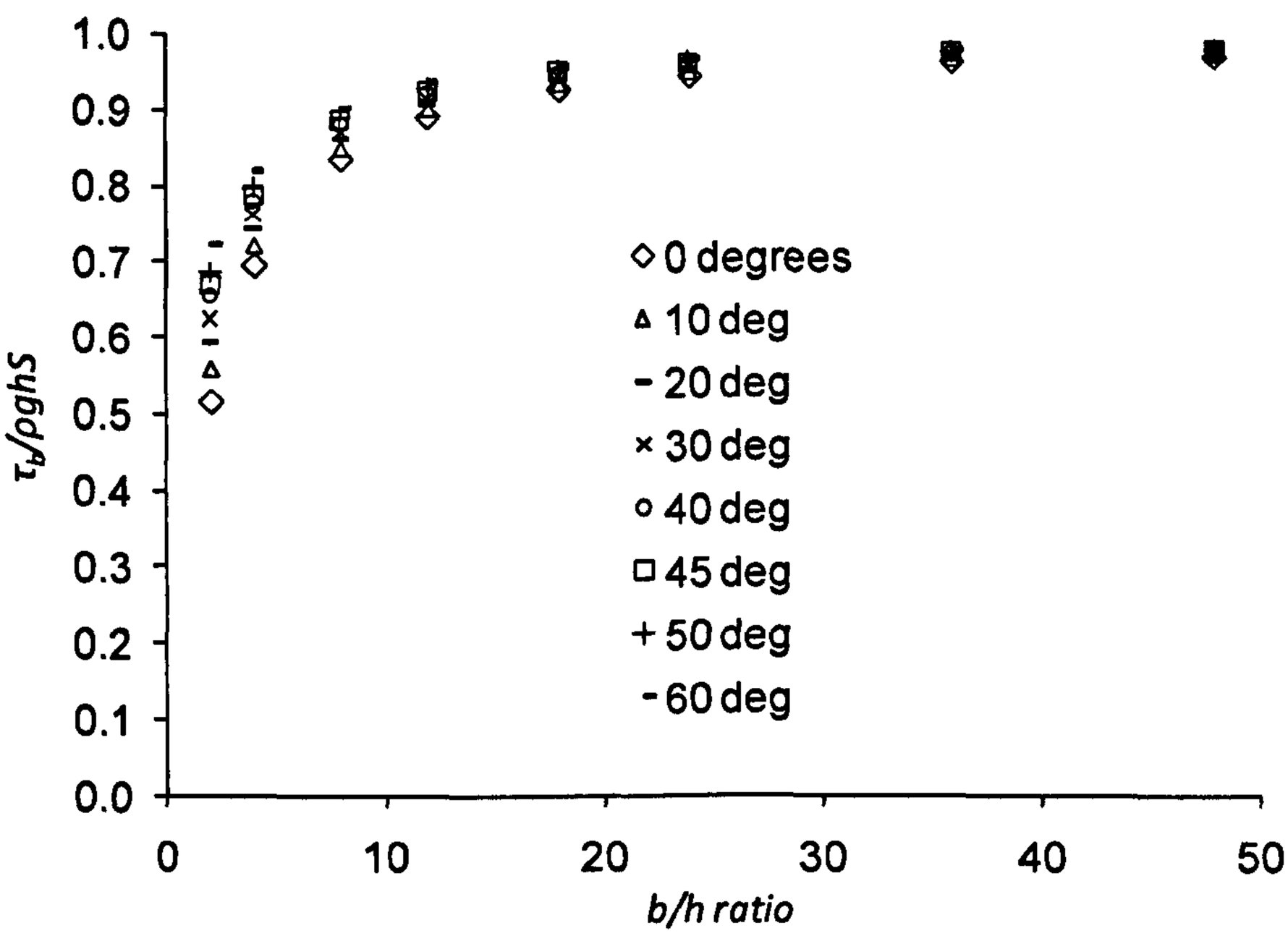

Figure 5.14 Variation of non-dimensionalised mean bed shear stress $\overline{\tau_b}/\rho ghS$ against aspect ratio b/h with variation in slant angle for CFD simulations having bed roughness of 0.1 mm.

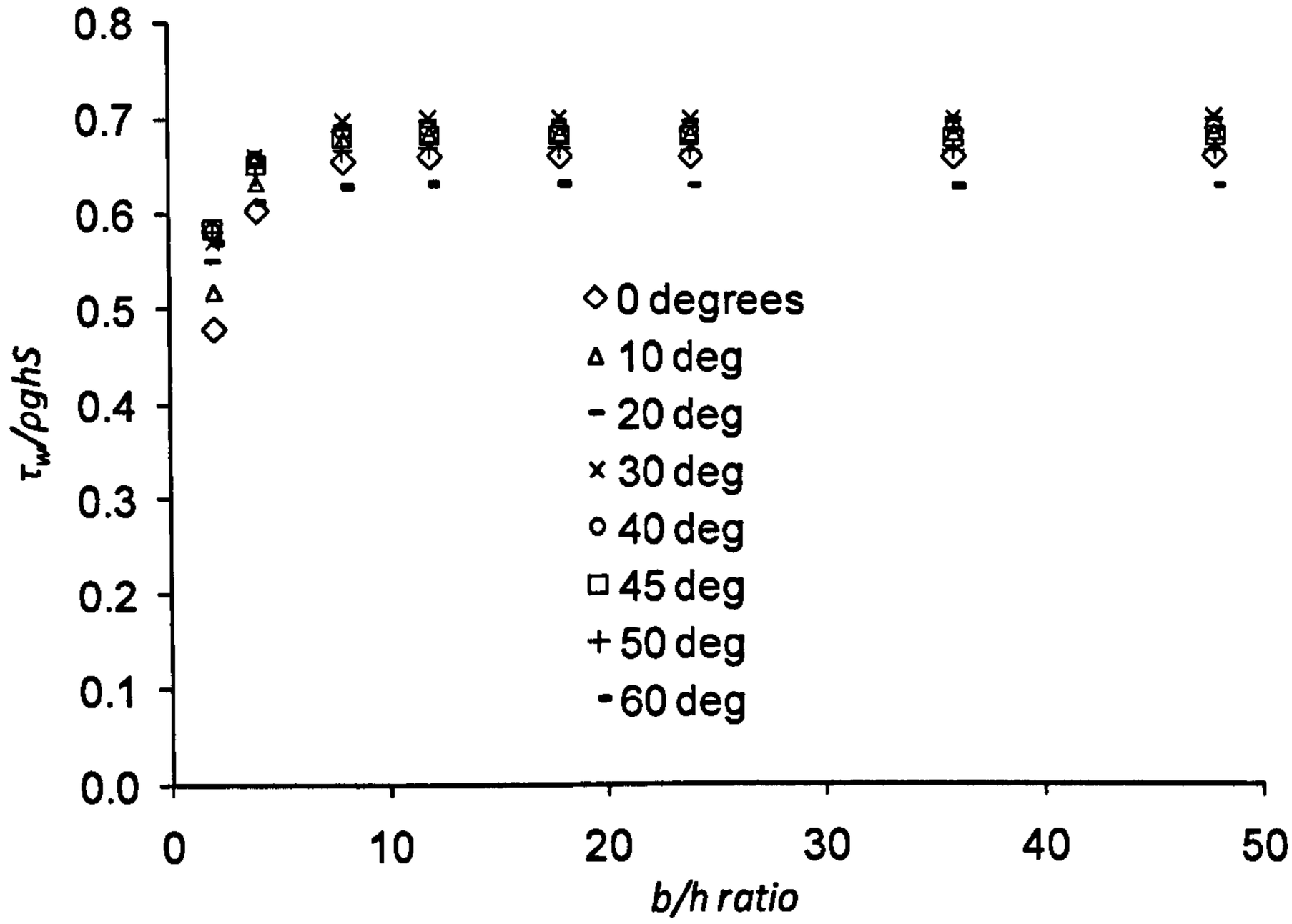

Figure 5.15 Variation of non-dimensionalised mean sidewall shear stress $\overline{\tau_w}/\rho ghS$ against aspect ratio b/h with variation in slant angle for CFD simulations having bed roughness of 0.1 mm.

Graphs are also plotted for non-dimensionalised mean bed shear stress $\overline{\tau_b}/\rho ghS$, and mean sidewall shear stress $\overline{\tau_w}/\rho ghS$ against slant angle with variation in aspect ratio b/h for CFD simulations. Figure 5.16 shows the plots for the non-dimensionalised mean bed shear stress $\overline{\tau_b}/\rho ghS$ against slant angle for CFD simulations having bed roughness of 0.1 mm. The graph shows that the mean shear on the bed increases with b/h ratio for a given slant angle. This variation in the shear stress is large for small aspect ratios (narrow channels) but very small for large aspect ratios (wide channels). Similarly Figure 5.17 shows the plots for the non-dimensionalised mean sidewall shear stress $\overline{\tau_w}/\rho ghS$ against slant angle for CFD simulations having bed roughness of 0.1 mm. The graph shows that for a given slant angle the shear stress on the sidewall increases with the aspect ratio until around $b/h = 8$ and then remains constant. This shows that the shear stress on the sidewalls for wide channels remains constant irrespective of the aspect ratio.

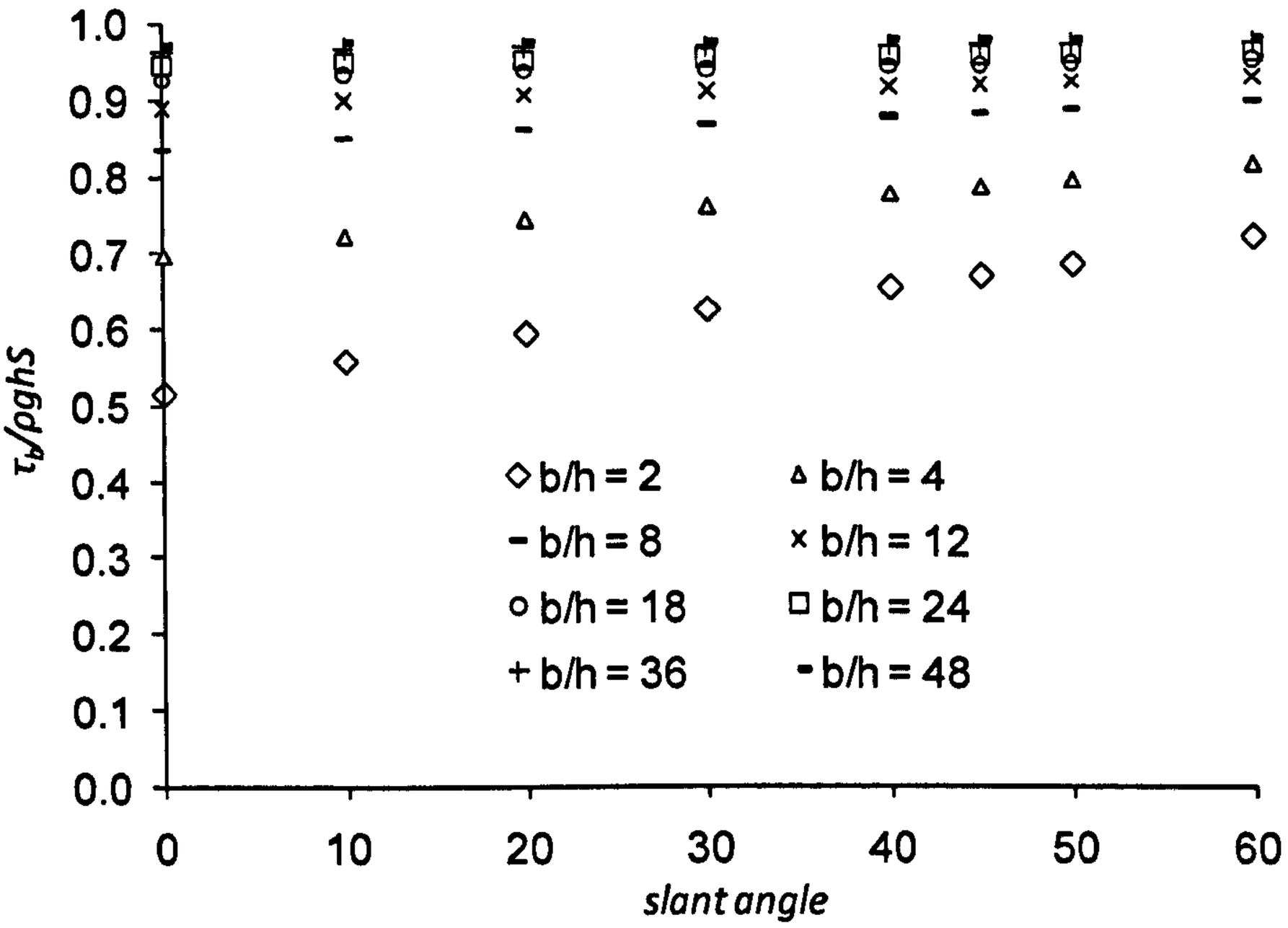

Figure 5.16 Variation of non-dimensionalised mean bed shear stress $\overline{\tau_b}/\rho ghS$ against slant angle (degrees) with variation in aspect ratio b/h for CFD simulations having bed roughness of 0.1 mm.

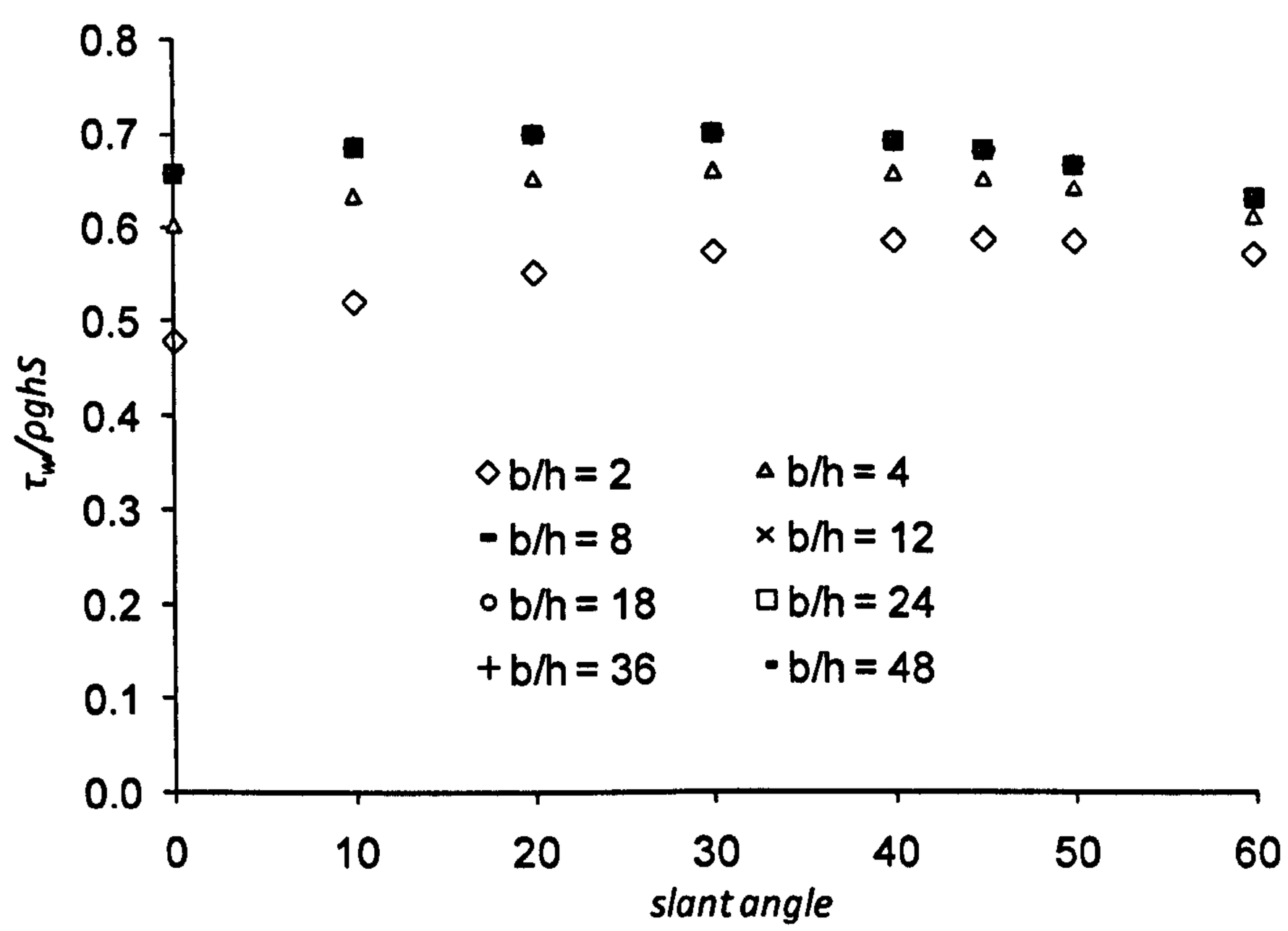

Figure 5.17 Variation of non-dimensionalised mean sidewall shear stress $\overline{\tau_w}/\rho ghS$ against slant angle (degrees) with variation in aspect ratio b/h for CFD simulations having bed roughness of 0.1 mm.

5.5.1.4 Variation of non-dimensionalised local bed and side wall shear stress

The variation of the non-dimensionalised local bed and sidewall shear stress is plotted on the wetted perimeter of the channels. An analysis is done for this variation with change in slant angle of the channels for constant aspect ratios. Graphs are plotted for three aspect ratios of 2, 4 and 8 so as to cover both narrow and wide channels. Figure 5.18 shows the variation of non-dimensionalised local shear stress on the bed $\tau_b/\rho ghS$ with slant angle for CFD channels with aspect ratio of 2 and bed roughness of 0.0015 mm. The local shear stress at any point on the bed is seen to increase with the increase in the slant angle. It is found to be almost constant throughout the width of the channel except for near the corner region where it is seen to decrease. Figure 5.19 shows the variation of non-dimensionalised local shear stress on the sidewalls $\tau_w/\rho ghS$ with slant angle for CFD channels with aspect ratio of 2 and bed roughness of 0.0015 mm. As the slant angle increases the wall shear stress shifts dramatically from the top to the middle part of the wall, reflecting the creation of an additional secondary cell as shown in Figure 5.20 which shows the same effect. As this happens a far higher shear stress exists at the foot of the bank wall. This is consistent with what is visible in Figure 5.19, which shows an increase on the outer bed side too, though the changes in the middle part of the channel are small, highlighting the localised effects associated with corners and the prominence of these features in relatively low aspect ratio channels.

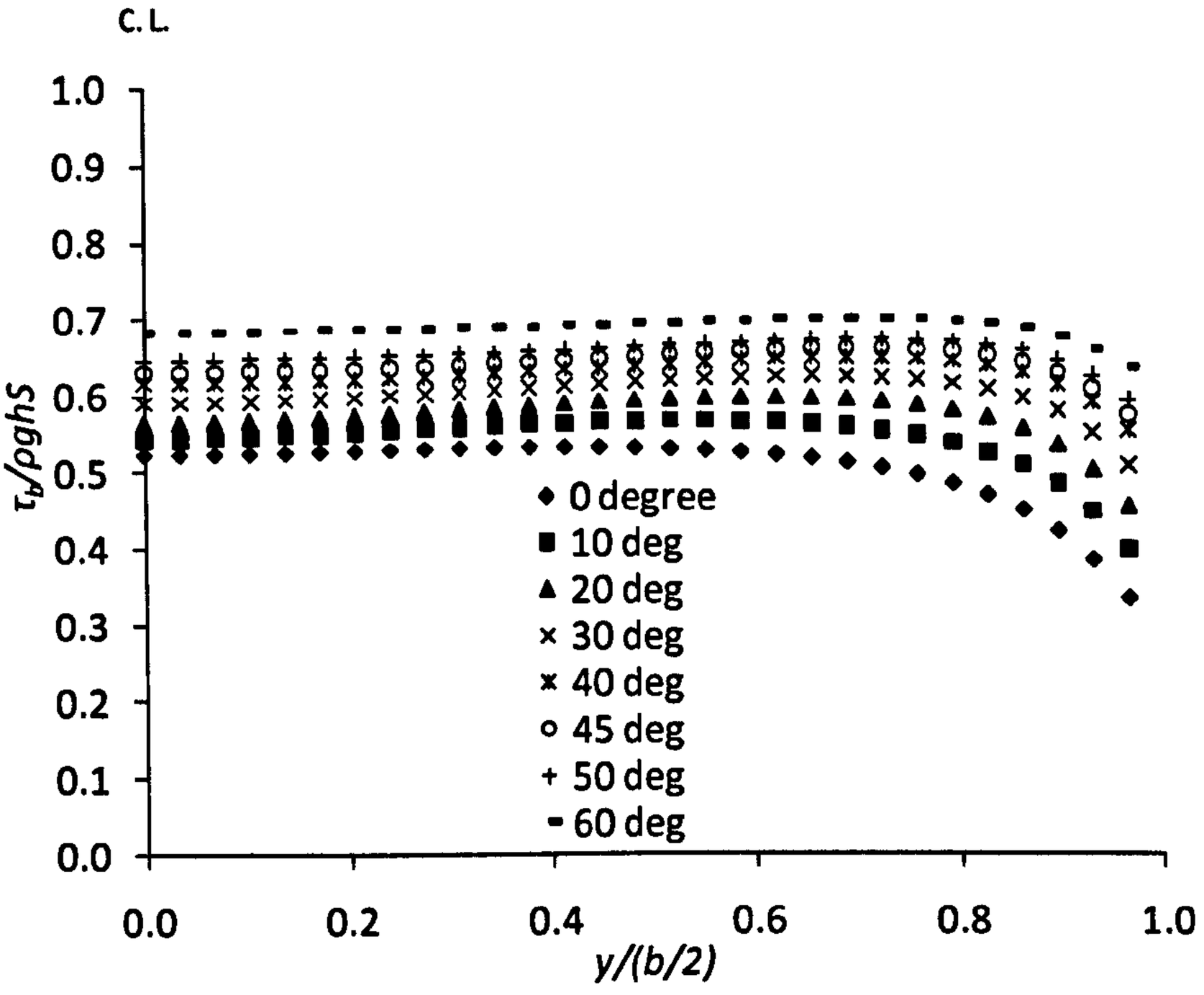

Figure 5.18 Variation of non-dimensionalised local shear stress on the bed $\tau_b/\rho ghS$ with slant angle for CFD channels with aspect ratio of 2 and bed roughness of 0.0015 mm.

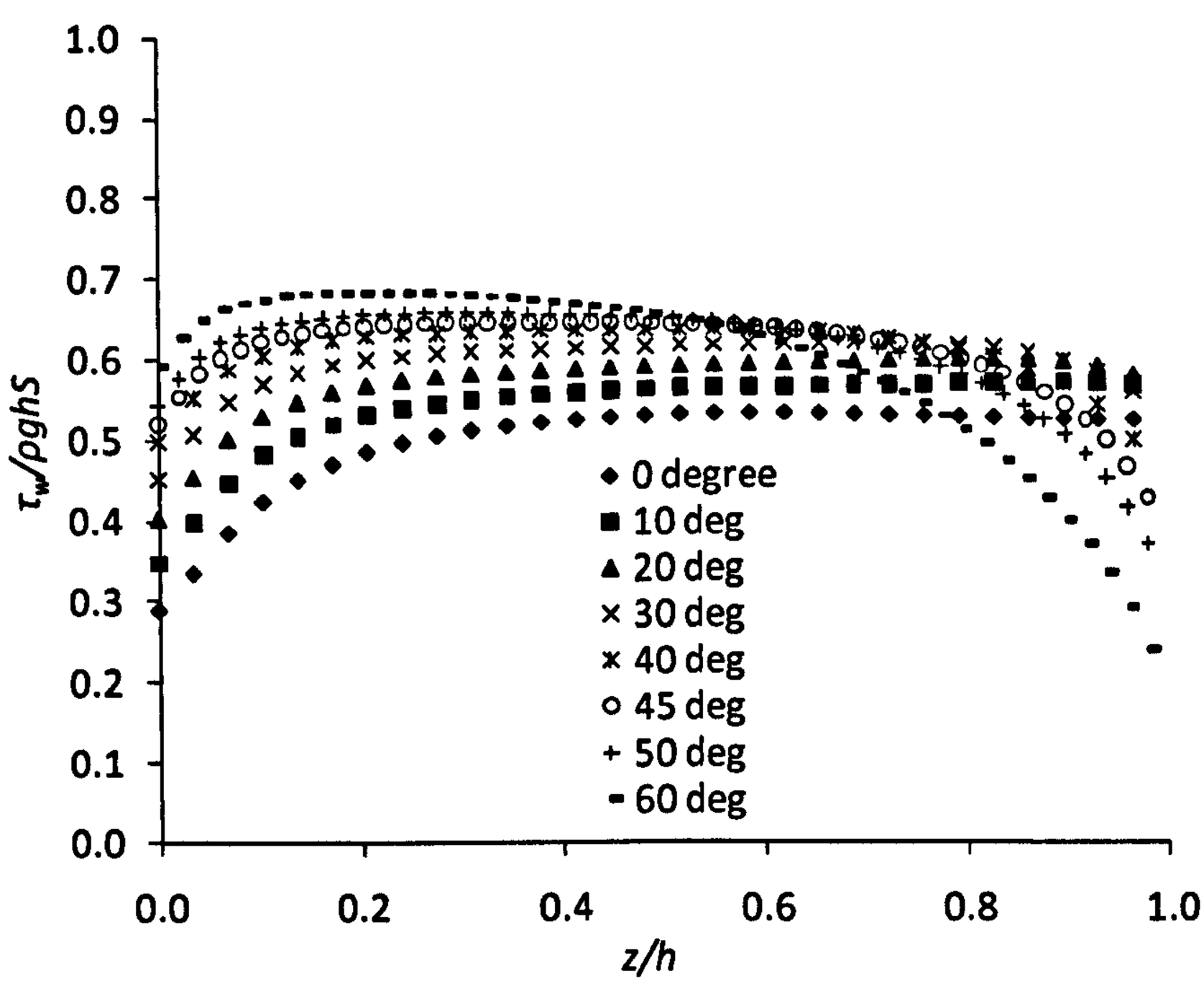

Figure 5.19 Variation of non-dimensionalised local shear stress on the sidewalls $\tau_w/\rho ghS$ with slant angle for CFD channels with aspect ratio of 2 and bed roughness of 0.0015 mm.

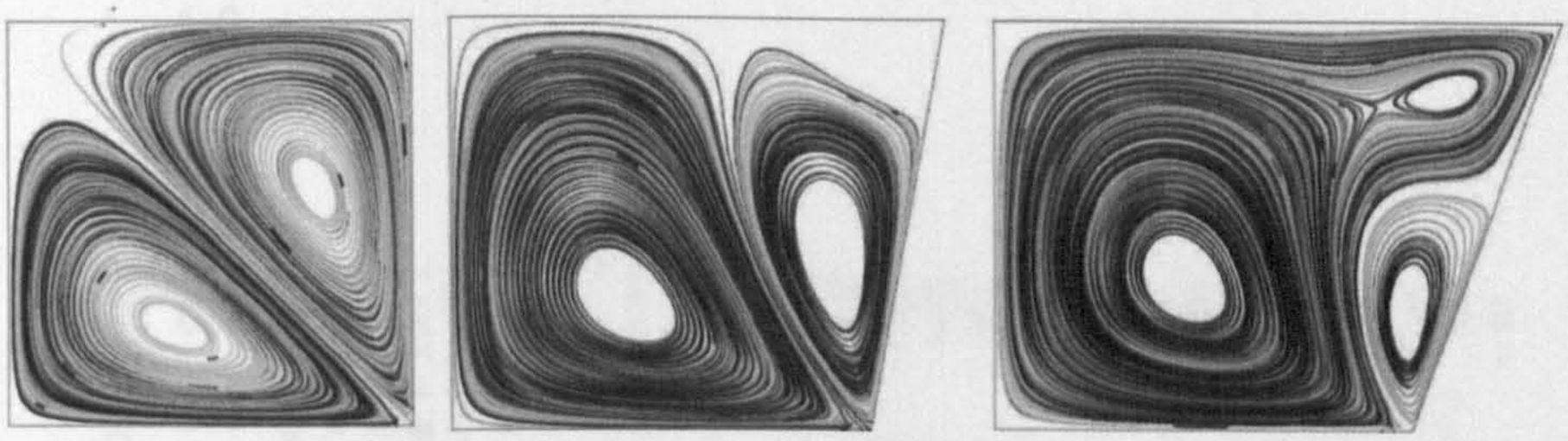

(a) (b) (c)

Figure 5.20: Secondary current streamlines for channels with aspect ratio of 2 and equal bed and side wall roughness for slant angles of (a) 0, (b) 10 and (c) 20°.

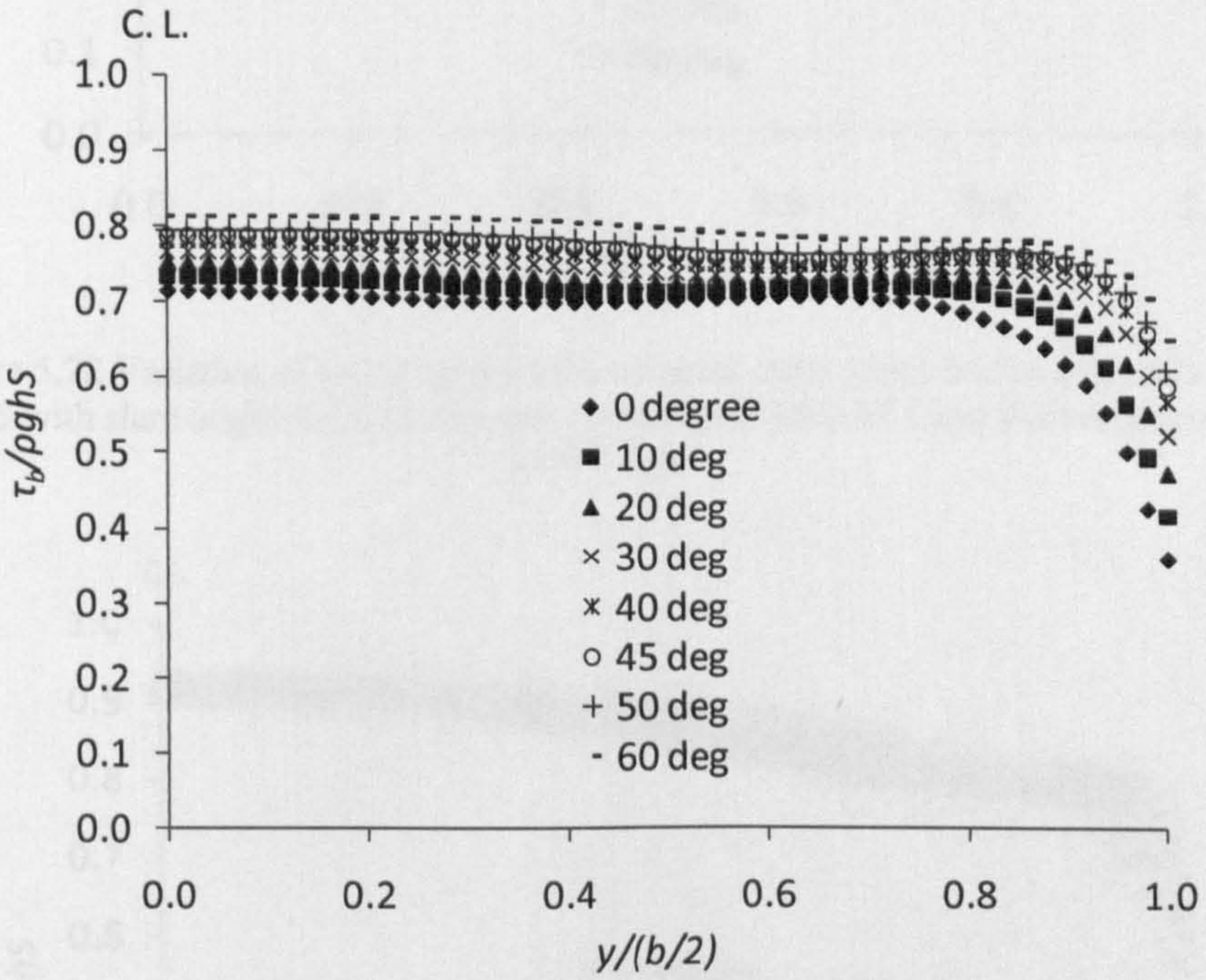

Figure 5.21 Variation of non-dimensionalised local shear stress on the bed $\tau_b/\rho ghS$ with slant angle for CFD channels with aspect ratio of 4 and bed roughness of 0.0015 mm.

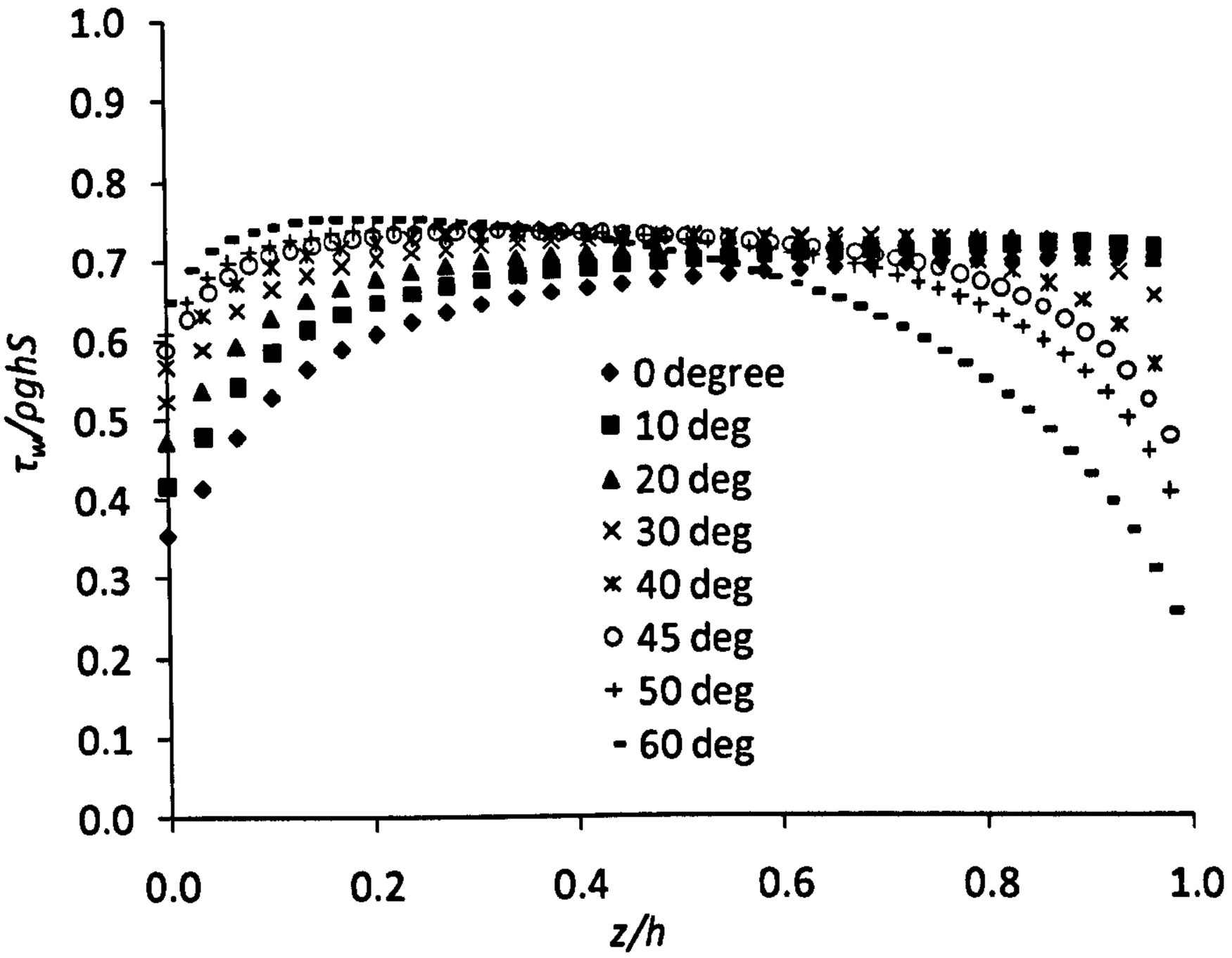

Figure 5.22 Variation of non-dimensionalised local shear stress on the sidewalls $\tau_w/\rho ghS$ with slant angle for CFD channels with aspect ratio of 4 and bed roughness of 0.0015 mm.

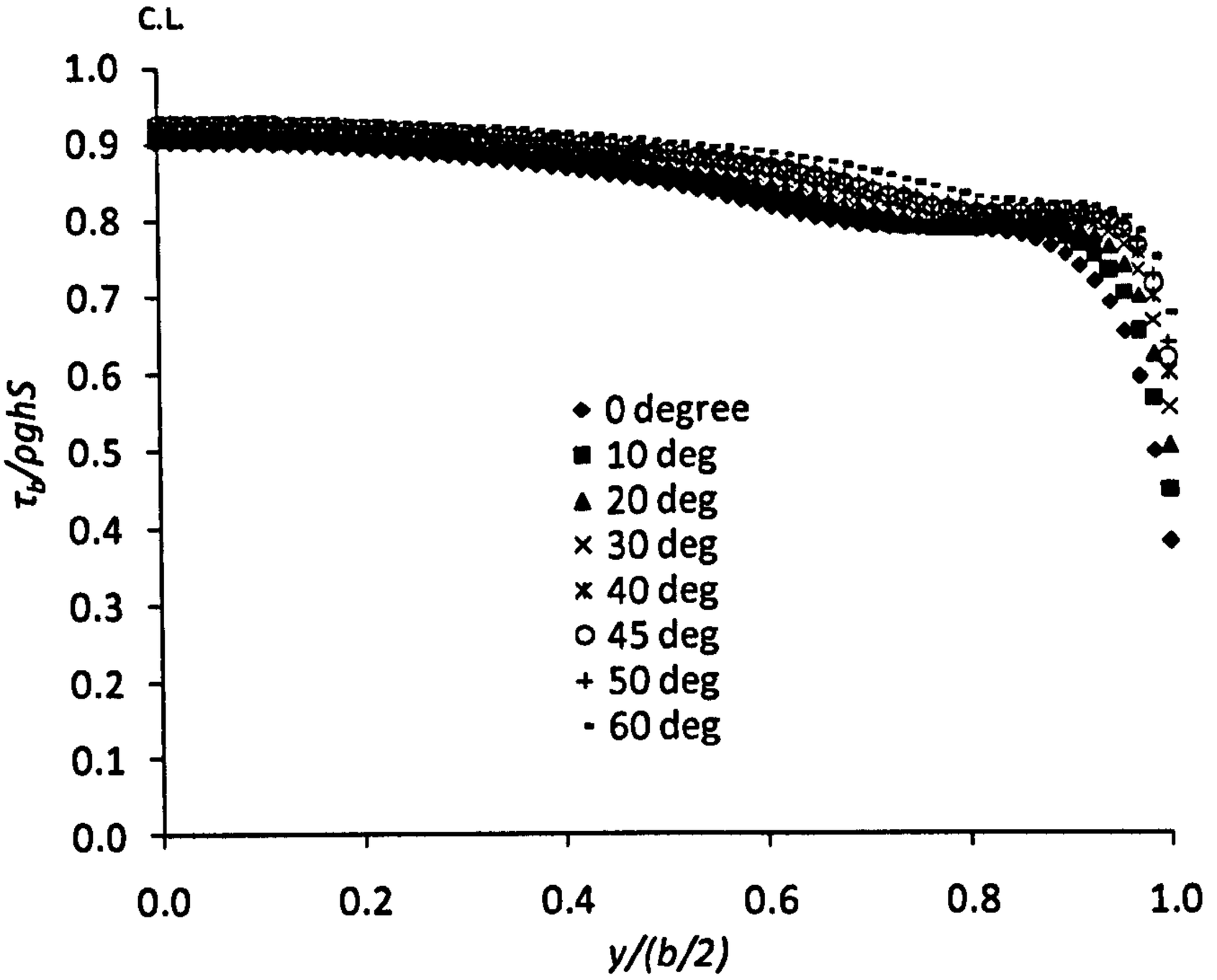

Figure 5.23 Variation of non-dimensionalised local shear stress on the bed $\tau_b/\rho ghS$ with slant angle for CFD channels with aspect ratio of 8 and bed roughness of 0.0015 mm.

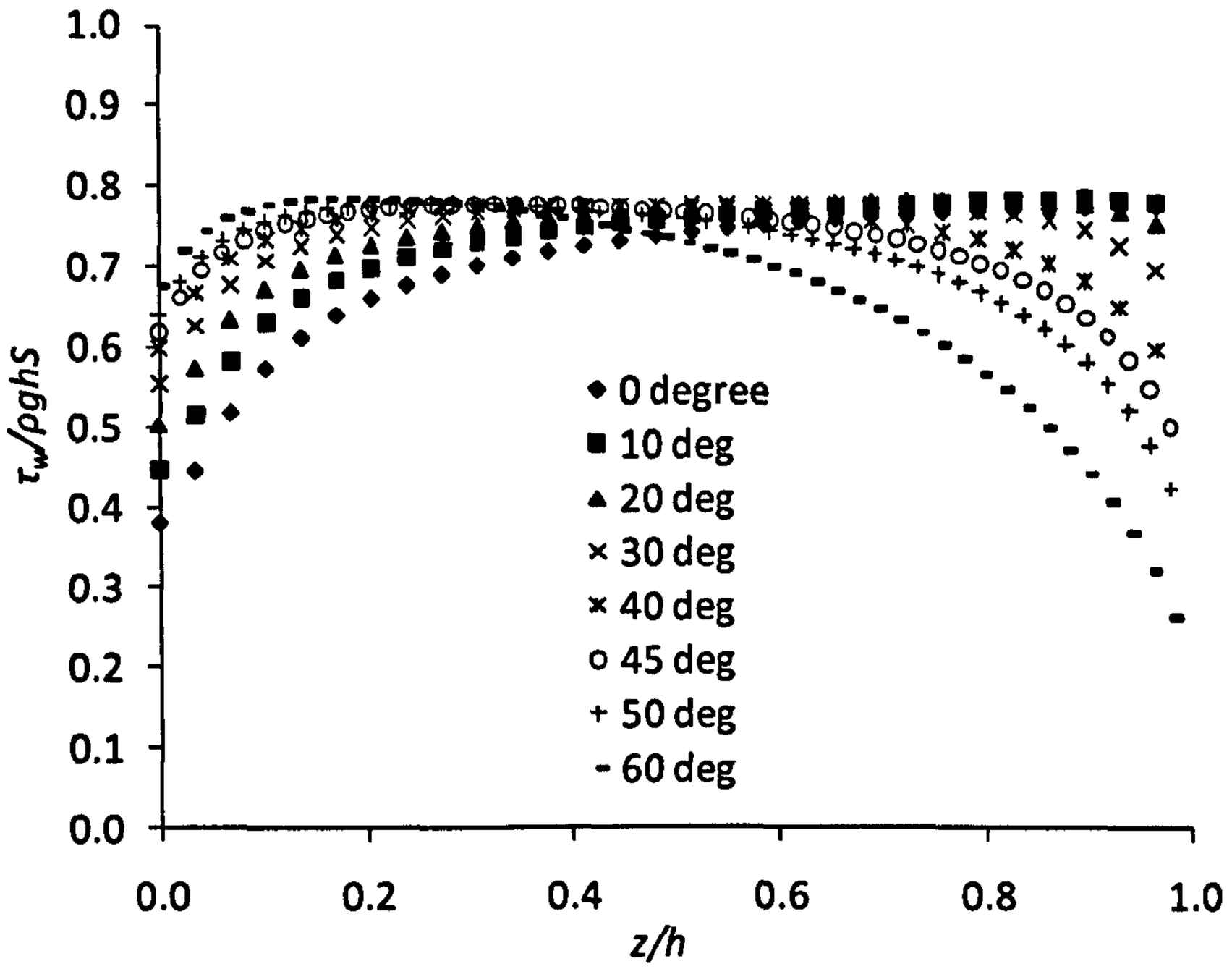

Figure 5.24 Variation of non-dimensionalised local shear stress on the sidewalls $\tau_w/\rho ghS$ with slant angle for CFD channels with aspect ratio of 8 and bed roughness of 0.0015 mm.

5.5.2 Analysis of shear stress based on the division line concept

5.5.2.1 Background

Following the Leighly's (1932) concept of partitioning the channel based on the isovel pattern, the division lines were created according to the method proposed by Cacqueray *et al.* (2009) for their rectangular channels. The construction of line is done in the CFD post-processor by first creating a point locator at (0, *b/2*, 0) at the junction of the bed and sidewall and then creating a vector variable $(\partial u/\partial x, \partial u/\partial y, \partial u/\partial z)$. This actually is a 3D gradient vector and follows the maximum change of stream-wise velocity component u in x, y and z directions. As there is no change of u in stream-wise direction because the flow is fully developed therefore this vector effectively becomes a 2D vector and cuts the isovels perpendicularly. A streamline is then released from the corner point locator following the vector field already created.

Guo and Julien (2005) proposed an extended set of equations for both bed and sidewall shear stresses. These equations have three components: gravitation (similar to Einstein's (1942) proposal); secondary currents; and internal fluid

shear stress at the interface of two fluid regions. The method of Guo and Julien relies on the use of a division line (the dashed line CH in Figure 5.1) along which the secondary current and internal shear stress values are computed. Defining the line along which they need to evaluate two complex integrals is the crux of their formulation. The authors eventually propose some basic equations for the delineating lines but still need to neglect or simplify the effects of secondary currents and the eddy viscosity term because they cannot solve for the second and third integral terms in their formulation. Therefore the benefit of their derivation is lost as they have to revert to the concept laid in the 1930s and 1940s; and it remains theoretical. But with the help of CFD it is possible to calculate the shear stress τ_{yx}, τ_{zx}, the components of the velocity, u, v and w along the division line and then calculate the integrals by exporting the data in Matlab (The Mathworks, 2006). The Matlab code used in the present study is given in Appendix A.

The average bed and sidewall shear stress equations for rectangular open channels as derived by Guo and Julien (2005) are,

$$\overline{\tau_b} = \frac{\rho g S A_b}{b} - \frac{2}{b}\int_{CH}\rho u(v dz - w dy) + \frac{2}{b}\int_{CH}(\tau_{yx} dz - \tau_{zx} dy) \qquad (5.5)$$

I II III

$$\overline{\tau_w} = \frac{\rho g S A_w}{2h} + \frac{1}{h}\int_{CH}\rho u(v dz - w dy) - \frac{1}{h}\int_{CH}(\tau_{yx} dz - \tau_{zx} dy) \qquad (5.6)$$

I II III

where A_b and A_w are the areas of the channel corresponding to the bed and side walls respectively.

Some modification for the average shear stress for sidewalls is done to account for the length of the sidewall which for trapezoidal sections is $h' = h/\cos\theta$ instead of h for rectangular sections, where h is the depth of water in the channel and θ is the sidewall inclination with respect to vertical axis. These equations have three terms on the right hand side, the first term (I) corresponds to the gravitational contribution, the second term (II) corresponds to the secondary current's effects and the third term (III) corresponds to the fluid shear stress at the interface of the

two areas related to bed and sidewalls. The integral is along the Division Line, CH, (or any other line that divides the channel) from Figure 5.1.

The procedure for the calculation of cross-sectional area corresponding to the bed A_b and consequently the cross-sectional area corresponding to the sidewalls A_w after the creation of the division line is adopted after Cacqueray *et al.* (2009) which they successfully implemented for their rectangular channels. It includes construction of the division line as a streamline departing from the intersection of the bed and side walls and which follows the normal gradient of the isovels and then exporting the co-ordinates of the curve in Matlab (The Mathworks, 2006). In Matlab the area under the curve i.e. the area corresponding to the bed, and the two integrals are calculated.

It is instructive to present a selection of division lines from the trapezoidal channels at this point, Figure 5.25. The effects of increasing the slant angle at a fixed aspect ratio of 2 and equal bed and wall roughnesses can be seen. The perfect bisector for the rectangular (slant angle 0°) becomes distorted as the channel opens up. The appearance of more complex secondary flow cell patterns goes some way to explaining this movement of the division lines, Figure 5.20. More results and illustrations of this have appeared in Morvan and Hargreaves (2009), together with a first analysis of the link between slant angle, cell and shear stress distributions on the side wall.

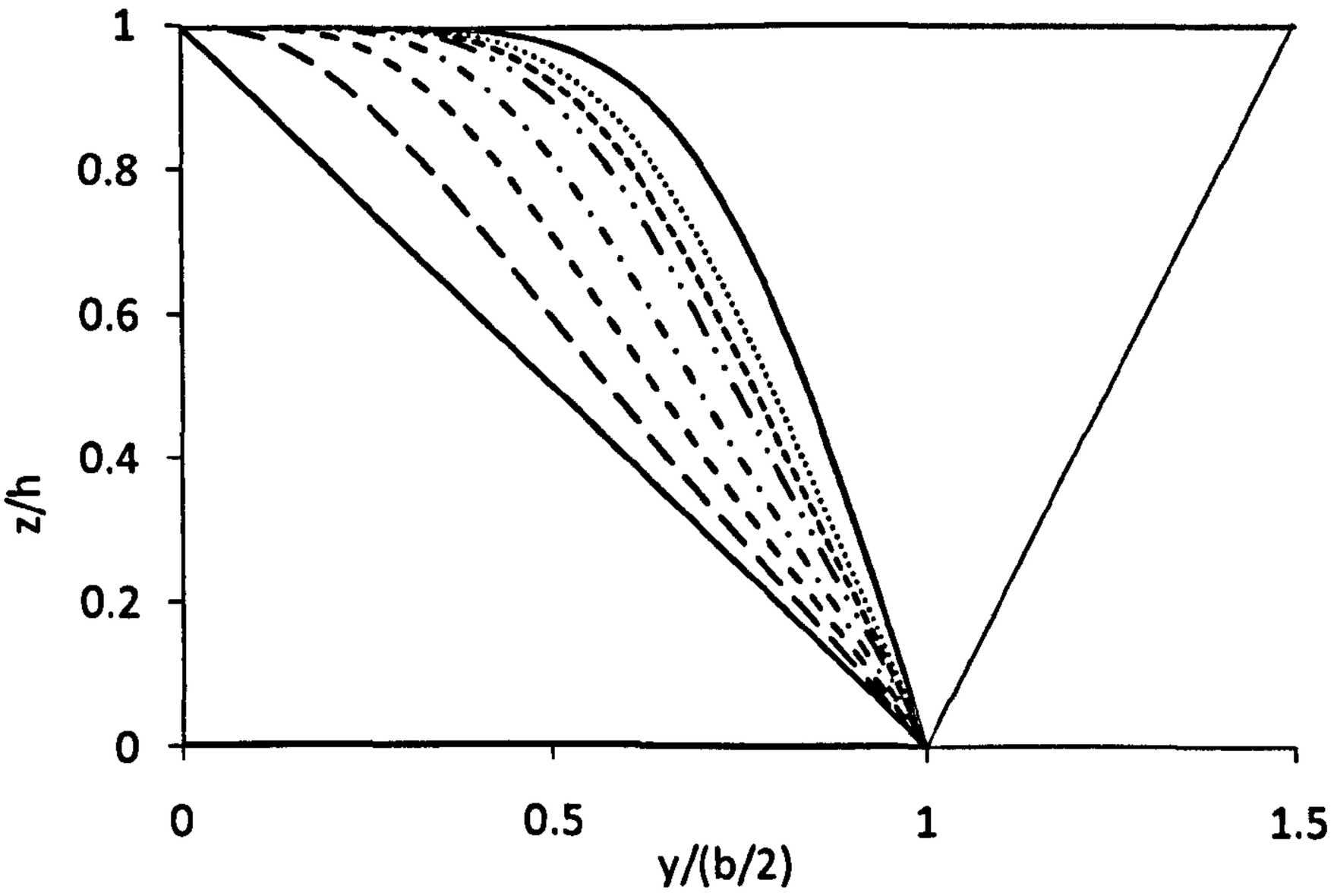

Figure 5.25: Division lines from the CFD simulations with equal bed and wall roughness and an aspect ratio of 2 and varying slant angles. The solid black line is for a slant angle of 0°, followed by angles of 10, 20, 30, 40, 45, 50 and 60° going in order from bottom left to top right.

After calculating the three parts of the equations an analysis is done for the contribution of secondary currents and the interfacial shear stress on the over all mean shear stress on the bed and sidewalls. The Guo and Julien (2005) equations for average bed and sidewalls shear stress may be modified as,

$$\overline{\tau_b} = I + II + III$$

$$\text{or } \overline{\tau_b} = \left(\frac{I+II+III}{I}\right) I$$

$$\text{or } \overline{\tau_b} = \alpha_b . \frac{\rho g S A_b}{b} \tag{5.7}$$

$$\text{and } \overline{\tau_w} = \alpha_w . \frac{\rho g S A_w}{2h'} \tag{5.8}$$

where, alpha, α, is the ratio of the all three terms of the equation to the first term, or in other words the effect of the secondary currents and fluid internal shear stress due to eddy viscosity on the mean shear stress, and is calculated for all the cases. Or it is rather, a way of quantifying the effect of the secondary currents and fluid internal shear stresses on the mean shear stress – a value closer to unity means that terms II and III are negligible.

5.5.2.2 Analysis of α_b

Figure 5.26 shows the variation of α_b with slant angle and aspect ratio for those cases where the bed roughness is 0.1 mm. It can be seen in all cases that α_b tends to unity as the aspect ratio increases. This indicates that the effects of secondary currents and internal shear are limited to the area of the channel close to the side wall and become proportionally less important as the channel width is increased.

It is also seen from Figure 5.26 that α_b decreases as the slant angle increases, but only up to about 45° for the lower aspect ratio cases, after which the trend reverses. For the larger aspect ratio cases, α_b tends towards a constant value as the slant angle increases beyond 45°. This tends to support the view that the

secondary current effects are limited to the near side wall region and do not extend further into the channel as the aspect ratio increases. Even so, for all the cases presented, α_b never comes to unity, suggesting that the secondary currents are present at all times.

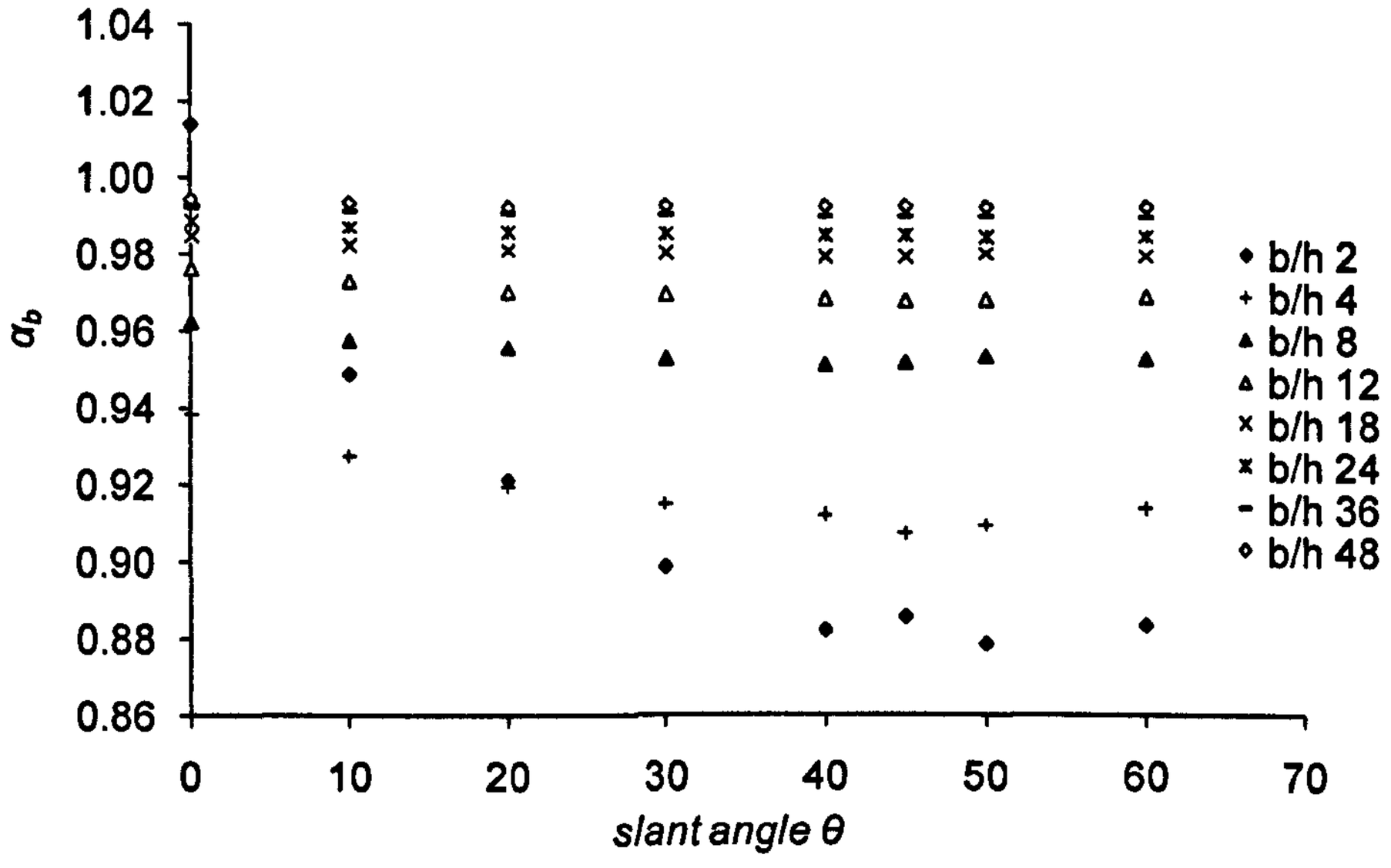

Figure 5.26: Variation of α_b with slant angle and aspect ratio for the CFD simulations with a bed roughness of 0.1 mm.

Figure 5.27 demonstrates how, for a fixed aspect ratio of 4, α_b varies as the bed roughness is varied. The role played by the secondary currents and internal shear terms (II and III) is diminished as the bed roughness increases, suggesting that the increased wall shear in these cases tend to dominate. While the secondary current and internal shear terms might be said to become more important as slant angle increases, there is a very definite decrease in their importance as the slant angle passes through 40° to 50°.

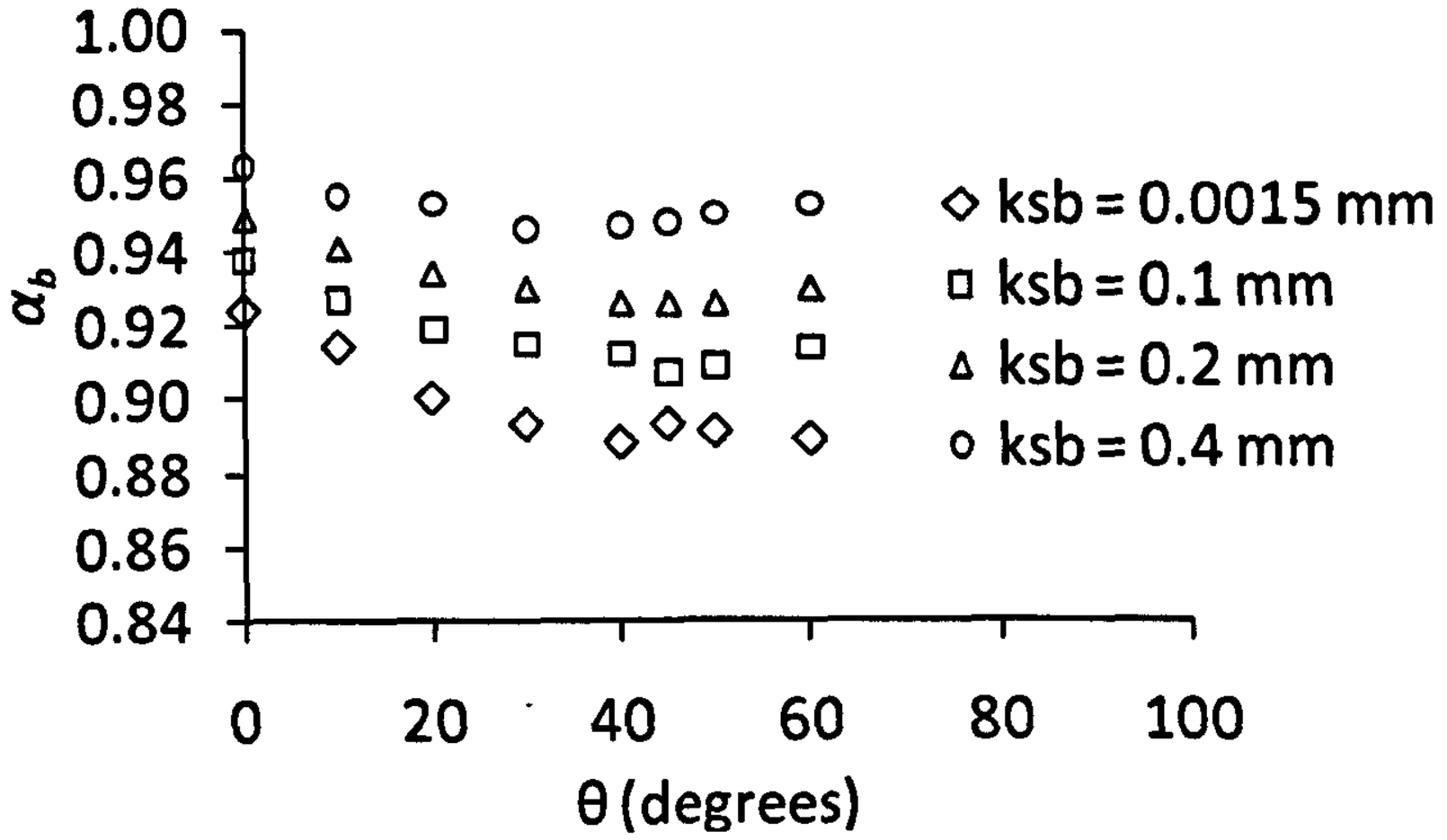

Figure 5.27 Variation of α_b with slant angle and bed roughness for the CFD simulations with an aspect ratio b/h of 4.

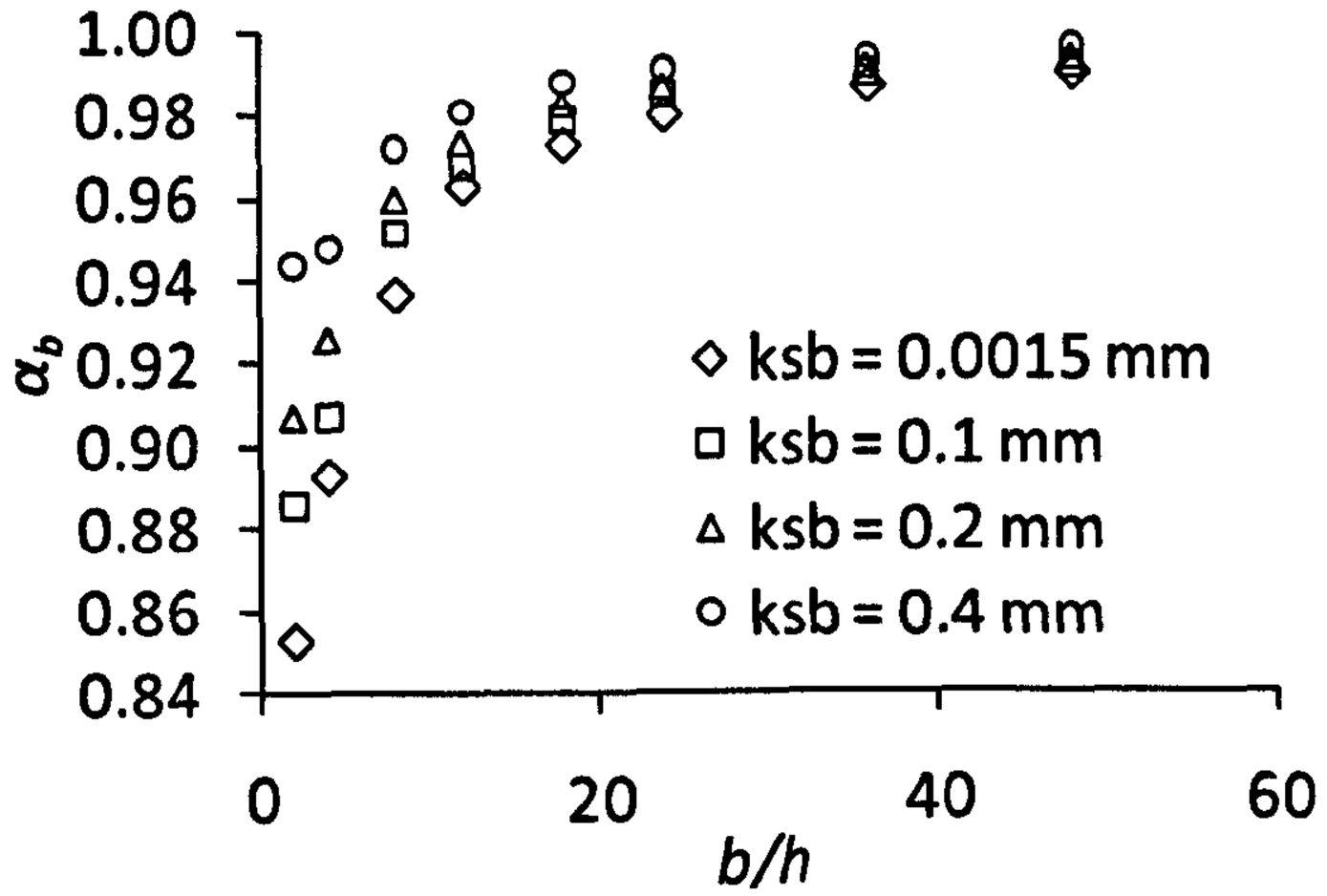

Figure 5.28 Variation of α_b with aspect ratio b/h and bed roughness for the CFD simulations with a slant angle of 45°.

It can be seen from Figure 5.28 that for a fixed slant angle of 45°, the spread in values of α_b from the smoothest to roughest beds decreases as the aspect ratio increases. It becomes increasingly clear, therefore, that for large aspect ratio channels or channels with a rough bed and smooth walls that the first term in Equation (5.5) will provide a good approximation to the shear stress acting on the bed.

5.5.2.3 Analysis of α_w

The first thing that becomes clear from Figure 5.29, which shows the variation of α_w with slant angle and aspect ratio, is that the aspect ratio has a fairly negligible effect on the value of α_w. This is because α_w is a measure of the effects of secondary currents and internal shear – an effect that, as has been seen already, limited to the vicinity of the side walls. Therefore, the integrals of Equation (5.6) and the near side wall flows they represent are relatively unaffected by any increases in channel width.

The other fact to note from Figure 5.29 is that the values of α_w are always greater than unity. This differs from α_b mainly because of the sign of the third terms in Equations (5.5) and (5.6) and the way in which these terms dominate over the second terms. Also, it can be seen that α_w peaks around the 20° slant angle, which can be explained by the appearance of a new secondary current vortex in the angle made by the bed and side wall.

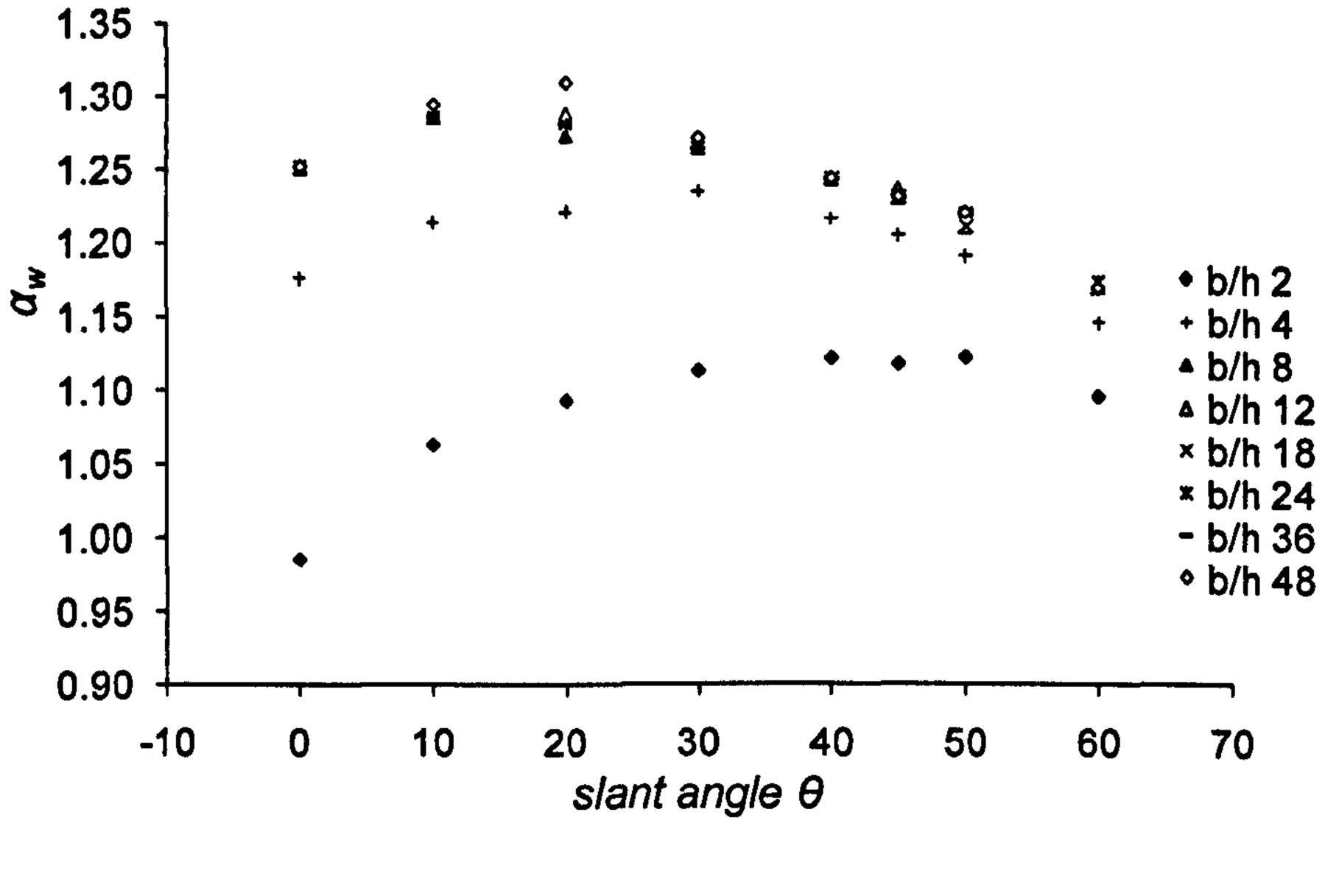

Figure 5.29: Variation of α_w with slant angle and aspect ratio for the CFD simulations with a bed roughness of 0.1 mm.

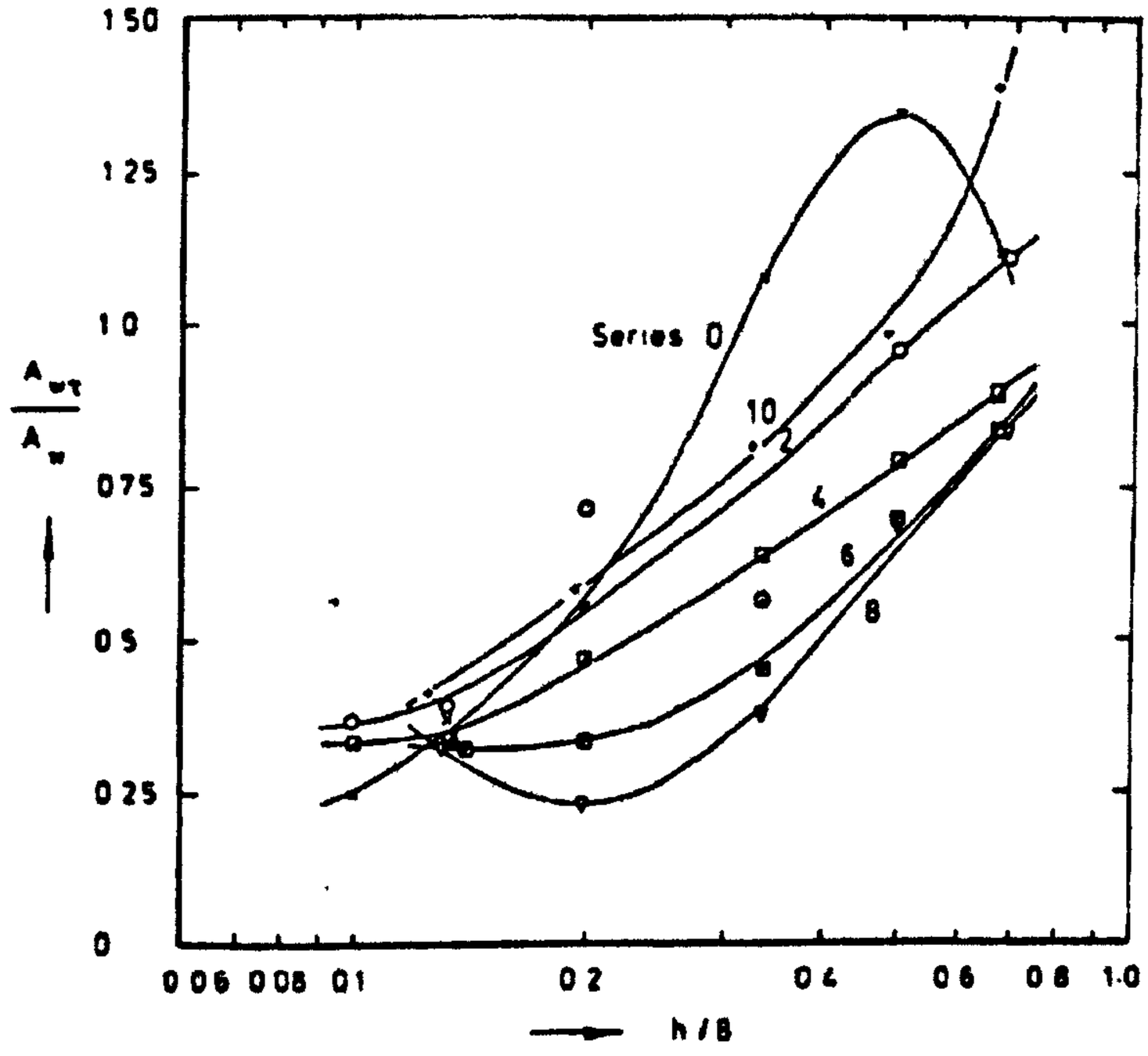

Figure 5.30 Ratio of wall areas against *h/b* after Knight and Macdonald (1979).

Figure 5.29 can also be compared with Figure 5.30 shown by Knight and Macdonald (1979) as for higher bed roghnesses they are almost the same. This study may be extended to include some cases with much higher bed roughnesses so as to compare the results with the work done by Knight and Macdonald (1979).

To assess the effect changing bed roughness has on the value of α_w, Figure 5.31 and Figure 5.32 show how α_w changes with slant angle for a fixed aspect ratio of 12 and then with aspect ratio with a fixed slant angle of 45° respectively. For a fixed aspect ratio, the value of α_w decreases with increasing slant angle, which may be due to the first term in Equation (5.6) dominating more as the length of the side wall increases as well as the complex changes in the secondary current flow patterns as the slant angle increase. When the slant angle is fixed, again the values of α_w for the rougher beds are lower indicating that there is a decreased effect of the secondary currents and internal shear. Quite why this is the case is not clear at present. Aspect ratio increases again are less important when considering α_w because it is dominated by the near sidewall region. This is consistent with the fact that the local corner effect is less relevant to the overall

channel dynamics and shear stress distribution, and implies that for practical river engineering Einstein's (1942) idea provides a very good approximation.

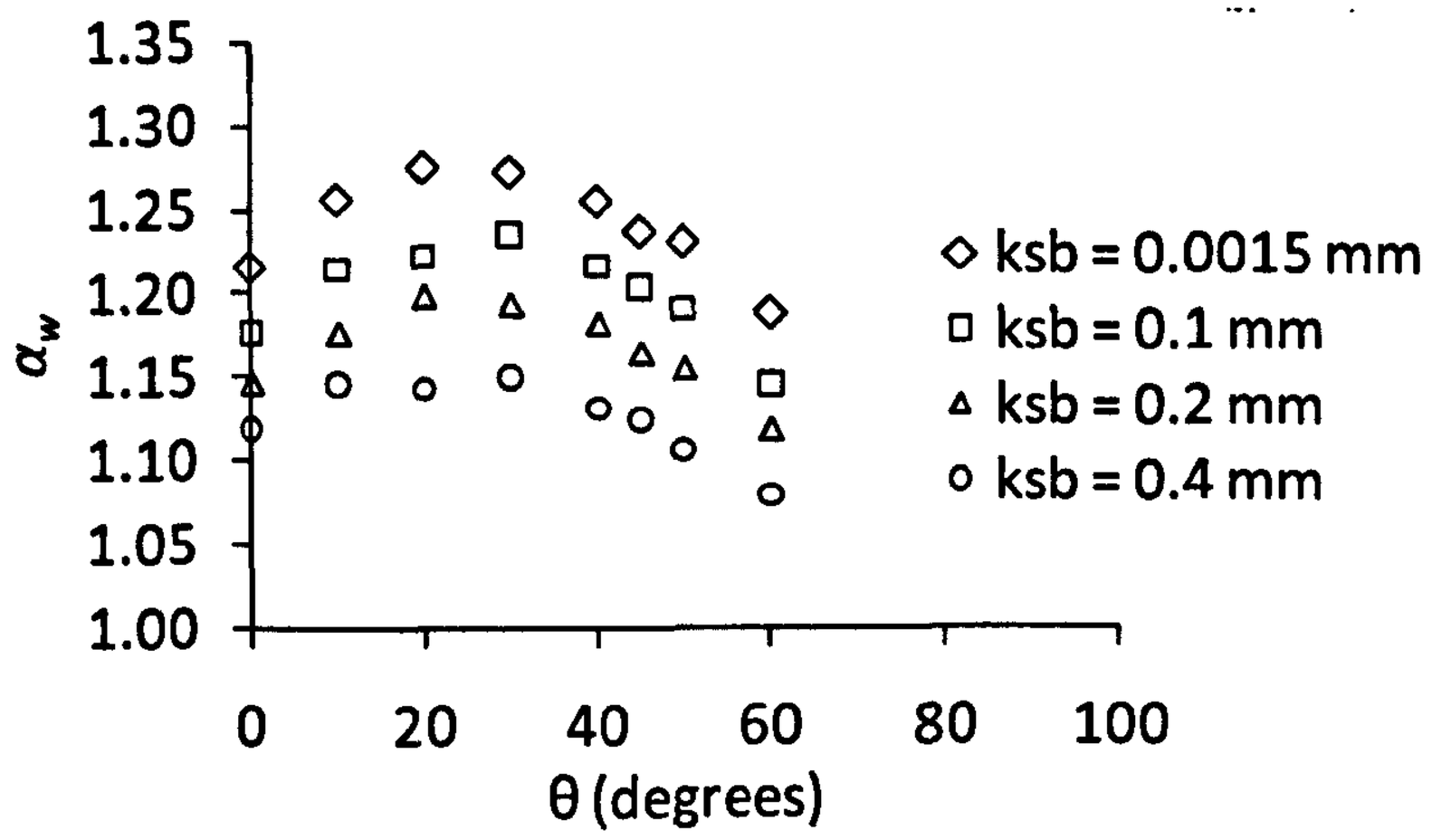

Figure 5.31 Variation of α_w with slant angle and bed roughness for the CFD simulations with an aspect ratio b/h of 4.

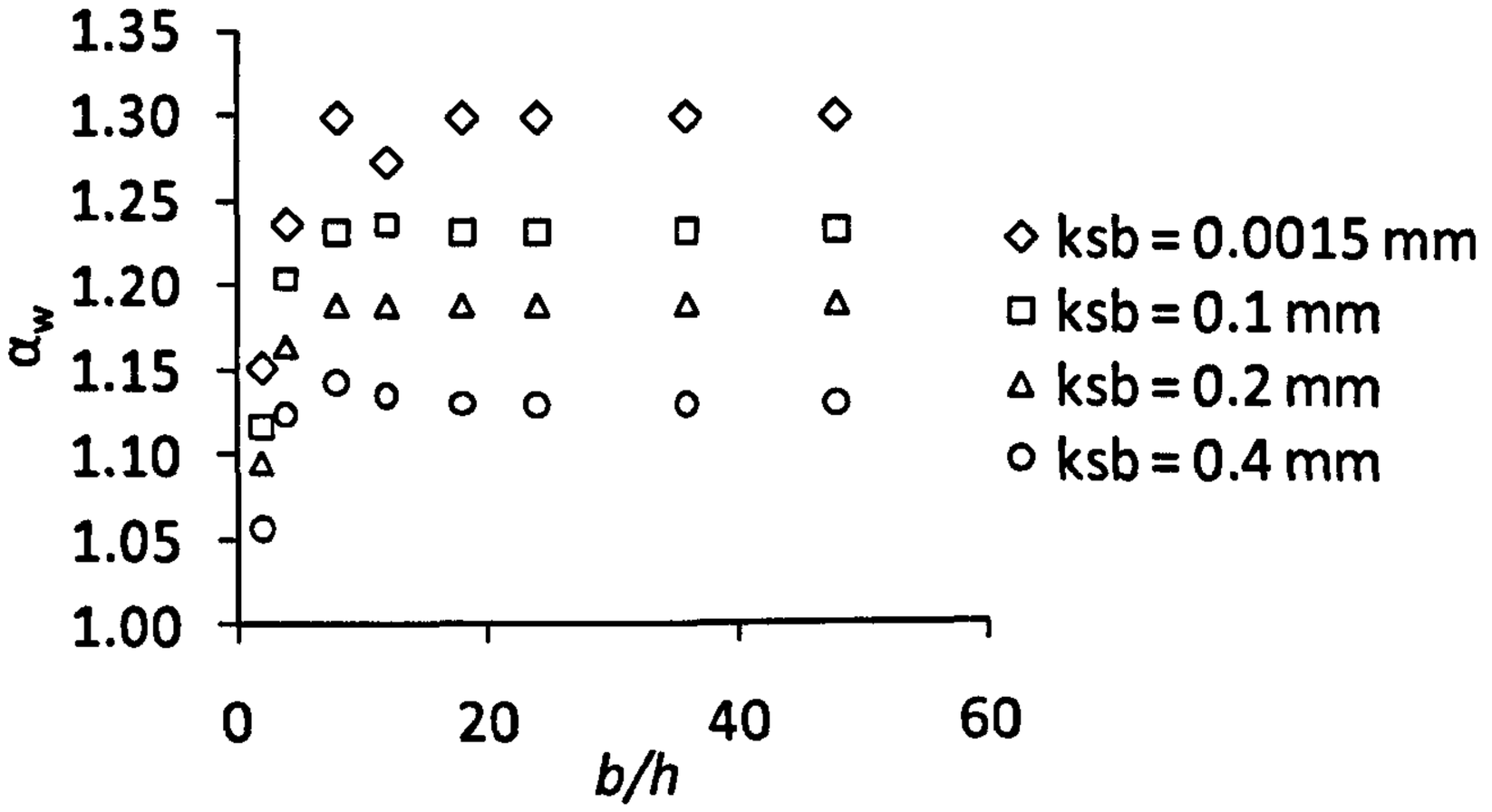

Figure 5.32 Variation of α_w with aspect ratio b/h and bed roughness for the CFD simulations with a slant angle of 45°.

5.6 Conclusions

The validation of model with the experimental results of Tominaga *et al.* (1989) and other published results shows good agreement. The construction of the division line in the trapezoidal channels has been successful.

In the second part, the results of the analysis of Guo and Julien (2005) equations on this division line show that the contribution of secondary currents and fluid

internal shear stress is not negligible in the calculation of shear stresses on the bed and sidewalls separately. The variation of the slant angle and aspect ratio bring significant changes to the distribution of the shear stress at the boundaries, consistent with changes in the flow structures as previously shown by Morvan and Hargreaves (2009), in particular for low aspect ratio channels. The introduction of new variables, which quantify the relative contributions from the gravitational term in the formulation of Guo and Julien (2005) to those from the secondary currents and internal shear stresses, is shown to be highly useful in gaining insights into the different flow regimes in the channel.

CHAPTER 6

OPEN CHANNELS WITH LONGITUDINAL BED FORMS

6.1 Introduction

In this chapter, an in depth analysis is carried out on the distribution of secondary currents and shear stresses in straight prismatic open channels with artificial bed forms. The presence of the lines of boil, consisting of low speed streaks, periodically in the transverse direction, is reported in literature due to the initiation of the sand ridges. Simulations are run on channel sections having variation in number of ridges on the bed as well as size of the ridges. The effect of these variations on the flow structures and shear stress distribution in wide open channels is reported. The results offer an interesting insight into the three-dimensional flow structures involved and the link between flow structures and bed morpho-dynamics in prismatic channels.

6.2 Background

The study of the cellular secondary currents in open channel hydraulics is very important as they are responsible for the three dimensional nature of flow patterns, and determine wall shear stress distributions, sediment transport and bed forms (Nezu and Rodi, 1985). Open channel flows are mostly complex and the along channel flow, is greatly affected by the secondary flow in the cross stream and vertical directions. Prandtl (1952) classified secondary flows into two categories. Secondary flow of first kind, which is usually seen in curved or meandering channels in which the flow may circulate in the cross-sectional plane either driven by centrifugal or transverse pressure gradients. Secondary flow of the second kind is related to the non-homogeneity and anisotropy of the turbulence and may be caused due to number of reasons such as asymmetry of the channel boundaries, free surface effects or variation in bed conditions (Wang and Cheng, 2006).

After studying the wall shear and secondary current variation in trapezoidal channels as discussed in the last chapter (Chapter 5), it was found that no secondary currents were generated in the central portion of the wide channels ($b/h > 5$) with rigid beds as shown in Figure 6.1. It was thus decided to investigate this issue further. This chapter is therefore focused on the 3-dimensional steady flow structures created in the central portion of wide channels after the formation of ridges on the bed. These areas are known to have purely 2-dimensional flow in the absence of these longitudinal bed forms. A fixed bed has been used in the simulations and the ridges have been artificially added sequentially on the bed, from the outside to the inside, to simulate the formation of longitudinal ridges and troughs along the bed.

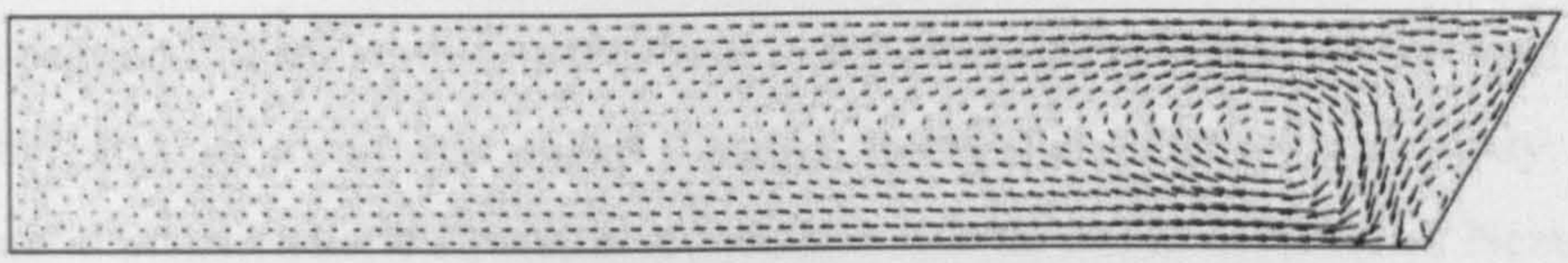

Figure 6.1 Secondary current vectors for channel section of aspect ratio 12 and slant angle of 30 degrees.

6.3 Geometry used

The channels sections are 900 mm wide at the bed and have a fixed depth of water of 80 mm. With reference to Figure 6.2, the channels have three different cross sections of ridges fixed on their bed and have been named accordingly e.g. Case 75-10-6 means the width of the ridge, b_1, is 75 mm, the height of the ridge, h_1, is 10 mm and the number of ridges on bed are 6. The centre-to-centre distance between two adjacent ridges, λ, is fixed as 150 mm which is nearly equal to twice the depth of water in the channel. The first ridges near the sidewalls are fixed at a distance of $\lambda/2$. The cross section has been divided into sections and numbered from left wall, odd numbers being the troughs and even numbers being the ridges, as shown in Figure 6.2.

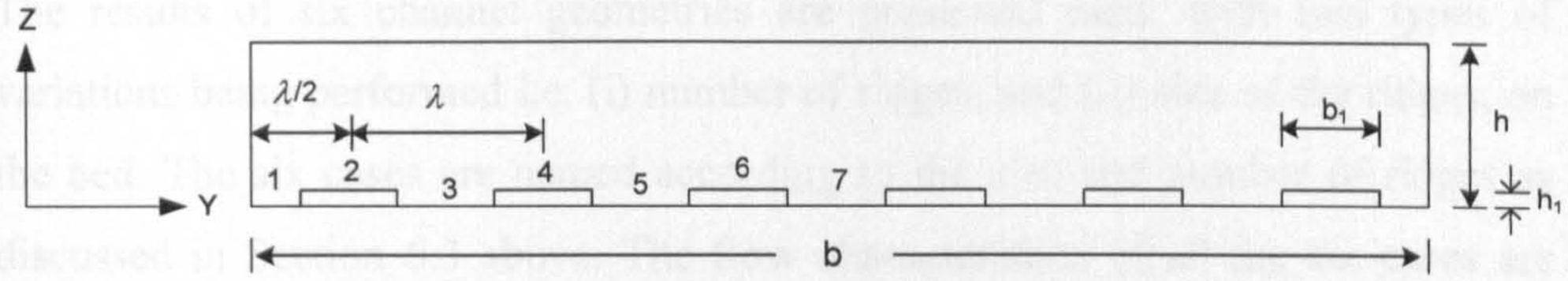

Figure 6.2 Typical cross section of open channel with longitudinal bed forms.

6.4 Results

6.4.1 Validation of the model used

Before the start of the actual study one simulation was run on the channel section used by Nezu and Nakagawa (1984) during their experimental work. The purpose of this simulation was to verify the prediction of re-circulations obtained in the cross-section of the channel section due to the presence of ridges on the beds. The channel section used was called Case-J during the experimental study. The channel dimensions and hydraulic conditions can be found in detail in Nezu and Nakagawa (1984).

Figure 6.3(a) shows the flow pattern of cellular secondary currents of Case-J as measured by Nezu and Nakagawa (1984) during their experimental study and Figure 6.3(b) show the flow pattern of cellular secondary currents as predicted by CFD simulation. The results are very encouraging as CFD simulations are able to predict accurately the flow pattern of the secondary currents. The validation of the numerical model is also done extensively in the previous chapter as well.

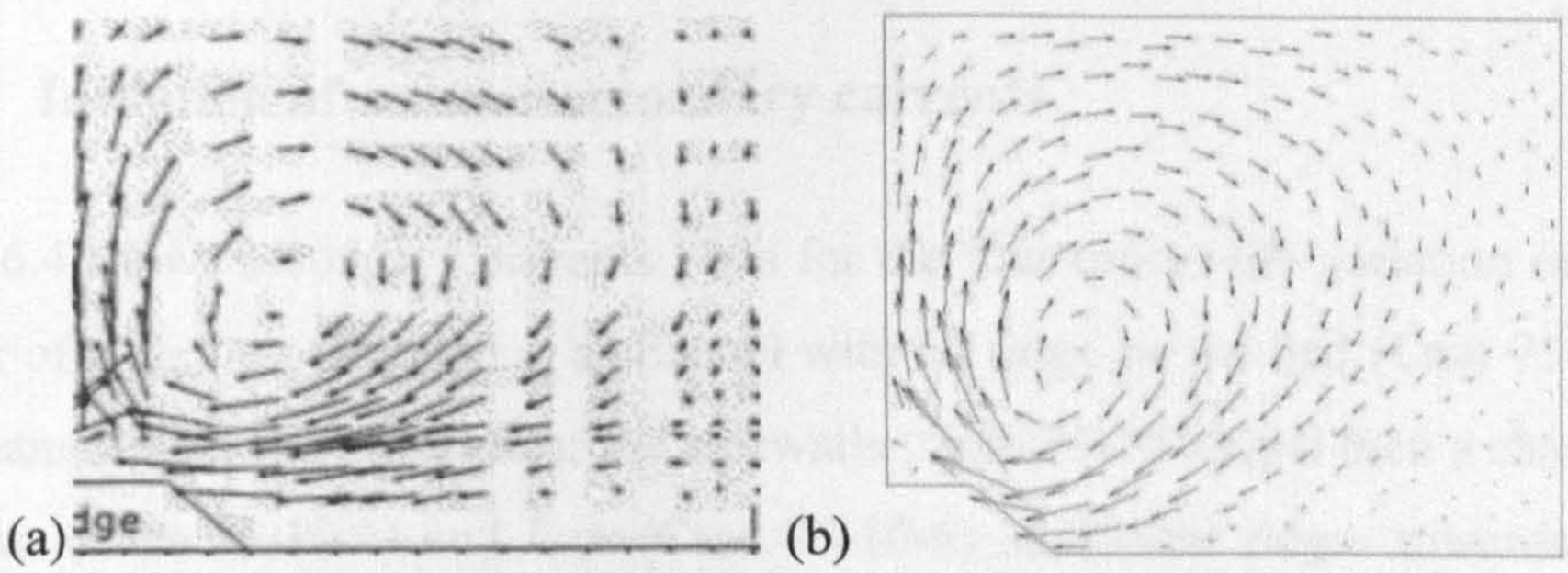

Figure 6.3 Flow pattern and secondary currents (Case-J) Nezu and Nakagawa (1984) (a) experimental and (b) CFD.

The results of six channel geometries are presented next, with two types of variations being performed i.e. (i) number of ridges, and (ii) size of the ridges, on the bed. The six cases are named according to the size and number of ridges as discussed in Section 6.3 above. The flow characteristics of all the six cases are given in Table 6.1. The results based on CFD simulations are discussed below.

Table 6.1 Flow characteristics of channels.

Case number	Discharge Q ($m^3.s^{-1}$)	Mean Velocity U_m ($m.s^{-1}$)	Maximum Velocity U_{max} ($m.s^{-1}$)	Reynolds number R_e	Froude number F_r
75-10-0	0.0322	0.446	0.524	135684	0.50
75-10-2	0.0309	0.437	0.522	125440	0.49
75-10-4	0.0293	0.423	0.514	114809	0.48
75-10-6	0.0277	0.408	0.485	104712	0.46
75-05-6	0.0300	0.428	0.506	119484	0.48
50-10-6	0.0287	0.414	0.492	108517	0.47

6.4.2 Initiation of ridges on the bed

The secondary currents and wall shear are plotted to assess whether the presence of secondary currents is a possible mechanism for the initiation of ridges on the bed. Ikeda (1981) has shown the formation of longitudinal sand ridges over the entire width of the movable bed.

6.4.2.1 Initiation of cellular secondary currents

Figure 6.4 shows secondary currents plots for the four cases with variation in the number of ridges on the bed i.e. a channel with no ridge on the bed (Case 75-10-0), a channel with two ridges near the sidewalls (Case 75-10-2) and then a channel with two (Case 75-10-4) and four (Case 75-10-6) additional ridges towards the middle portion. The channel without any ridge on the bed shows a strong cellular flow only near the wall as a result of the local unbalance in the Reynolds stresses. Away from the wall towards the central portion, the currents reduce in strength and, in fact, virtually vanish, as shown in Figure 6.4(a). This strong circulation

near the sidewalls on the other hand could well be responsible for the initiation of the sand ridges on the bed, as hypothesized by others, e.g. Nezu and Nakagawa (1984).

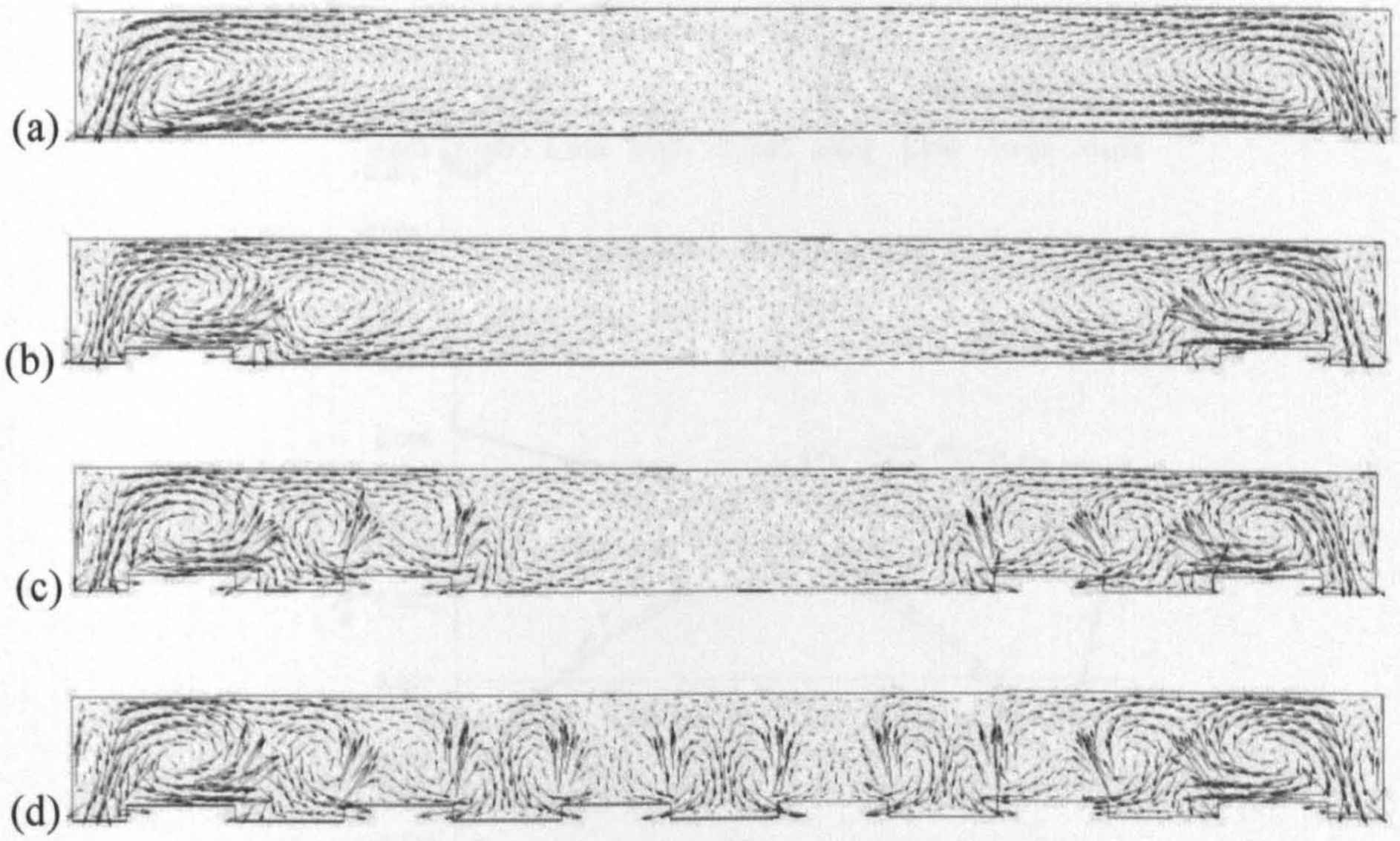

Figure 6.4 Variation of secondary currents with development of ridges, (a) No ridges (b) two corner ridges (c) two corner and two additional ridges and (d) two corner and four additional ridges.

In Figure 6.4(b) an additional vortex appears as soon as the two ridges near the sidewalls are added. The secondary currents in the area just after the ridges become stronger due to the presence of the ridges, which, again and in turn, could be arguably responsible for the creation of additional ridges towards the central portion of the channel leading to Figure 6.4(c) and (d).

Figure 6.5 shows the velocity component, v, in the transverse (y-axis) direction, near the bed at four different sections for four Cases 75-10-0, 75-10-2, 75-10-4 and 75-10-6. The graph shows that velocity v is continuously increasing in Region 1 (location defined in Figure 6.2), when there is no ridge, and may be responsible for the creation of the corner ridge. Just after the formation of the first corner ridge the transverse velocity is seen to stabilise and little variation is observed.

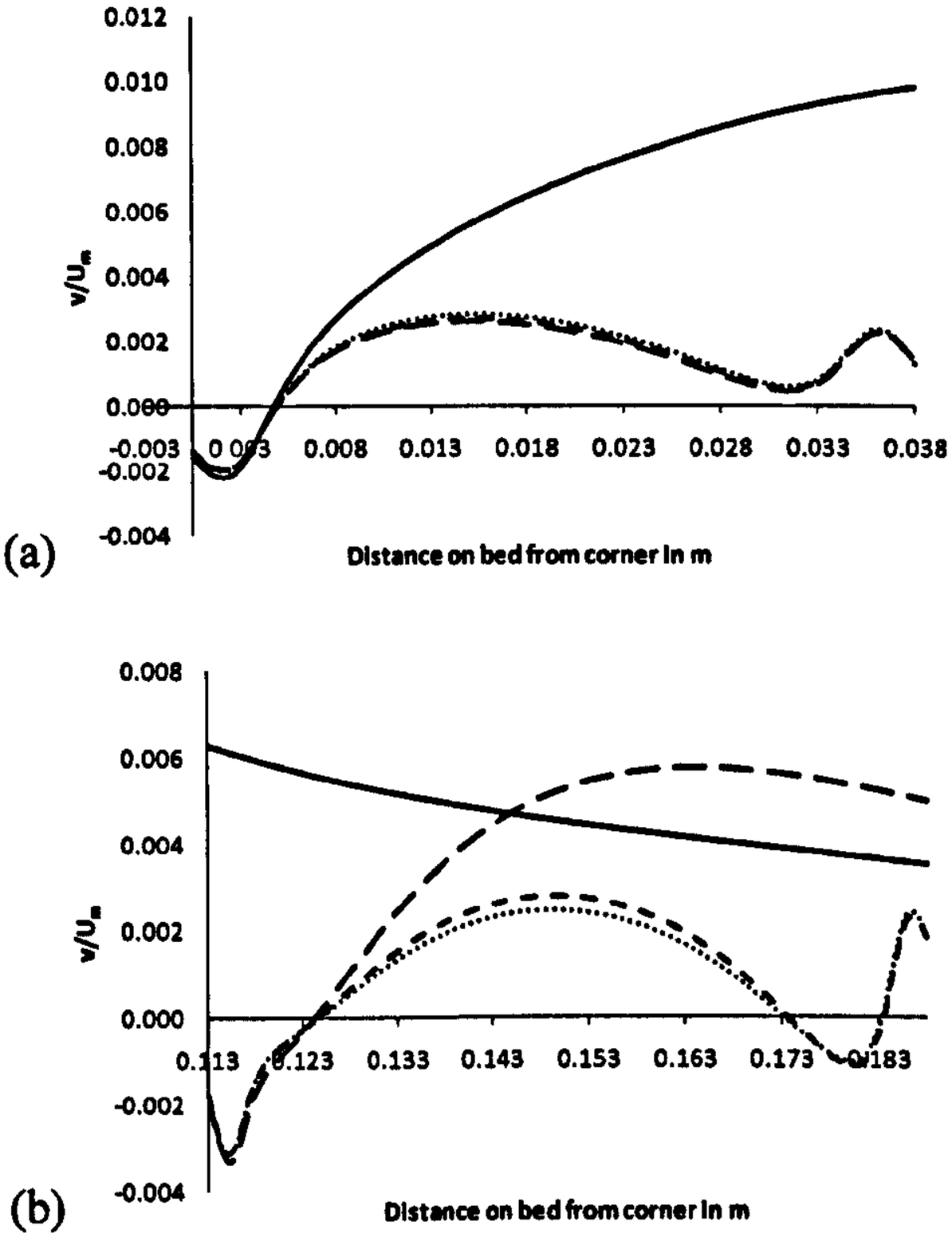

Figure 6.5 Variation of cross stream velocity, v, with ridge development at sections (a) 1 (b) 3 (c) 5 and (d) 7.

At Location 3, which immediately follows the corner ridge, the cross stream velocity is seen to be continuously decreasing when there are no ridges. The appearance of the first corner ridge leads to a second large peak in velocity. This increase in velocity could in turn be responsible for the creation of an additional ridge towards the centre of the channel. Similar results are seen at Locations 5 and 7 where the cross stream velocity is seen to increase as a result of the creation of new ridges.

6.4.2.2 Variation of wall shear on the bed

The non-dimensionalized wall shear, $\tau_{bx}/\rho ghS$ on the bed in the stream wise and cross stream directions is plotted for the Case 75-10-0 (i.e. the channel without the bed forms) and is shown in Figure 6.6 and Figure 6.7. The wall shear in the stream wise direction is seen to peak initially in the wall zone and then attains its maximum in the central portion of the channel. The peak in the wall zone could explain local scouring of the bed and ultimately the development of the first trough near the walls; the peak in the wall shear in the cross stream direction which is found to be around the same area could also be responsible for the shift of the scoured bed material towards one side and ultimately responsible for the creation of the first ridge near the walls, as was suggested by Nezu *et al.* (1985).

Figure 6.6 Wall shear in flow direction on the bed across the width of the channel.

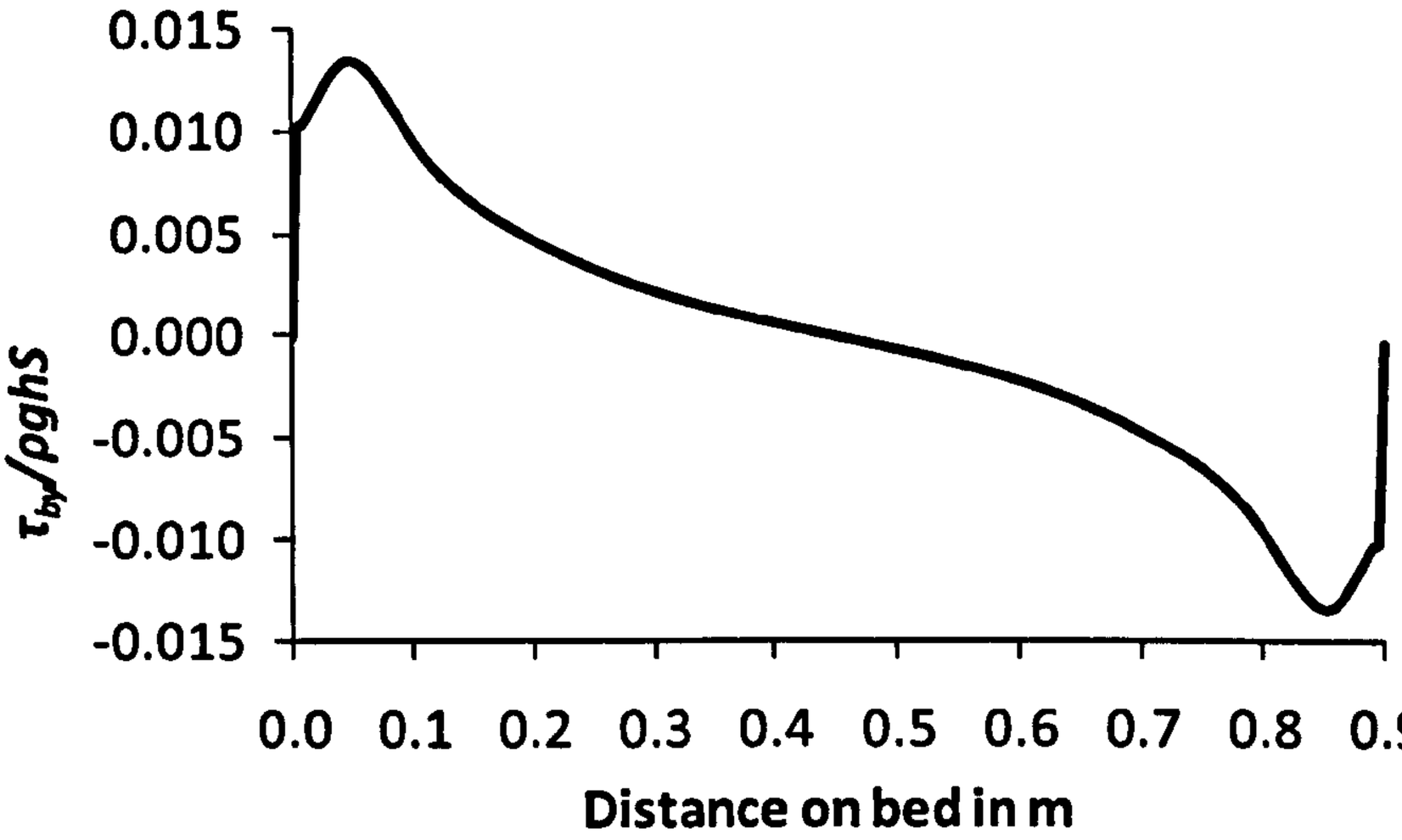

Figure 6.7 Wall shear in cross stream direction on the bed across the width of the channel.

Figure 6.8 shows non-dimensionalised wall shear on the bed in the mainstream direction, with variation in the number of ridges, at four different Locations for Cases 75-10-0, 75-10-2, 75-10-4 and 75-10-6. The graph shows that wall shear at each location, i.e. Locations 1, 3, 5 and 7 (as defined in Figure 6.2), is seen to be falling with the development of a ridge adjacent to the region it and remains at a similar lower value as other ridges appear.

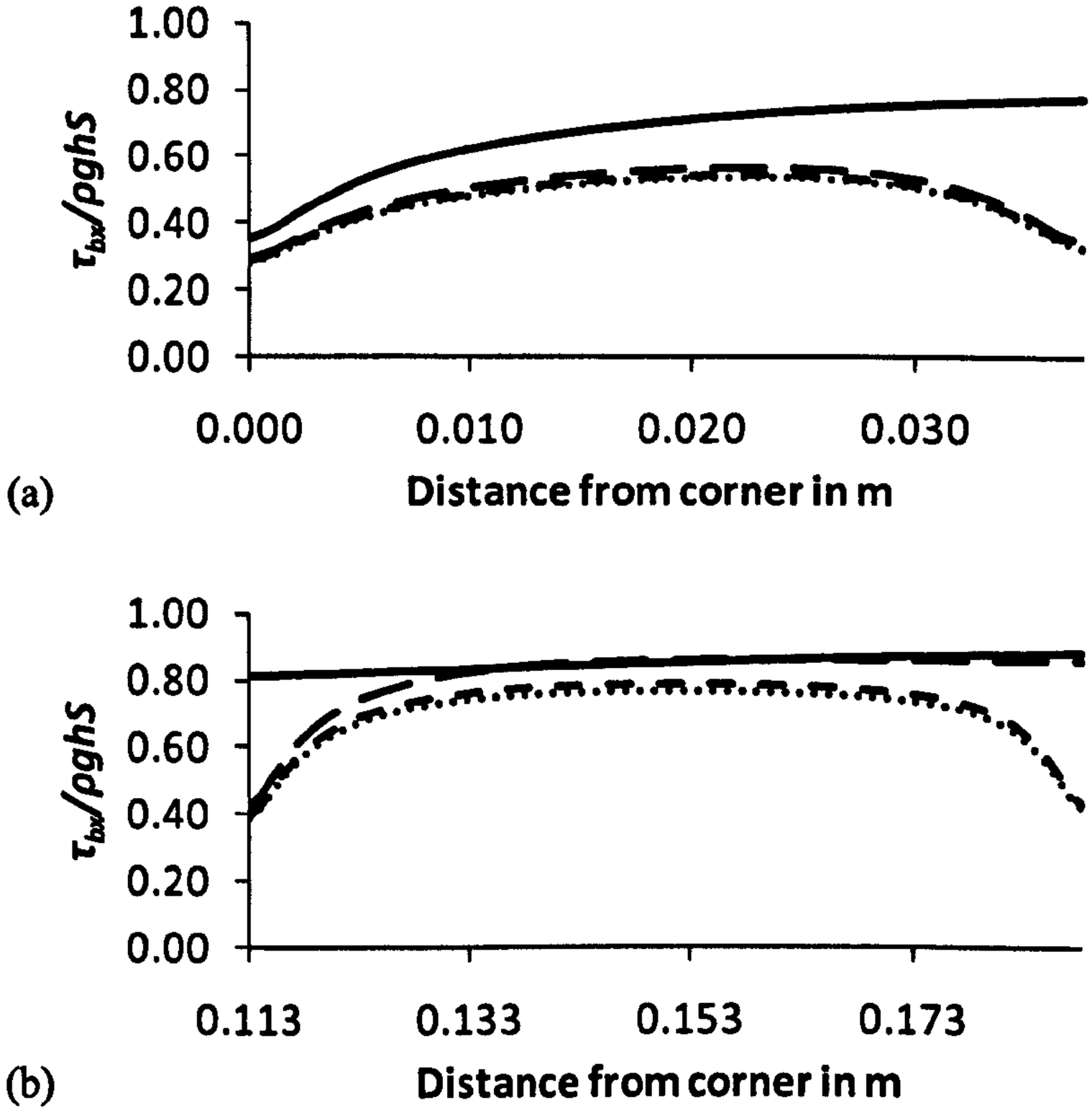

Figure 6.8 Variation of non-dimensionalised wall shear on bed, $\tau_{bx}/\rho ghS$, in mainstream direction with ridge development at Locations (a) 1 (b) 3 (c) 5 and (d) 7, (as defined in Figure 1).

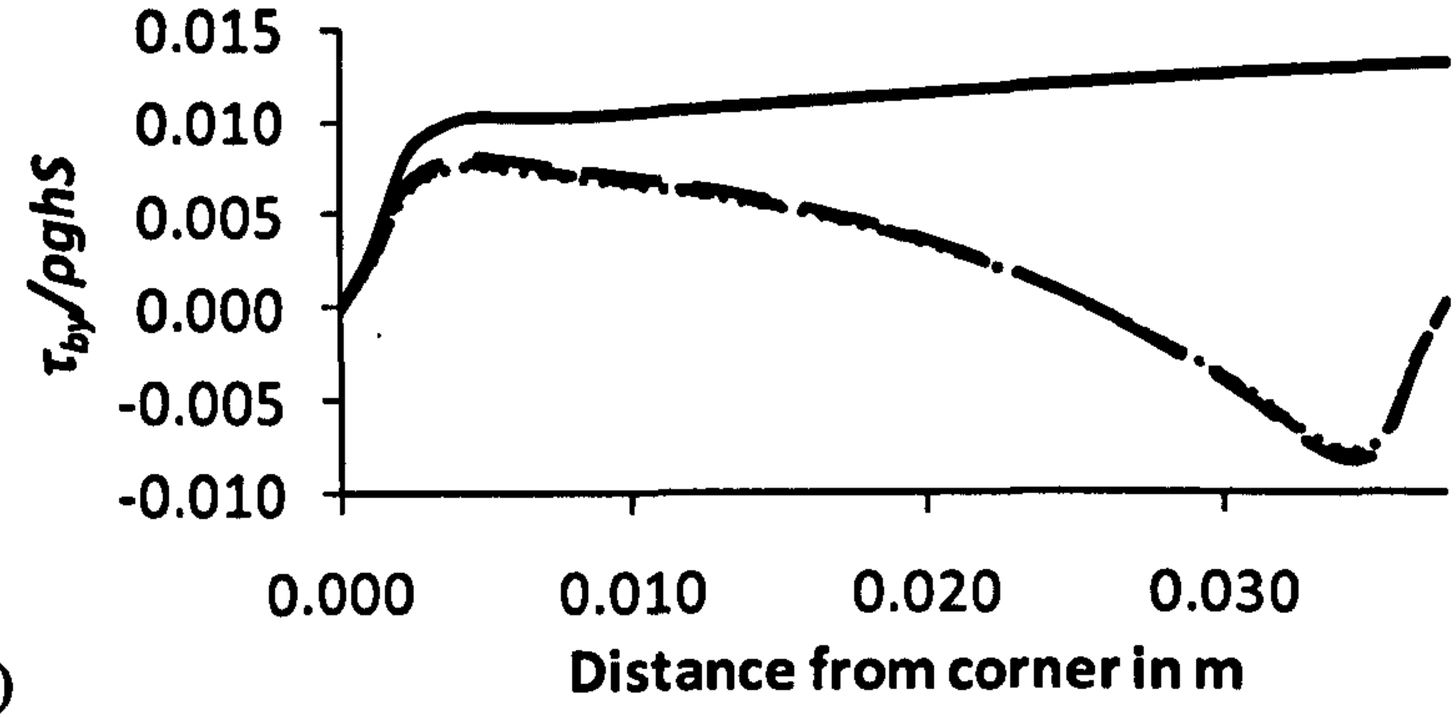

(a)

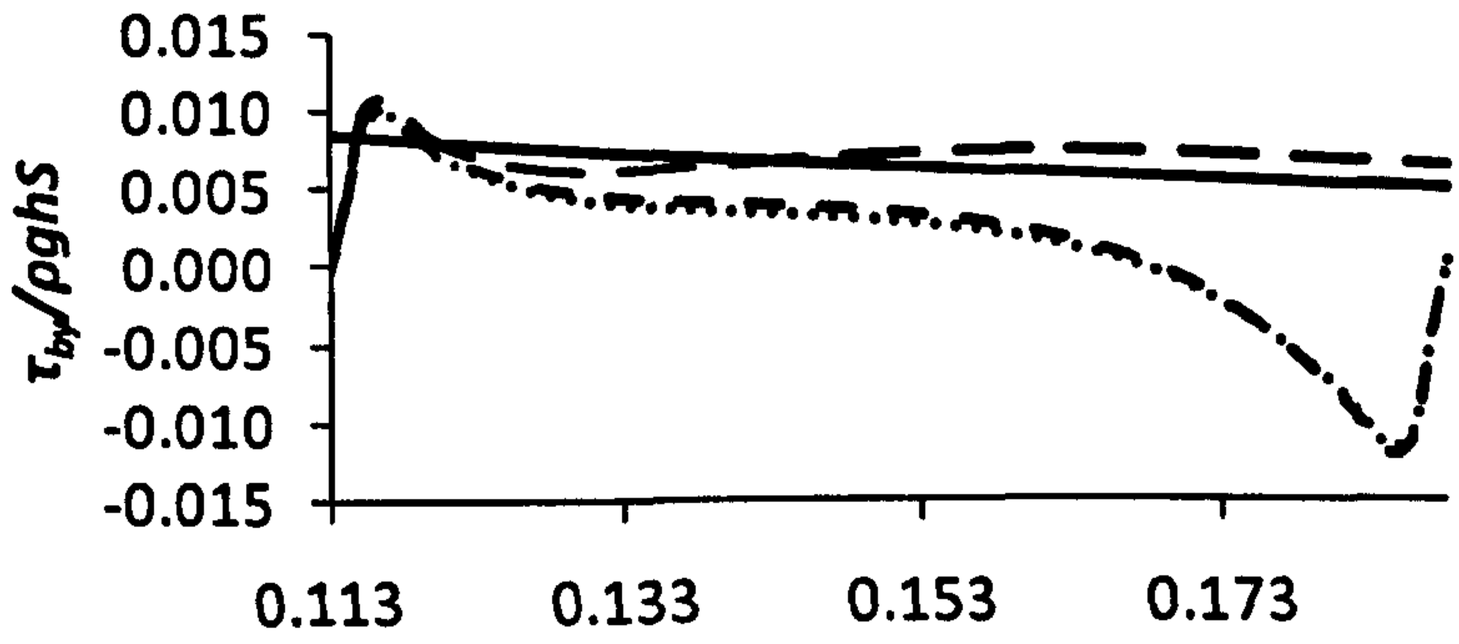

(b)

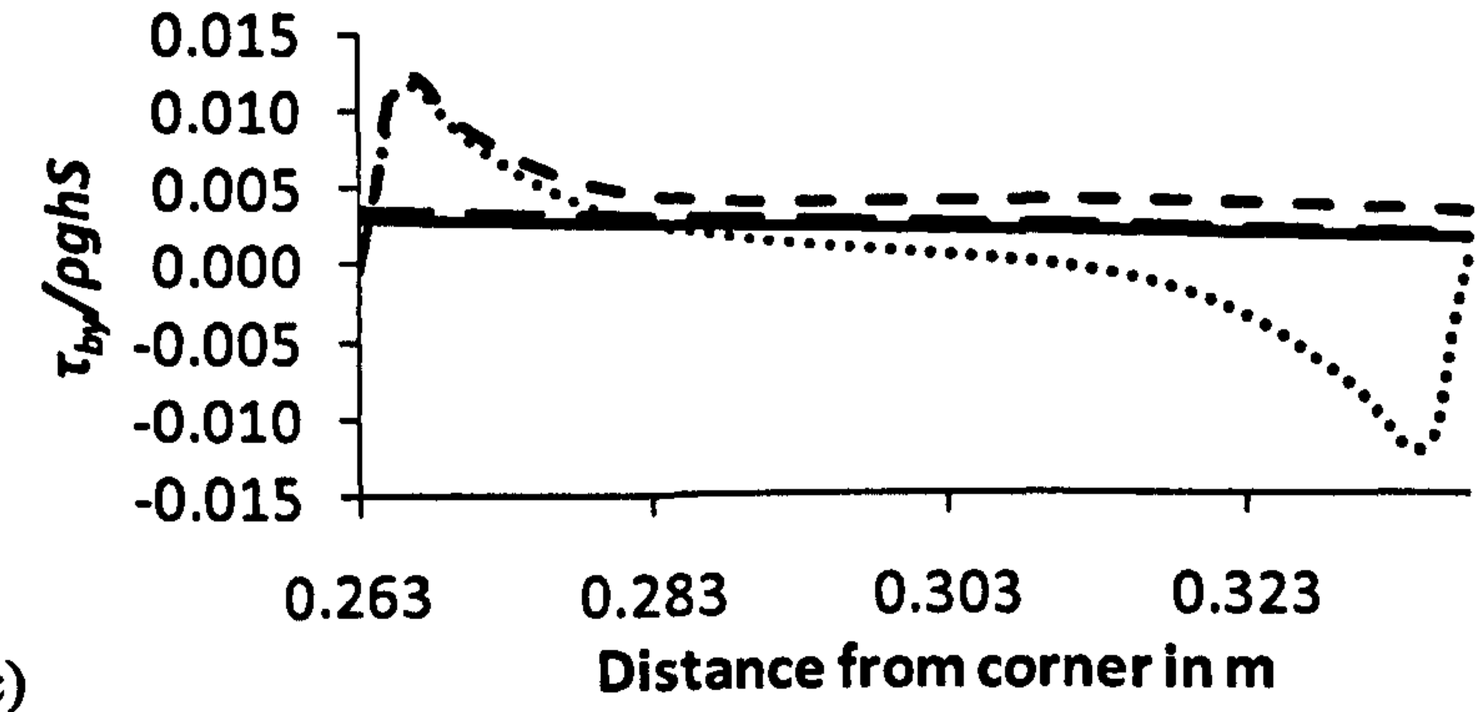

(c)

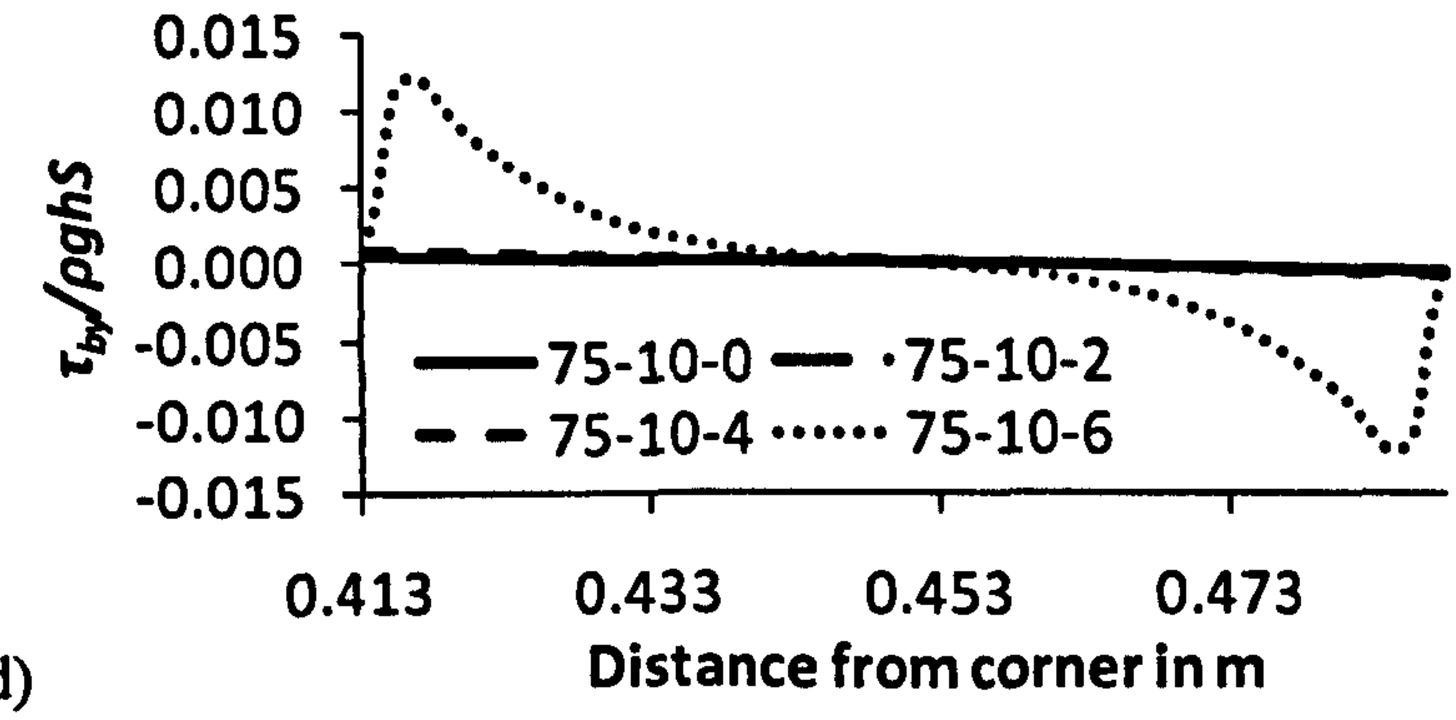

(d)

Figure 6.9 Variation of non-dimensionalised wall shear on bed, $\tau_{by}/\rho ghS$, in cross-stream direction with ridge development at Locations (a) 1 (b) 3 (c) 5 and (d) 7, (as defined in Figure 1).

Figure 6.9 shows the non-dimensionalised wall shear on the bed in the cross-stream direction, $\tau_{by}/\rho ghS$, with variation in the number of ridges, at four different Locations for Cases 75-10-0, 75-10-2, 75-10-4 and 75-10-6. The graph shows wall shear which is peaking only at Location 1 (as defined in Figure 6.2) when there is no ridge, is found to be increasing with the development of a ridge adjacent (towards corner) to it and remains unchanged until the end of the ridge development.

These results suggest that one possible mechanism for the creation of ridges would be tied to secondary circulations, and wall shear on the bed in the wall zone. As the corner ridges form due to the corner vortex and peak wall shear in Location 1, the re-circulations would form and "propagate" towards the channel central line, which would then lead to formation of the next ridge(s) on the bed. As ridges appear they themselves are responsible for localised increase in velocity and shear again with the potential to erode material and reshape the bed. Eventually a trough-and-ridge bed would be formed across the channel bed section related to strong secondary currents activity, leading in turn to surface boils as in Ikeda (1981).

6.4.3 Variation of wall shear after ridge formation

Average shear stresses on the bed and sidewalls are calculated at every section of cross section as shown in Figure 6.2 and are non-dimensionalised by ρghS. The results are tabulated in Table 6.2 for the Cases 75-10-0, 75-10-2, 75-10-4 and 75-10-6. The table clearly shows that the average shear stress in any section within the cross section of the channel keeps on decreasing with the development of the ridges. This shows that a state of equilibrium may be reached on the channel boundaries as part of the interaction between bed form and currents (balance between secondary flow and bed response/form).

Table 6.2 Variation of wall shear on bed and sidewall with ridge development.

Location	Shear stress $\tau_b/\rho ghS$			
	No ridges	Two ridges	Four ridges	Six ridges
Section 1	0.66220	0.49216	0.47338	0.46748
Section 2	0.79574	0.76812	0.72591	0.71251
Section 3	0.84892	0.81478	0.71828	0.69967
Section 4	0.90171	0.88136	0.85765	0.81695
Section 5	0.93317	0.91992	0.86387	0.76656
Section 6	0.95024	0.93996	0.90787	0.85799
Section 7	0.95560	0.94634	0.91845	0.78193
Left wall	0.70913	0.62894	0.60224	0.59396

6.4.4 Variation of shear stress with slant angle

The effect of the variation of sidewall inclination on the boundary shear stress on the bed and sidewalls is also analysed on a fully formed channel i.e. a channel having four ridges on the bed in the present case. The results are given in Table 6.3. The line 1, 3 and 5 are on the troughs and lines 2 and 4 are the ridges. The wall shear on the bed on any particular section increases with the increase in the slant angle of the sidewalls i.e. when the channel walls open up. Whereas for sidewall it increases first with the increase in slant angle until 30° and then begins to decrease again.

Table 6.3 Variation of wall shear with slant angle.

Location	Sidewall inclination from vertical axis ($\tau_b/\rho ghS$)					
	0°	10°	20°	30°	40°	50°
Section 1	0.46192	0.50301	0.53733	0.56329	0.58309	0.60190
Section 2	0.70558	0.71604	0.72495	0.73532	0.74552	0.75940
Section 3	0.68800	0.69869	0.70721	0.71645	0.72454	0.73426
Section 4	0.79864	0.80531	0.81117	0.81682	0.82165	0.82758
Section 5	0.73497	0.74084	0.74584	0.75106	0.75588	0.76248
Left wall	0.58987	0.61457	0.63142	0.63843	0.63478	0.61990

6.4.5 Isovel pattern

Figure 6.10 shows the isovel patterns plotted for the mainstream velocity for cases (a) 75-10-6, (b) 75-05-6 and (c) 50-10-6. They show a periodic variation in the span wise direction. A low speed zone is formed on the regions above the ridges while a high speed zone is formed in the regions above the troughs.

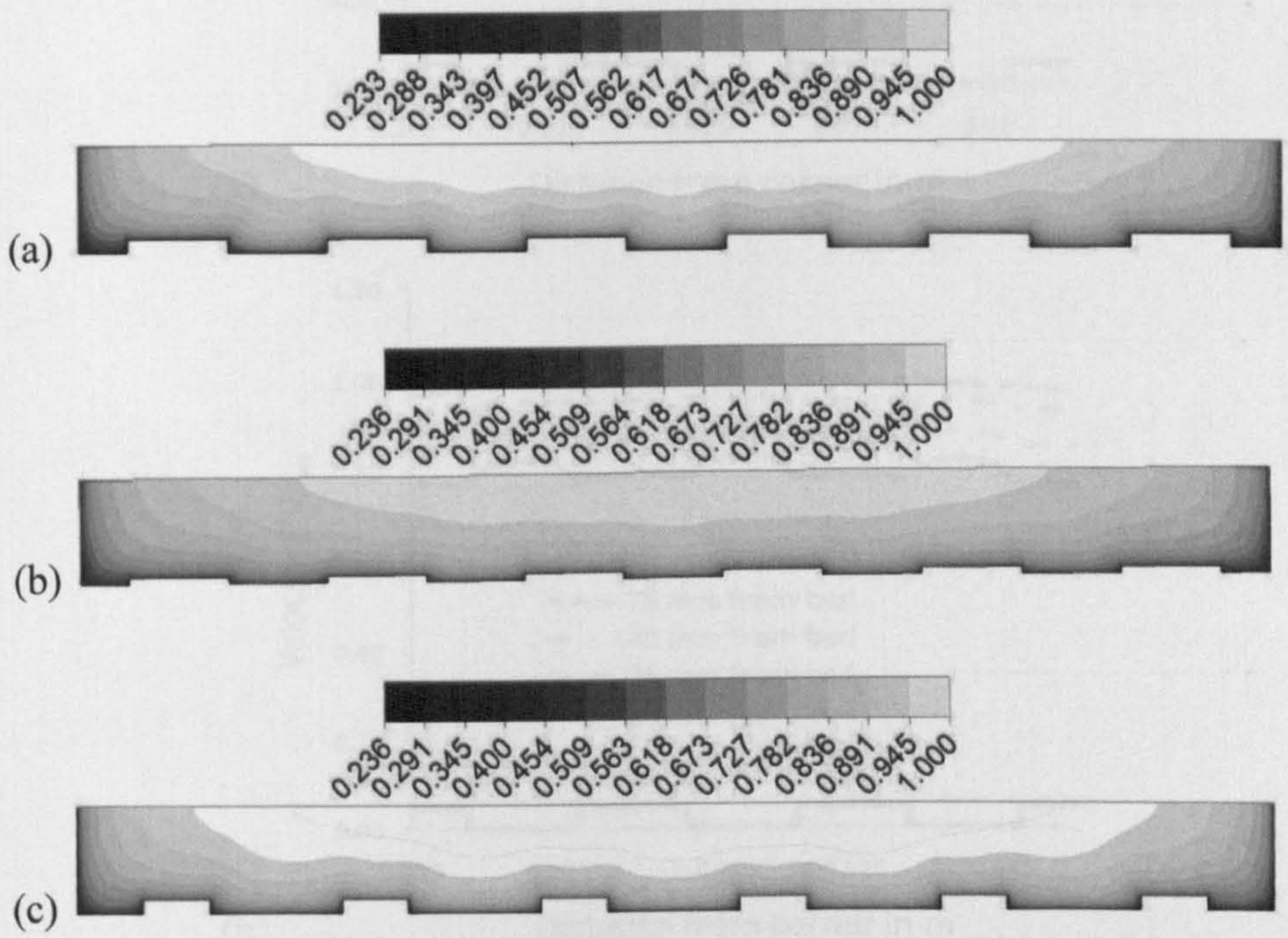

Figure 6.10 Plot of the isovels for u/U_{max} for cases (a) 75-10-6, (b) 75-05-6 and (c) 50-10-6.

The mainstream velocity is also plotted at different depths in the central zones of the channel and is shown in Figure 6.11. The results show high velocity flow over the troughs and comparatively low velocity flow over the ridges at the same distance from the bed. The difference of velocities is higher near the ridges and goes on decreasing near the free surface. It can thus be concluded that low speed and high speed streams of water flow side by side periodically throughout the width of the channel. The low speed streams contain high sediment concentration as has been reported by previous researchers like Nezu, (2005).

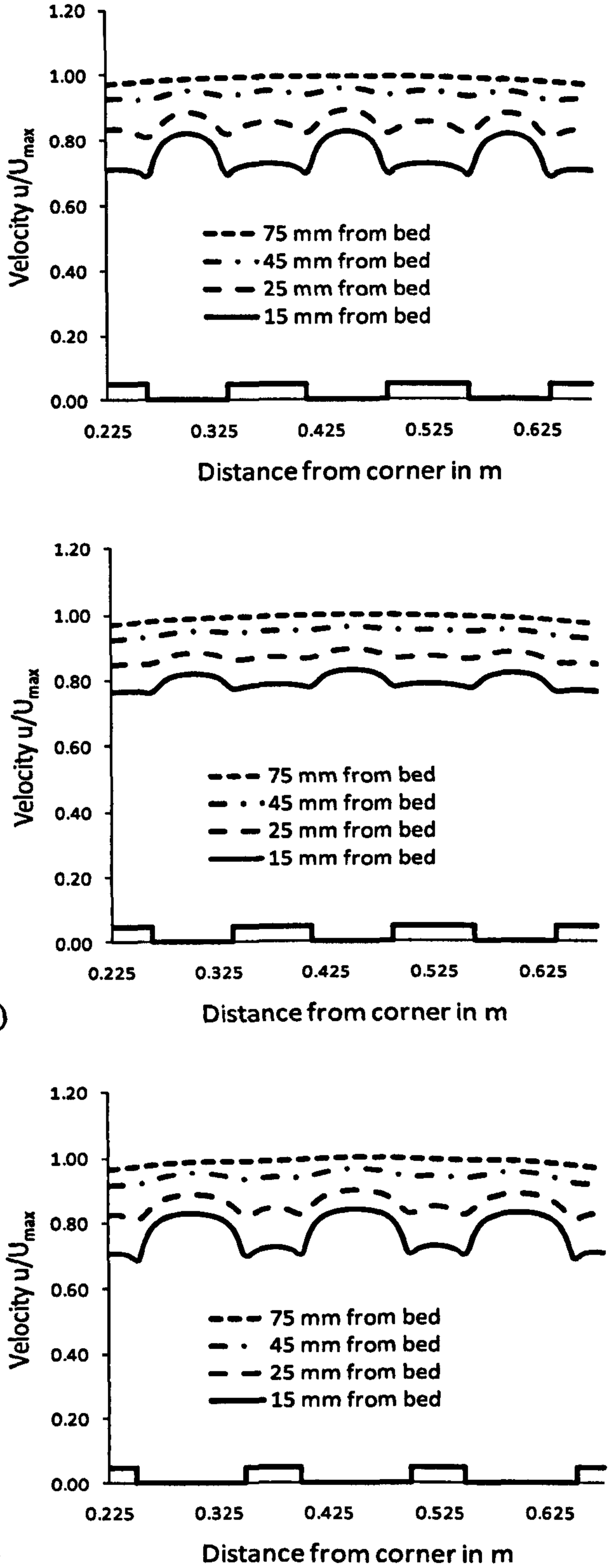

Figure 6.11 Variation of mainstream velocity with depth for cases (a) 75-10-6, (b) 75-05-6 and (c) 50-10-6.

6.4.6 Variation of secondary currents with depth

Figure 6.12 shows the vectors of the cellular secondary currents for the three cases 75-10-6, 75-05-6 and 50-10-6. Figure 6.11 and Figure 6.13 to Figure 6.18 shows the non-dimensionalised three components of the velocity *u*, *v*, and *w* plotted for the three cases 75-10-6, 75-05-6 and 50-10-6 at four different elevations i.e. 15 mm, 25 mm, 45 mm and 75 mm from the bed level.

In Figure 6.11 the mainstream velocity, *u*, is seen to be varying such that there is lower velocity over the ridges and comparatively higher velocity over the troughs. This difference is higher near the bed and goes on decreasing towards the free surface where almost same velocity is observed throughout the central portion.

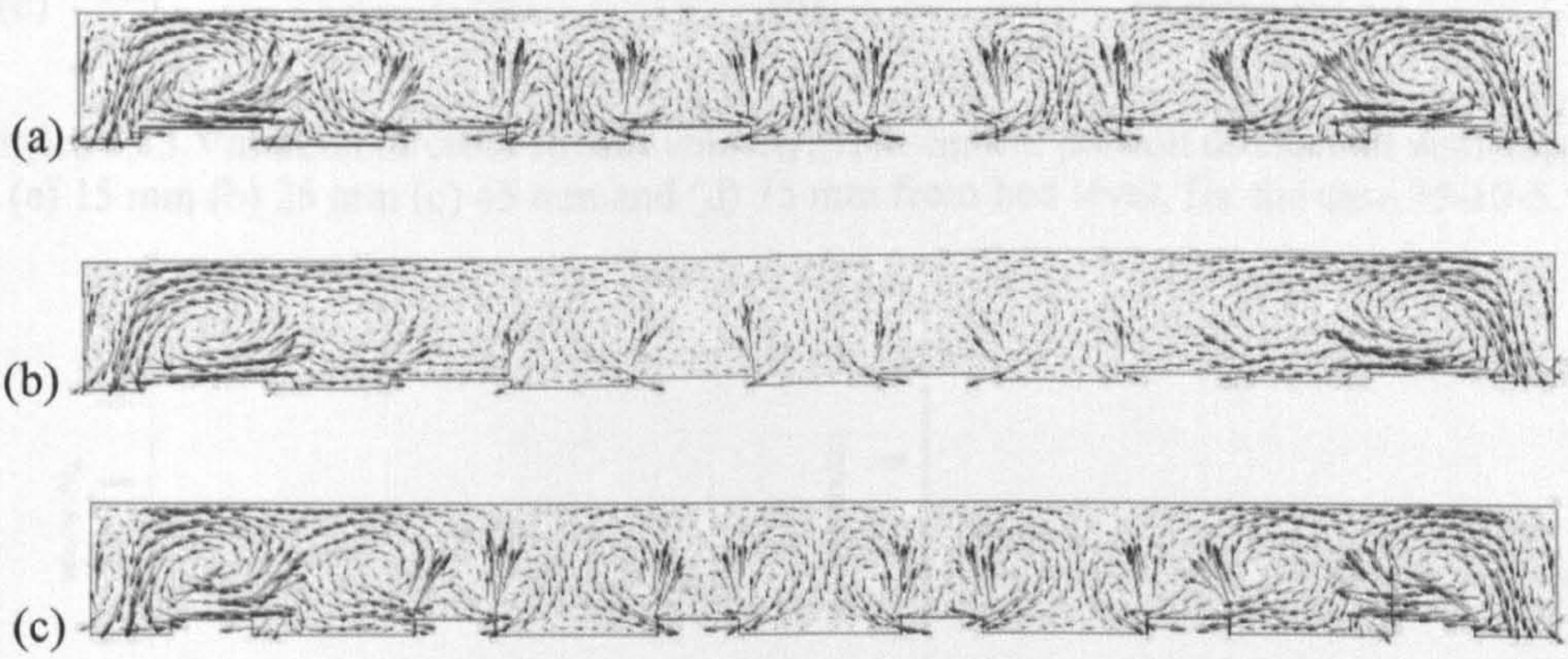

Figure 6.12 Variation of cellular secondary currents with size of ridges for cases (a) 75-10-6 (b) 75-05-6 and (c) 50-10-6.

The cross stream velocity, *v*, is seen to have higher magnitudes over the troughs as compared to ridges as shown in Figure 6.13, 6.13 and 6.14. The magnitude of the velocity is greater near the bed and gets decreased in the central portion but is again found to increase near the free surface. The velocity is seen to change sign over the centres of both troughs and ridges and hence two cells (a pair) of counter rotating currents are formed over each section. Near the free surface the velocity only changes sign over the middle trough (section 7, Figure 6.2) of the channel which means that effect of the ridges is very negligible near the free surface and only two large counter rotating cells are seen on either side of the centre.

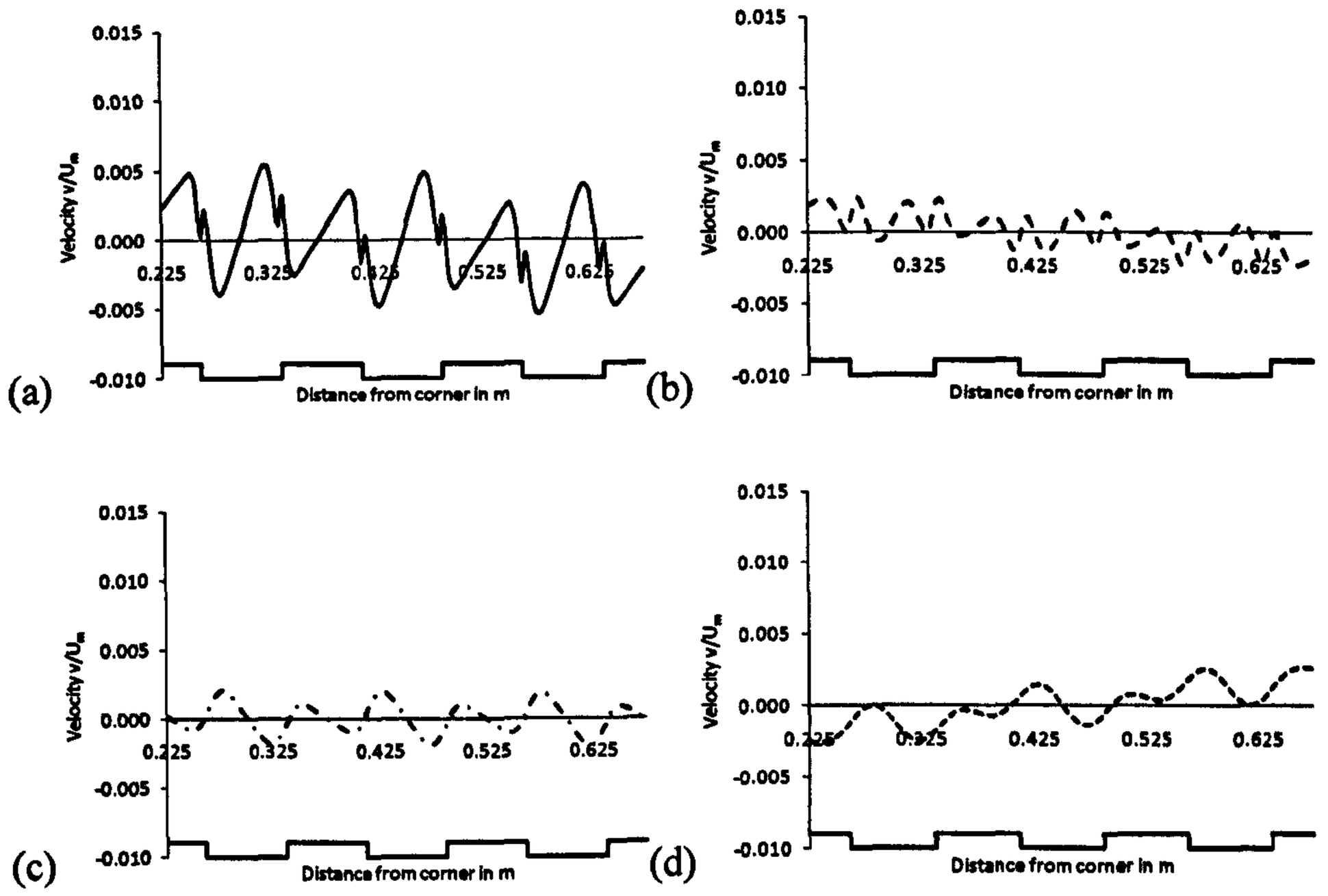

Figure 6.13 Variation of cross stream velocity, v, in central portion of channel with depth (a) 15 mm (b) 25 mm (c) 45 mm and (d) 75 mm from bed level, for the case 75-10-6.

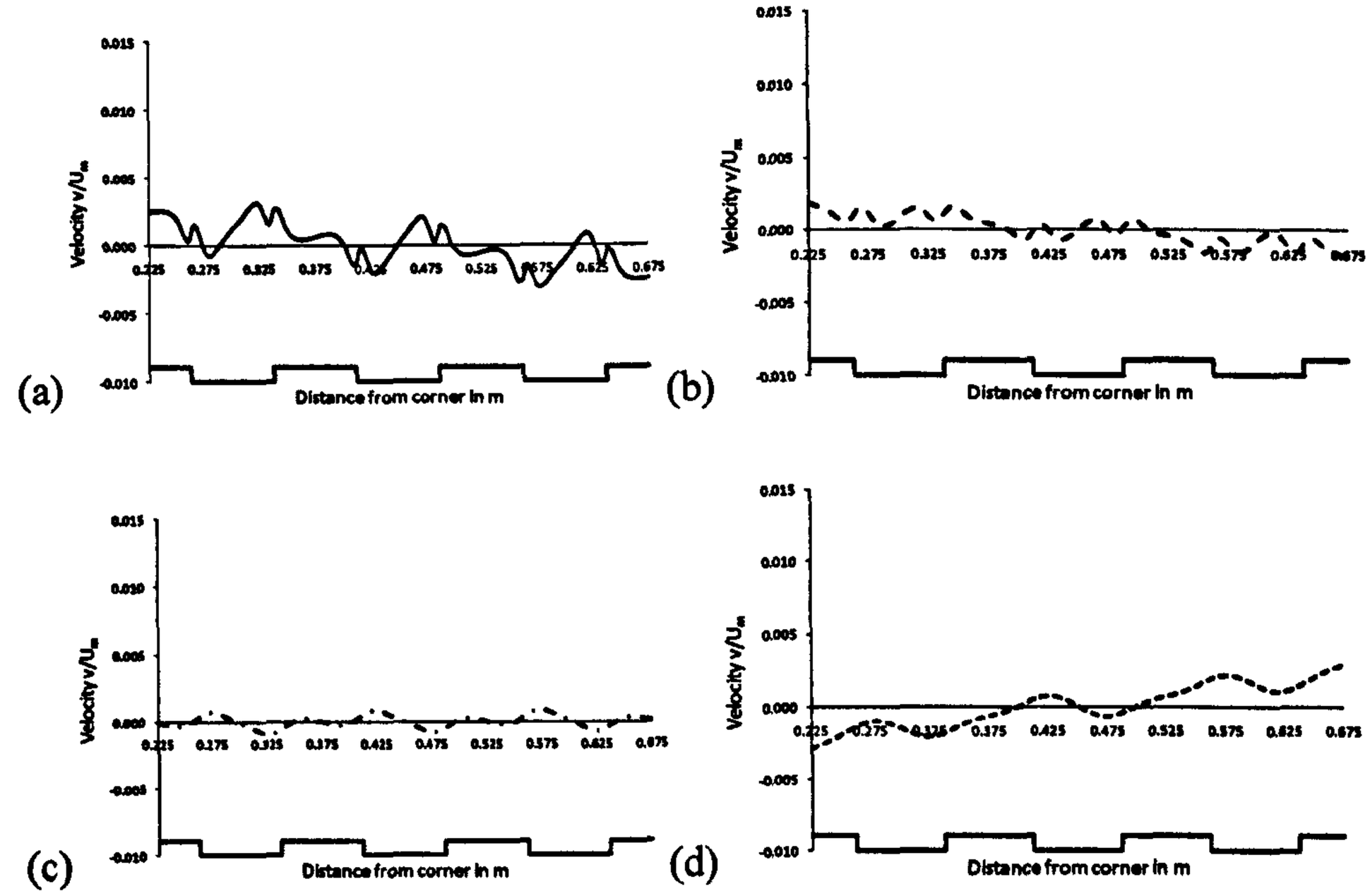

Figure 6.14 Variation of cross stream velocity, v, in central portion of channel with depth (a) 15 mm (b) 25 mm (c) 45 mm and (d) 75 mm from bed level, for the case 75-05-6.

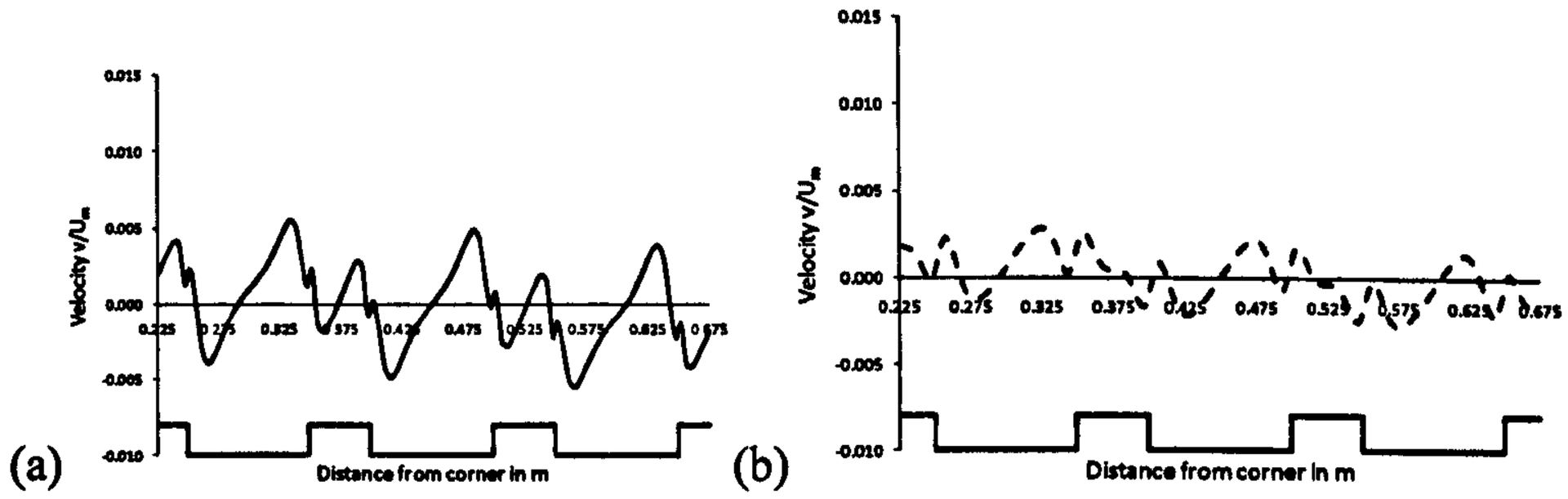

Figure 6.15 Variation of cross stream velocity, v, in central portion of channel with depth (a) 15 mm (b) 25 mm (c) 45 mm and (d) 75 mm from bed level, for the case 50-10-6.

The vertical velocity, *w*, is taken positive upward and negative downward. It is seen to be highest in magnitude over the edges of the ridges as shown in Figure 6.16, 6.16 and 6.17. It is found to be positive over the areas where troughs and ridges meet and negative over the middle portions of both troughs and ridges as shown in Figure 6.16. The upward velocities are higher in magnitude than the downward velocities. The downward velocity is higher over troughs as compared to ridges and hence may be responsible for the high sediment concentration over the ridges as seen previously. The vertical velocities are found to be higher near the bed and decrease near the free surface.

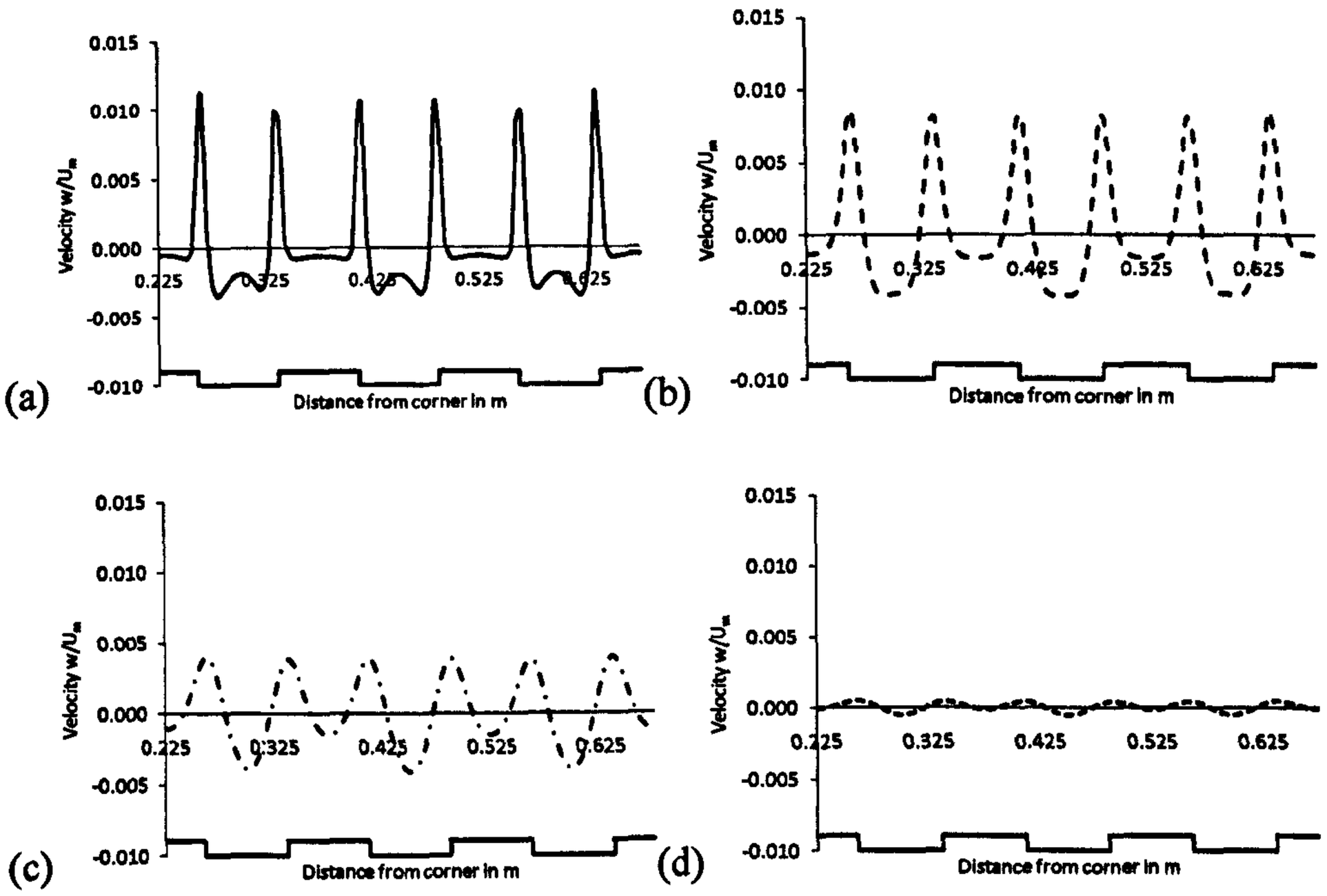

Figure 6.16 Variation of vertical velocity, *w*, in central portion of channel with depth (a) 15 mm (b) 25 mm (c) 45 mm and (d) 75 mm from bed level, for the case 75-10-6.

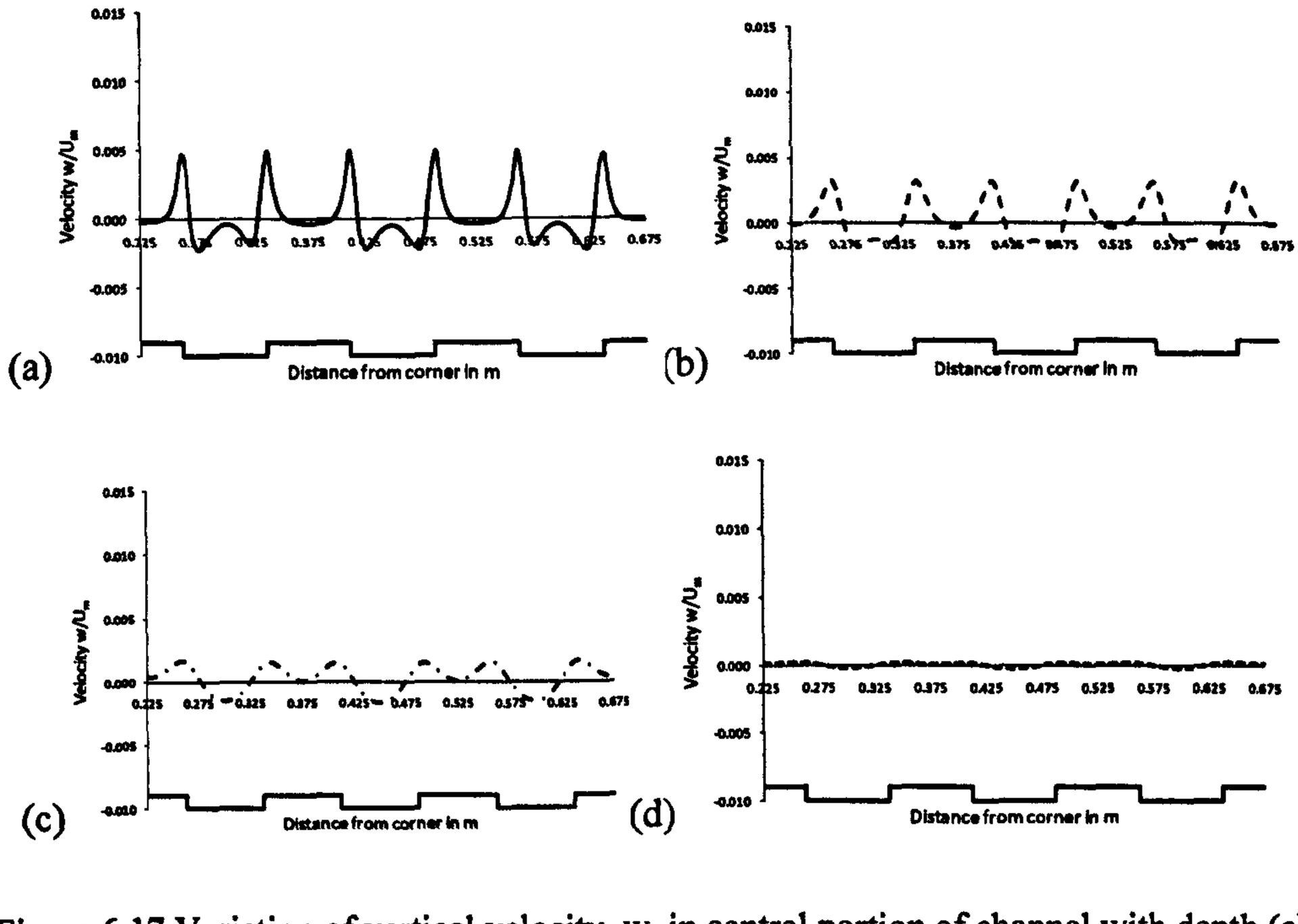

Figure 6.17 Variation of vertical velocity, w, in central portion of channel with depth (a) 15 mm (b) 25 mm (c) 45 mm and (d) 75 mm from bed level, for the case 75-05-6.

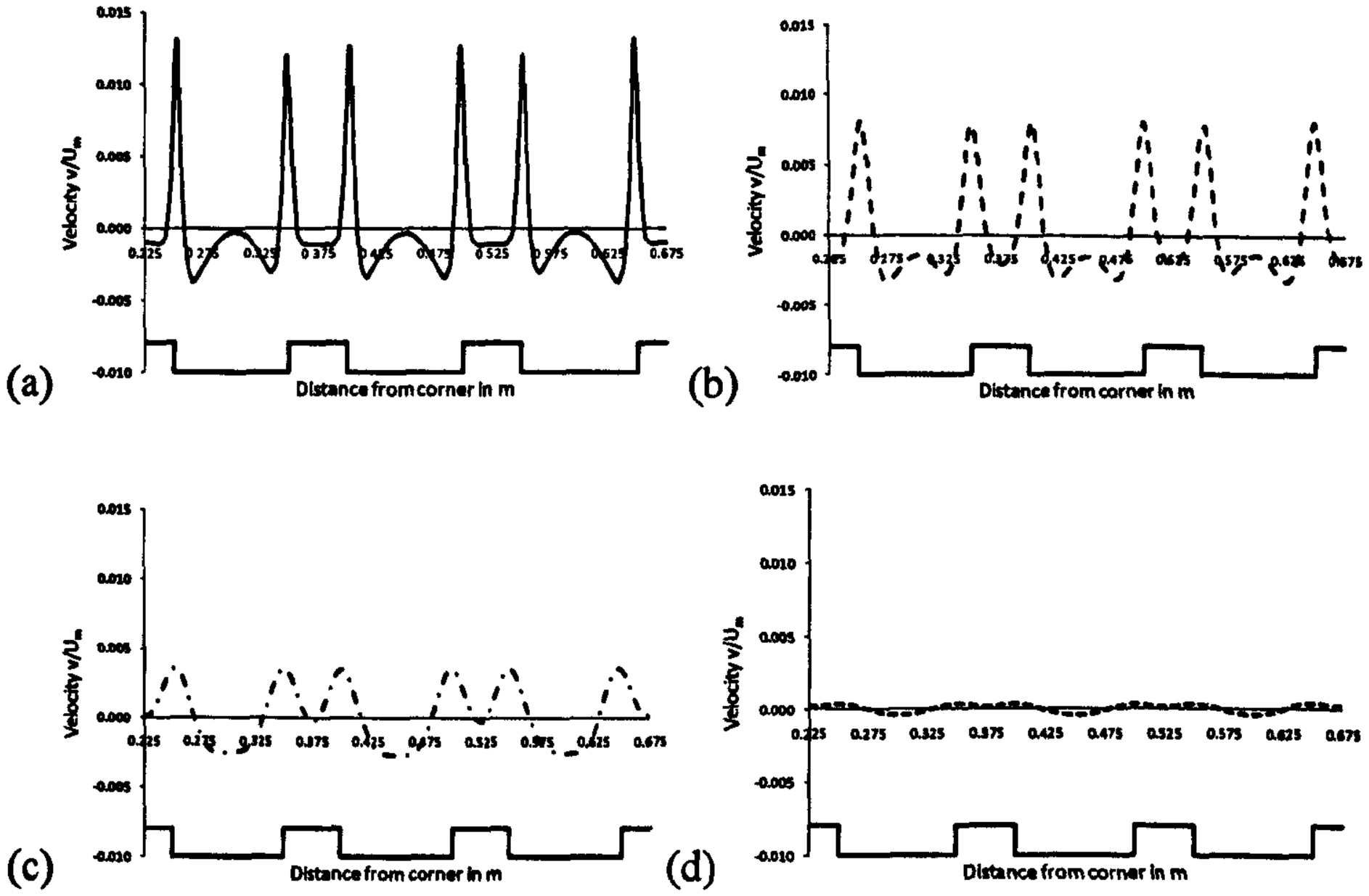

Figure 6.18 Variation of vertical velocity, w, in central portion of channel with depth (a) 15 mm (b) 25 mm (c) 45 mm and (d) 75 mm from bed level, for the case 50-10-6.

6.4.7 Sensitivity to height of ridge

Comparison of flow structures is done between cases 75-10-6 and 75-05-6 to see the effect of the height of the ridge on the cellular secondary currents. The velocities are plotted at depths 15 mm and 10 mm from the bed for the two cases 75-10-6 and 75-05-6 respectively, to keep an equal distance of 5 mm from the top of the ridges and are shown in Figure 6.19.

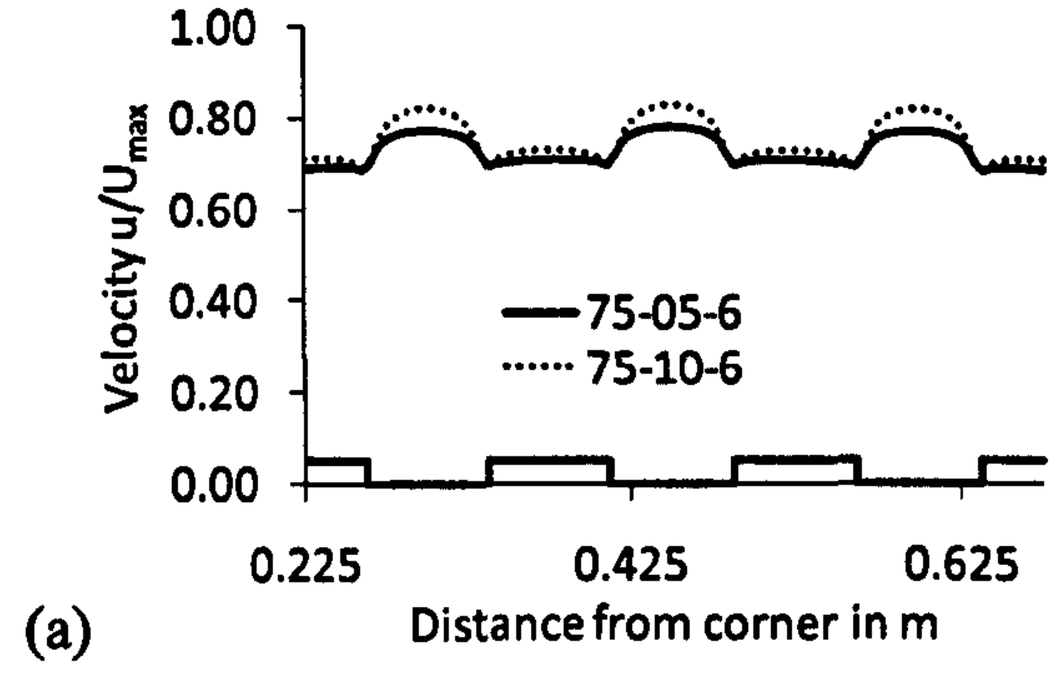

(a)

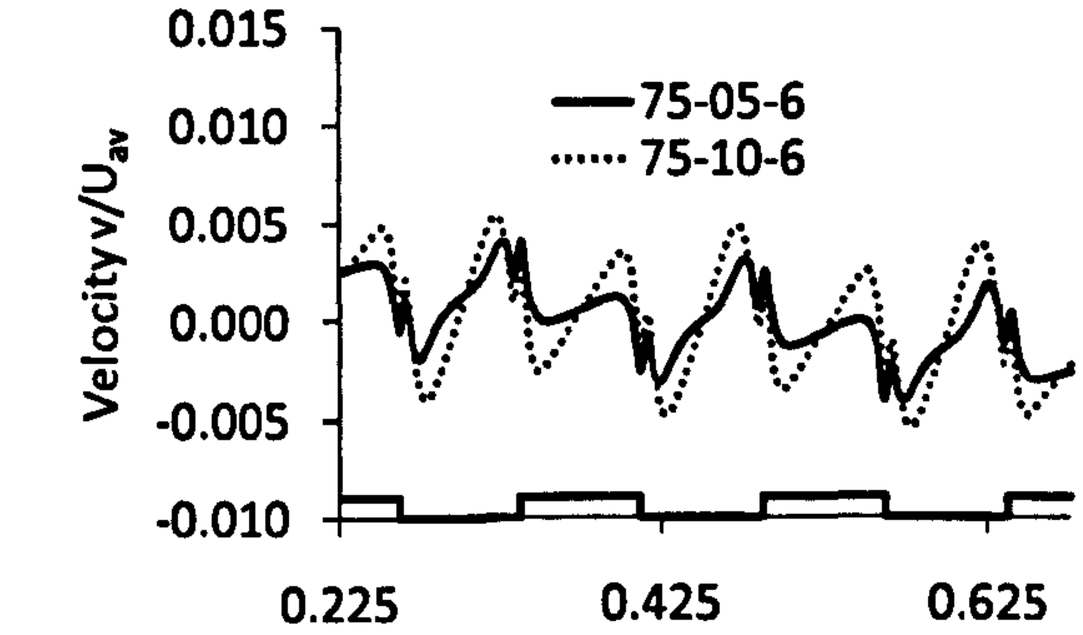

(b)

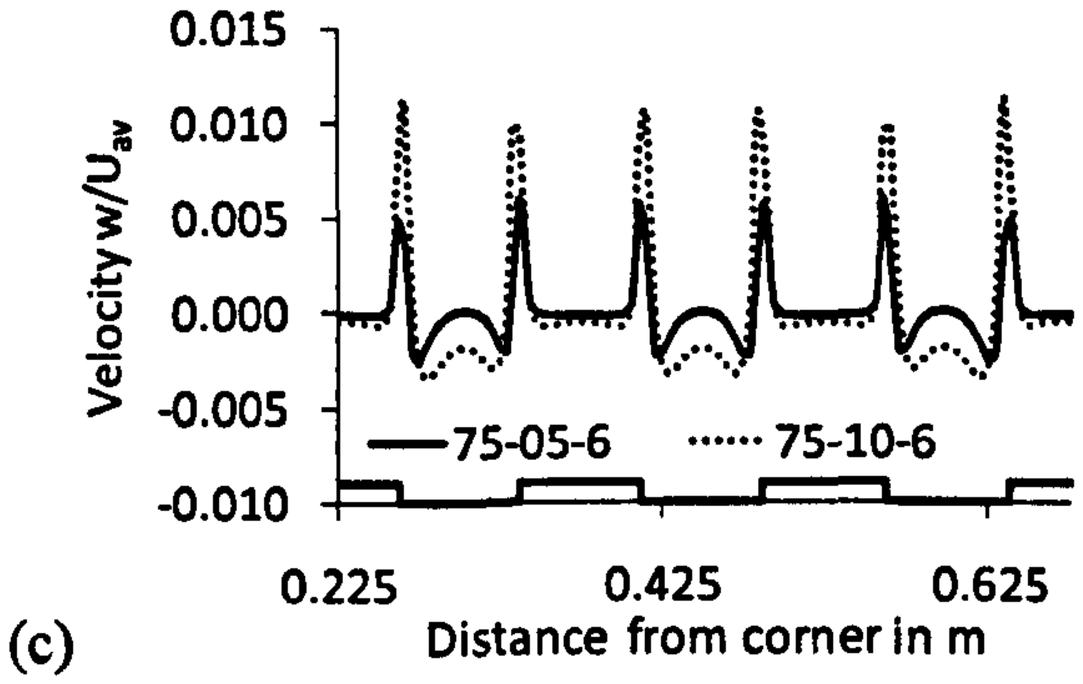

(c)

Figure 6.19 Variation of velocity with ridge height at 5 mm from ridge top.

Not much effect is seen on the mainstream velocity, *u*, with the variation in ridge height. However in the cross stream velocity, *v*, it is found that two circulations are visible over the troughs as the velocity is changing sign but over the ridges it is seen to be going in one direction i.e. away from the wall for the case 75-05-6. Whereas, the flow seems to have fully developed when height of the ridge increases to 10 mm as two counter rotating circulations are visible on both troughs and ridges. The vertical velocity, *w*, is found to have the maximum difference specially the upward velocity and is seen to be directly proportional to the ridge height.

6.4.8 Sensitivity to length of ridge

Comparison of flow structures is done between cases 75-10-6 and 50-10-6 to see the effect of the length of the ridge on the cellular secondary currents. The velocities are plotted at depth 15 mm from the bed for the two cases 75-10-6 and 50-10-6 respectively, as shown in Figure 6.20. Again not much effect is seen on the mainstream velocity, u, and the cross-stream velocity, v, with the variation in ridge length. The vertical velocity, w, is found to have the some difference here as well specially the upward velocity and is seen to increase further with the decrease in length of the ridge.

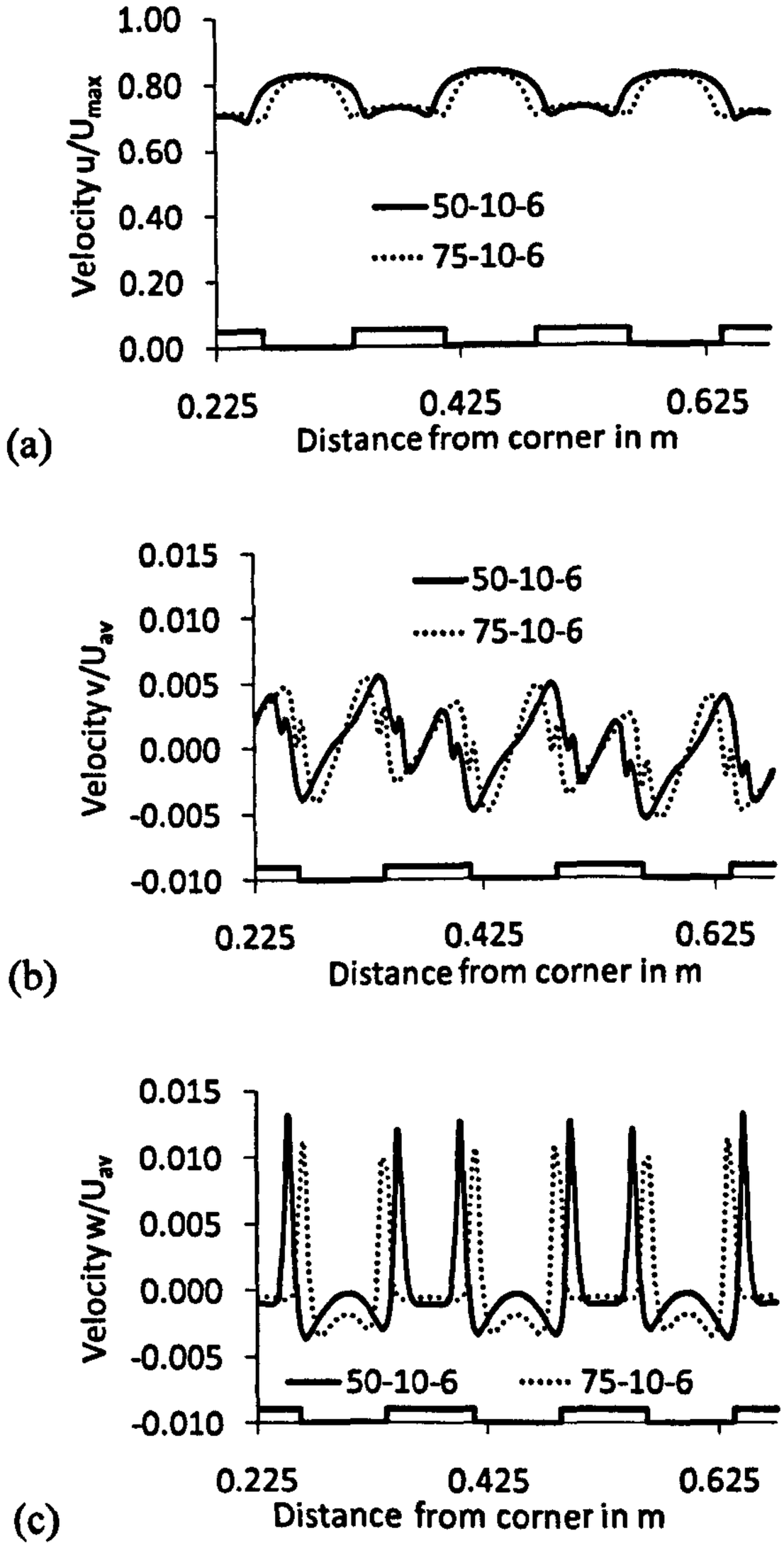

Figure 6.20 Variation of velocity with ridge length at 15 mm from bed level.

6.5 Conclusions

The pattern of the secondary currents as observed shows that the presence of the sidewalls could initially be responsible for the creation of the corner ridges. These, in turn, may be responsible for the formation of an additional cell of circulation which again creates another ridge and so on until the whole channel develops these ridges and troughs and a state of equilibrium is reached. This would provide an explanation for the mechanism leading to ridge formation and appearance of lines of boil, consistent with earlier hypotheses found in the literature. The vertical velocity is found to be upward over the edges of the ridges and downward over centres of both the troughs and ridges, which shows a pair of counter rotating cells over both troughs and ridges. The perturbations of secondary flow are strong near the bed and get significantly reduced near the free surface. The wall shear is seen to be decreasing with the increase in the ridges on the bed which shows that the bed forms ultimately bring some stability on the boundaries in the section.

CHAPTER 7

SHEAR STRESS IN CURVES/BENDS OF TRAPEZOIDAL CHANNELS

7.1 Introduction

An extensive analysis is carried out on the development of flow structures and variation of shear stress inside an open channel bend. A bend section is selected from the experimental channels used by Ippen and Drinker (1962). First, the simulations are run on the same channel section with symmetry-wall boundary condition as the free surface boundary condition, as has been done previously for the straight prismatic channels, Chapter 5. However, because water flowing inside a bend experiences centrifugal force, the free surface tends to rise higher on the outer bank as compared to the inner bank. Recourse to a predetermined fixed free surface boundary is not straightforward: (1) its position is not known a priori and (2) it may well affect the distribution of flow quantities inside the cross section leading to erroneous shear stress predictions and re-circulations for example. Consequently, one simulation is also run using the Volume of Fluid (VOF) method to ascertain the influence of the top surface boundary on the results. Next, the simulations using the symmetry boundary condition at the free surface are run with three turbulence models, (i) SSG (ii) RNG $k-\varepsilon$ and (iii) standard $k-\varepsilon$ and the one with VOF method is run using only RNG $k-\varepsilon$ turbulence model. Finally, two sets of simulations are run with lid, varying the sidewall inclination, to analyse its effect on the shear stress distribution inside a bend.

Since one of the aims of the study is to analyse the flow structures and shear stress in the bend of a channel section this chapter covers the results and analyses based on simulations run on channel sections having a bend. Although there have been several other experimental studies like Shiono and Muto (1998) but he channel section is also selected from Ippen and Drinker (1962) keeping in mind the bends usually found in the irrigation and drainage channels in Pakistan since this study is taken keeping in view the channels used there.

7.2 CFD Model setup

7.2.1 Domain and boundary conditions

A typical plan view of the channel section used is shown in Figure 7.1 and a typical section at bend entry is shown in Figure 7.2. The trapezoidal channels have constant width at the channel bed, b, equal to 60.96 cm, constant depth of the water in the channels, h, equal to 7.57 cm. The sidewalls are inclined at angles θ of 30°, 45° and 63° to the vertical. Due to the variation in side slopes the top widths, T, of the channels are 69.70 cm, 76.10 cm, and 90.67 cm respectively for the 3 angles of slope. The channels have straight approach, L_{in}, and exit, L_{out}, sections. The channels have a single curve of 60° with the radius of curvature, R, equal to 152.4 cm with the centre line of the channel section, based on the Ippen and Drinker (1962) flume. The origin of the axes, O, is placed at the centre of curvature of the bend. The x-axis is the flow direction in the straight approach section, the y-axis is the cross-stream direction and z-axis is positive upward from the bed level of the channel.

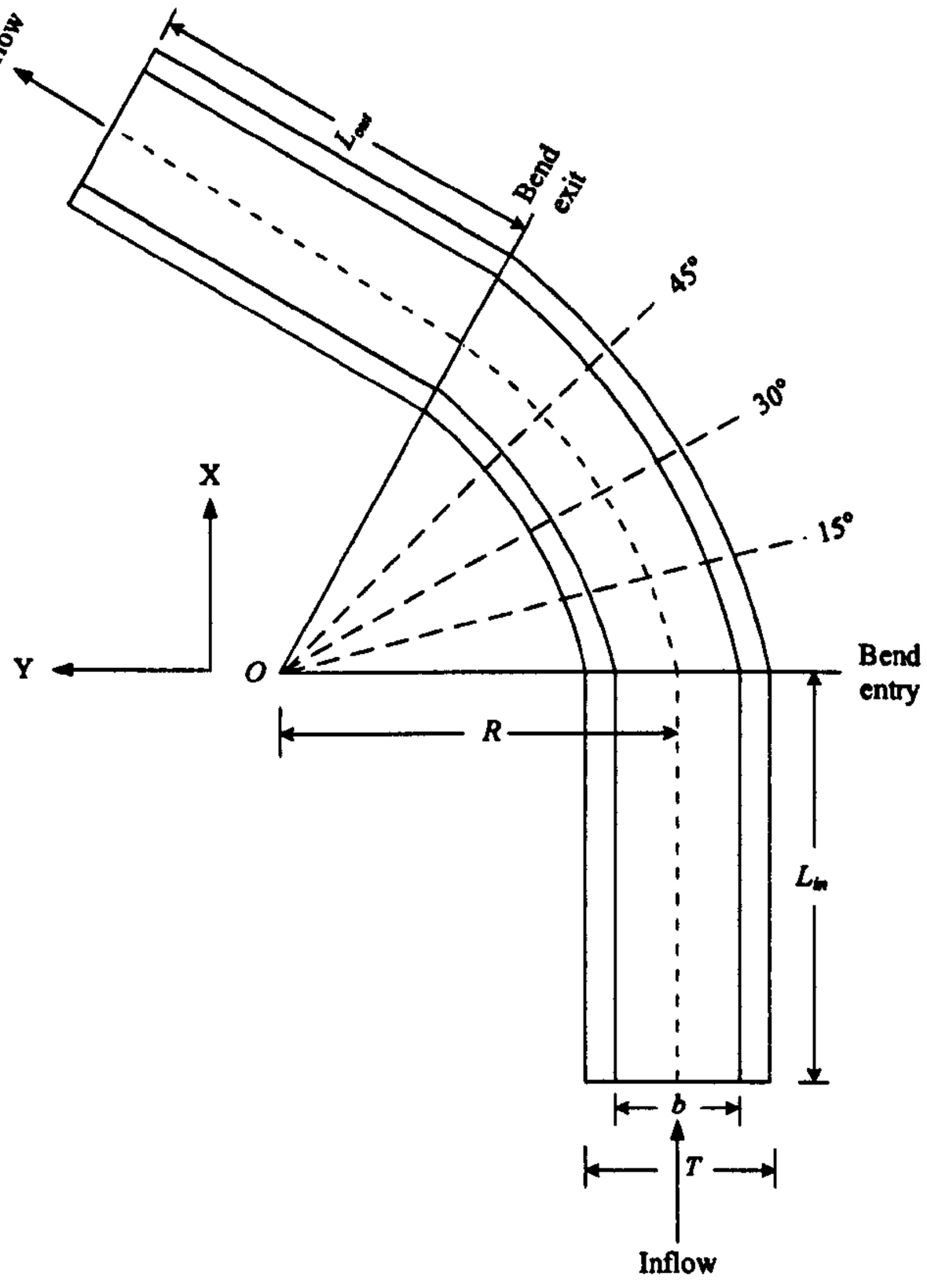

Figure 7.1 Typical plan view of the channels used after Ippen and Drinker (1962).

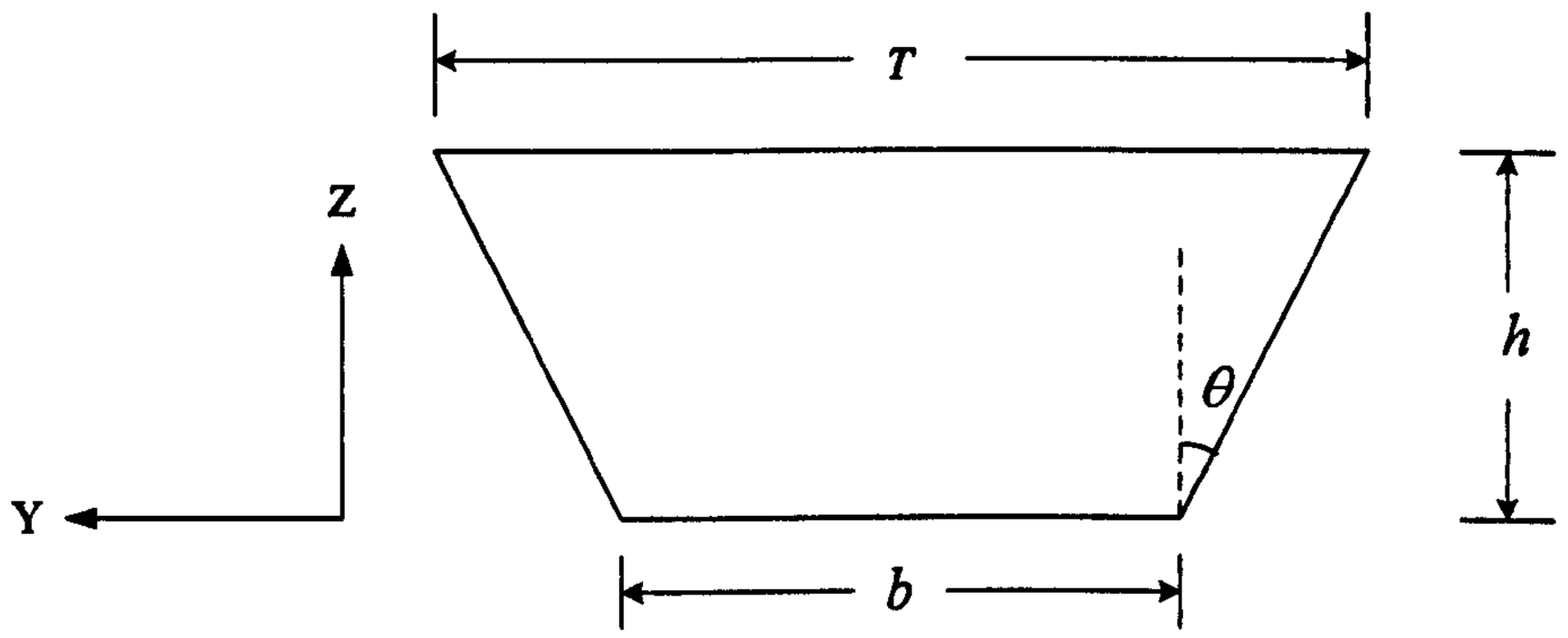

Figure 7.2 Typical cross section of the channel at the bend entry after Ippen and Drinker (1962).

Two methods are employed for the simulations on the bends, the first called the rigid lid method, the second, the Volume of Fluid (VOF) method. The boundary conditions for the two are described below.

7.2.1.1 Rigid lid method

Most of the simulations were solved as single phase, steady state problems with water used as the fluid. Symmetry-wall boundary condition was used at the free surface. Both the walls (bed and side) were taken as non-slip smooth walls and the ANSYS-CFX standard wall function approach was employed. "Inlet" boundary condition was taken at inlet and "Opening" boundary condition was taken at outlet with mass and momentum option being specified as "entrainment". These simulations were run using three turbulence models namely SSG Reynolds stress, RNG k-ε and standard k-ε.

7.2.1.2 VOF method

Three simulations were also run on the volume of fluid (VOF) method. It solves as a two phase, transient problem with water and air used as fluid. Both the walls (bed and side) were taken as non-slip smooth walls and the ANSYS-CFX standard wall function approach was employed. "Inlet" boundary condition was taken at inlet and "Opening" boundary condition was taken at outlet with mass and momentum option specified as "opening pressure and direction" and the relative pressure is taken as hydrostatic pressure. This simulation was run using RNG k-ε turbulence model. It was necessary to run few simulations using VOF method to capture the changes in the free surface during the flow inside a bend.

7.2.2 Convergence Criteria

For steady-state problems in CFX, a time step is used as an "acceleration parameter" to guide the solution process. Here the time step was 0.1 second. All the residual targets were set a value of 10^{-9}. It was found necessary to use such low targets to ensure that the shear forces on the bed and sidewall had reached steady values and matched the applied body force. Such tight convergence criteria were also required because the secondary currents took a great number of iterations to establish themselves. For transient simulations (VOF cases) the total time duration was taken as 120 seconds and each time step was taken as 0.05 seconds.

7.3 CFD approach used

The CFD approach used in solving for the bend section includes the following:-

First of all a single cell thick section having the same cross-sectional dimensions was built and run. The periodic domain interface boundary condition was used in the stream wise direction and the bed of the channel was kept horizontal. A driving force equal to ρgS, where ρ is the density of water taken as 997 kg/m^3, g is the acceleration due to gravity taken as 9.81 m/s and S is the slope of the channel equal to 0.00064, was introduced as a momentum source in the stream wise x-direction.

Next when the solution described here above converged and the shear force on the bed and the two sidewalls stabilised, an inlet boundary profile containing all the six Reynolds Stresses namely $\tau_{xx} = -\rho\overline{u'^2}$, $\tau_{yy} = -\rho\overline{v'^2}$, $\tau_{zz} = -\rho\overline{w'^2}$, $\tau_{xy} = -\rho\overline{u'v'}$, $\tau_{xz} = -\rho\overline{u'w'}$ and $\tau_{yz} = -\rho\overline{v'w'}$ plus all the three components of the velocity u, v and w and the turbulence eddy dissipation, ε, were exported and used as the boundary condition profile file for the bend case.

The straight upstream section was kept some distance upstream from the bend to limit the impact of the "Inlet" boundary condition upon the bend solution. The impact of the straight sections before and after the bend are discussed next.

7.3.1 Length of straight approach and exit sections

The channel section used by Ippen and Drinker (1962) during their experiments had a straight entry portion of 609.6 cm and a straight exit portion of 304.8 cm. They had to install a sluice gate at the end of the channel section because the backwater effects of the channel outfall had been observed to extend through the curve and well into the approach section. Keeping in mind the fact that the asymetry of the flow continues for a long distance after the bend it was decided to increase the straight portion "L_{out}". Investigations on the pipe bends have shown that the flow may not return to normal within a distance less than fifty pipe diameters e.g. Einstein and Harder (1954). In order to verify how long it takes for the flow to become normal after passing through the bend and also to see at what

distance before a bend the flow starts to become asymmetrical, few simulations were run with variations to the lengths of the straight portions before and after the bend.

Table 7.1 Length of the straight portions before and after the bend with asymmetry of the mainstream velocity observed in the Ippen and Drinker (1962) simulation work.

Name	Length of straight portion in metres		Distance before the bend in metres			
			Bend entry	0.381	0.762	1.524
	L_{in}	L_{out}	Asymmetry in percentage			
Case 1	6.096	6.096	1636.78	61.47	12.66	0.81
Case 2	3.048	12.192	1214.28	55.48	12.47	1.20
Case 3	1.524	18.288	870.81	55.84	11.74	4.39
Case 4	3.048	36.576	1068.32	54.52	12.78	1.43
Case 5	3.048	3.048	2276.97	62.97	13.84	1.44

Table 7.1 shows five different simulations carried out with different straight portions before and after the bend and the asymmetry observed in the mainstream velocity before the start of the bend at different locations. The asymmetry is calculated by evaluating the difference in mainstream velocity at equal distance from both the sidewalls and then computing the percentage difference with respect to the higher velocity observed. From the results it is concluded that for all the cases the asymmetry in the mainstream velocity starts at least 1.524 m from the start of the bend which incidentally is also the radius of curvature of the bend itself. Figure 7.3 shows the contours of the isovels of the mainstream velocity at the free surface. It was clearly seen that asymmetry of the velocity continues for a long time after the flow leaves a bend and for non of the cases the flow was found to come back to normal course even for case 4 which had a straight portion of 36.576 m, sixty times the width of the channel, 0.6096 m, after the bend. After looking at the results it was decided to run the simulations on channels with sufficient equal straight portions before the bend such that the flow is fully developed well before it anticipates a curve and also it is long enough after the bend that its backwater effects does not interfere in the results of the bend. For this it was decided to add straight portions of 6.096 m before and after the bend.

The results and analyses of the simulations with straight portions on both the sides of the bend are discussed in detail ahead.

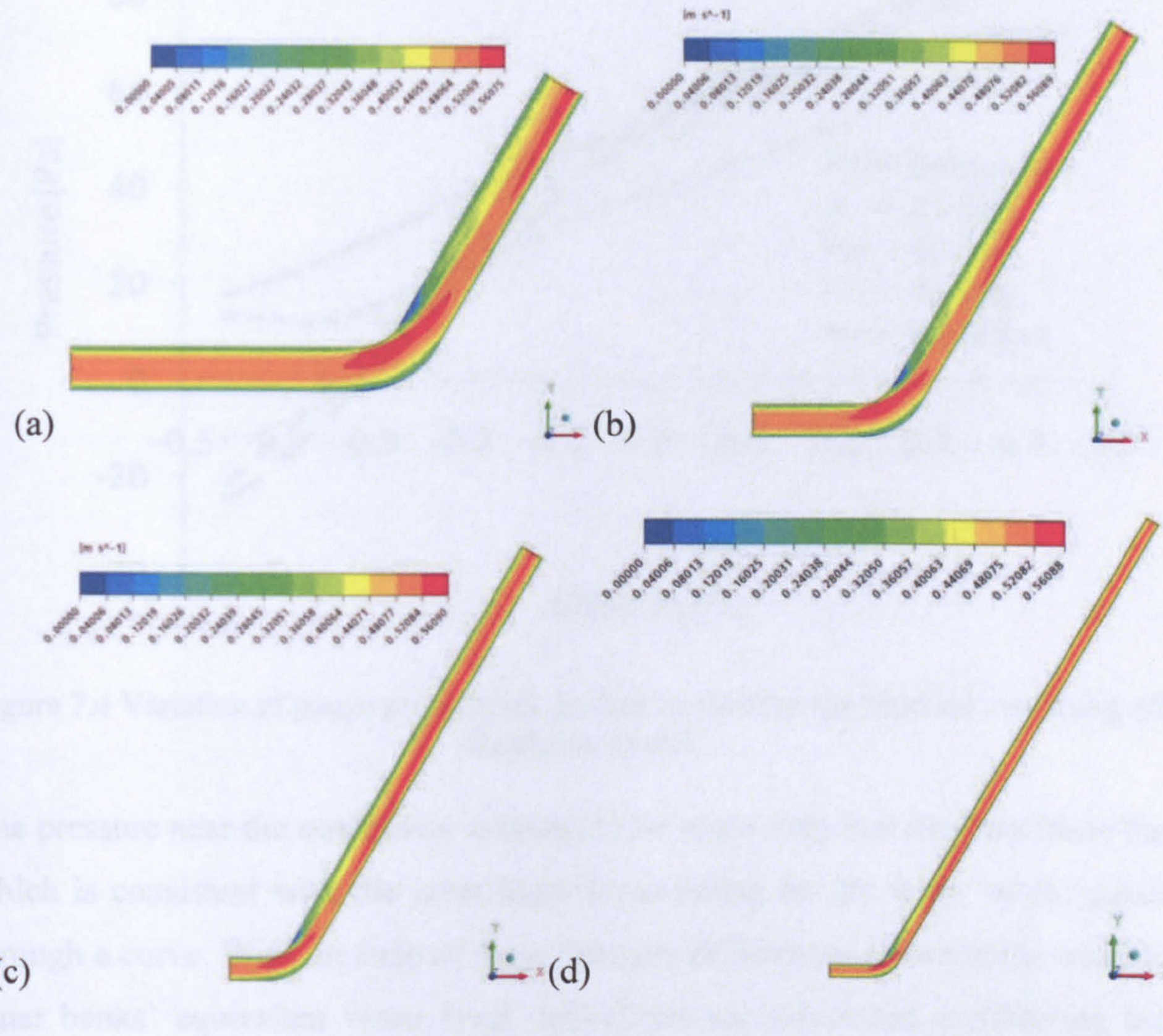

Figure 7.3 Plots of the contours of the isovels of mainstream velocity at free surface (a) Case 1 (b) Case 2 (c) Case 3 and (d) Case 4.

7.3.2 Pressure on the lid

Since the symmetry boundary condition is applied at the free surface, which acts as a lid, a local pressure analysis is carried out to check the validity of this simplification. Pressure is calculated at the free surface between the inner and outer banks at five different sections i.e. at the entrance, exit and at three intermediate sections at 15°, 30°, and 45° of the bend. Figure 7.4 shows the pressure plot at the free surface across the channel width for the simulation using SSG turbulence model.

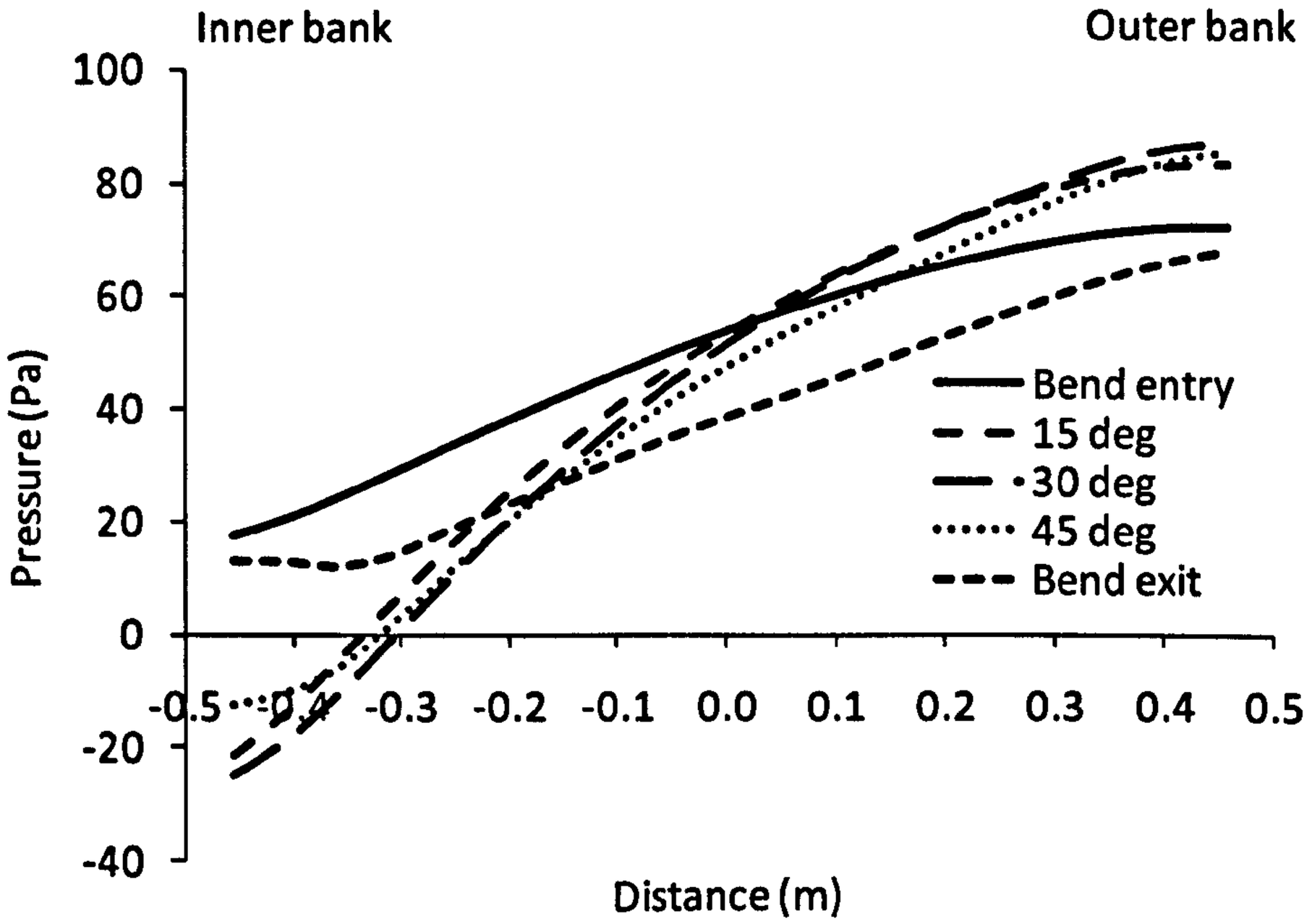

Figure 7.4 Variation of gauge pressure on the free surface for the rigid lid case using SSG turbulence model.

The pressure near the outer bank is found to be more than that near the inner bank which is consistent with the centrifugal force acting on the water while passing through a curve. With the help of these pressure differences between the outer and inner banks' equivalent water level deflections are calculated considering local hydrostatic pressure. These deflections are shown in Table 7.2. "Super-elevation outer" is calculated using the difference between the maximum pressure and mean pressures whereas the "Super-elevation total" is calculated using the difference between maximum and minimum pressures.

It is found that the maximum total deflection or super-elevation is at the 30° section and is between 10.95 mm to 11.50 mm for the three turbulence models used which corresponds to 14.60 to 15.33 percent of the depth of water in the channel.

Table 7.2 Variation of pressure and the deflection thus caused (assuming hydrostatic conversion) for the rigid lid cases.

Location	Turbulence model	Pressure (Pa)			Super-elevation (mm)		Super-elevation %	
		Min.	Max.	Average	Outer	Total	Outer	Total
Bend entry	SSG	17.27	72.39	50.27	2.26	5.64	3.02	7.51
	St. k-ε	22.91	78.32	56.29	2.25	5.67	3.00	7.55
	RNG k-ε	21.47	76.63	54.52	2.26	5.64	3.01	7.52
15°	SSG	-21.61	83.51	44.69	3.97	10.75	5.29	14.33
	St. k-ε	-15.85	88.43	50.62	3.87	10.66	5.15	14.22
	RNG k-ε	-16.26	86.11	48.85	3.81	10.47	5.08	13.96
30°	SSG	-24.81	87.65	43.17	4.55	11.50	6.06	15.33
	St. k-ε	-19.56	90.41	48.36	4.30	11.24	5.73	14.99
	RNG k-ε	-17.90	89.20	47.16	4.30	10.95	5.73	14.60
45°	SSG	-12.46	86.02	42.33	4.47	10.07	5.96	13.43
	St. k-ε	-4.98	87.45	47.28	4.11	9.45	5.48	12.60
	RNG k-ε	-0.88	87.30	46.51	4.17	9.02	5.56	12.02
Bend exit	SSG	11.85	68.43	38.47	3.06	5.78	4.08	7.71
	St. k-ε	11.49	68.84	39.54	3.00	5.86	3.99	7.82
	RNG k-ε	10.19	68.17	36.61	3.23	5.93	4.30	7.90

In wide channels for subcritical flows and assuming a hydrostatic pressure distribution, Chang (1988) has derived a basic equation for maximum super-elevation ΔZ between outside bank and inside bank as,

$$\Delta Z = \frac{U_m^2 T}{gR}$$

where, U_m is the cross sectional average velocity, T is the surface width, g is acceleration due to gravity and R is the radius of curvature of the bend. Using the equation, the maximum super-elevation that would be expected based on the flow conditions used would be,

$$\Delta Z = \frac{U_m^2 T}{gR} = \frac{0.43^2 \times 0.91}{9.81 \times 1.524} = 0.01125 \text{ m}$$

or $\Delta Z = 11.25$ mm

The maximum super-elevation found through the Chang (1988) equation therefore comes out to be 11.25 mm or 14.86 percent of the depth of flow in the channel. It can thus be concluded that the above results are comparable with Chang's result and are of the same magnitude.

7.3.3 Super-elevation in VOF case

The results of the lid cases are also compared with the super-elevations created using the VOF case. The plots of the water surface profiles created during the flow of water inside the bend using the VOF method are shown in Figure 7.5. The super-elevations thus created are given in Table 7.3. The maximum super-elevation is found at section 15 degrees inside the bend which is 10.01 mm or 13.22 percent of the depth of water in the channel. These results also lie within 10 % of the results found using the lid case.

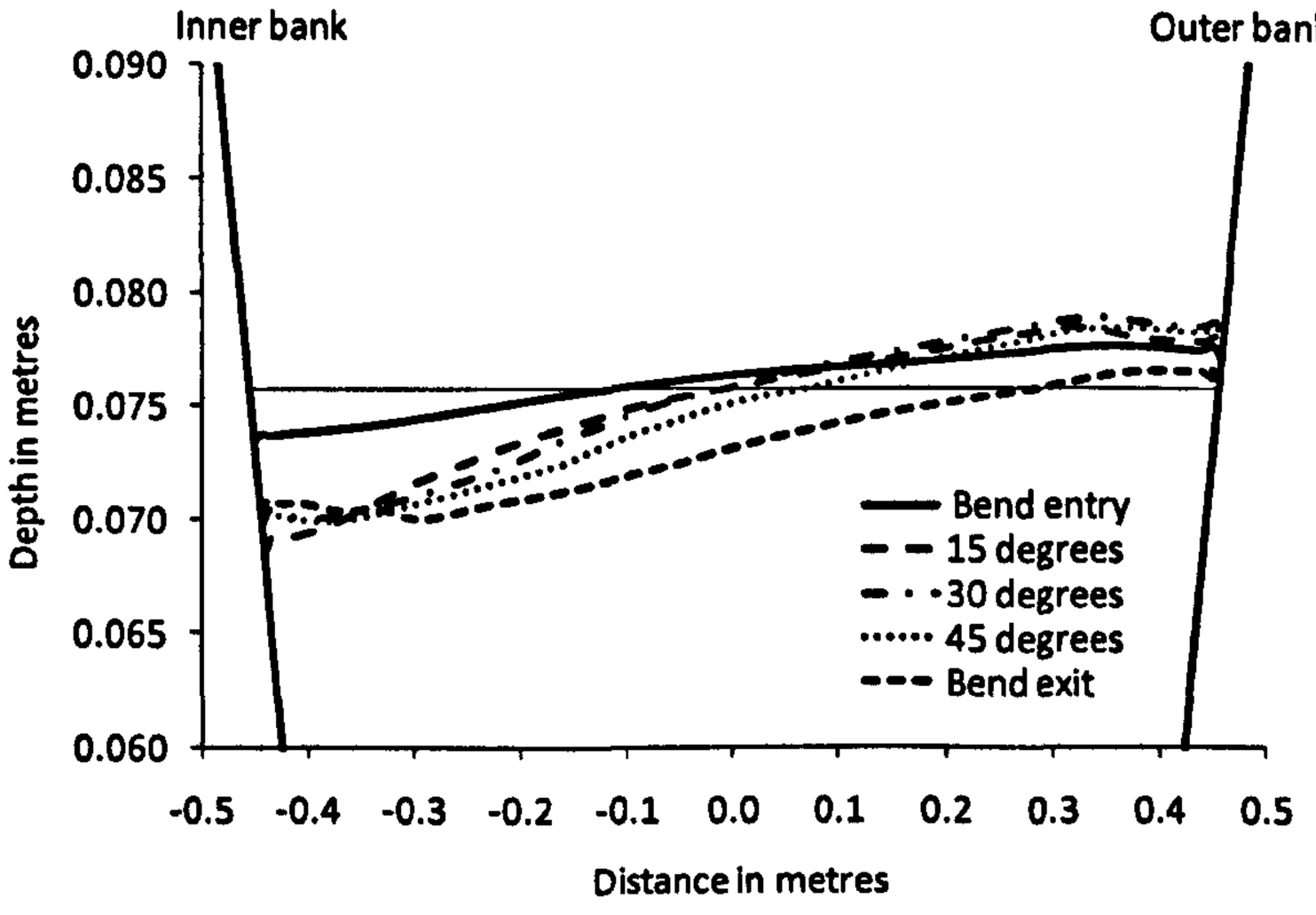

Figure 7.5 Water surface profiles in the cross section from bend entry to exit using VOF method.

Table 7.3 Super-elevations inside the bend from entry to exit using VOF method.

Section	Super-elevation	
	(mm)	% of depth of water
Bend entry	4.16	5.49
15 degrees	10.01	13.22
30 degrees	9.18	12.13
45 degrees	8.53	11.27
Bend exit	6.52	8.61

The comparison of the results between the lid cases with Chang's equation and VOF case shows that the forces produced in the water using the symmetry boundary condition at the free surface are comparable with those produced using the VOF method and also with those found during the experimental results as given by Chang.

7.4 Results and analysis

The results from the simulations and their analysis is discussed below:-

7.4.1 Isovel Pattern and main stream velocity

In ANSYS CFX the components of the velocity can only be exported with respect to the global co-ordinate axis, in this case u, v, and w aligned to the x- y- and z- axes respectively. Inside the bend the main stream velocity vectors perpendicular to any section have been named u_θ and have been calculated as,

$$u_\theta = u.cos\theta + v.sin\theta \tag{7.1}$$

where θ is the angle of the section inside the bend with respect to straight approaching section.

Isovels of non-dimensionalized mainstream velocity u_θ/U_{max} are plotted at five different sections i.e. bend entry, bend exit, and three intermediate sections of 15°, 30°, and 45° inside the bend for the rigid lid cases. Figure 7.6 shows the velocity contours at the bend entry using the SSG turbulence model. It can be clearly seen

that the flow is asymmetrical with respect to the centre line of the channel and the maximum velocity is found to be towards the inner bank of the channel. The flow keeps moving towards the inner bank and after the 30° section it is seen to be shifting towards the outer bank.

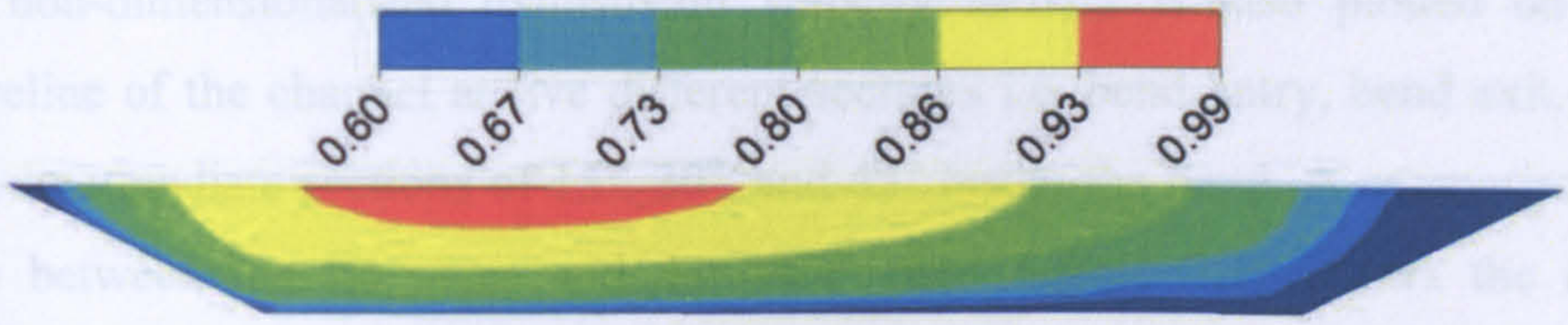

Figure 7.6 Isovels of non-dimensionalized mainstream velocity u_θ/U_{max} at bend entry.

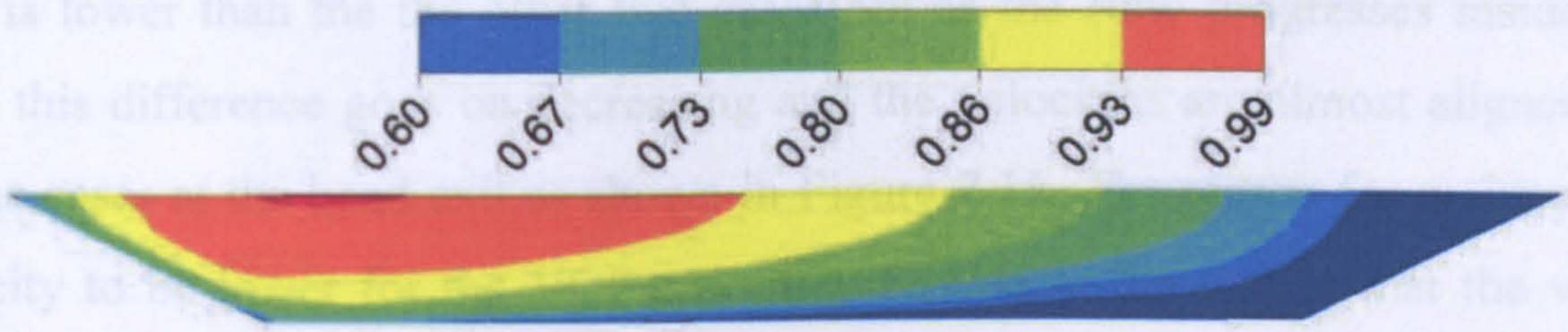

Figure 7.7 Isovels of non-dimensionalized mainstream velocity u_θ/U_{max} at a section 15 degrees inside bend.

Figure 7.8 Isovels of non-dimensionalized mainstream velocity u_θ/U_{max} at a section 30 degrees inside bend.

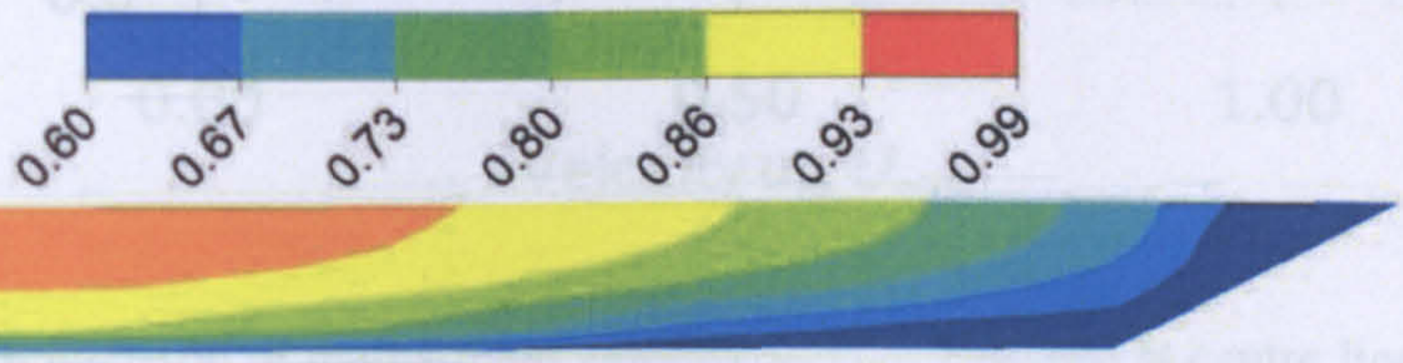

Figure 7.9 Isovels of non-dimensionalized mainstream velocity u_θ/U_{max} at a section 45 degrees inside bend.

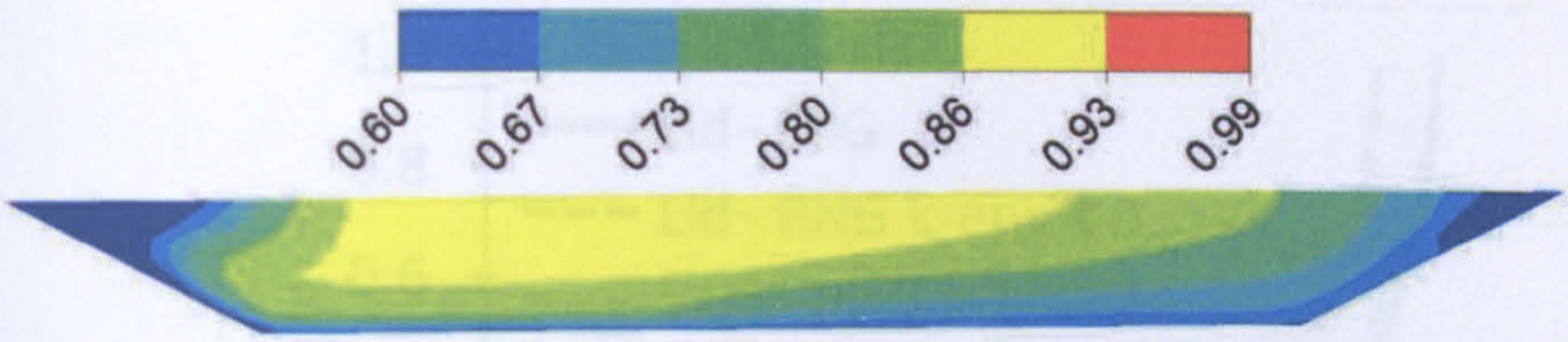

Figure 7.10 Isovels of non-dimensionalized mainstream velocity u_θ/U_{max} at bend exit.

The non-dimensionalized mainstream velocity u_θ/U_{max} is also plotted on the centreline of the channel at five different sections i.e. bend entry, bend exit, and three intermediate sections of 15°, 30°, and 45° inside the bend. A comparison is done between the lid cases and the VOF case. Figure 7.11 shows the non-dimensionalized mainstream velocity u_θ/U_{max} plotted on the centreline of the channel at the bend entry. It is found that the mainstream velocity for the VOF case is lower than the the other two cases but as the flow progresses inside the bend this difference goes on decreasing and the velocities are almost aligned for all the cases at the bend exit as shown in Figure 7.15. The reason for mainstream velocity to be lower for the VOF case may be due to the reason that the water starts to move towards the inner bank earlier as it has got the liberty to move up and down at the free surface.

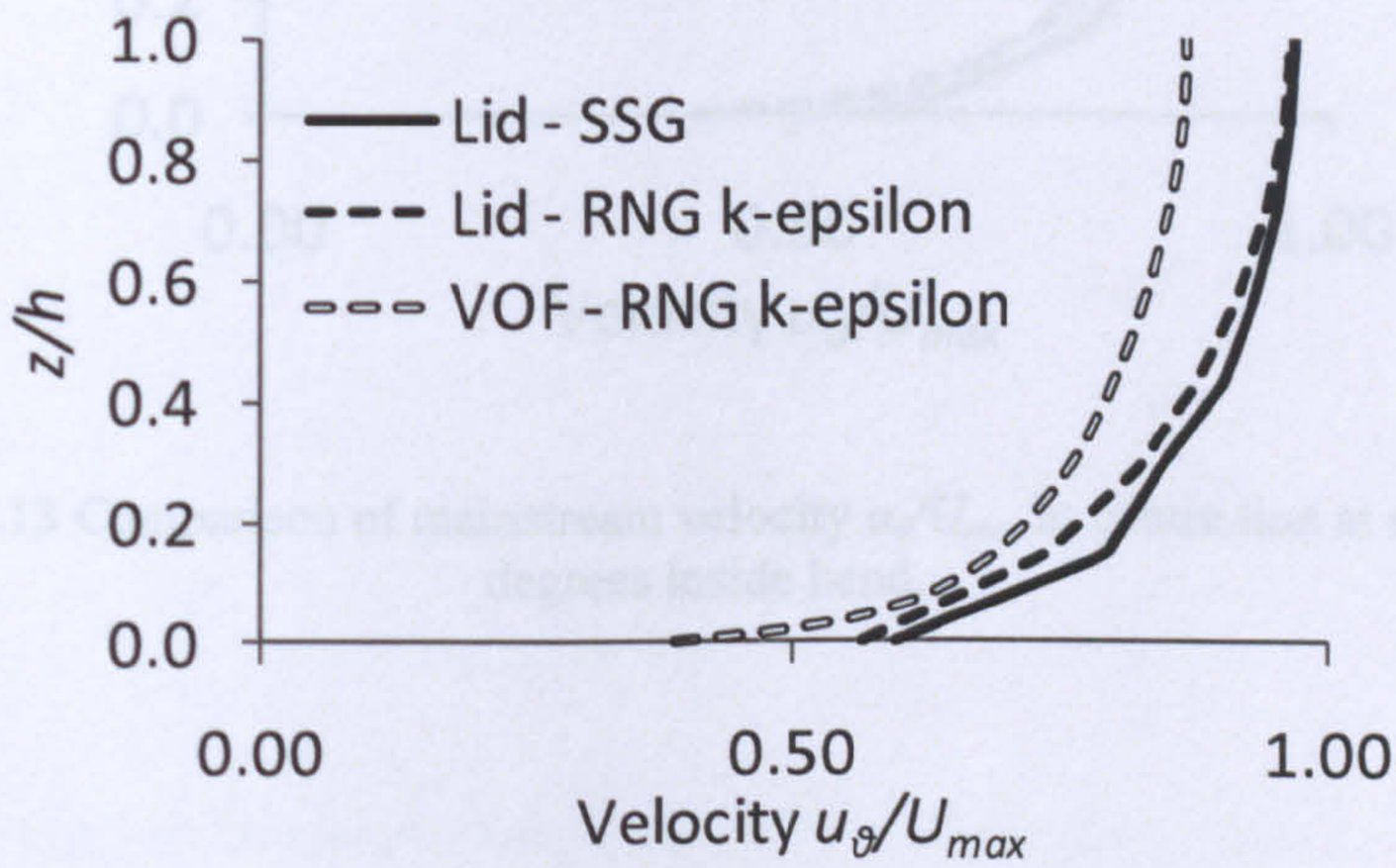

Figure 7.11 Comparison of mainstream velocity u_θ/U_{max} between at centre line at bend entry.

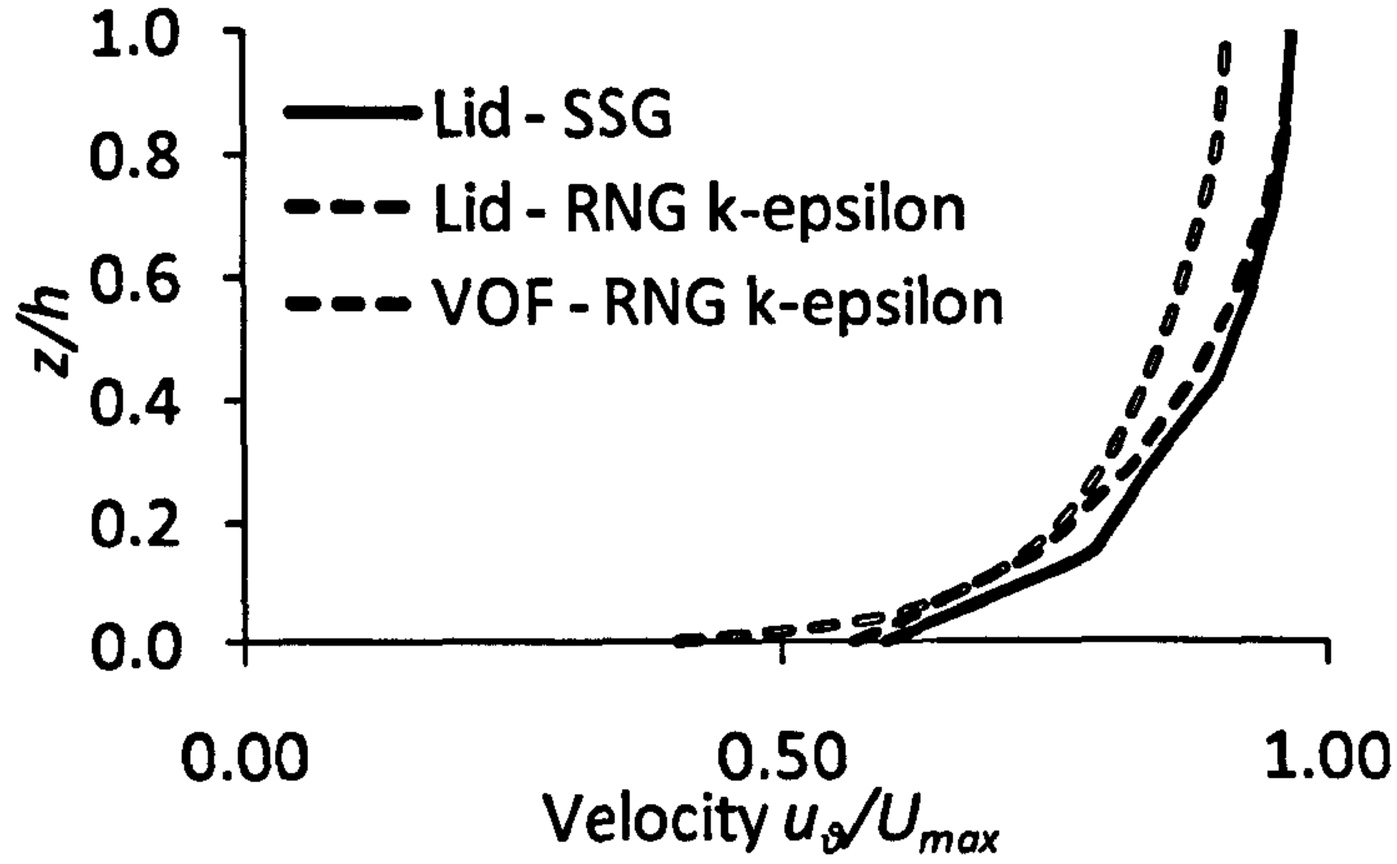

Figure 7.12 Comparison of mainstream velocity u_θ/U_{max} at centre line at section 15 degrees inside bend.

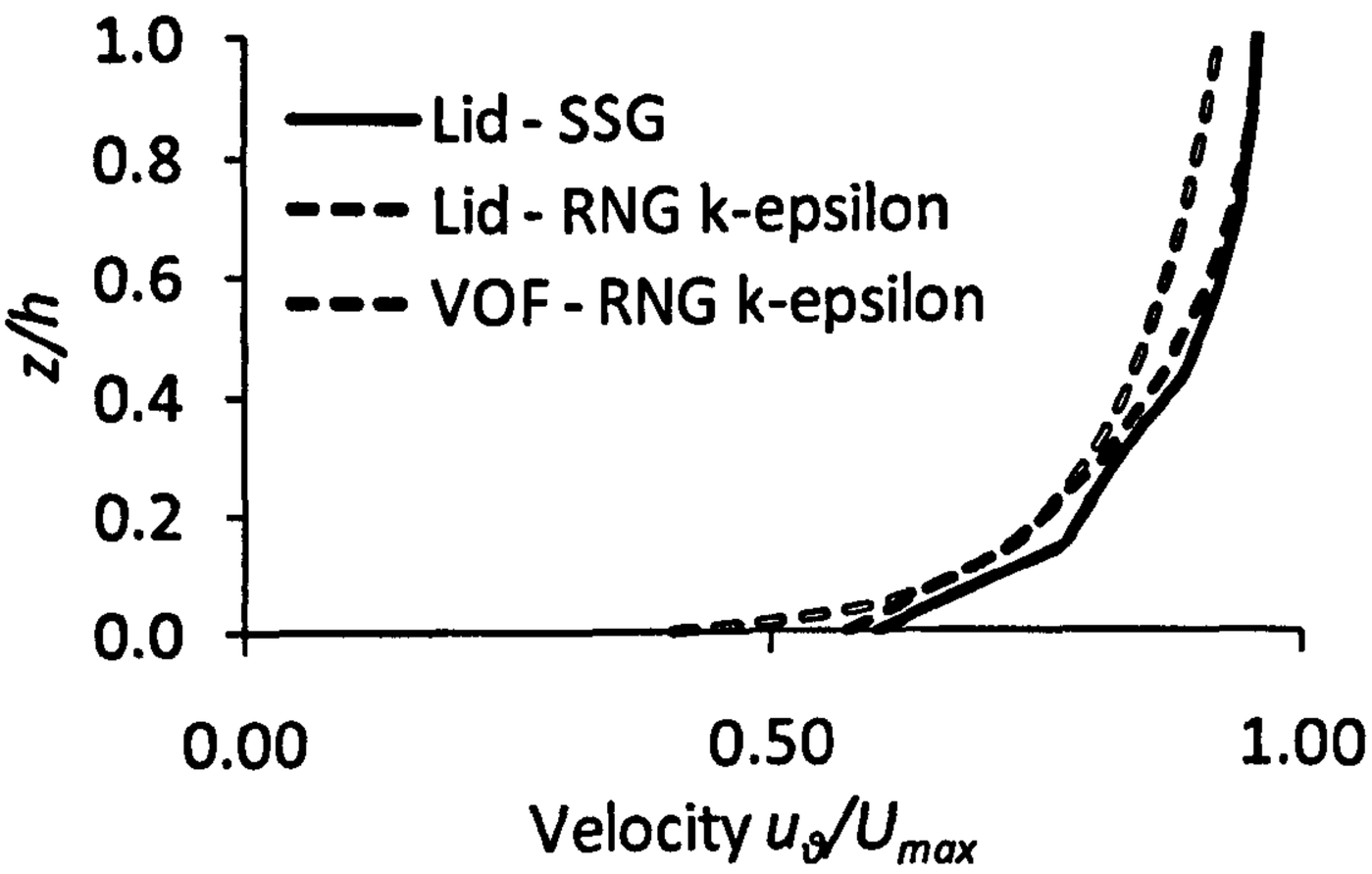

Figure 7.13 Comparison of mainstream velocity u_θ/U_{max} at centre line at section 30 degrees inside bend.

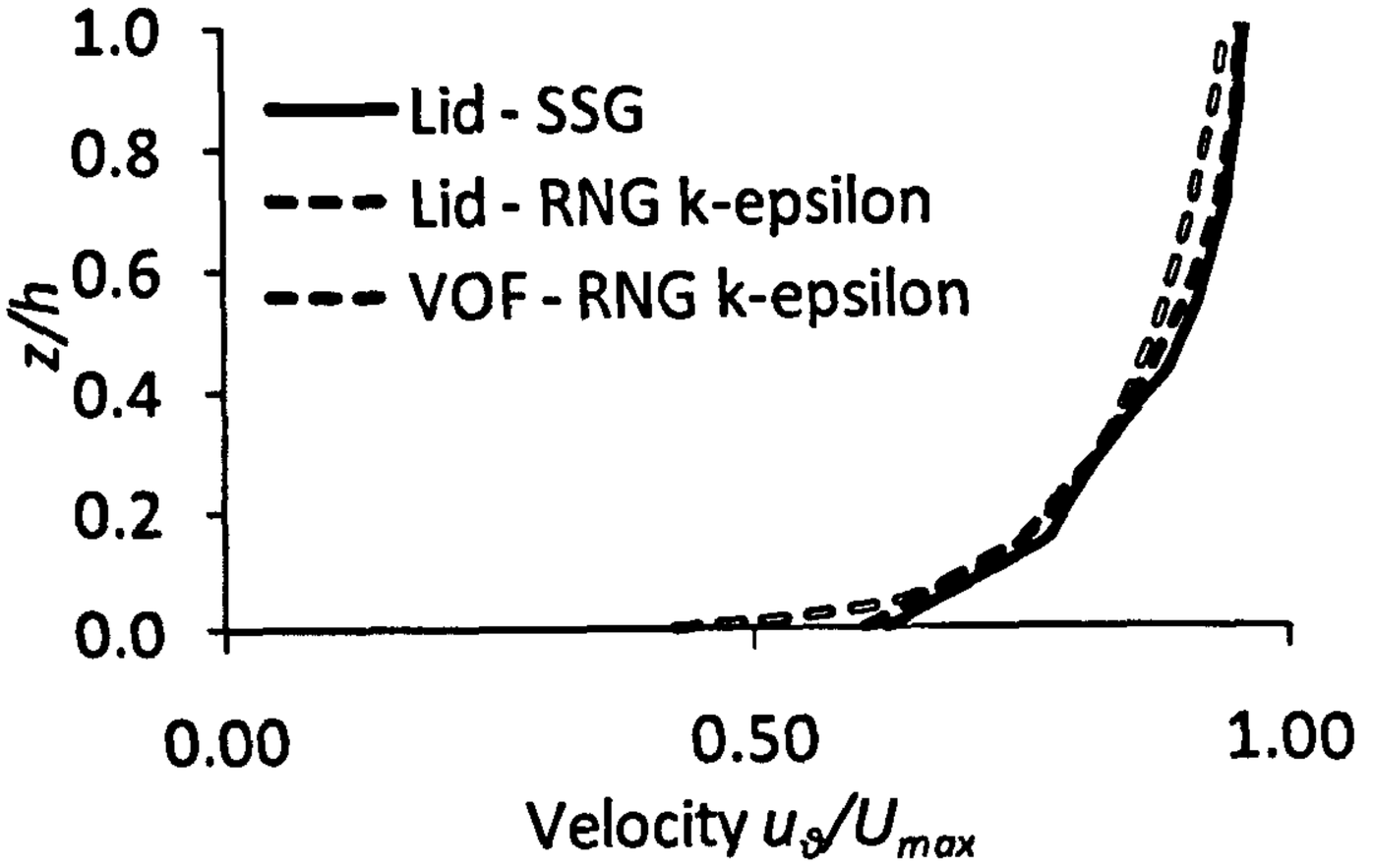

Figure 7.14 Comparison of mainstream velocity u_θ/U_{max} at centre line at section 45 degrees inside bend.

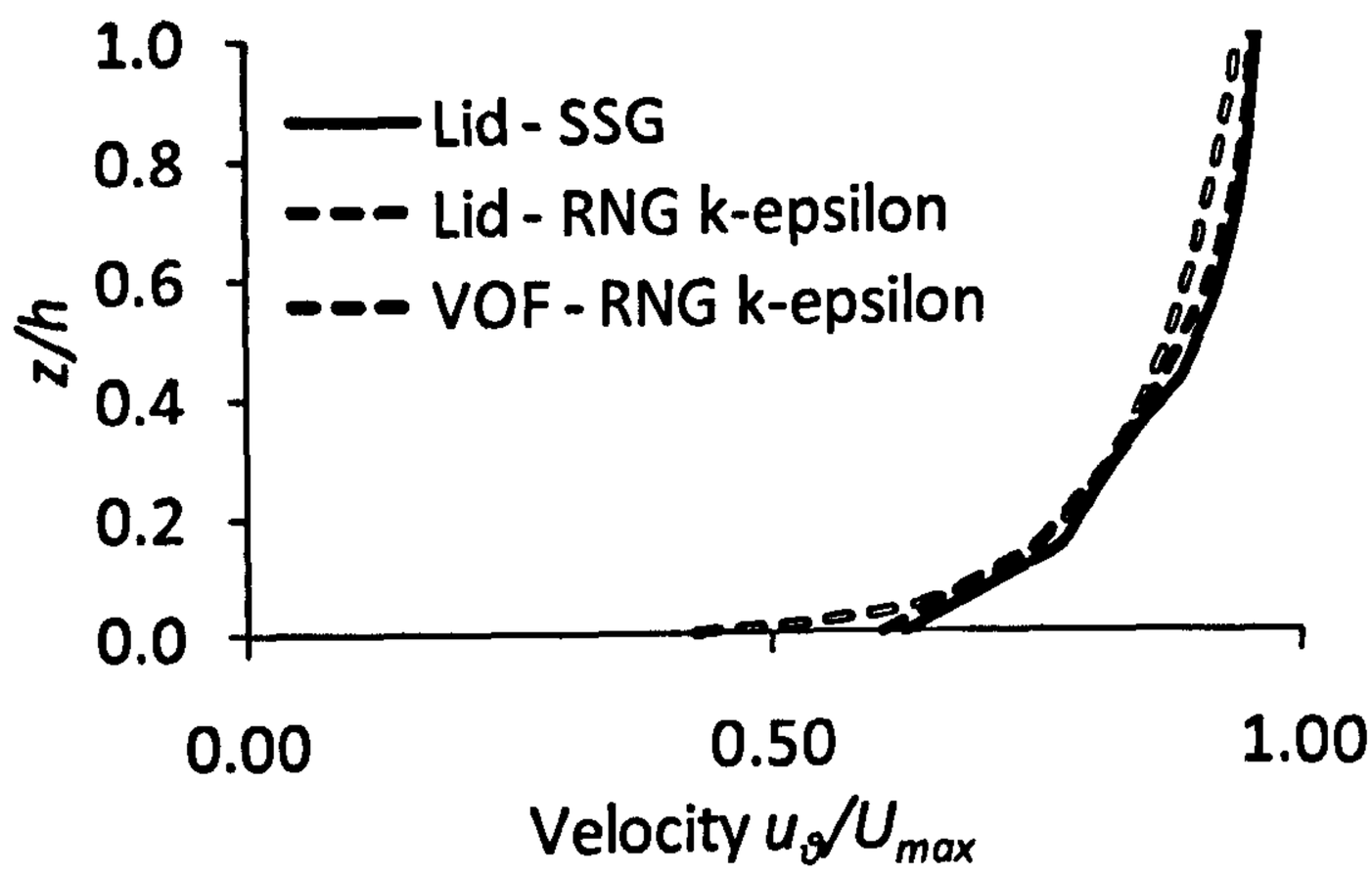

Figure 7.15 Comparison of mainstream velocity u_θ/U_{max} at centre line at bend exit.

7.4.1.1 Variation of mainstream velocity with slant angle

The non-dimensionalized mainstream velocity u_θ/U_{max} is plotted on the centreline of the channel at five different sections i.e. bend entry, bend exit, and three intermediate sections of 15°, 30°, and 45° inside the bend with three different slant angles of the sidewalls. The sidewalls are inclined at angles 30°, 45°, and 63° to the vertical. A comparison is done for the variation of mainstream velocity with

variation in slant angle. The results for the lid cases using the SSG turbulence model are shown in Figure 7.16 to Figure 7.20. The mainstream velocity is seen to be lower at the centre line for the 30° slant angle as compared to the 45° and 63° cases at the bend entry, as shown in Figure 7.16, and this might be due to the early shift of the velocity towards the inner bank with lower slant angles. This shift is seen to be ineffective for larger slant angles as no significant difference is found for the two cases with larger slant angles. This difference between the mainstream velocities at the centre line is found to be decreasing as the flow progresses inside the bend velocities are seen to be almost aligned with each other at the bend exit as shown in Figure 7.20.

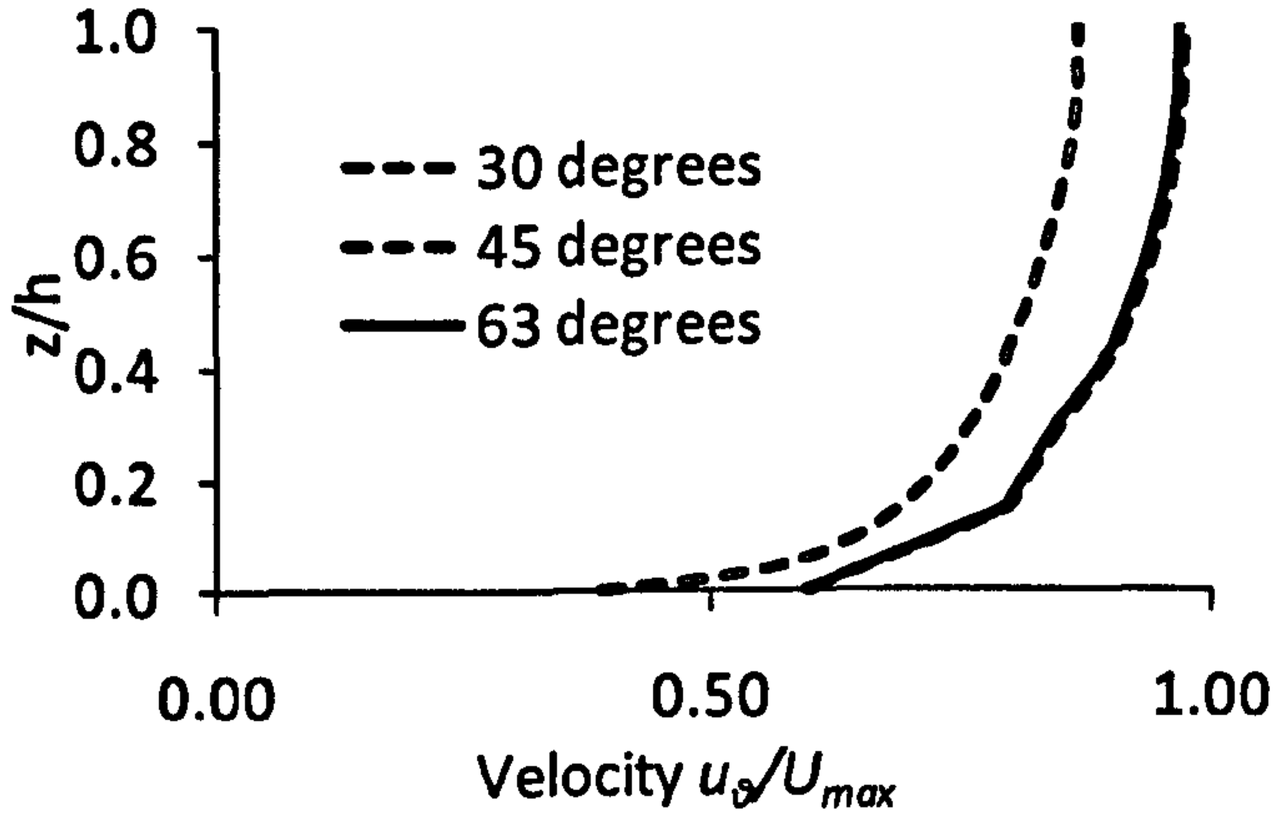

Figure 7.16 Comparison of mainstream velocity u_θ/U_{max} at centre line with slant angle at bend entry.

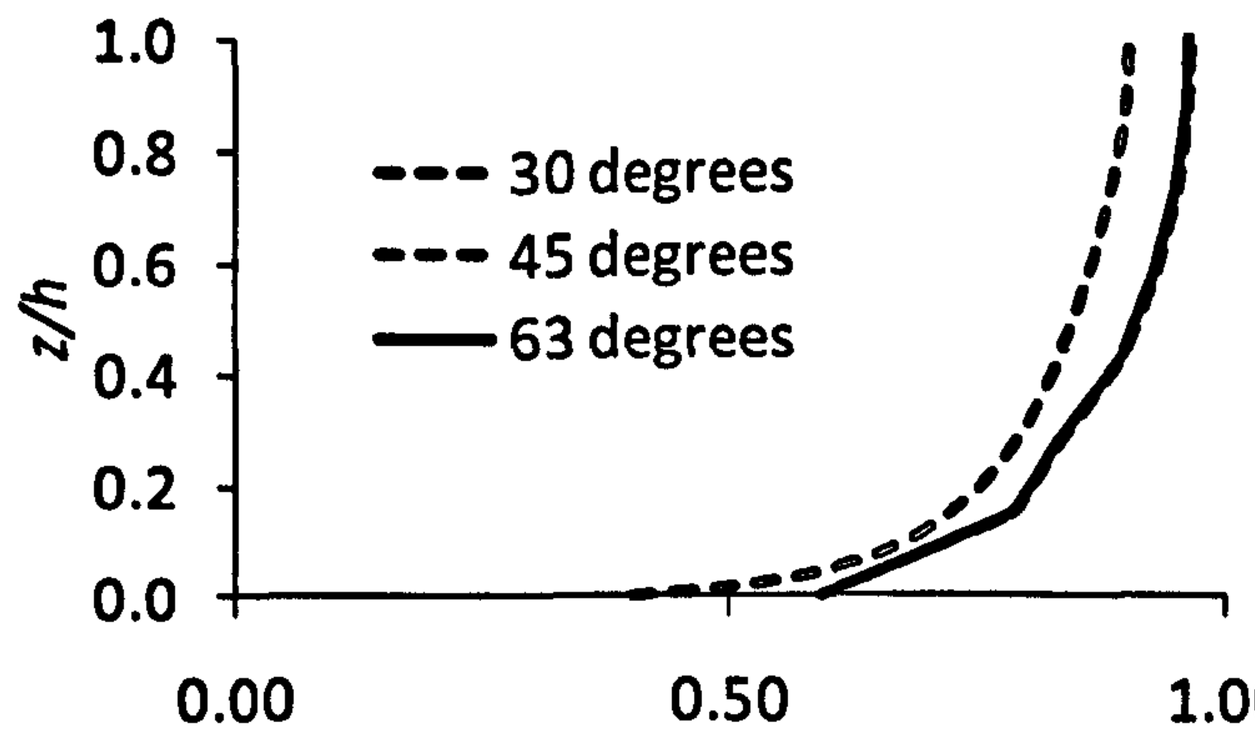

Figure 7.17 Comparison of mainstream velocity u_θ/U_{max} at centre line with slant angle at a section 15 degrees inside bend.

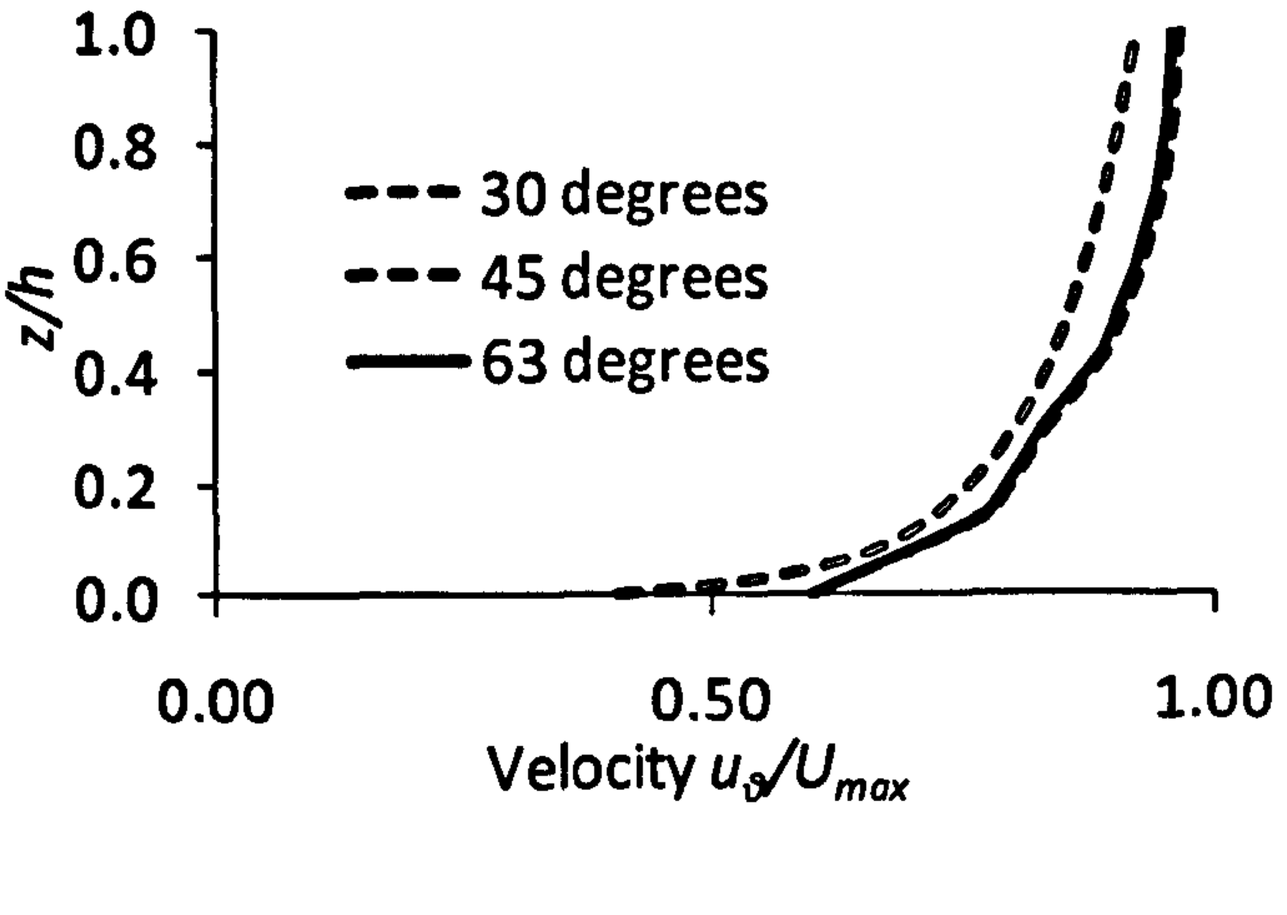

Figure 7.18 Comparison of mainstream velocity u_θ/U_{max} at centre line with slant angle at a section 30 degrees inside bend.

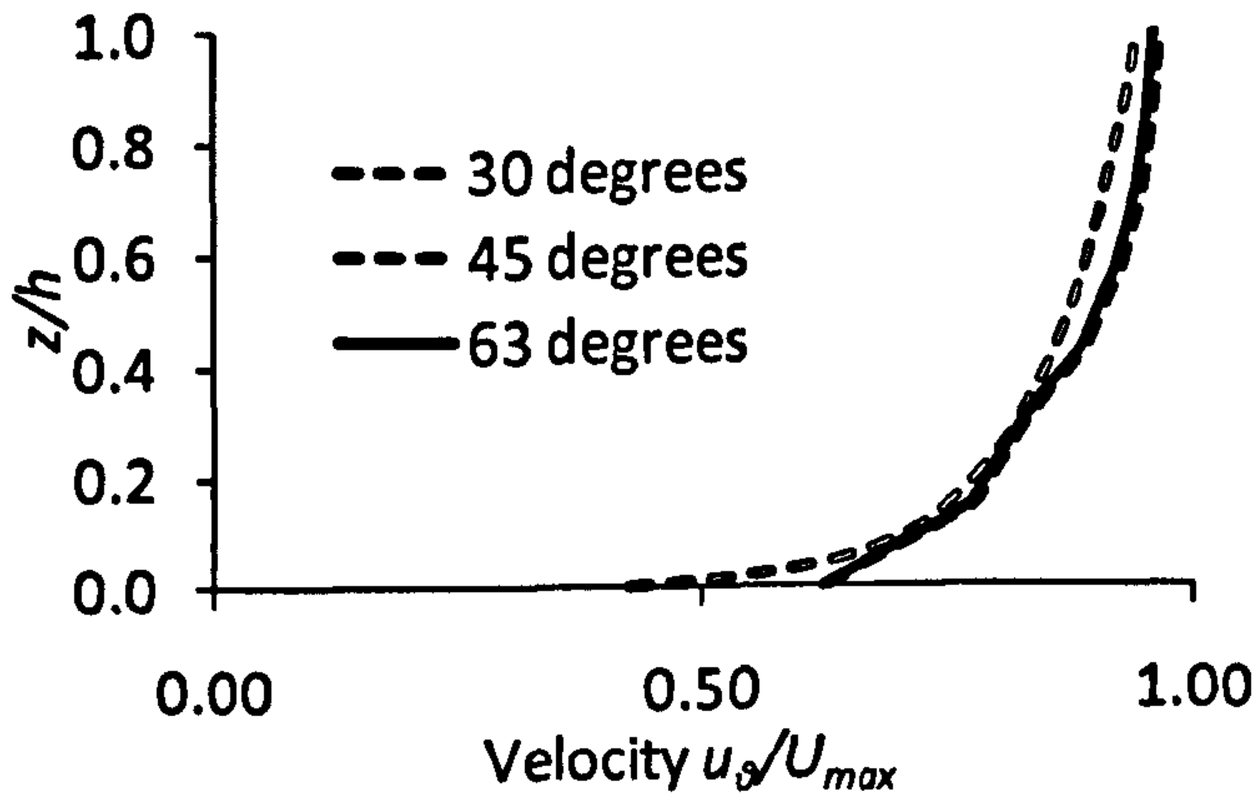

Figure 7.19 Comparison of mainstream velocity u_θ/U_{max} at centre line with slant angle at a section 45 degrees inside bend.

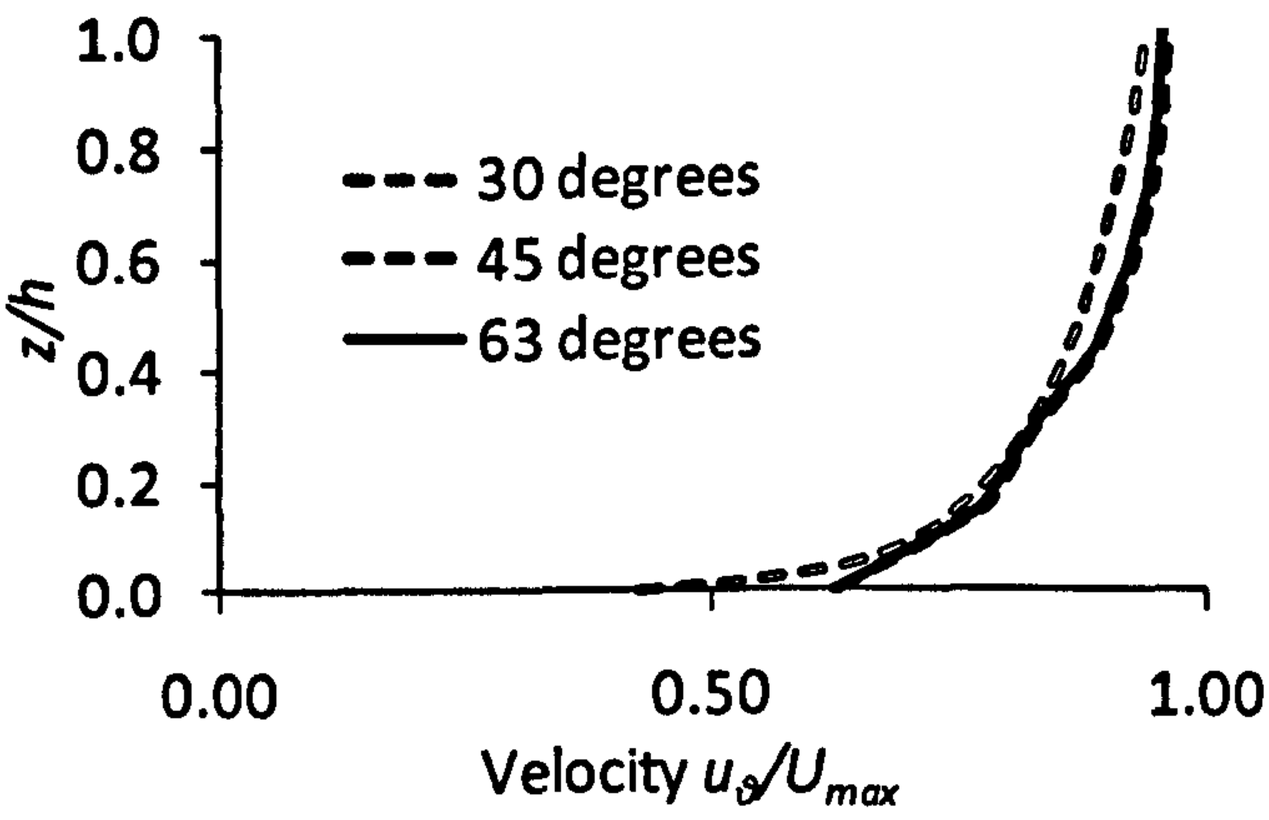

Figure 7.20 Comparison of mainstream velocity u_θ/U_{max} at centre line with slant angle at bend exit.

7.4.2 Secondary currents

As mentioned earlier, in ANSYS CFX the components of the velocity can only be exported with respect to the global co-ordinate axis in this case being u, v, and w being aligned to x- y- and z- axes respectively. Inside the bend the velocity vectors tangential to any section have been named v_θ and have been calculated as,

$$v_\theta = v.cos\theta - u.sin \tag{7.2}$$

where, θ is the angle of the section inside the bend with respect to straight approaching section.

Figure 7.21 shows the secondary currents at the bend entry. It is found that the velocity vectors tangential to the section are all moving from the outer bank towards the inner bank. This is due to the fact that as the flow anticipates a bend the maximum velocity shifts towards the inner bank and the momentum of flow is found to be towards the inner bank. Figure 7.22 shows the secondary currents or velocity vectors tangential to the section inside the bend at 15°. Here small circulations are visible throughout the entire section due to the centrifugal effects. The secondary currents are found to be moving towards the outer bank near the free surface due to the centrifugal forces acting on the flow due to the bend and are found to be moving towards the inner bank near the bed due to the hydrostatic pressure being exerted on the outer bank which pushes the flow downwards and ultimately starts a full recirculation inside the whole section of the channel. The strength of the velocity vectors moving from inner bank towards the outer bank near the free surface is found to be increasing as compared to the vectors moving in the opposite direction near the bed as the flow flow progresses inside the bend as shown in Figure 7.23 to Figure 7.25. This is due to the shifting of the momentum from the inner bank towards the outer bank as the flow leaves a bend. This asymmetry is found to continue for a long distance after the flow leaves a bend which has been reported in the literature.

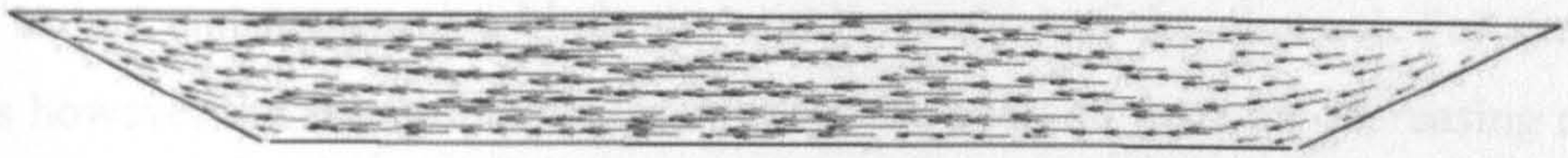

Figure 7.21 Secondary currents at bend entry using lid approach and SSG turbulence model (left side being inner bank).

Figure 7.22 Secondary currents at section 15 degrees inside the bend using lid approach and SSG turbulence model (left side being inner bank).

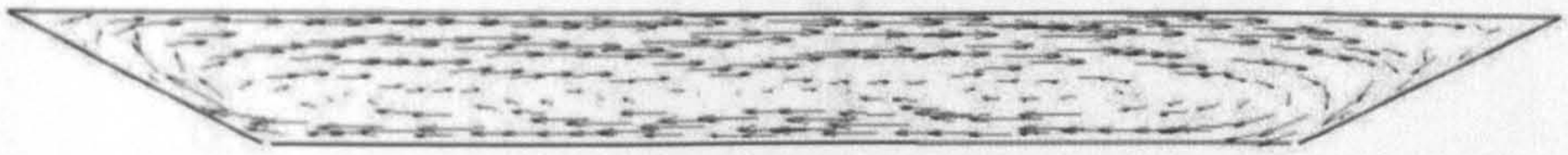

Figure 7.23 Secondary currents at section 30 degrees inside the bend using lid approach and SSG turbulence model (left side being inner bank).

Figure 7.24 Secondary currents at section 30 degrees inside the bend using lid approach and SSG turbulence model (left side being inner bank).

Figure 7.25 Secondary currents at bend exit using lid approach and SSG turbulence model (left side being inner bank).

The non-dimensionalized cross stream velocity v_θ/U_m is plotted on the centreline of the channel at five different sections i.e. bend entry, bend exit, and three intermediate sections of 15°, 30°, and 45° inside the bend. A comparison is also done between the lid cases and the VOF case. The non-dimensionalized cross stream velocity v_θ/U_m is positive flowing from outer bank towards inner bank and negative flowing in the opposite direction. Figure 7.26 shows the non-dimensionalized cross stream velocity v_θ/U_m plotted on the centreline of the channel at the bend entry. It is found to be all positive which means the velocity vectors are moving from the outer bank towards the inner bank. For the VOF case the strength of the vectors is found to be stronger both near the free surface as

well as bed and decreases a bit in the middle portion of the channel. For the lid cases however the strength is maximum near the bed and goes on decreasing near the free surface. This might be due to the symmetry-wall boundary condition being applied at the free surface for the lid cases.

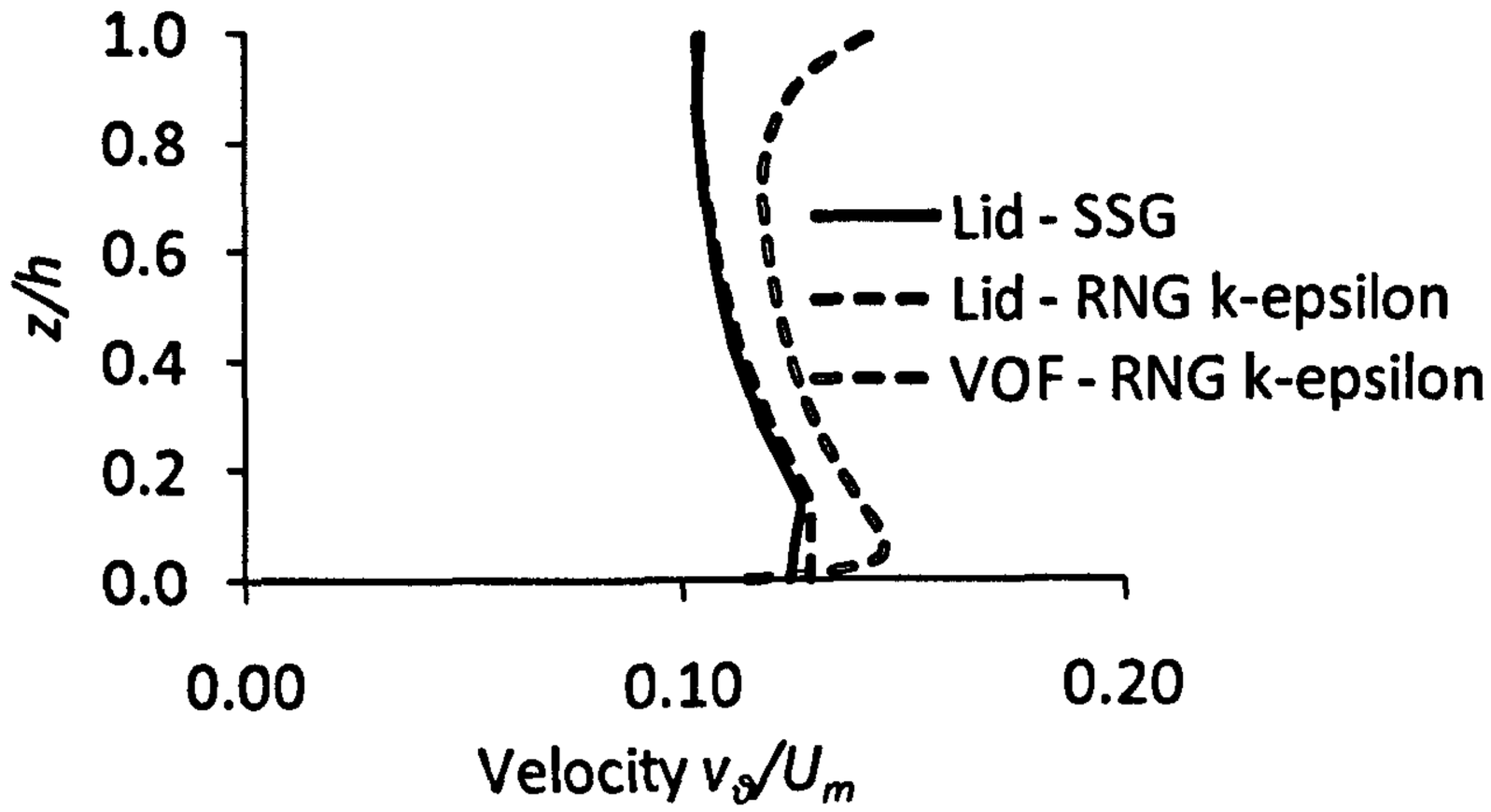

Figure 7.26 Comparison of cross stream velocity vθ/Um at centre line at bend entry.

Figure 7.27 shows the non-dimensionalized cross stream velocity v_θ/U_m plotted on the centreline of the channel at a section 15° inside the bend. The velocity is found to be positive near the bed which means flow from outer bank to inner bank. Whereas is found to be negative in the upper portion meaning flow from inner bank to outer bank. The flow is seen to be stronger near the bed as compared to the free surface. The velocity is also found to be changing sign nearly in the middle of the section.

As the flow progresses inside the bend a stronger current is visible near the free surface as compared to near the bed as shown in Figure 7.28 to Figure 7.30. The velocity is also found to change sign very early near the bed showing strong momentum towards the outer bank as the flow approaches the end of the bend.

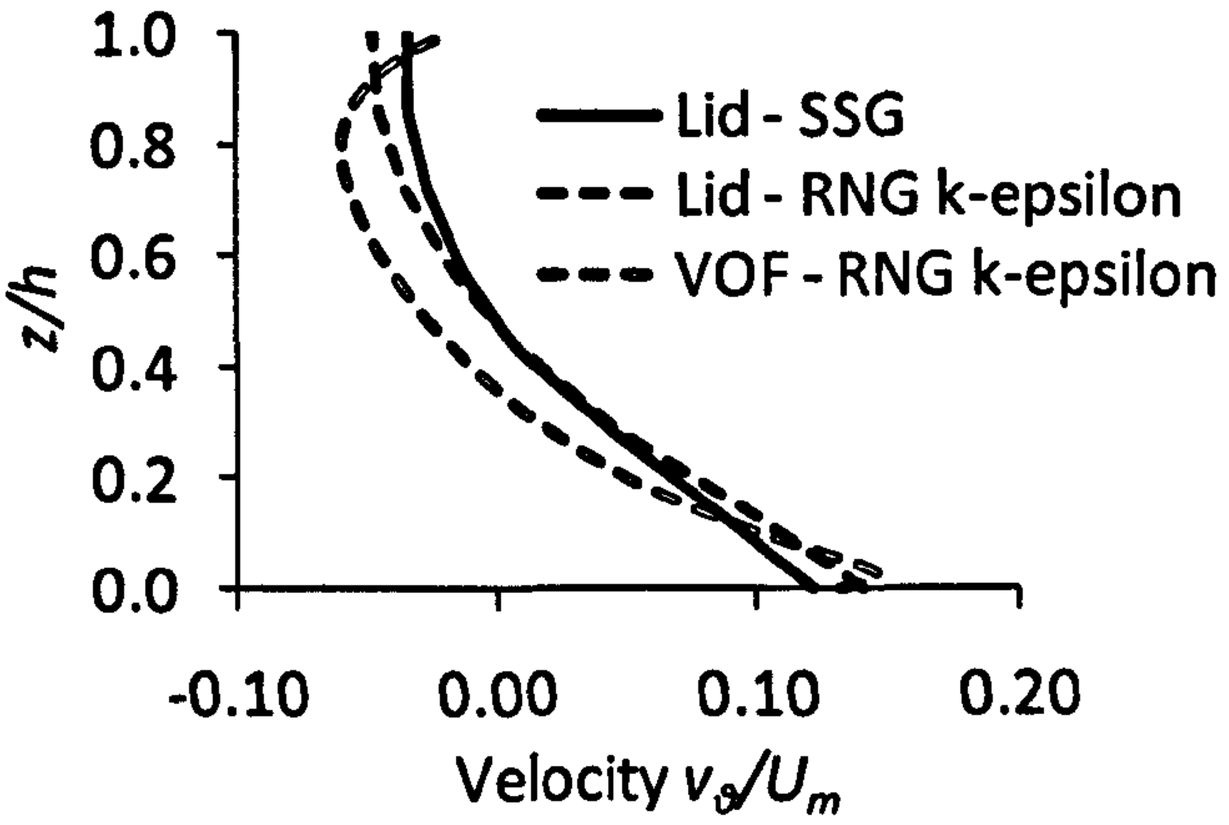

Figure 7.27 Comparison of cross stream velocity vθ/Um at centre line at section 15 degrees inside bend.

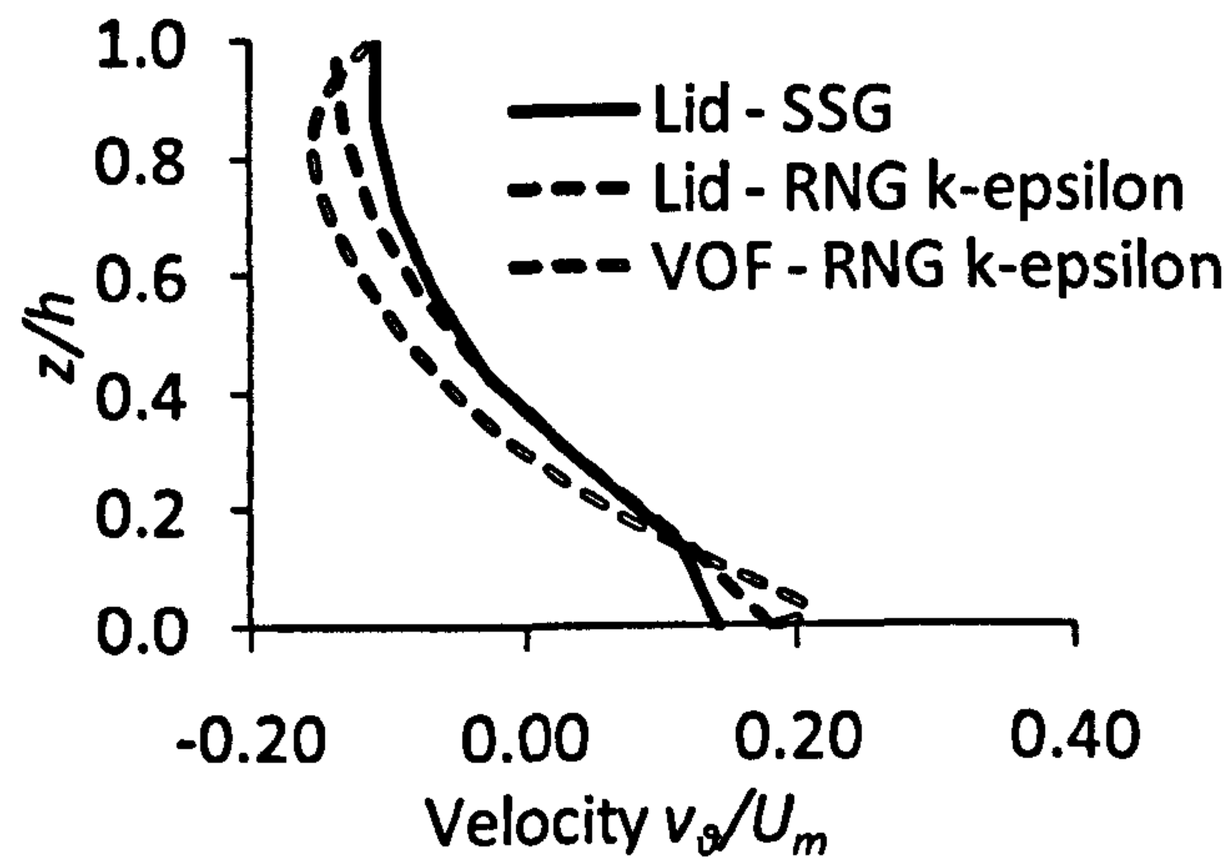

Figure 7.28 Comparison of cross-stream velocity v_θ/U_m at centre line at section 30 degrees inside bend.

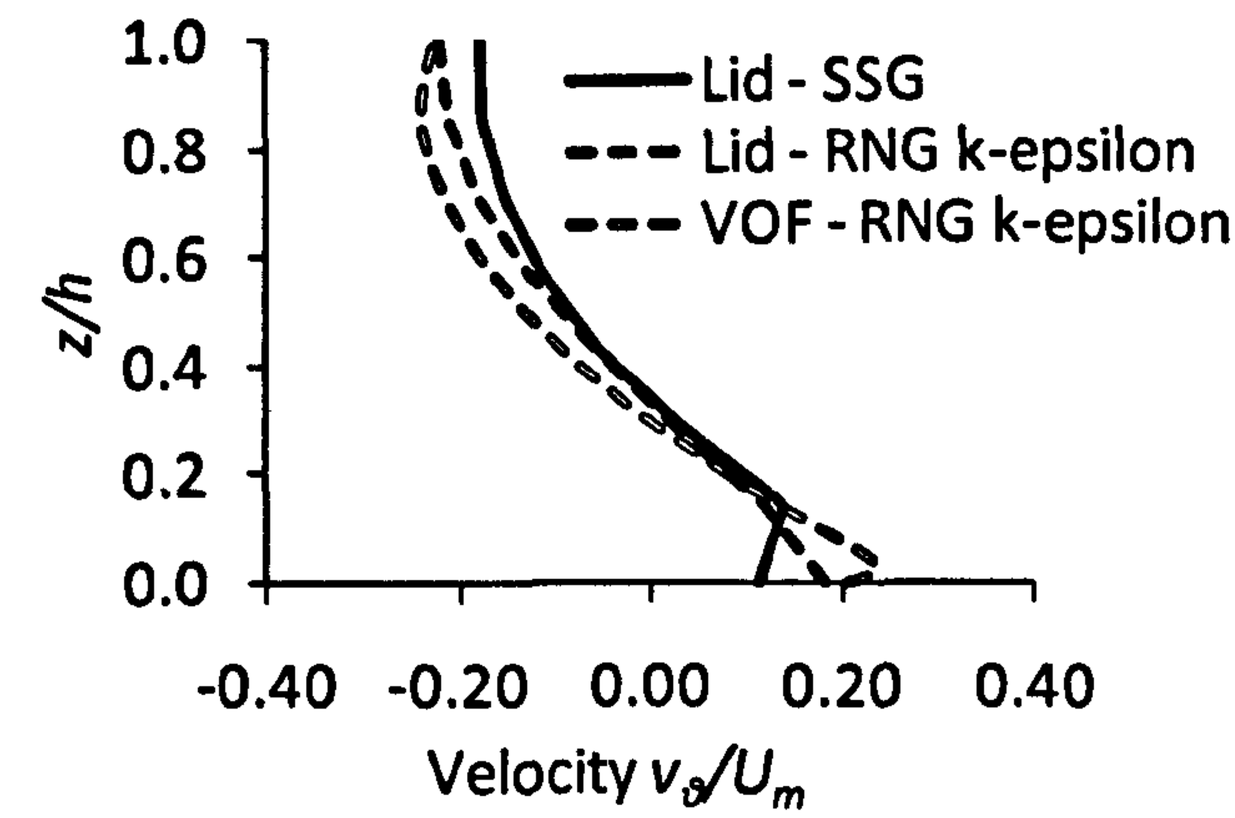

Figure 7.29 Comparison of cross-stream velocity v_θ/U_m at centre line at section 45 degrees inside bend.

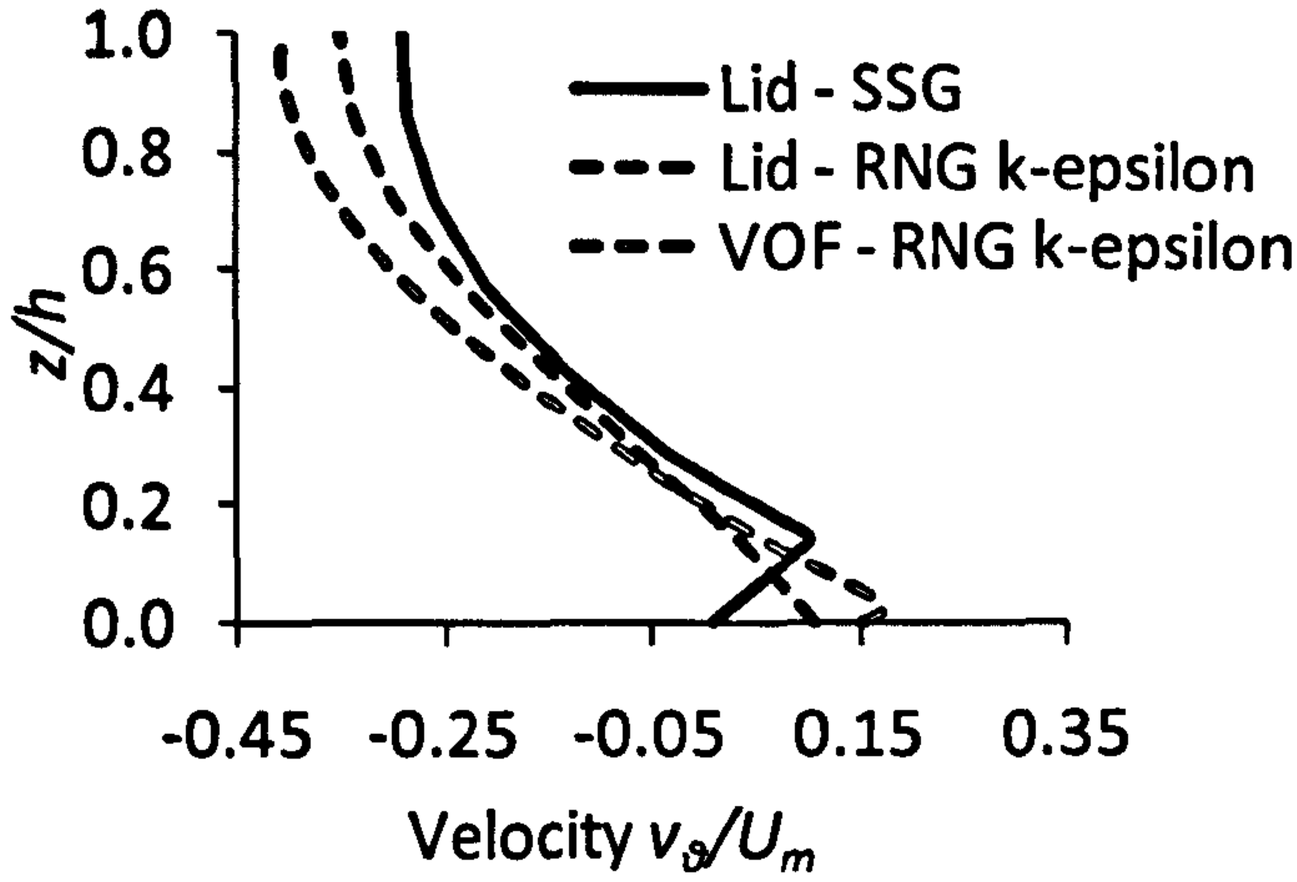

Figure 7.30 Comparison of cross stream velocity v_θ/U_m at centre line at bend exit.

7.4.2.1 Variation of secondary currents with slant angle

The non-dimensionalized cross stream velocity v_θ/U_m is plotted on the centreline of the channel at five different sections i.e. bend entry, bend exit, and three intermediate sections of 15°, 30°, and 45° inside the bend with three different slant angles of the sidewalls using the lid approach and SSG turbulence model. The sidewalls are inclined at angles 30°, 45°, and 63° to the vertical. A comparison is done for the variation of cross stream velocity with variation in slant angle.

The cross stream velocity is seen to be lower at the centre line for the 63° slant angle as compared to the 30° and 45° cases at the bend entry as shown in Figure 7.31 and this might be due to strong recirculations inside the bend with large slant angles. This difference is seen to be non-significant as the flow progresses inside the bend and the velocities are seen to be almost aligned with each other at the other sections as shown in Figure 7.32 to Figure 7.35.

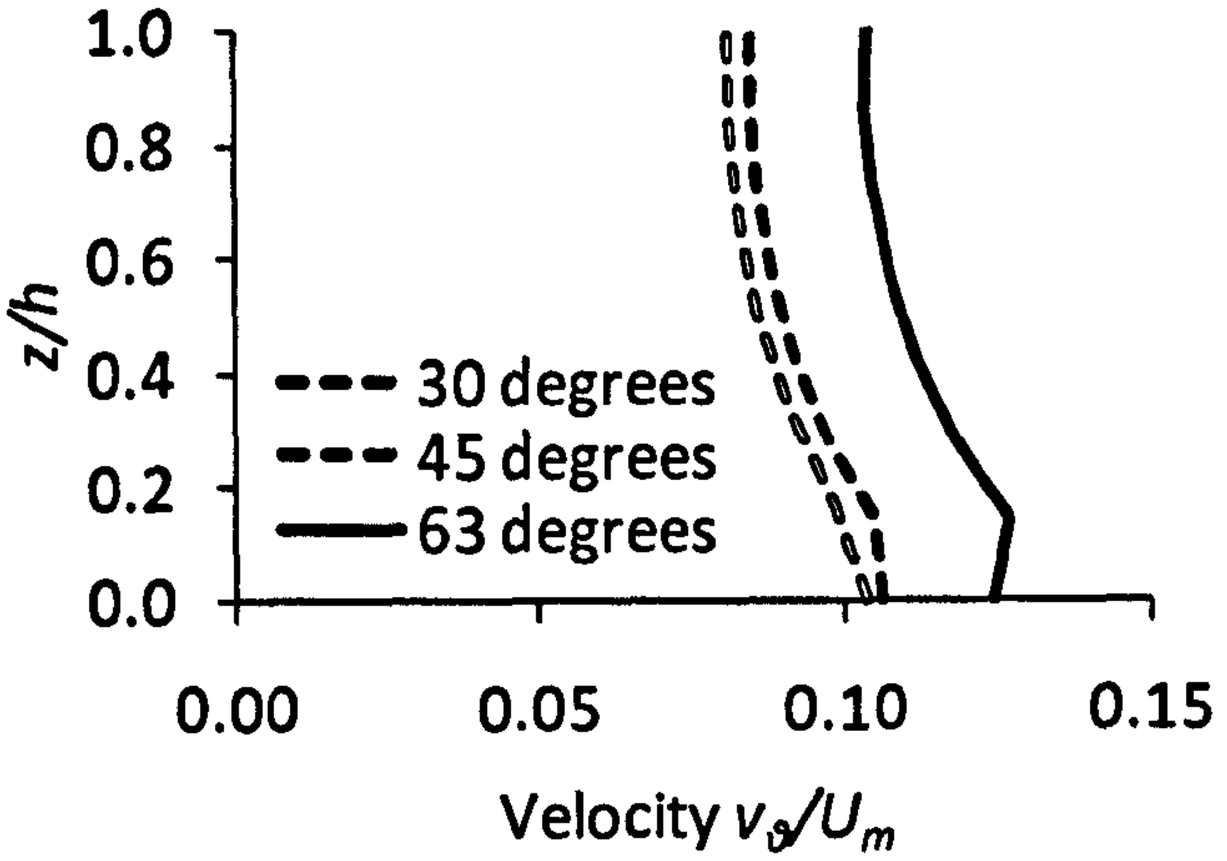

Figure 7.31 Comparison of cross stream velocity v_θ/U_m at centre line at bend entry.

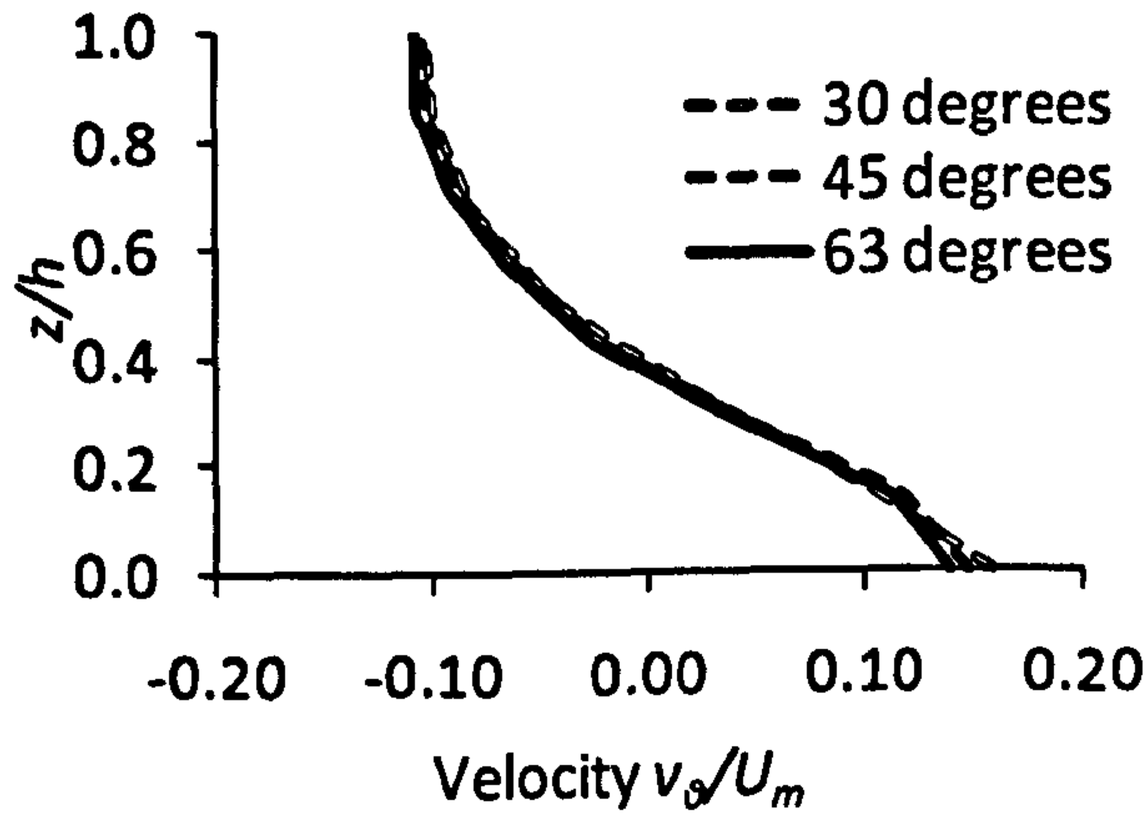

Figure 7.32 Comparison of cross stream velocity v_θ/U_m at centre line at a section 15 degrees inside bend.

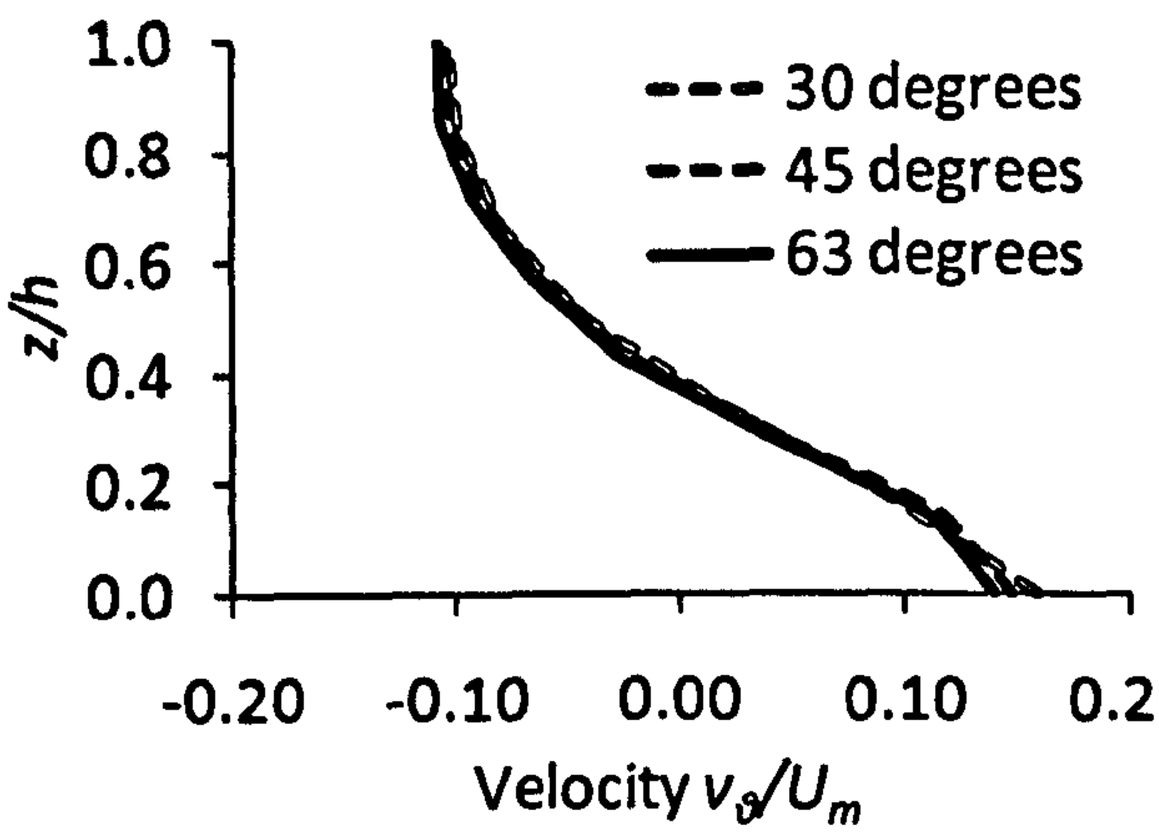

Figure 7.33 Comparison of cross stream velocity v_θ/U_m at centre line at a section 30 degrees inside bend.

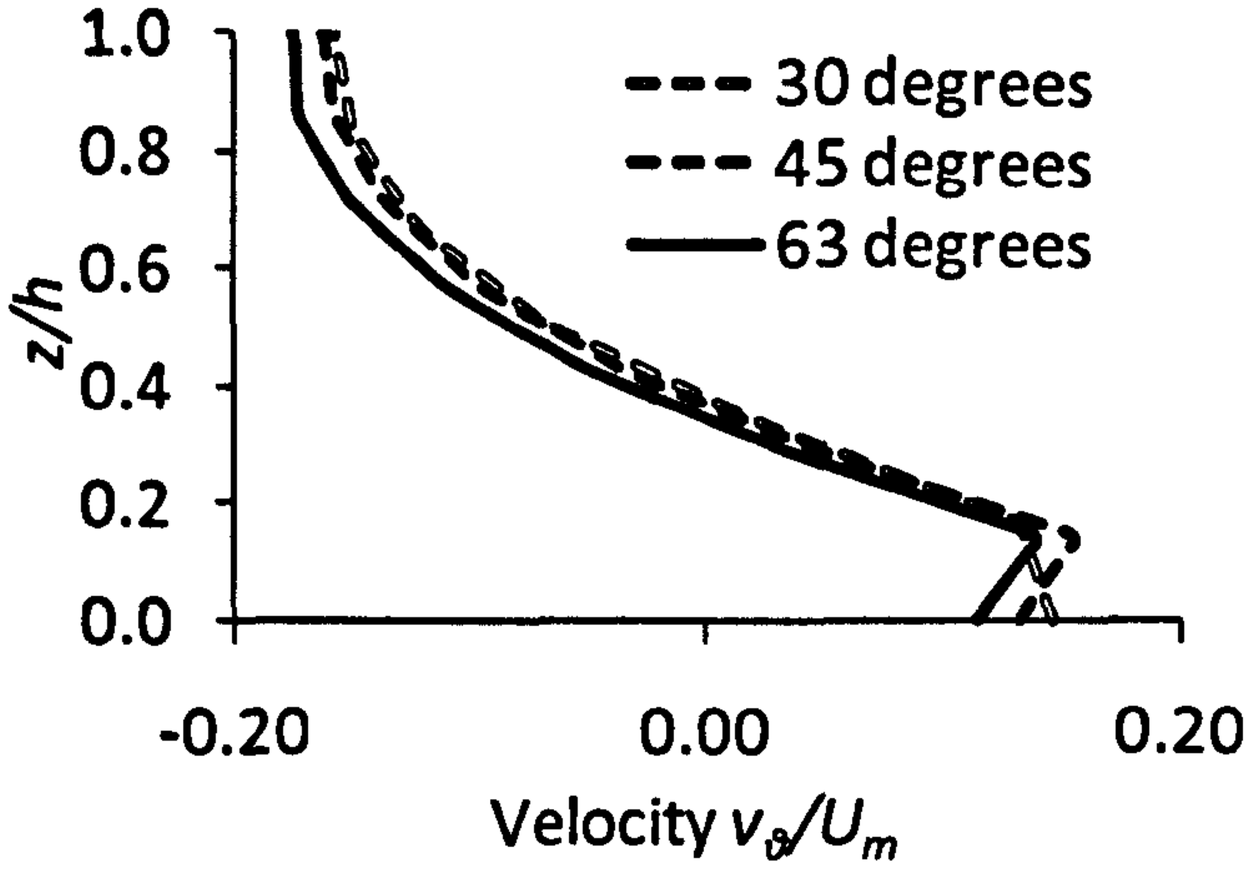

Figure 7.34 Comparison of cross stream velocity v_θ/U_m at centre line at a section 45 degrees inside bend.

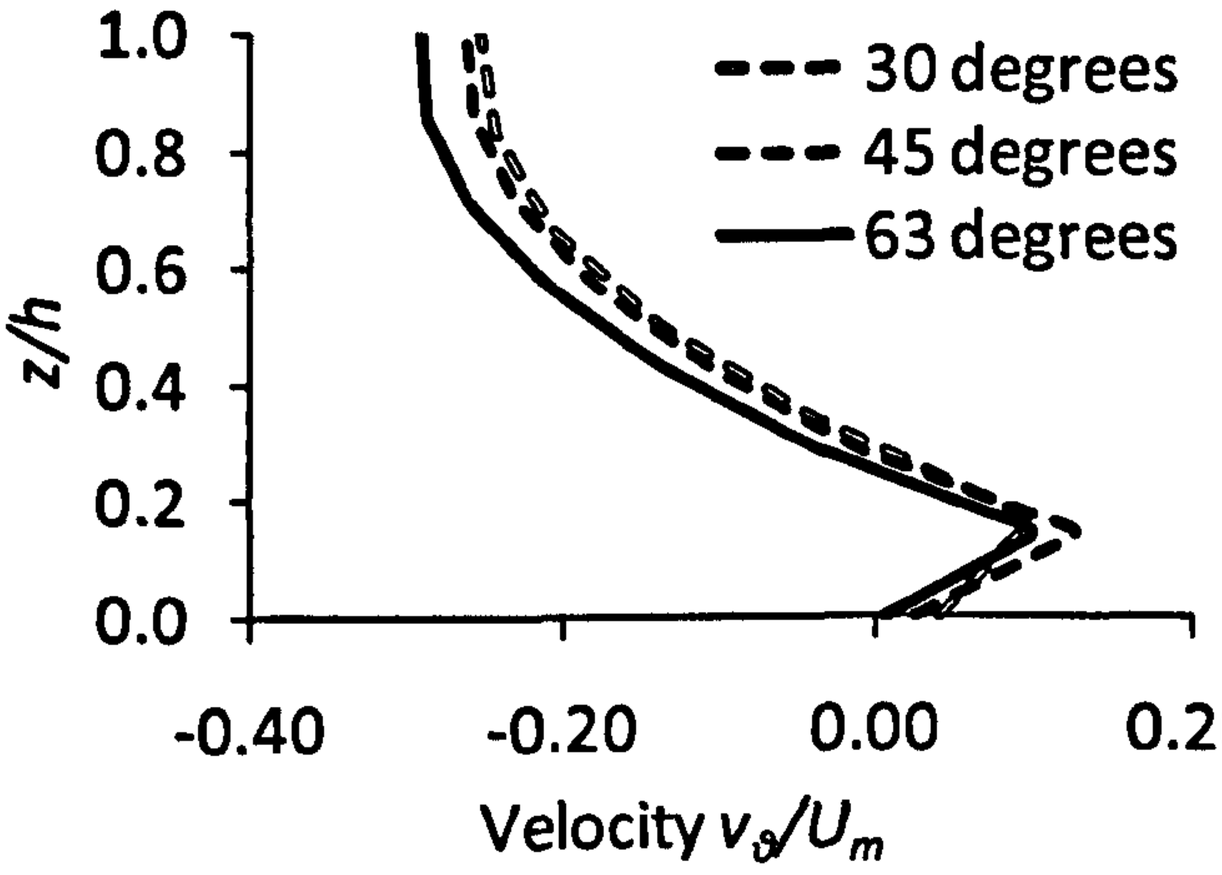

Figure 7.35 Comparison of cross stream velocity v_θ/U_m at centre line at bend exit.

7.4.3 Variation of local boundary shear inside a bend

Boundary shear stress in curved channels is usually analyzed in terms of its (i) tangential or longitudinal and (ii) radial or transverse components (Chang, 1988). An analysis on the variation of shear on the wetted perimeter is therefore carried out on the longitudinal (mainstream flow) as well as transverse (cross-stream flow) directions. Three simulations are taken into account, two with the lid using SSG and RNG k-ε turbulence models and one using the VOF method with RNG k-ε turbulence model, all having a slant angle of 63°. A comparison is therefore possible between the results of the turbulence models used and also between the lid and VOF approaches at the free surface.

Figure 7.36 shows the variation of non-dimensionalised local wall shear $\tau_o/\rho ghS$ on the wetted perimeter from bend entry to exit for a channel section with slant angle of 63° using SSG turbulence model and having a symmetry-wall boundary condition at the free surface. The shear on the inner bank is seen to increase first from the bend entry to 15° section and then is found to go on decreasing as the flow progresses inside the bend. It is found to be very low at the exit of the bend when the whole momentum of the flow seems to have shifted towards the outer bank. The shear on the bed on the inner side is higher at the start of the bend and goes on decreasing towards the outer side. However, as the water moves ahead inside the bend the shear on the outer side increases and is almost of the same magnitude as at the inner side. This may be because the maximum velocity moves towards the inner bank first in a bend and then progressively moves towards the outer bank. The shear on the outer bank shows a stable trend and goes on increasing through the bend. It is found to be maximum at the exit of the bend.

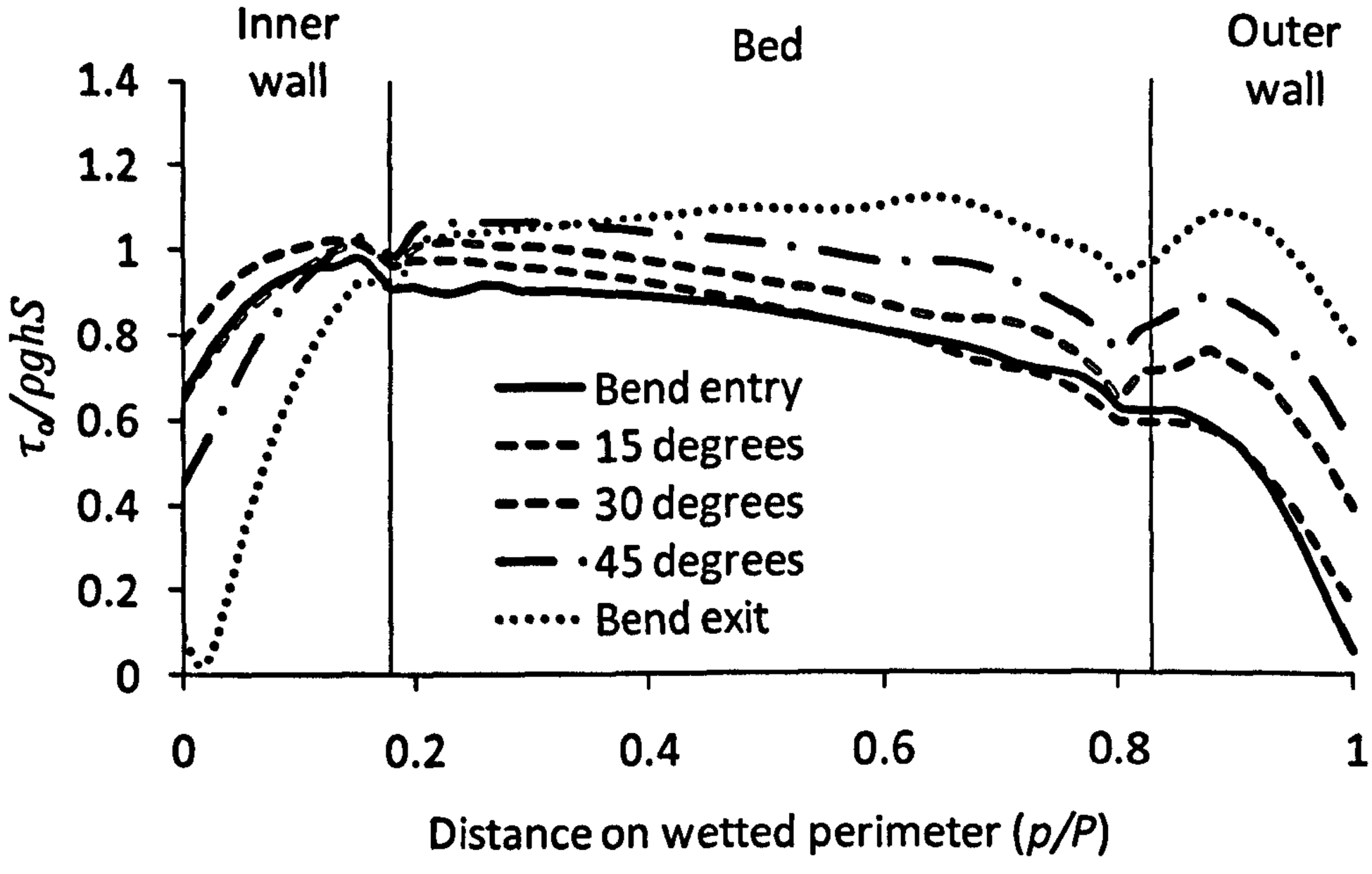

Figure 7.36 Variation of non-dimensionalised local wall shear on the wetted perimeter from bend entry to exit for a channel section with slant angle of 63 degrees using lid approach and SSG turbulence model.

A similar plot of the variation of non-dimensionalised local wall shear $\tau_o/\rho ghS$ on the wetted perimeter from bend entry to exit for a channel section with slant angle of 63 degrees using RNG k – ε turbulence model and having a symmetry-wall

boundary condition at the free surface is shown in Figure 7.37. The shear on the inner bank is seen to increase first from the bend entry to 30° section and then is found to go on decreasing as the flow progresses inside the bend. It is found to be very low at the exit of the bend when the whole momentum of the flow seems to have shifted towards the outer bank as was found in the previous case. The shear on the bed on the inner side is higher at the start of the bend and goes on decreasing towards the outer side. But as the water moves ahead inside the bend the shear on the outer side increases and is almost of the same magnitude as at the inner side but not as much as was found in the previous case. The shear on the outer bank here shows a decreasing from start of the bend up to 30° section and then goes on increasing until the end of the bend. It is found to be maximum at the exit of the bend.

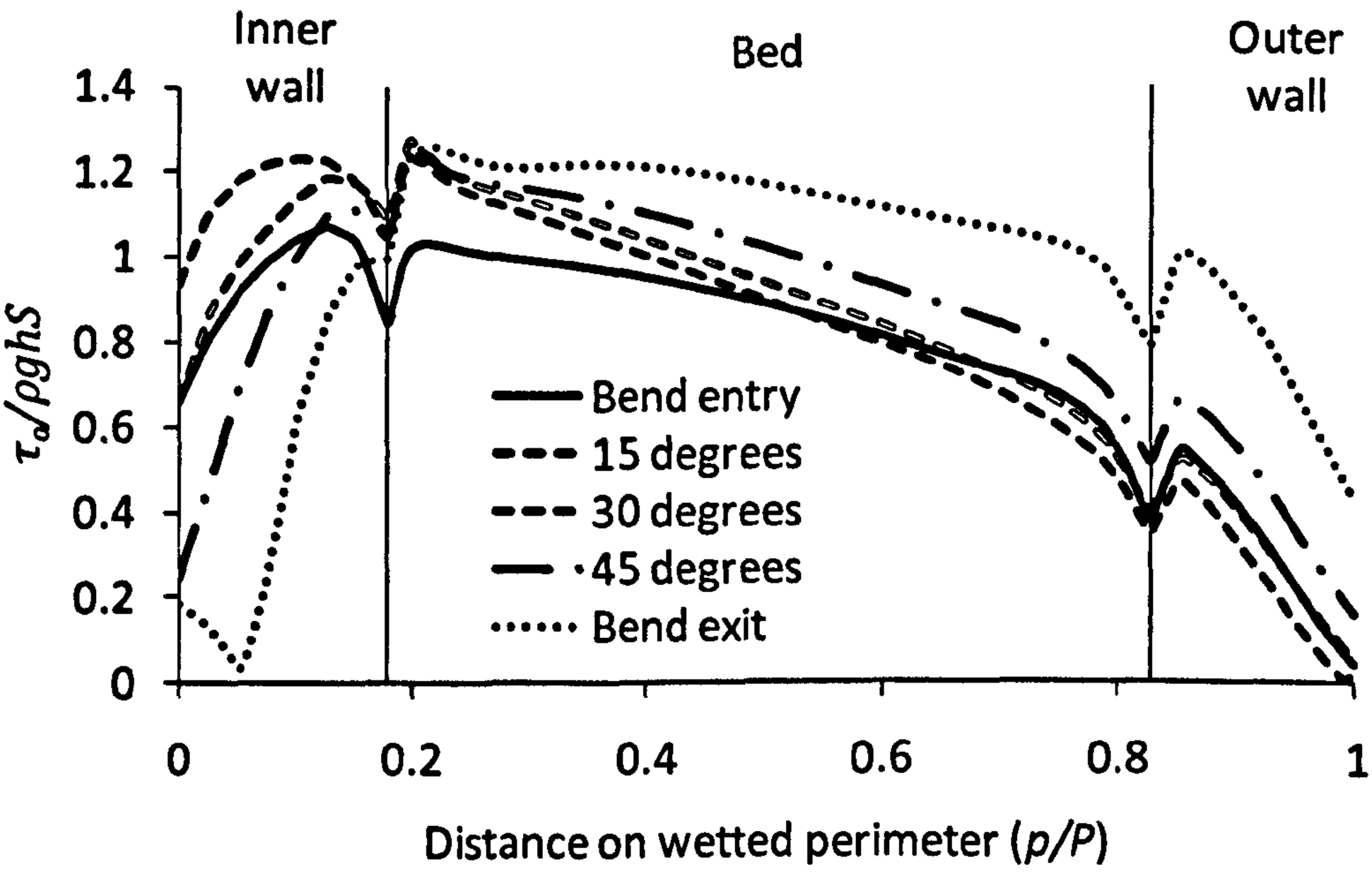

Figure 7.37 Variation of non-dimensionalised local wall shear on the wetted perimeter from bend entry to exit for a channel section with slant angle of 63 degrees using lid approach and RNG $k-\varepsilon$ turbulence model.

Similarly Figure 7.38 shows the variation of non-dimensionalised local wall shear $\tau_o/\rho ghS$ on the wetted perimeter from bend entry to exit for a channel section with slant angle of 63 degrees using VOF method with RNG k – ε turbulence model. Here the shear on the inner bank is seen to be minimum at the start of the bend and maximum at the 15° section and then is found to go on decreasing as the flow

progresses inside the bend. It is found to be very low at the exit of the bend when the whole momentum of the flow seems to have shifted towards the outer bank as was found in the previous cases. The shear on the bed is found to increase from entry to the exit of the bend. It is seen to be stable throughout the width of the channel at the start as well as exit of the bend whereas in the intermediate section it is seen higher near the inner bank and goes on decreasing towards the outer bank. The shear on the outer bank here shows a decreasing from start of the bend up to 15° section and then goes on increasing until the end of the bend. It is found to be maximum at the exit of the bend.

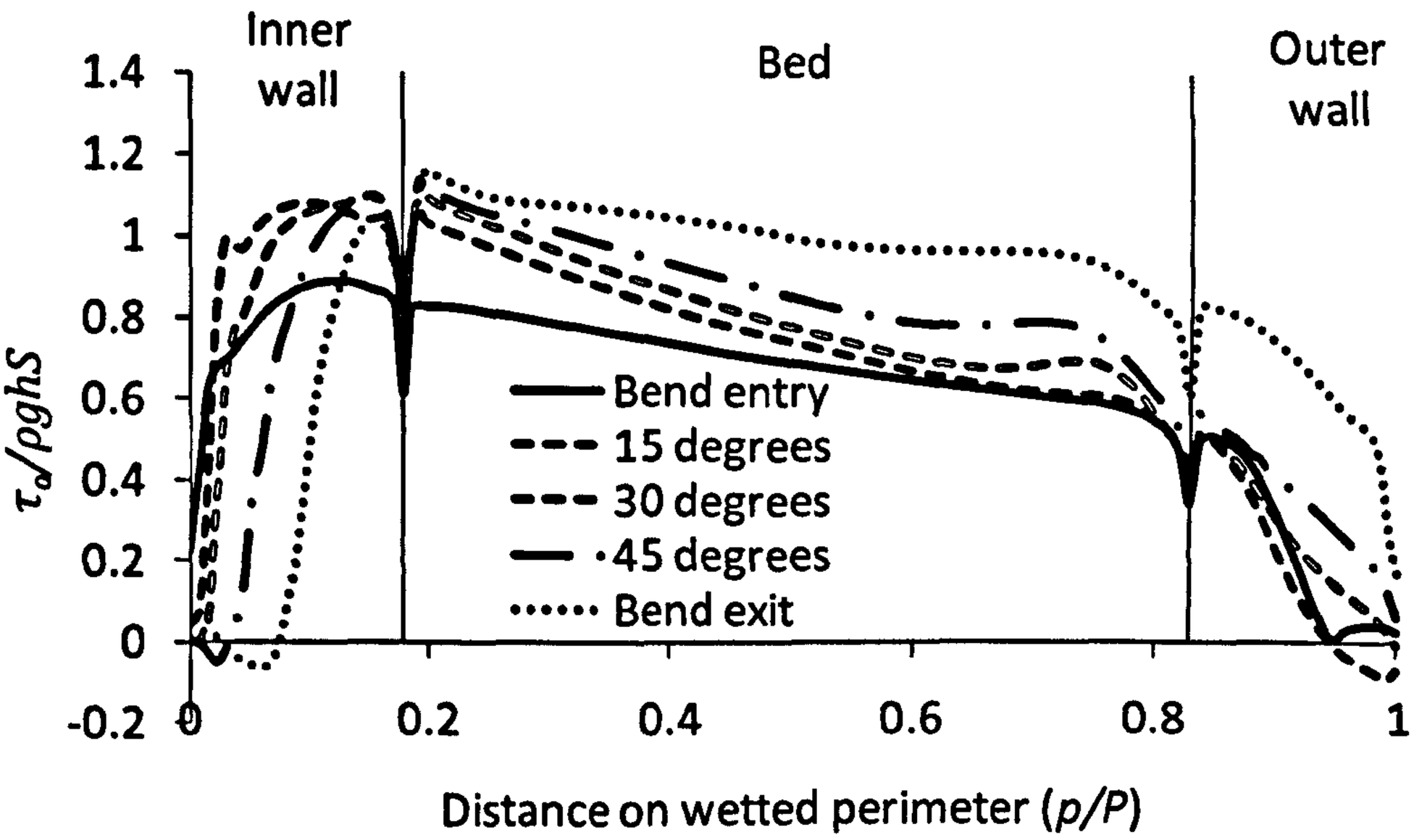

Figure 7.38 Variation of non-dimensionalised local wall shear on the wetted perimeter from bend entry to exit for a channel section with slant angle of 63 degrees using VOF method and RNG $k-\varepsilon$ turbulence model.

A comparison of the non-dimensionalised local wall shear $\tau_o/\rho ghS$ is also carried out at each section between the three cases i.e. lid approach using SSG turbulence model, lid approach using RNG k-ε model and VOF approach using RNG k-ε and are shown in Appendix B. Similarly a comparison of the non-dimensionalised local wall shear $\tau_o/\rho ghS$ in the cross-stream direction is also carried out at each section between the three cases just discussed. The cross-stream shear is also found to be significant i.e. as high as 35 percent of the average shear in a cross section ρghS as shown in Figure 7.39 to Figure 7.43. It is seen to be increasing as the flow progresses inside the bend until 45° section and then is seen to decrease

again. The wall shear found using VOF method is seen to be lower than the rigid lid method initially at the bend entry but becomes stronger as the flow progresses inside the bend.

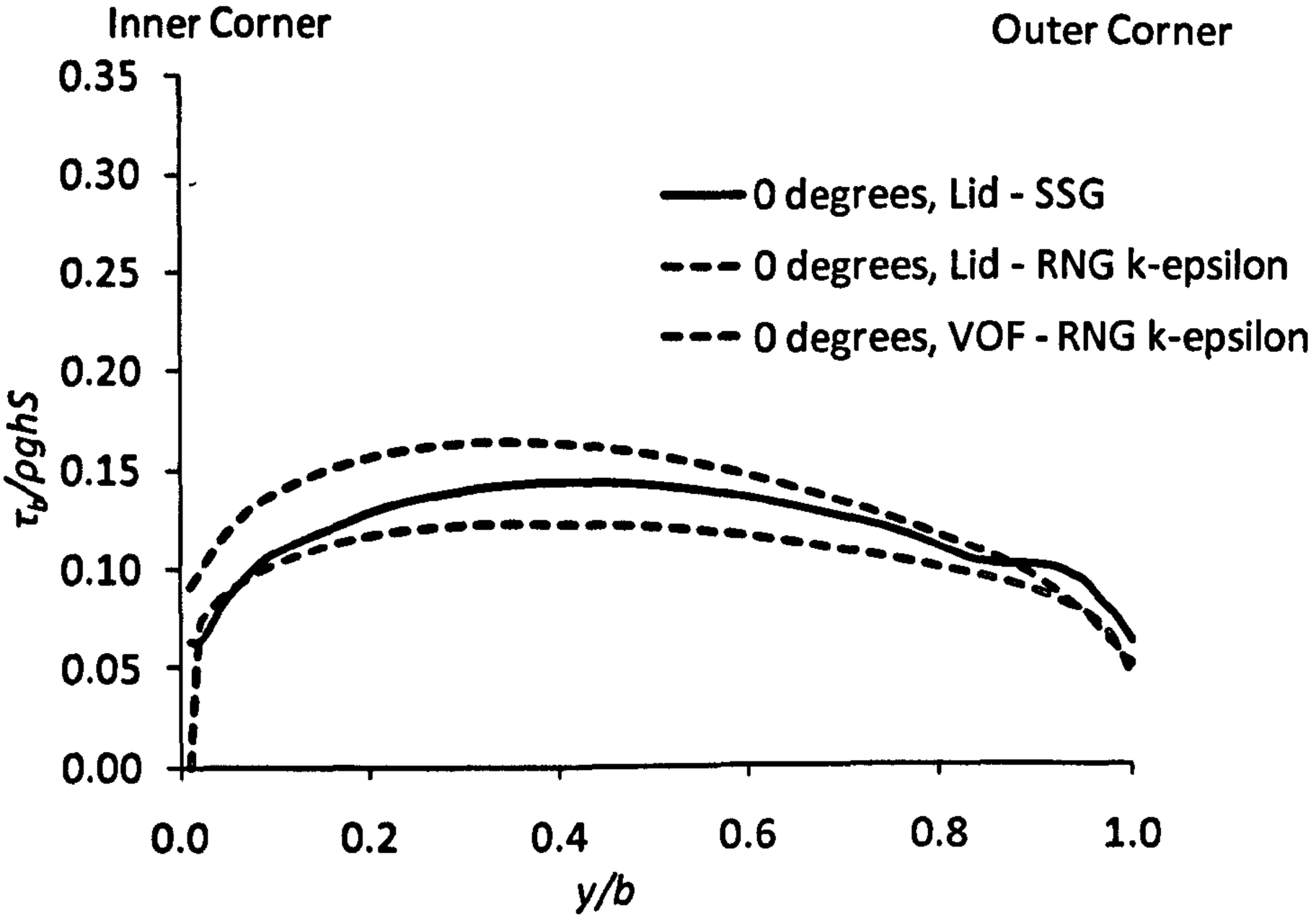

Figure 7.39 Comparison of non-dimensionalised wall shear in cross-stream direction on the bed at bend entry.

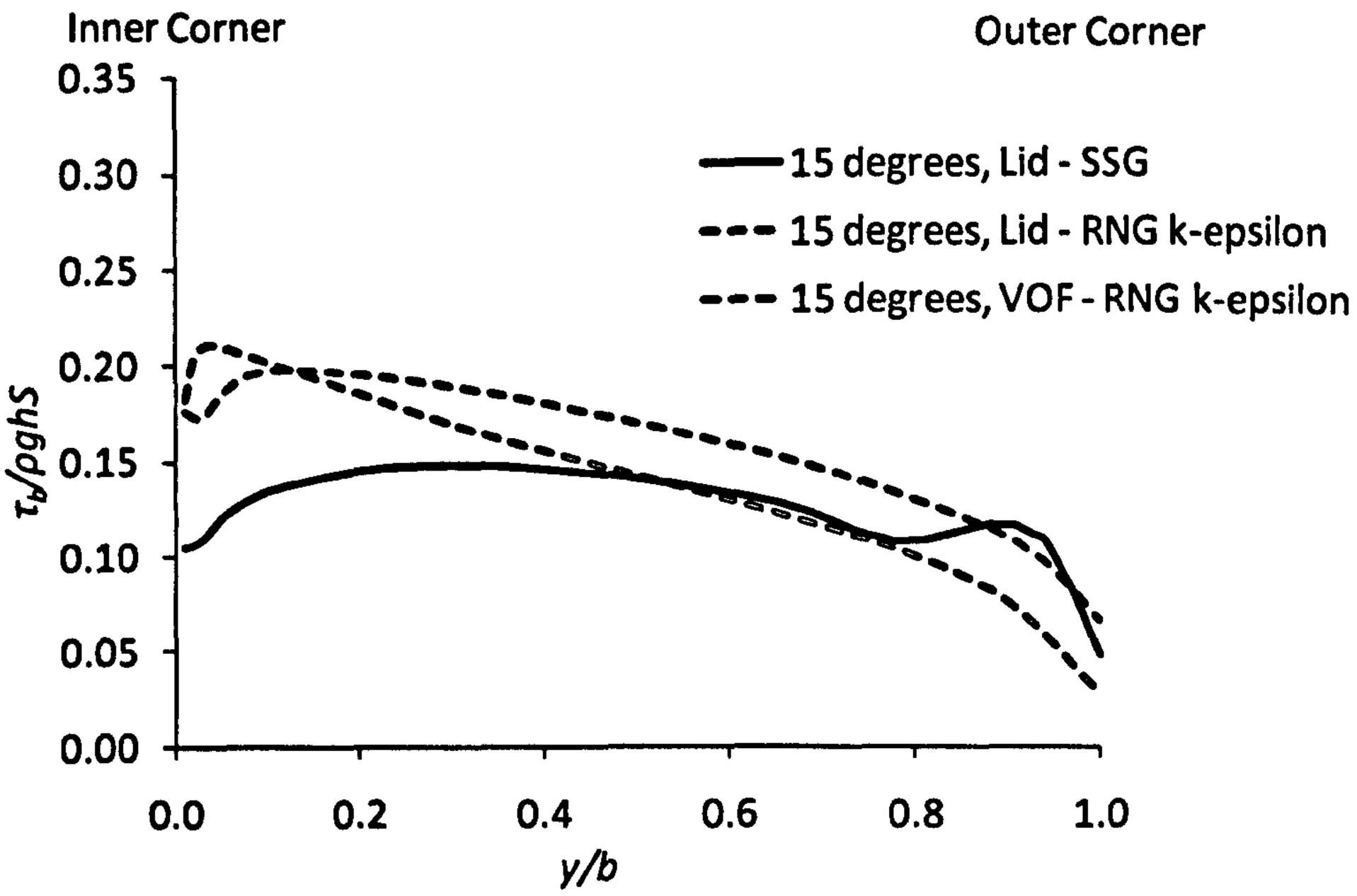

Figure 7.40 Comparison of non-dimensionalised wall shear in cross-stream direction on the bed at a section 15 degrees inside bend.

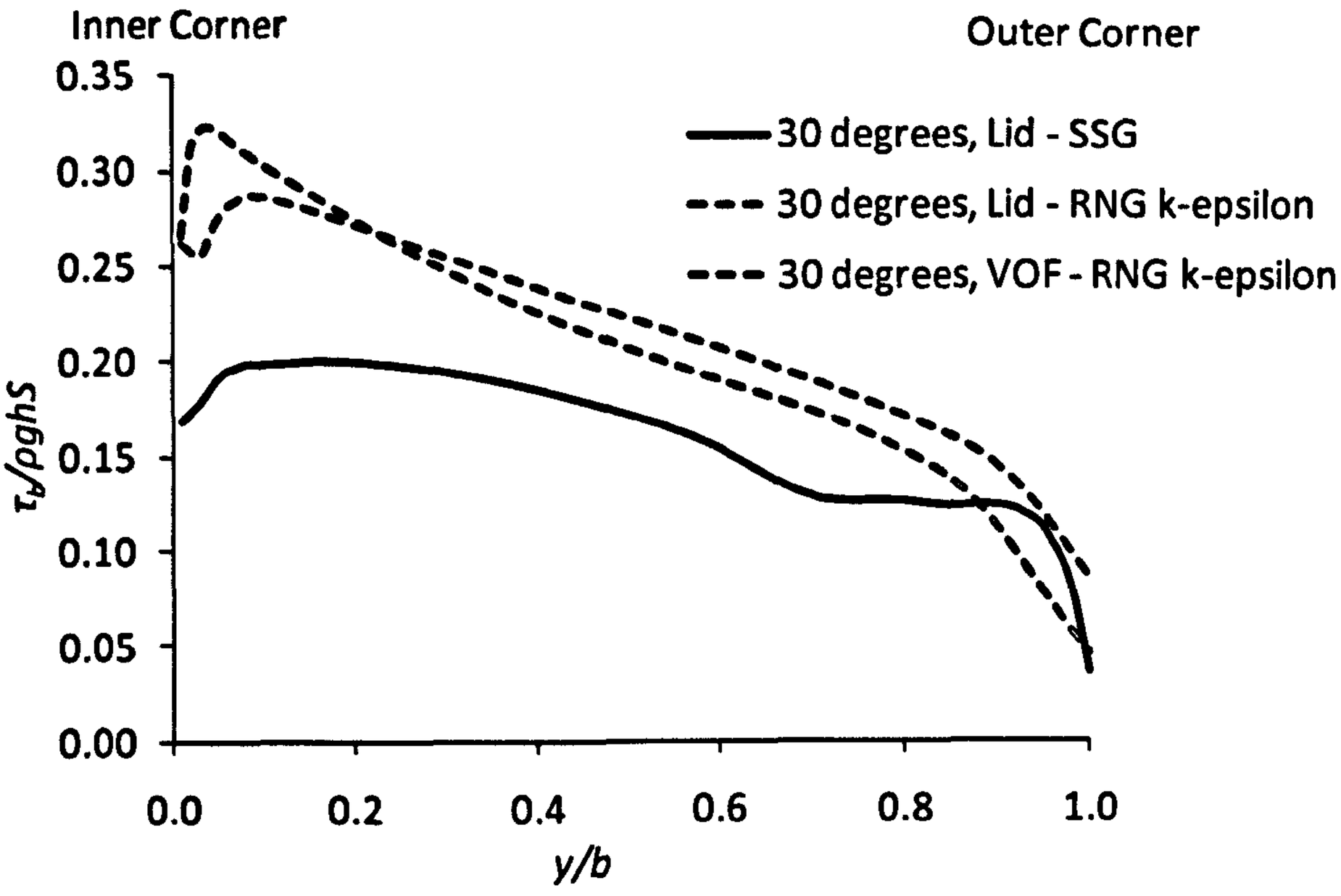

Figure 7.41 Comparison of non-dimensionalised wall shear in cross-stream direction on the bed at a section 30 degrees inside bend.

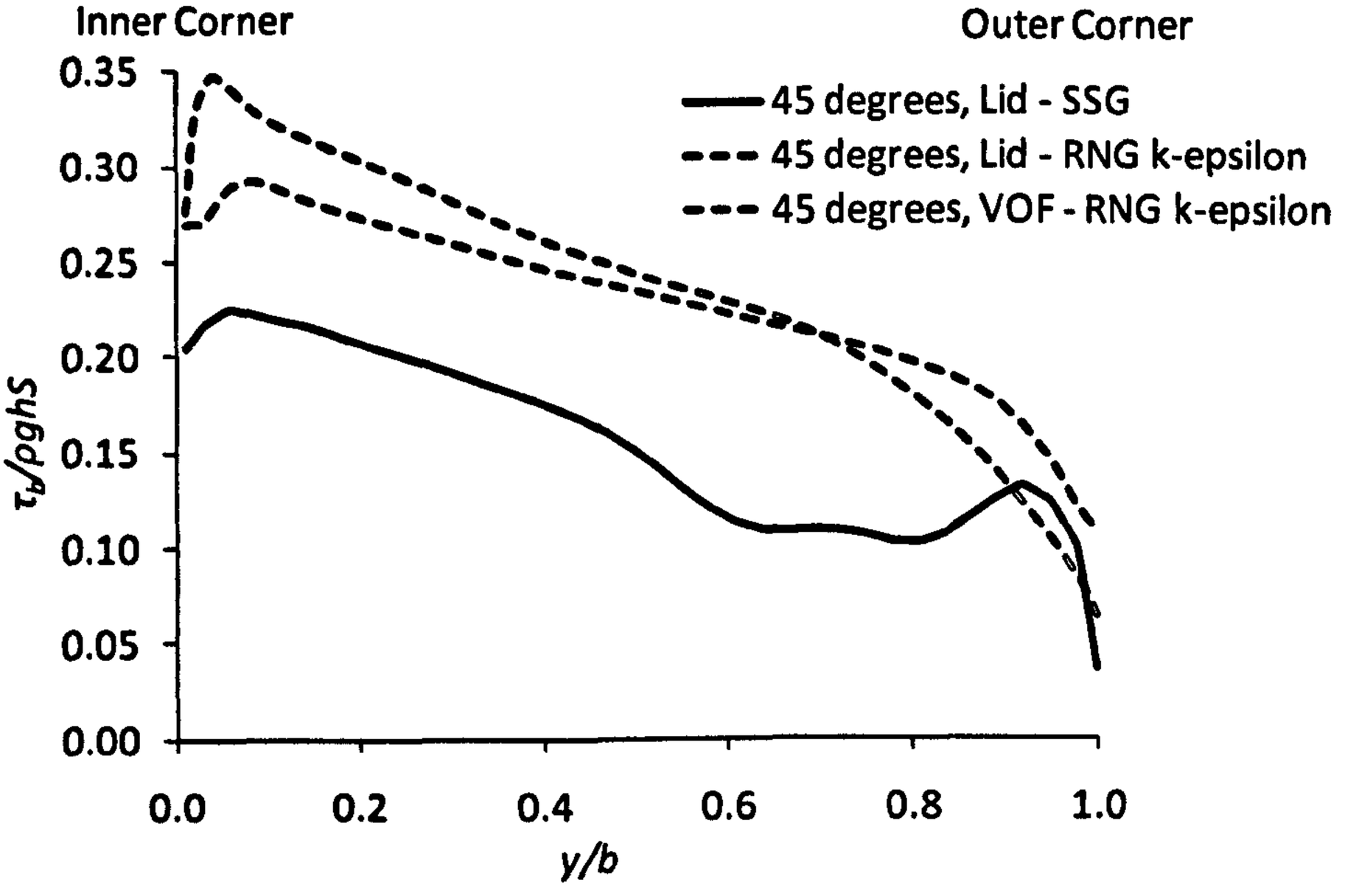

Figure 7.42 Comparison of non-dimensionalised wall shear in cross-stream direction on the bed at a section 45 degrees inside bend.

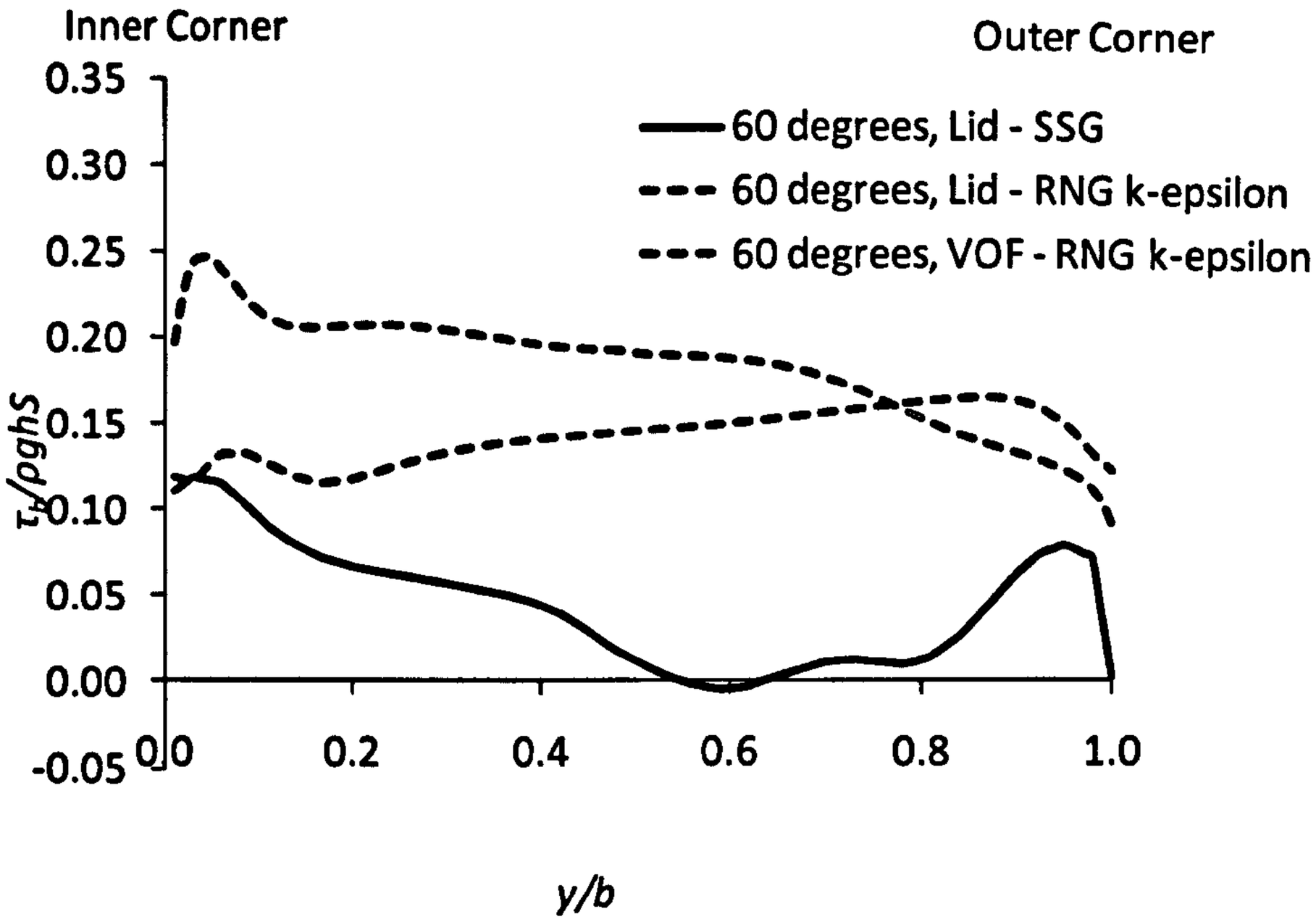

Figure 7.43 Comparison of non-dimensionalised wall shear in cross-stream direction on the bed at bend exit.

7.4.4 Variation of boundary shear with slant angle

An analysis is carried out by simulating three trapezoidal channels with varying slant angles. Slant angles of 30°, 45° and 63° with the vertical are selected. The boundary shear along the bed and two sidewalls at five different sections i.e. bend entry, bend exit, 15°, 30°, and 45° are plotted for all the three sections and analysed to study the variation. The mean bed and sidewall shear stresses are non-dimensionalised by the two dimensional bed shear stress $\tau_o/\rho ghS$ after Knight *et al.* (1984).

Figure 7.44 shows the wall shear plotted, for the three cases, on the wetted perimeter at the bend entry. The wall shear found on bed is almost the same for all the cases but is seen to differ specially on the outer wall. On the outer wall as the slant angle increases i.e. as the wall open the shear is found to decrease. Whereas on the inner wall it is found to increase with the slant angle for the lower half.

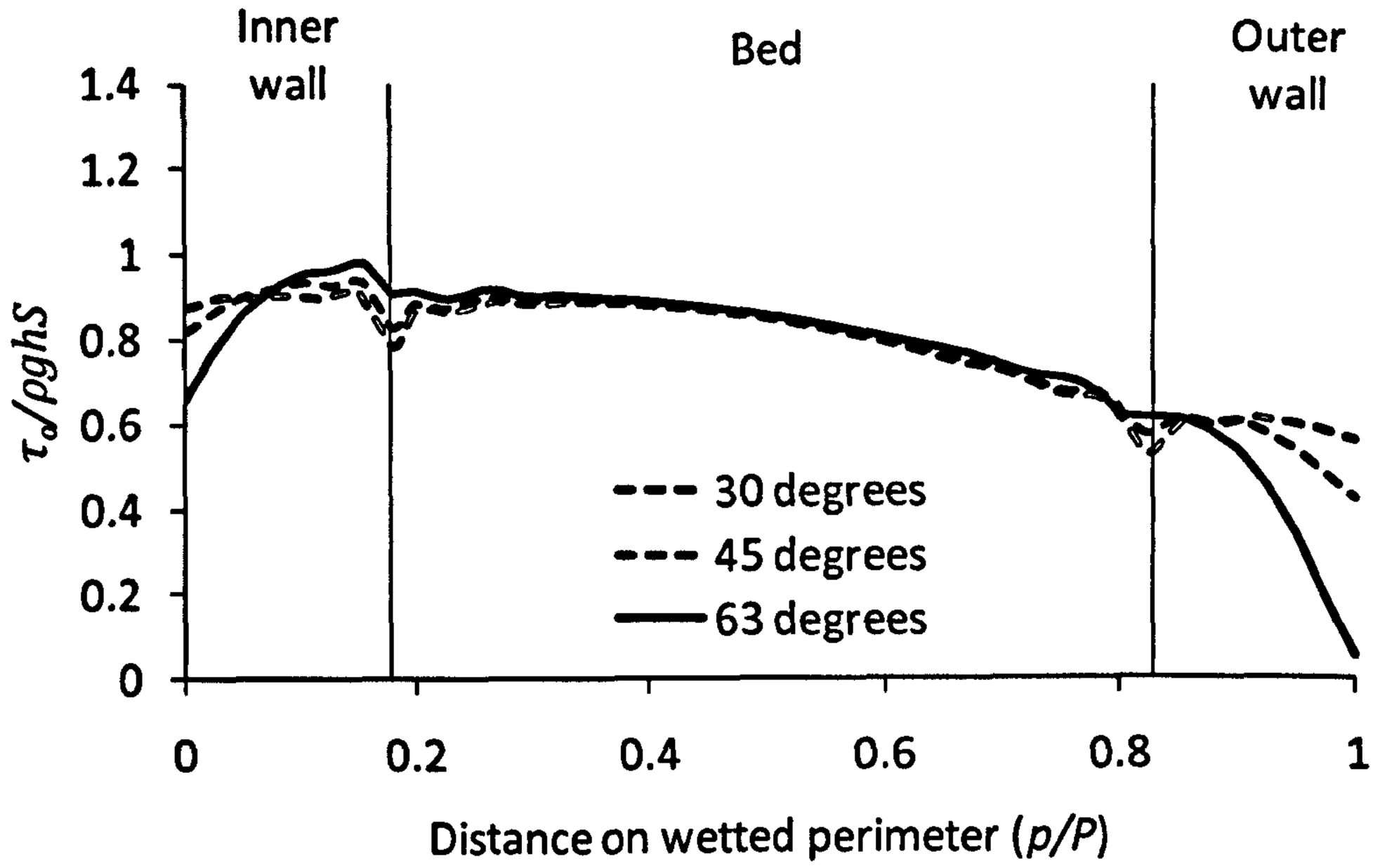

Figure 7.44 Comparison of non-dimensionalised local wall shear with slant angle on the wetted perimeter at bend entry.

Figure 7.45 to Figure 7.48 shows the wall shear plotted, for the three cases, on the wetted perimeter from 15° section to the exit of the bend. These plots almost depict similar results. The wall shear found on bed is almost the same for all the cases but is seen to differ on the two sidewalls. The lower portions of the walls seem to have very low effect on the wall shear variation due to change in slant angle but the upper portions show large differences. On the inner walls the wall shear is higher with higher slant angle in the lower portion but is the other way round in the higher portion near the free surface. On the outer wall the wall shear is almost same in the lower portion but goes on decreasing with increase in slant angle near the free surface.

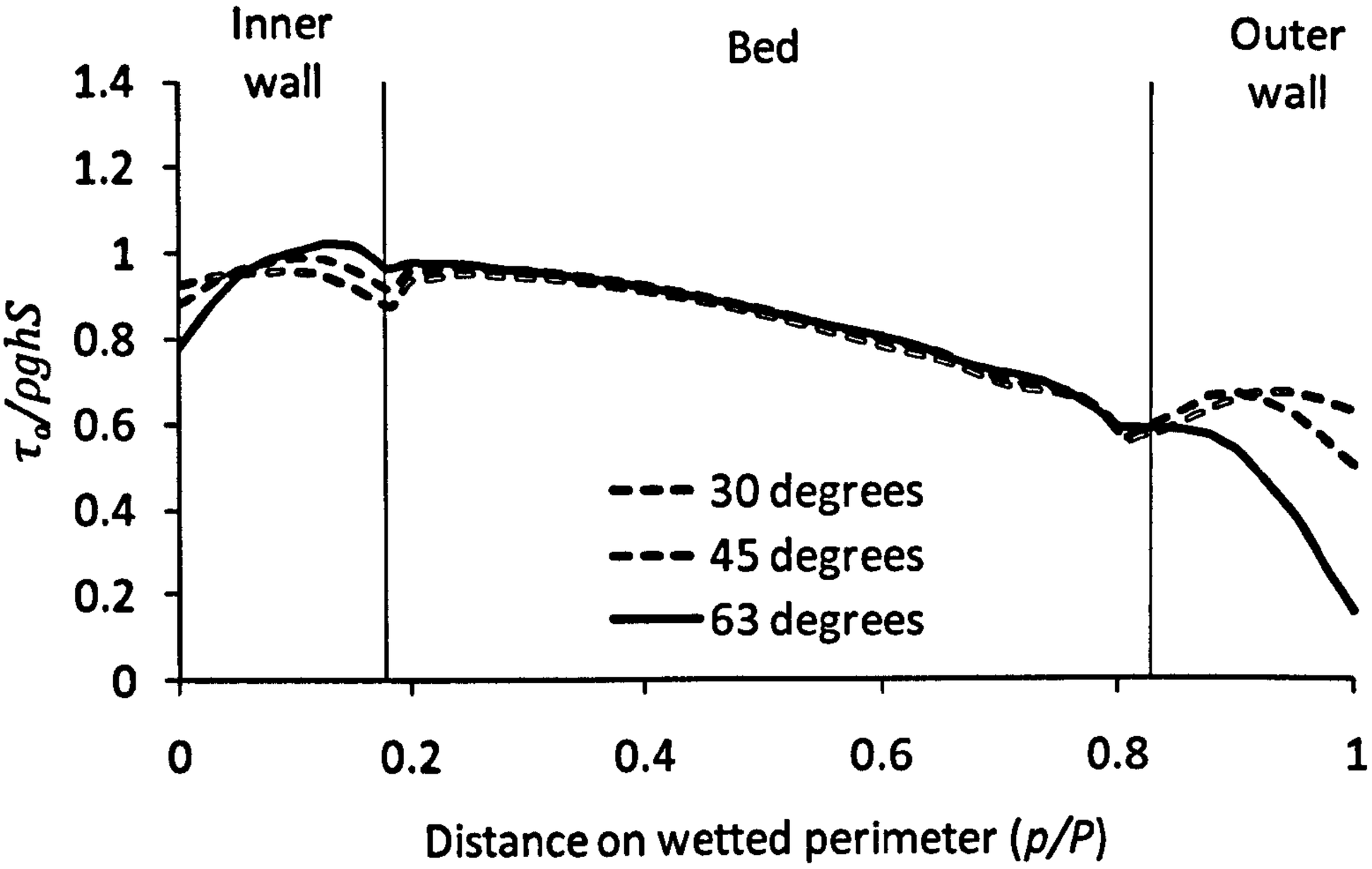

Figure 7.45 Comparison of non-dimensionalised local wall shear with slant angle on the wetted perimeter at a section 15° inside bend using lid approach and SSG turbulence model.

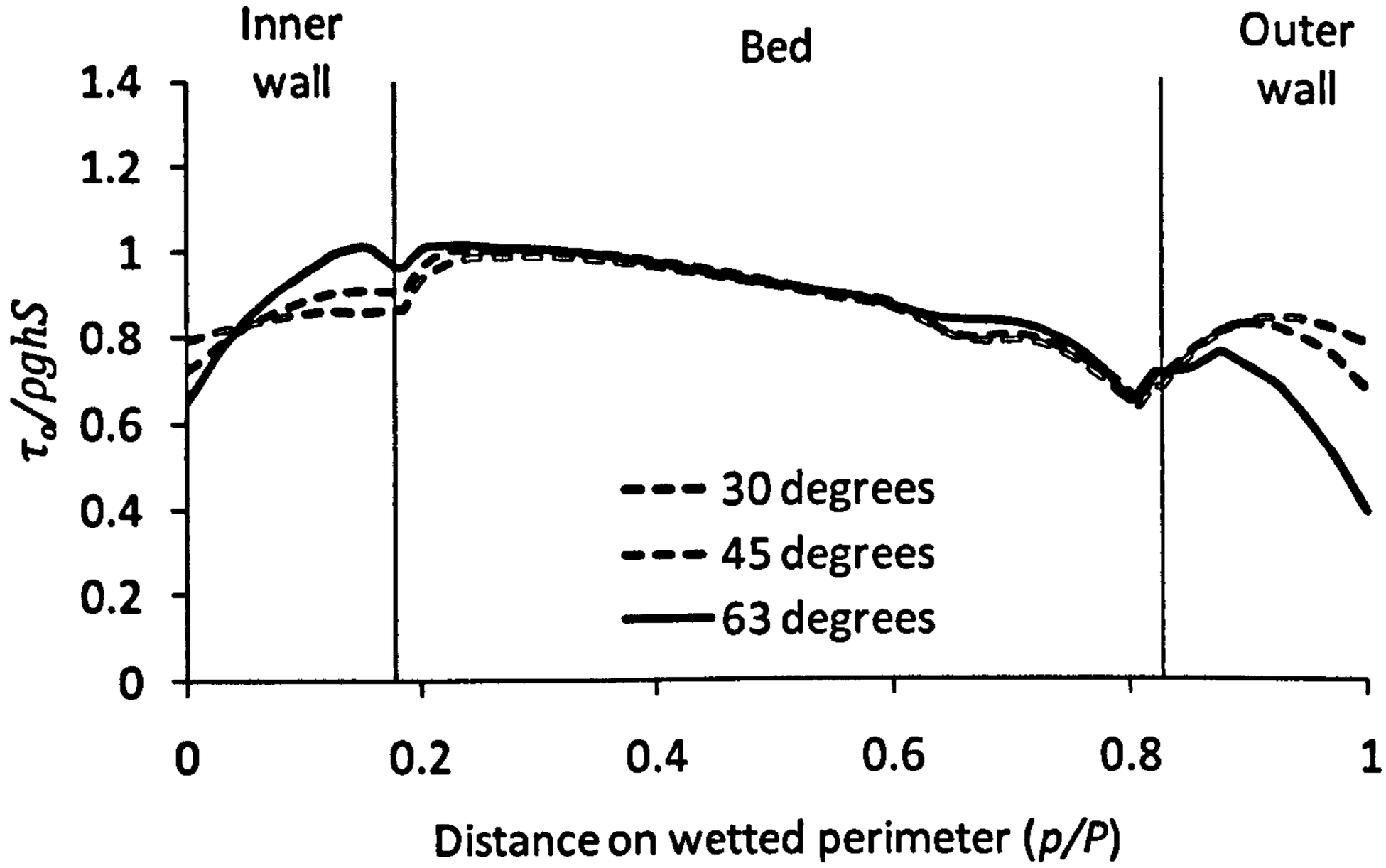

Figure 7.46 Comparison of non-dimensionalised local wall shear with slant angle on the wetted perimeter at a section 30° inside bend using lid approach and SSG turbulence model.

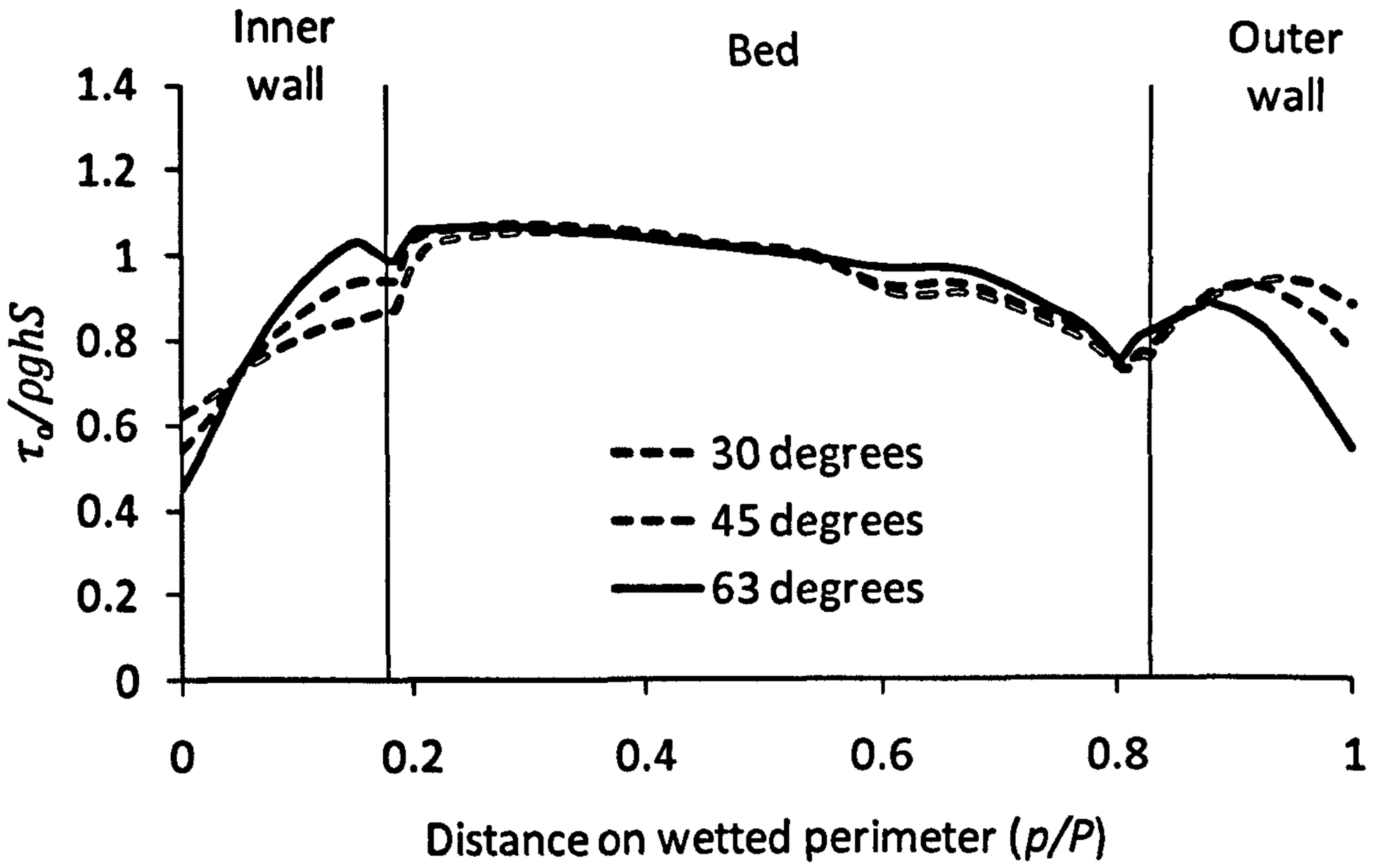

Figure 7.47 Comparison of non-dimensionalised local wall shear with slant angle on the wetted perimeter at a section 45° inside bend using lid approach and SSG turbulence model.

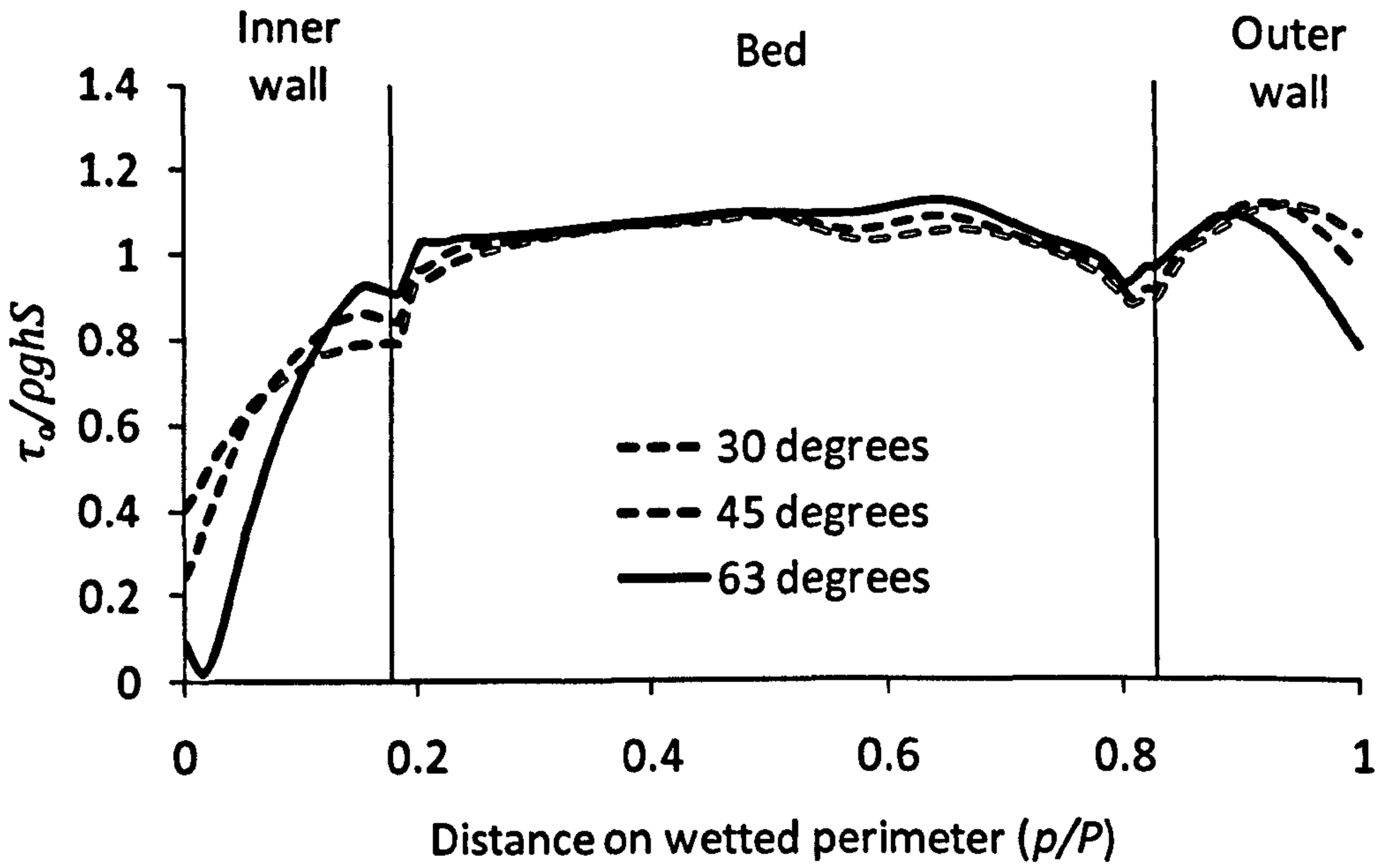

Figure 7.48 Comparison of non-dimensionalised local wall shear with slant angle on the wetted perimeter at bend exit using lid approach and SSG turbulence model.

7.4.4.1 Wall shear in cross-stream direction

A comparison of the non-dimensionalised local wall shear $\tau_o/\rho ghS$ on the bed in the cross-stream direction is also carried out at each section between the three

cases just discussed. Figure 7.49 shows the plot of the non-dimensionalised local wall shear on the bed in cross-stream direction at the bend entry. It is found that the wall shear is increasing with the increase in the slant angle. As the flow progresses inside the bend from 15° section to the bend exit, the shear is found to be decreasing with the increase in slant angle. Hence, the shear in the cross-stream direction is higher for high slant angles at the bend entry but becomes lower as the flow progresses inside the bend.

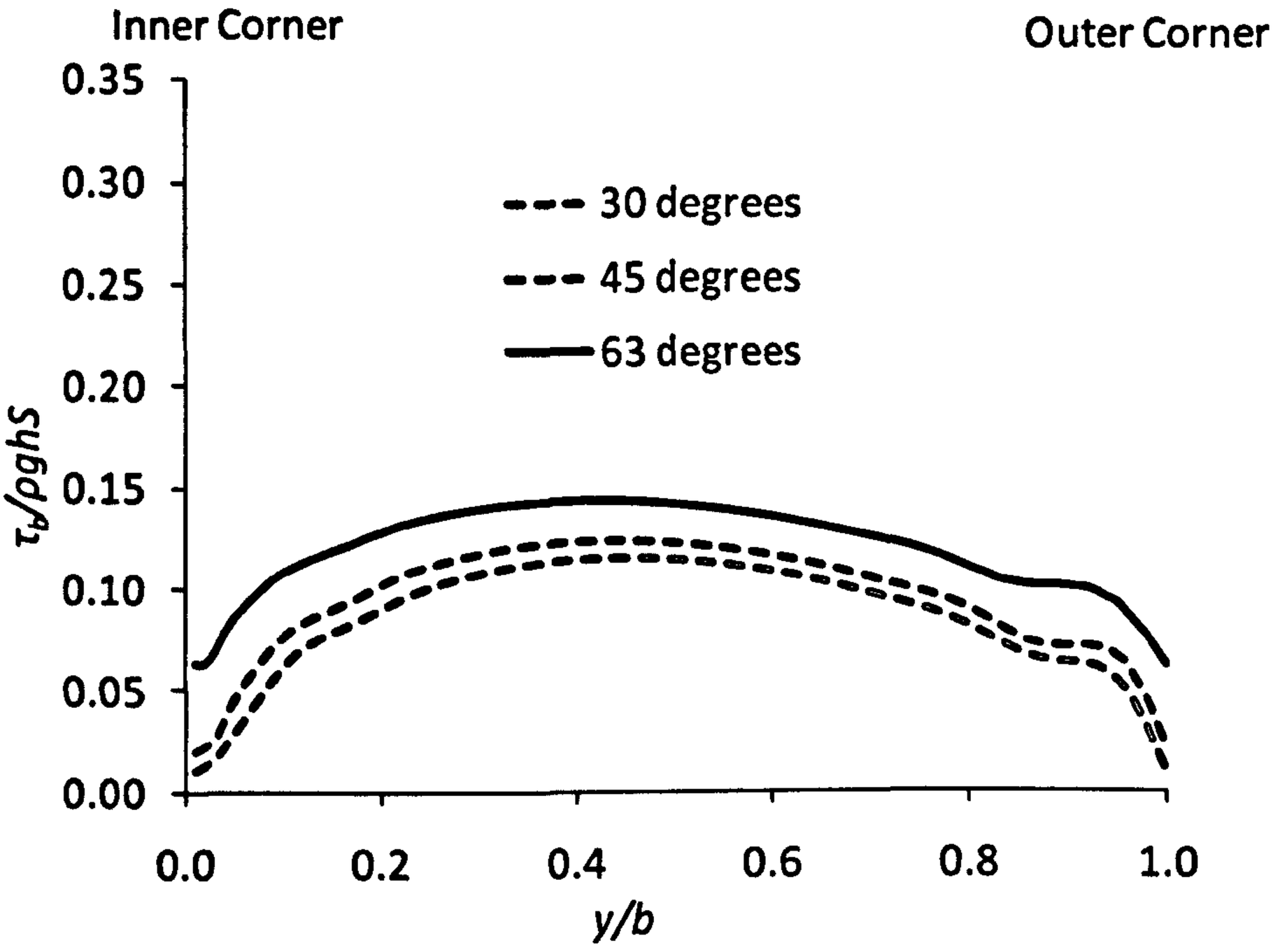

Figure 7.49 Comparison of non-dimensionalized local wall shear with slant angle on the bed in cross stream direction at bend entry.

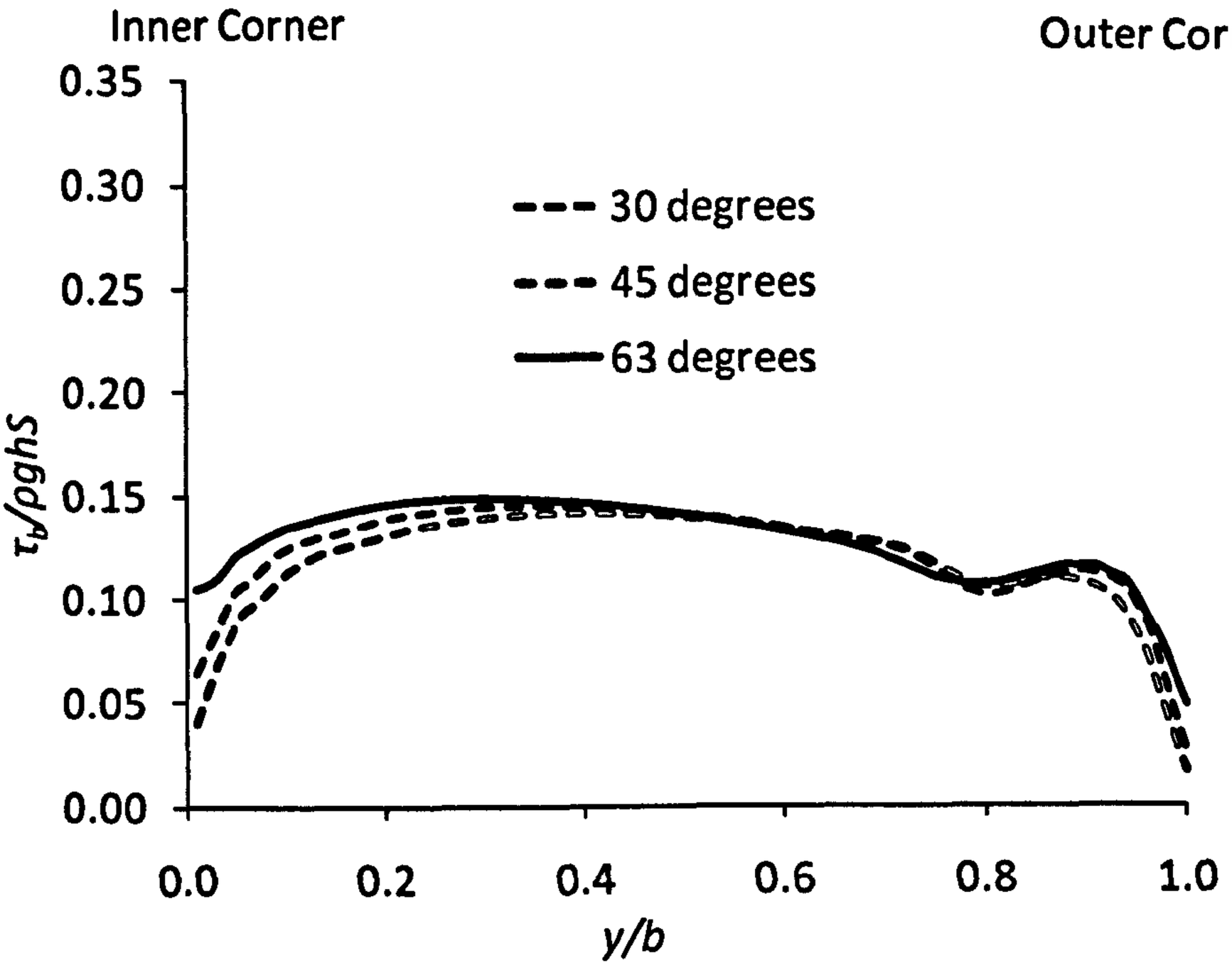

Figure 7.50 Comparison of non-dimensionalized local wall shear with slant angle on the bed in cross stream direction at a section 15 degrees inside bend.

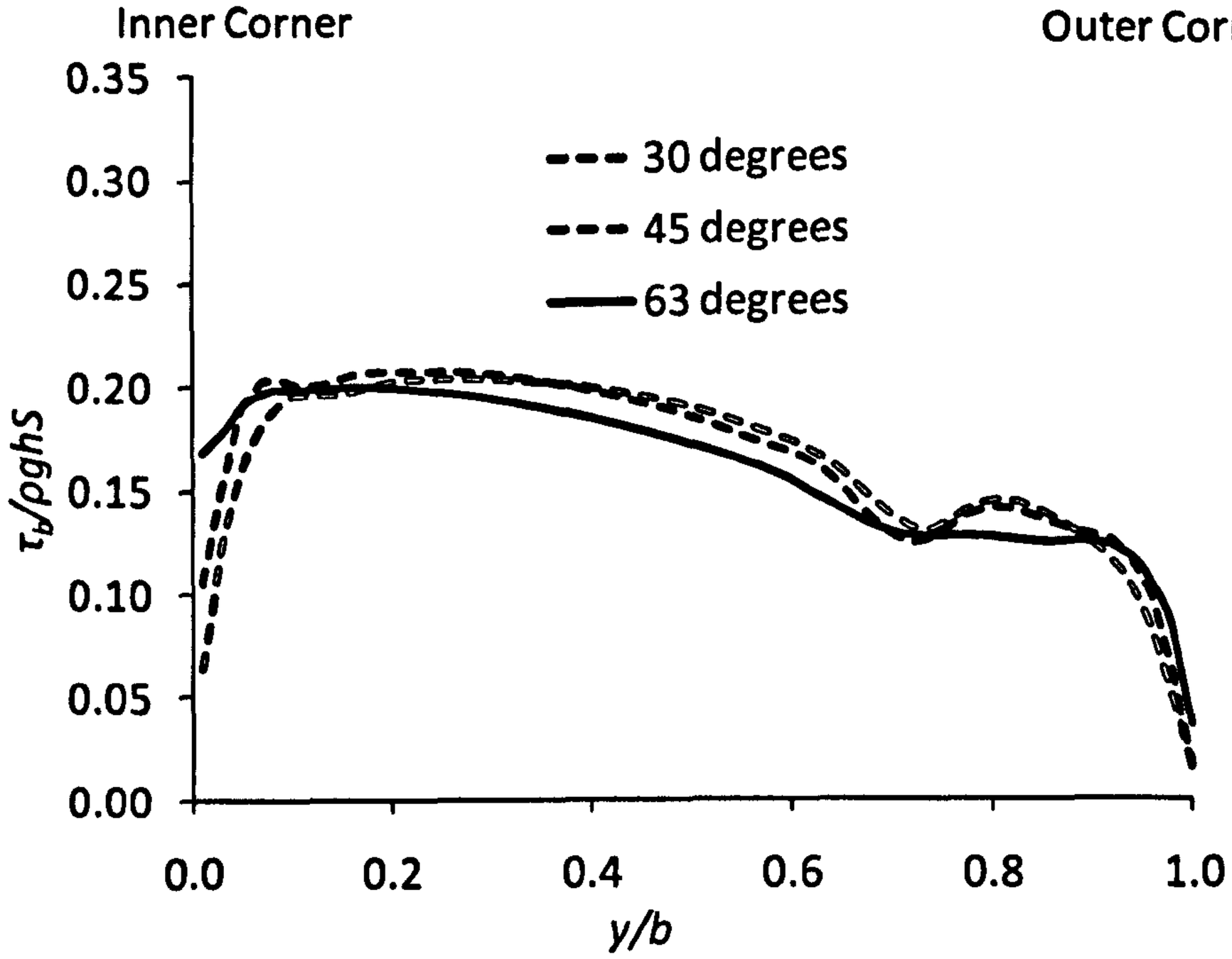

Figure 7.51 Comparison of non-dimensionalized local wall shear with slant angle on the bed in cross stream direction at a section 30 degrees inside bend.

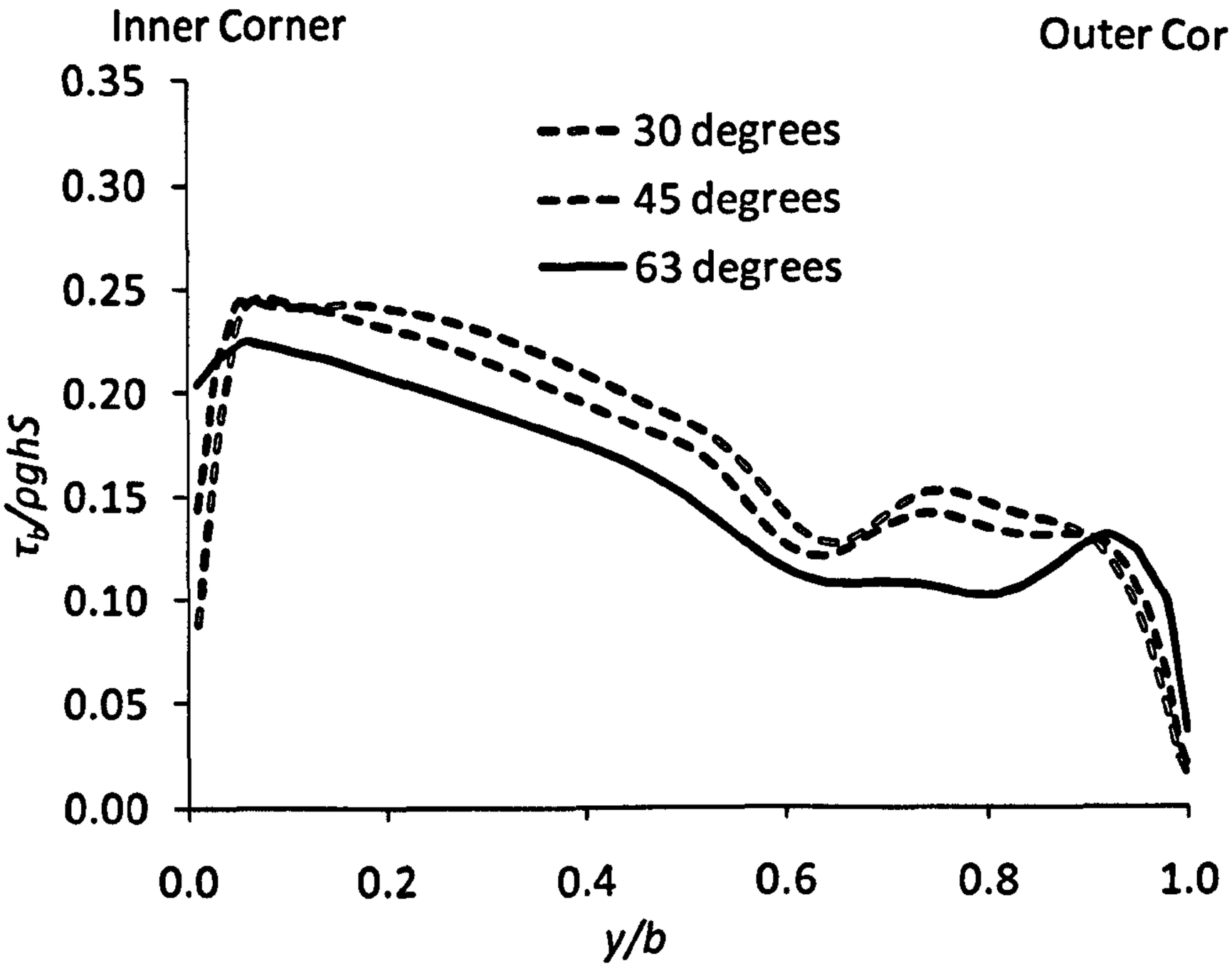

Figure 7.52 Comparison of non-dimensionalized local wall shear with slant angle on the bed in cross-stream direction at a section 45 degrees inside bend.

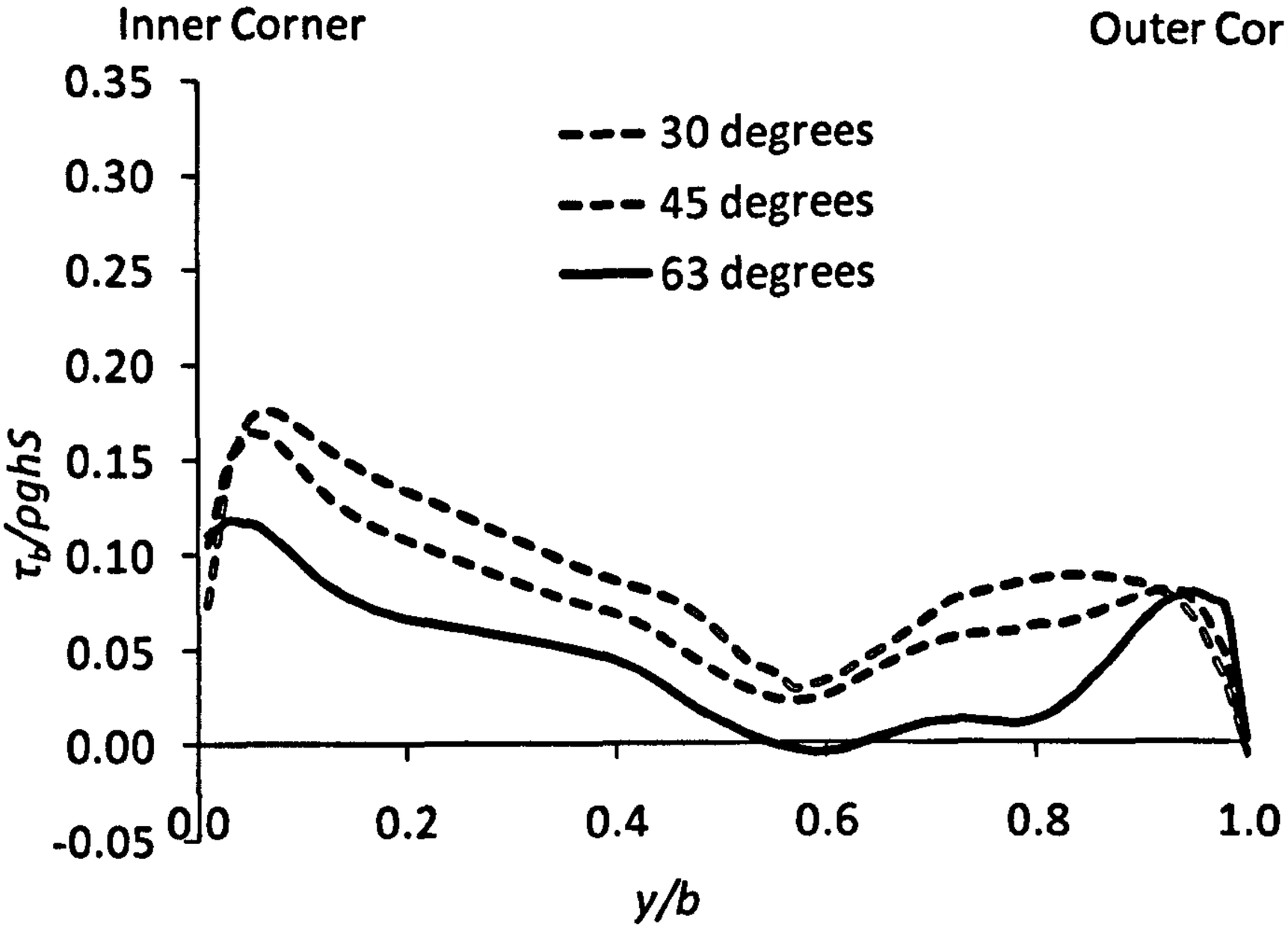

Figure 7.53 Comparison of non-dimensionalized local wall shear with slant angle on the bed in cross stream direction at bend exit.

7.5 Division Line

An attempt is made to construct the division lines inside the bend as well as was done for the straight prismatic channels. As far as the construction of the division lines from the two base corners of the channel are concerned, the approach includes the following steps,

- Two points are created at the two corners where the bed and the two sidewalls meet.
- A three dimensional vector gradient is created $\frac{du}{dx} + \frac{du}{dy} + \frac{du}{dz}$ starting from the two corner points, which follows the change of velocity u in the cross-section of the channel.
- A streamline is created, which follows the vector gradient.

It is well known that as the flow of water approaches a curve or bend it anticipates a change of velocity and the asymmetry of the velocity takes place well before the start of the bend, so to get the vector gradient in a two dimensional cross section was a problem. A new approach was adopted to set the first part to zero to get the change of velocity u in y- and z- axes only. Unfortunately a local co-ordinate system cannot be used for this purpose in the CFX post so five different channels were meshed having their x-axis inclined at 0 degrees, 15 degrees, 30 degrees, 45 degrees and 60 degrees inside the curved portion of the bend. The division lines thus obtained are shown in Figure 7.54.

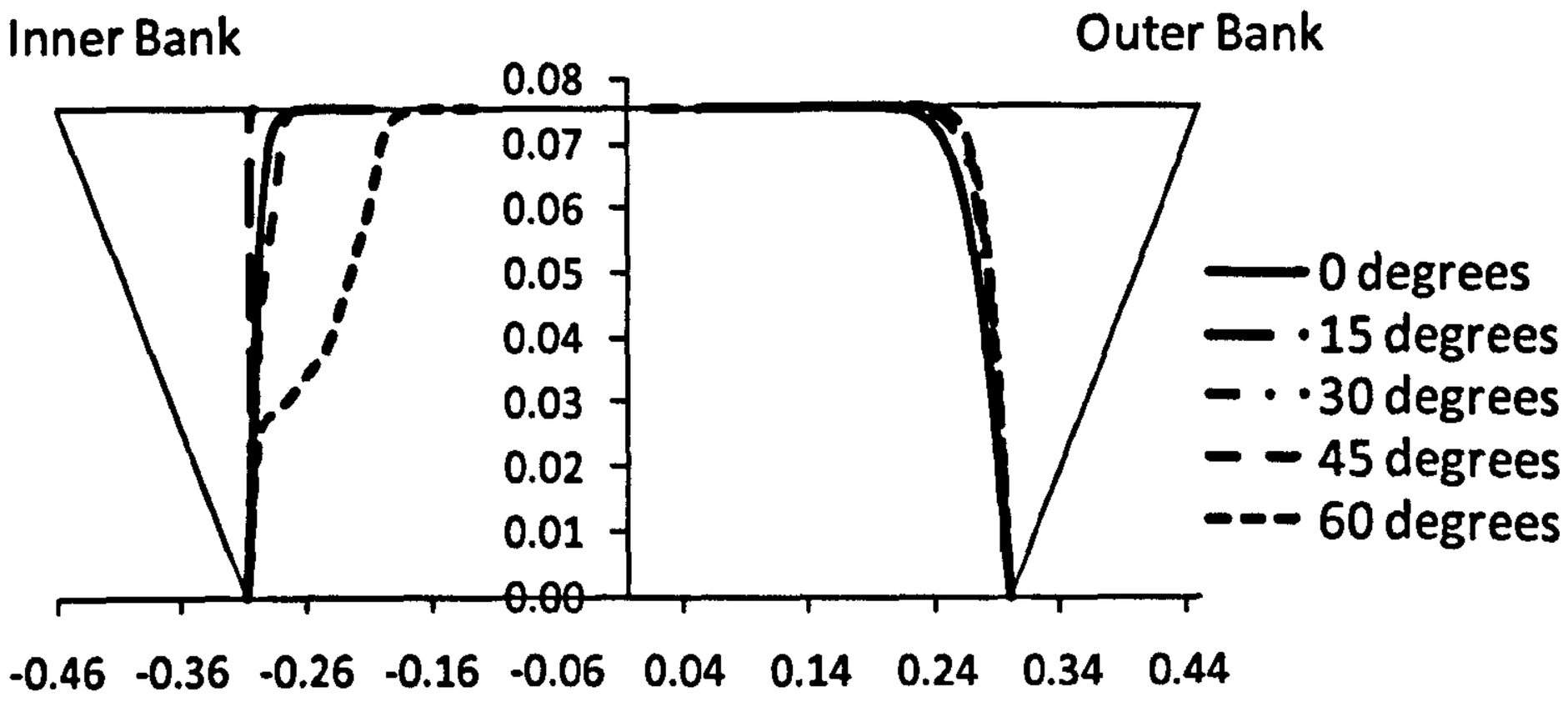

Figure 7.54 Plots of division lines (DL) inside the bend.

An analysis was carried out on these division lines with the Guo and Julien (2005) equations. But unfortunately no satisfactory results were achieved as these equations were derived assuming flow in straight prismatic channels and the strong re-circulations developed when flow is passing through the bend or curve were ignored.

7.6 Conclusions

An extensive analysis is carried out on the development of flow structures and variation of shear stress inside an open channel bend. The main findings of the study are given below:

- The pressure analysis on the free surface using the lid approach and the super-elevation found using the VOF approach both correspond well to the super-elevation observed experimentally as given by Chang (1988).
- The asymmetry of the flow starts significantly before the start of the bend and carries on well after the end of the bend.
- The asymmetry in the mainstream velocity starts early if the slant angle is small due to the effect of the sidewalls, but this effect is negligible when the slant angle is greater than 45°.
- The secondary currents are initially observed to be moving towards the inner bank at the start of the bend and as the flow progresses inside the bend a strong re-circulation is seen in the whole cross section of the channel. The re-circulation shows the flow moving towards the outer bank near the free surface and towards the inner bank near the bed.
- The effect of the slant angle on the secondary currents is found to be more near the bend entry and goes on decreasing as the flow progresses inside the bend. The secondary currents are almost identical at the bend exit.
- The local wall shear on the inner bank increases first until 15° inside the bend and then is found to decrease continuously afterwards.
- The local wall shear on the outer wall on the other hand decreases first and then as the flow progresses inside the bend is found to be continuously increasing.

CHAPTER 8

CONCLUSIONS AND RECOMMENDATIONS FOR FURTHER RESEARCH

8.1 Conclusions

The conclusions are divided into three parts for the three different sections of the study and are summarised below.

8.1.1 Straight prismatic channels

The main conclusions on the study of shear stress distribution in the straight prismatic trapezoidal channels are:

- The comparisons of the CFD results with the published results in the literature show good agreement and validate the CFD methodology adopted.
- The analysis of Guo and Julien (2005) equations on this division line show that the contribution of secondary currents and fluid internal shear stress is not negligible in the calculation of shear stresses on the bed and sidewalls separately. This extends the work of Cacqueray *et al.* (2009).
- The variation of the slant angle and aspect ratio bring significant changes to the distribution of the shear stress at the boundaries, consistent with changes in the flow structures as previously shown by Morvan and Hargreaves (2009), in particular for low aspect ratio channels.
- The introduction of new variables, α_b and α_w, which quantify the relative contributions from the gravitational term in the formulation of Guo and Julien (2005) to those from the secondary currents and internal shear stresses, is shown to be useful in gaining insights into the different flow regimes in the channel.

8.1.2 Straight prismatic channels with bed forms

A mechanism for the creation of ridges on the bed in wide channels and its interaction with secondary currents and wall shear is proposed. This may be regarded as an extension of the work done by Knight and Patel (1985) and Nezu and Nakagawa (1984). The main points of this mechanism are given below:

- The pattern of the secondary currents as observed shows that the presence of the sidewalls could initially be responsible for the creation of the corner ridges.
- The corner ridges in turn, may be responsible for the formation of an additional cell of circulation which again creates another ridge and so on until the whole channel develops these ridges and troughs and a state of equilibrium is reached.
- The vertical velocity is found to be upward over the edges of the ridges and downward over centres of both the troughs and ridges, which shows a pair of counter rotating cells over both troughs and ridges.
- The perturbations of secondary flow are strong near the bed and get significantly reduced near the free surface.
- The wall shear is seen to be decreasing with the increase in the ridges on the bed which shows that the bed forms ultimately bring some stability on the boundaries in the section.

8.1.3 Prismatic channels with a bend

The main findings on the study of shear stress distribution and flow structures inside a bend are given here under:

- The pressure analysis on the free surface using the lid approach and the super-elevation found using the VOF approach both correspond well to the super-elevation observed experimentally as given by Chang (1988).
- The asymmetry of the flow starts significantly before the start of the bend and carries on well after the end of the bend. The asymmetry in flow after the bend was observed even up to sixty times the width of the channel.

- The asymmetry in the mainstream velocity starts early if the slant angle is small due to the effect of the sidewalls, but this effect is negligible when the slant angle is greater than 45°.
- The secondary currents are initially observed to be moving towards the inner bank at the start of the bend and as the flow progresses inside the bend a strong re-circulation is seen in the whole cross section of the channel. The re-circulation shows the flow moving towards the outer bank near the free surface and towards the inner bank near the bed.
- The effect of the slant angle on the secondary currents is found to be more near the bend entry and goes on decreasing as the flow progresses inside the bend. The secondary currents are almost identical at the bend exit.
- The local wall shear on the inner bank increases up to a slant angle of 15° inside the bend and then is found to decrease continuously afterwards.
- The local wall shear on the outer wall on the other hand decreases first and then as the flow progresses inside the bend is found to increase.

8.2 Recommendations for further research

During the course of the study some potential research aspects were identified, further work on which could not be carried out due to lack of time. A summary of the ideas related to further research is given below:

- Further investigation of CFD applied to the data (and equations) presented in the comprehensive summary of the earlier experimental work undertaken by Knight in the 1980's, contained in the paper by Knight, Yuen & Alhamid (1994). In particular, it is suggested that the slight dependence of mean wall and bed shear stresses on the Reynolds and Froude numbers, observed in empirical data, should be examined further via CFD (i.e. sub and supercritical flow effects).
- Further investigation of CFD applied to the data on trapezoidal channels with very rough sidewalls, contained in the paper by Knight, Al-Hamid & Yuen (1992) and further analyzed via 4 objective functions in the paper by Sharifi, Knight & Sterling, (2009).

- The problems associated with applying CFD to open channel flow cases where the wall or bed roughness makes the y^+ value an issue.
- Investigate the extension of Fig. 5.8 to higher values of k_{sb}/k_{sw} or k_{sw}/k_{sb} (e.g. k_{sw} = 32 mm in Knight, Al-Hamid & Yuen (1992)).
- Compare the wall area factor, α_w, results in Fig. 5.29 with those contained in Fig. 5.30 of Knight & Macdonald (1979). This may involve considering and solving y^+ value issue.
- Compare the general efficacy of the simple lateral distribution model proposed by Shiono & Knight (1991) originally for overbank flows, but applied later to deal with both inbank and overbank flows, with that of CFD for estimation of mean boundary shear stresses and distributions. The method is outlined in general terms by Knight, Tang, Sterling, Shiono & Mc Gahey (2010), with further details given in Tang & Knight (2008) and in the book on the CES (Conveyance Estimation System) software by Knight, Mc Gahey, Lamb & Samuels (2010).
- Further investigation on the mechanism of the creation of sand ridges on the bed of wide channels needs to be done. The simulations in the present study were done by planting the ridges on the bed but some numerical analysis may be carried out with movable bed to ascertain the effect of the secondary currents and wall shear.
- Investigate the experimental data contained in Tominaga & Nezu (1991) using CFD, and in particular examine the hypothesis of a linearly varying depth averaged $(UV)_d$ term contained in their Fig. 12.
- These quasi-linear distributions should be investigated through CFD and compared with the theoretically based linear $(UV)_d$ distributions proposed by Knight, Omran & Tang (2007) in their analysis of secondary flow effects in trapezoidal channels and as also used in the CES (Conveyance Estimation System) software, described in the book by Knight, Mc Gahey, Lamb & Samuels (2010).
- Investigate the 'equivalent secondary flow cell' approach adopted in the LES simulations for flow in a rectangular channel by Omran, Knight, Beaman & Morvan (2008) to see if it has wider relevance.

- The division lines were constructed and the Guo and Julien (2005) equation analysis was carried out at different sections inside a bend. Unfortunately the results were not good enough due to the fact that these equations were derived for straight prismatic channels and do not consider the effects of the large circulations that take place inside a bend. It is thus recommended that some work on the derivation of some analytical equations may be done and division line analysis may be carried out with those equations inside a bend.
- In addition to the data of Ippen & Drinker used in Chapter 7, consideration should be given to using the data of Blanckaert (2002), Booij (2002a & b, 2004, etc.), Muto (1997), Shiono & Muto (1998) and from the Flood Channel Facility (FCF) studies undertaken by Bristol University (e.g. see paper Knight, Yuan & Fares (1992)).
- Investigate division line concept for overbank flows and link it with the inbank flow CFD results. See for example paper by Knight & Tang (2008).

Notations used

A	=	Area of cross section of the channel
A_b	=	Flow area corresponding to bed region
A_w	=	Flow area corresponding to sidewall region
b	=	Bottom width of the trapezoidal channel
b/h	=	Aspect ratio
F_r	=	Froude number
g	=	Acceleration due to gravity
h	=	Depth of channel
h'	=	length of the side wall
k	=	Turbulent kinetic energy
k_s	=	Nikuradse equivalent sand roughness size
k_{sb}	=	Nikuradse equivalent sand roughness size for bed
k_{sw}	=	Nikuradse equivalent sand roughness size for sidewalls
P	=	Total cross sectional wetted perimeter
P_b	=	Wetted perimeter corresponding to bed
P_w	=	Wetted perimeter corresponding to sidewalls
P_b / P_w	=	Perimeter ratio
p	=	Pressure

R	=	Hydraulic radius
R_e	=	Reynolds number
S	=	Slope of the channel bed / energy line / water surface
T	=	Top width of the trapezoidal channel
u_*	=	Shear velocity
u_i	=	Velocity
u_i'	=	Fluctuating component of the velocity
u, v, w	=	Cartesian components of the velocity
$\overline{u_i' u_j'}$	=	Reynolds stresses
x, y, z	=	Cartesian co-ordinates
x	=	Stream wise flow direction
y	=	Transverse span wise distance measured from the channel centre
z	=	Vertical distance measured from the channel bed
ε	=	Turbulent kinetic energy dissipation rate
ν	=	Kinematic viscosity
μ	=	Dynamic viscosity
μ_t	=	Eddy viscosity
ρ	=	Density of water

$\overline{\tau_b}$ = Mean shear stress on bed region

$\overline{\tau_w}$ = Mean shear stress on wall region

$\tau_o/\rho ghS$ = Non-dimensionalized local shear stress on the wetted perimeter

$\tau_b/\rho ghS$ = Non-dimensionalized local shear stress on the bed region

τ_{ij} = Shear stress tensor

θ = Slant angle (Sidewall inclination of channel w. r. t. vertical axis)

$\%SF_w$ = Percentage of the total shear force carried by the walls

REFERENCES

Ansari, K., Morvan, H. P. and Hargreaves, D. M. (2011). "A numerical investigation into secondary currents and wall shear in trapezoidal channels." *Journal of Hydraulic Engineering, ASCE*, 137(4), p. 432 – 440.

Ackers, P. and White, W. R. (1973). "Sediment transport: New approach and analysis." *Journal of Hydraulic Division, ASCE*, 99(11), p. 2041 – 2060.

ANSYS, INC. (2008). Ansys-CFX, version 11.0 Southpointe, 275, Technology Drive, Canonsburg, PA, USA.

Bakker, B., Vermaas, H. and Choudri, A. M. (1989). "Regime theories updated or outdated." *Publication no. 416, Delft Hydraulics*, p. 1-7.

Birmingham University Flow Data. http://www.flowdata.bham.ac.uk/phd-data.shtml

Blanckaert, K., and De Vriend, H. J. (2005). "Turbulence structure in sharp open-channel bends." *Journal of Fluid Mechanics*, vol. 536, p. 27-48.

Blanckaert, K., and Graf, W. H. (2001). "Mean flow and turbulence in open-channel bend." *Journal of Hydraulic Engineering*, 127(10), p. 835-847.

Blanckaert, K., and Graf, W. H. (2004). "Momentum transport in sharp open-channel bends." *Journal of Hydraulic Engineering*, 130(3), p. 186-198.

Boysan, F. (1995). "Advanced turbulence modelling." *Short course notes at the University of Leeds, Fluent Europe Ltd.*, p. 1279-1298.

Brownlie, W. R. (1981). "Re-examination of Nikuradze roughness data." *Journal of Hydraulic Division, Proceedings of ASCE*, 107(1), p. 115-119.

Cacqueray, N. D., Hargreaves, D. M., and Morvan, H. P., (2009). "A computational study of shear stress in smooth rectangular channels." *Journal of Hydraulic Research*, 47(1), p. 50 – 57.

Cao, Z. X., Carling, P. And Oakley, R. (2003). "Flow reversal over a natural pool-riffle sequence: A computational study." *Earth Surface Processes and Landforms*, 28(7), p. 689-705.

Chang, H. H., (1988). "Fluvial processes in river engineering." *John Wiley and sons Inc.*, 1988.

Chiu, C. L. and Chiou, J. D., (1986). "Structure of 3-D flow in rectangular open channels." *Journal of Hydraulic Engineering, ASCE*, 112(11), p. 1050-1068.

Choi, S. U., Park, M., and Kang, H. (2007). "Numerical simulations of cellular secondary currents and suspended sediment transport in open-channel flows over smooth-rough bed strips." *Journal of Hydraulic Research*, 45(6), p. 829 – 840.

Chow, V. T. (1959).Open-Channel hydraulics, *McGraw Hill Inc.*

Chrisohoides, A., Sotiropoulos, F., and Sturm, T. W. (2003). "Coherent structures in flat-bed abutment flow: Computational Fluid Dynamics simulations and experiments." *Journal of Hydraulic Engineering, ASCE*, 129(3), p. 177-186.

Cokljat, D., (1993). "Turbulence models for non-circular ducts and channels." PhD thesis, Dept. of Civ. Engrg., City Univ., London, England.

Colombini, M. (1993). "Turbulence-driven secondary flows and formation of sand ridges." *Journal of Fluid Mechanics*, vol. 254, p. 701 – 719.

Cruff, R. W. (1965). "Cross-channel transfer of linear momentum in smooth rectangular channels." *Paper 1592-B, US Geological Survey*, p. B1-B26.

Douglas, J. F., Gasiorek, J. M., Swaffield, J. A. and Jack, L. B. (2005). Fluid Mechanics, *Pearson Education Inc.*

Einstein, H. A., (1942). "Formulas for the transportation of bed load." *Transactions of the ASCE*, 107, p. 561-597.

Flintham, T. P. and Carling, P. A., (1988). "The prediction of mean bed and wall boundary shear in uniform and compositely rough channels." *International Conference on River Regime, published by John Wiley & Sons Ltd.*, p. 267-287.

Fortier, S. and Scobey, F. C. (1926). "Permissible canal velocities." *Transactions of ASCE*, 89, p. 940-984.

French, R. H. (1985). "Open-channel hydraulics." *McGraw-Hill Inc.*

Ghosh, S. N. and Roy, N., (1970). "Boundary shear distribution in open channel flow." *Journal of Hydraulics Division, Proceedings of the ASCE*, 96(4), p. 967-994.

Grass, A. J., Stuart, R. J. and Mansour-Tehrani, M., (1991). "Vortical structures and coherent motion in turbulent flow over smooth and rough boundaries." *Phil. Trans. Royal Society, London, A*, Vol. 336, p. 35 - 65.

Guo, J. and Julien, P. Y., (2005). "Shear stress in smooth rectangular open-channel flows." *Journal of Hydraulic Engineering, ASCE*, 131(1), p. 30-37.

Hardy, R. J., Bates, P. D. And Anderson, M. G. (1999). "The importance of spatial resolution in hydraulic models for flood plain environments." *Journal of Hydrology*, 216, p. 124-136.

Henderson, F. M. (1966). Open channel flow, *Macmillan Publishing Co. Inc.*

Hirt, C. and Nichols, B. (1981). "Volume of fluid methods for the dynamics of free boundaries." *Journal of Computational Physics*, 39, p. 201.

Hsu, E. Y. (1955). "The measurement of local turbulent skin frictionby means of surface pitot tubes." *Report 957, D. W. Taylor Model Basin, US Department of Navy.*

Hwang, L. S. and Laursen, E. M. (1963). "Shear measurement technique for rough surfaces." *Journal of Hydraulic Division, ASCE*, 89(2), p. 19-37.

Ikeda, S. (1981). "Self-formed straight channels in sandy beds." Proc. of ASCE, Journal of Hydraulic Division, 107(4), p. 389-406.

Ingham, D. B., Bloor, M. I. G., Wen, X. And Ma, L. (1997). "Report of the British Gas research and technology centre on low and high pressure modellingof the uniform hydrocyclone separation behaviour and flow patterns." *Internal report, University of Leeds*, Leeds, UK.

Ippen, A. T., and Drinker, P. A. (1962). "Boundary shear stress in curved trapezoidal channels." *Journal of Hydraulic Division, Proceedings of ASCE,* 88(5), p. 143-179.

Ippen, A. T., Drinker, P. A., Jobin, W. R., and Nautsopoulos, G. K. (1960). "The distribution of boundary shear stress in curved trapezoidal channels." *Report no. 43, Hydrodynamics Lab., MIT.*

Jin, Y. C. and Steffler, P. M., (1993). "Predicting flow in curved open channels by depth-averaged method." *Journal of Hydraulic Engineering, ASCE,* 119(1), p. 109-124.

Jin, Y. C., Zarrati, A. R. and Zheng, Y. (2004). "Boundary shear distribution in straight ducts and open channels." *Journal of Hydraulic Engineering, ASCE,* 130(9), p. 924-928.

Julien, P. Y. (2002). "River mechanics." *Cambridge University Press, Cambridge, UK.*

Kartha, V. C. and Leutheusser, H. J. (1970). "Distribution of tractive force in open channels." *Journal of Hydraulics Division, Proceedings of the ASCE,* 96(7), p. 1469-1483.

Kennedy, R. G. (1895). "The prevention of silting in irrigation canals." Paper No. 2826, *Proceedings of the Institution of Civil Engineers, ICE (London),* 119, p. 281-290.

Keulegan, G. H., (1938). "Laws of turbulent flow in open channels." *Journal of Research of the National Bureau of Standards*, Volume 21, p. 708-741.

Knight, D. W., (2008). "Modelling overbank flows in rivers - data, concepts, models and calibration", Chapter 1 in Numerical Modelling of Hydrodynamics for Water Resources [Eds P. Garcia-Navarro & E. Playan], *Taylor & Francis*, p. 3 - 23.

Knight, D. W. (1981). "Boundary shear in smooth and rough channels." *Journal of Hydraulics Division, Proceedings of the ASCE*, 107(7), p. 839-851.

Knight, D. W., Demetriou, J. D. and Hamed, M. E., (1984). "Boundary shear in smooth rectangular channels." *Journal of Hydraulic Engineering, ASCE*, 110(4), p. 405-422.

Knight, D. W. and Macdonald, J. A. (1979a). "Hydraulic resistance of artificial strip roughness." *Journal of Hydraulics Division, Proceedings of the ASCE*, 105(6), p. 675-690.

Knight, D. W. and Macdonald, J. A. (1979b). "Open channel flow with varying bed roughness." *Journal of Hydraulics Division, Proceedings of the ASCE*, 105(9), p. 1167-1183.

Knight, D. W., Omran, M. and Tang, X., (2007). "Modelling depth-averaged velocity and boundary shear in trapezoidal channels with secondary flows." *Journal of Hydraulic Engineering, ASCE*, Vol. 133(1), p. 39 – 47.

Knight, D. W., Patel, S. (1985). "Boundary shear in smooth rectangular ducts." *Journal of Hydraulic Engineering, ASCE*, 111(1), p. 29-47.

Knight, D. W. and Sterling, M., (2000). "Boundary shear in circular pipes running partially full." *Journal of Hydraulic Engineering, ASCE*, 126(4), p. 263-275.

Knight, D. W. and Tang, X., (2008). "Zonal discharges and boundary shear in prismatic channels, Journal of Engineering and Computataional Mechanics." *Proceedings of Inst. Of Civil Engineers, London*, Vol. 161(2), p. 59 - 68.

Knight, D. W., Tang, X., Sterling, M., Shiono, K. and McGahey, C., (2010). "Solving open channel flow problems with a simple lateral distribution model." *Riverflow 2010, Proceedings of the Int, Conf. on Fluvial Hydraulics*, [Eds A.

Dittrich, K. Koll, J. Aberle, and P. Geisenhainer], Braunschweig, Germany, Sept. 8-10, Bundesantalt fur Wasserbau (BAW), Karlsruhe, Germany, Keynote address, Vol I, p. 41 - 48.

Knight, D. W., Yuen, K. W. H. and Alhamid, A. A. I., (1994). "Boundary shear stress distributions in open channel flow", in "Physical Mechanisms of Mixing and Transport in the Environment", [Eds K. Beven, P. Chatwin & J. Millbank], *J. Wiley*, Chapter 4, p. 51 – 87.

Lacey, G. (1930). "Stable channels in alluvium." Paper No. 4736, *Proceedings of the Institution of Civil Engineers, ICE (London)*, 229, p. 259-292.

Lane, E. W. (1955). "Design of stable channels." *Transactions of ASCE*, 120, p. 1234-1279.

Lane, S. N. (1998). "Hydraulic modelling in hydrology and geomorphology: A review of high resolution approaches." *Hydrological Processes*, 12, p. 1131-1150.

Launder, B. E., Reece, G. J. and Rodi, W., (1975). "Progress in the developments of a Reynolds-stress turbulence closure." *J. Fluid Mechanics*, Vol. 68, p.537-566.

Launder, B. E. And Spalding, D. B. (1974). "The numerical computation of turbulent flow." *Computer Methods in Applied Mechanics and Engineering*, 3, p. 269-289.

Leighly, J., (1932). "Toward a theory of the morphologic significance of turbulence in the flow of water in streams." *University of California Publications in Geography*, 6(1), p. 1-22.

Liao, H. and Knight, D. W. (2007). "Analytic stage-discharge formulae for flow in straight trapezoidal open channels." *Advances in Water Resources*, 30(11), p. 2283-2295.

Liao, H. and Knight, D. W. (2007). "Analytic stage-discharge formulas for flow in straight prismatic channels." *Journal of Hydraulic Engineering, ASCE*, 133(10), p. 1111-1122

Liepmann, H. W. and Dhawan, S. (1952). "Direct measurement of local skin friction in low speed and high speed flow." Proceedings, National Institute of Applied Mechanics, p. 869-874.

Lim, S. Y. and Yang, S. Q. (2005). "Simplified model of tractive-force distribution in closed conduits." *Journal of Hydraulic Engineering, ASCE*, 131(4), p. 322-329.

Ludweig, H. (1949). "Ein great zur messung der wandschubs pennung turbulentor reibungschichten." Ingenieur-Archiv, 17, p. 207-208.

Ma, L., Ashworth, P. J., Best, J. L., Ingham, D. B., Elliott, L. and Whitcombe, L. (2002). "Computational fluid dynamics (CFD) and physical modelling of an upland urban river." *Geomorphology*, 44, p. 375-391.

Mohammadi, B. and Pironneau, O. (1994). "Analysis of k-Epsilon turbulence model." *Wiley*, Chichester.

Mohammadi, M. and Knight, D. W., (2004). "Boundary shear stress distribution in a V-shaped channel." *Hydraulics of Dams and River Structures – Yazdandoost & Attari (eds)*, Taylor & Francis Group, London, p. 401-410.

Morvan, H. P. (2005). "Channel shape and turbulence issues in flood flow hydraulics." *Journal of Hydraulic Engineering, ASCE*, 131(10), p. 862-866.

Morvan, H. P., Crossley, A. J. and Wright, N. G. (2002). "Flood flow mechanics in 3D." *Joint ASME ASCE McMAT Conference*, Baton Ronge, USA.

Morvan, H. P., Hargreaves, D. M., (2009). "A computational study of secondary currents and wall shear stress in prismatic channels.", *Proceedings of the 33rd IAHR Congress*, Vancouver, Canada, August 2009.

Morvan, H. P., Knight, D. W., Wright, N. G., Tang, X. and Crossley, A. J., (2008). "The concept of roughness in fluvial hydraulics and its formulation in 1-D, 2-D and 3-D numerical simulation models." *Journal of Hydraulic Research*, 46(2), 191-208.

Morvan, H. P., Pender, G., Wright, N. G., and Ervine, D. A., (2005). "Three-dimensional hydrodynamics of meandering compound channels." *Journal of Hydraulic Engineering, ASCE*, 128(7), p. 674-682.

Murphy, J. S. and Smith, A. M. O. (1956). "Measurement of wall shearing stress in the boundary layer by means of an evaporating liquid film." *Journal of Applied Physics*, 27, p. 1097-1103.

Myers, W. R. C., (1978). "Momentum transfer in a compound channel." *Journal of Hydraulic Research*, 16(2), p. 139-150.

Nezu, I. (2005). "Open-channel flow turbulence and its research in 21st century." ASCE, *Journal of Hydraulic Engineering*, 131(4), p. 229 – 246.

Nezu, I., and Nakagawa, H. (1993). "Turbulence in open channel flows." *Belkema, Rotterdam, The Netherlands*.

Nezu, I., and Nakagawa, H. (1989). "Self forming mechanism of longitudinal sand ridgesand troughs." *Proceedings, 23rd IAHR Congress, Vol. B, Delft, The Netherlands*, p. 65-72.

Nezu, I., and Nakagawa, H. (1984). "Cellular secondary currents in straight conduits." *ASCE, Journal of Hydraulic Engineering*, 110(2), p. 173 – 193.

Nezu, I., Nakagawa, H., and Kawashima, N. (1988). "Cellular secondary currents and sand ribbons in fluvial channel flows." *6th Congress, Asian and Pacific Regional Division, IAHR, Kyoto, Japan*, p. 51 – 58.

Nezu, I., Nakagawa, H., and Tominaga, A. (1985). "Secondary currents in a straight channel flow and relation to its aspect ratio." *Turbulent Shear Flows 4*, Vol. 4, Springer, New York, p. 246 – 260.

Nezu, I., and Rodi, W. (1985). "Experimental study on secondary currents in open channel flow." *21st IAHR Congress*, Melbourne, Australia, p. 115 – 119.

Noutsopoulos, G. C. and Hadjipanos, P. A., (1982). "Discussion on boundary shear in smooth and rough channels by D. W. Knight." *Journal of Hydraulics Division, Proceedings of the ASCE*, 108(6), p. 809-812.

Prandtl, L. (1952). "Essentials of Fluid Dynamics: With Applications to Hydraulics, Aeronautics, Meteorology, and other Subjects." (English translation). *Blackie and Son Ltd.*, p. 145 – 149.

Preston, J. H. (1954). "The determination of turbulent skin friction by means of pitot tubes." *Journal of Royal Aeronautical Society, London*, 58, p. 109-121.

Rhodes, D. G. (1991). "An experimental investigation of the mean flow structure in wide ducts of simple rectangular and trapezoidal compound cross section, examining in particular zones of higher lateral shear." *PhD Thesis, University of Birmingham*, Birmingham, UK.

Rhodes, D. G. and Knight, D. W. (1994). "Distribution of shear force on boundary of smooth rectangular duct." *Journal of Hydraulic Engineering, ASCE*, 120(7), p. 787-807.

Rozovskii, I. L. (1957). "Flow of water in bends of open channel." *Ac. Sc. Ukr. SSR, Isr. Progr. Sc. Transl.*, Jerusalem, Israel.

Schlichting, H., and Gersten, K. (2000). Boundary-Layer Theory, *Springer-Verlag, Berlin, Heidelberg.*

Sharifi, S., Knight, D. W. and Sterling, M., (2009). "A novel application of a multi-objective evolutionary algorithm in open channel flow modelling." *Journal of Hydroinformatics, IWA Publishing*, 11(1), p. 31 - 50.

Shiono, K. and Muto, Y., (1998). "Complex flow mechanisms in compound meandering channels with overbank flow." *Journal of Fluid Mechanics*, Vol. 376, p. 221 – 261.

Shukry, A. (1950). "Flow around bends in an open flume." *Trans., Am. Soc. Civ. Eng.*, 115, p. 751-788.

Speziale, C. G., Sarkar, S., and Gatski, T. B., (1991). "Modelling the pressure-strain correlation of turbulence: an invariant dynamical systems approach." *Journal of Fluid Mechanics*, Vol. 227, p. 245 - 272.

Tennekes, H. and Lumley, J. L. (1972). "A first course of turbulence." *MIT Press.*

The Mathworks Inc., Matlab, version 7.3, (2006), 3 Apple Hill Drive, Natick, MA, USA.

Tominaga, A., Nezu, I., Ezaki, K., and Nakagawa, H., (1989). "Three-dimensional turbulent structure in straight open channel flows." *Journal of Hydraulic Research*, Vol. 27, No. 1, p. 149-173.

Tracy, H. J. (1965). "Turbulent flow in a three-dimensional channel." *Journal of Hydraulics Division, Proceedings of the ASCE*, 91(6), p. 9-35.

Vanoni, V. A., and Brooks, N. H. (1957). "Laboratory studies of the roughness and suspended load of alluvial streams." *Sedimentation Laboratory Report No. E68, 1957, California Institute of Technology, California.*

Versteeg, H. K., and Malalasekera, W. (2007). "An introduction to Computational Fluid Dynamics-The finite volume method." *Pearson education limited.*

Wang, Z. Q., and Cheng, N. S. (2006). "Time-mean structure of secondary flows in open channel with longitudinal bed forms." *Advances in Water Resources*, 29, p. 1634 – 1649.

Wang, Z. Q., and Cheng, N. S. (2005). "Secondary flows over artificial bed strips." Advances in Water Resources, 28, p. 441 – 450.

White, W. R., Bettess, R. and Paris, E. (1982). "Analytical approach to river regime." *Journal of hydraulics Division, ASCE*, Vol. 108(10), p. 1179-1193.

White, W. R., Bettess, R. and Paris, E. (1980). "The frictional characteristics of alluvial streams: A new approach." *Proc. of the Institution of Civil Engineers*, Part 2, Vol. 69, p. 737 - 750.

Yakhot, V. and Orszag, S. (1986). "Renormalisation group analysis of turbulence." *Journal of Science and Computing*, 1, p. 3-51.

Yang, S. Q. (2005). "Interactions of boundary shear stress, secondary currents and velocity." *Fluid Dynamics Research*, 36, p. 121-136.

Yang, S. Q. (2002). "1st and 2nd order approximate solutions of Reynolds equations in 3-D channels." *Proceedings of 13th IAHR-APD Congress, Vol. 1*, Singapore, p. 70-75.

Yang, S. Q. (1996). "Interaction of boundary shear stress, velocity distribution and flow resistance in 3-D channels." *PhD Dissertation, Nanyang Technological University*, Singapore.

Yang, S. Q. and McCorquodale, J. A. (2004). "Determination of boundary shear stress and Reynolds shear stress in smooth rectangular channel flows." *Journal of Hydraulic Engineering, ASCE*, 130(5), p. 458-462.

Yang, S. Q. and Lim, S. Y. (2006). "Discussion of shear stress in smooth rectangular open-channel flows" by Junke Gou and Pierre Y. Julien. *Journal of Hydraulic Engineering, ASCE*, 132(X), p. 629-632.

Yang, S. Q. and Lim, S. Y., (1998). "Boundary shear stress distribution in smooth rectangular open channel flows." *Proceedings of the Institution of Civil Engineers-Water, Maritime & Energy*, 130(3), p. 163-173.

Yang, S. Q. and Lim, S. Y., (1997). "Mechanism of energy transportation and turbulent flow in a 3D channel." *Journal of Hydraulic Engineering, ASCE*, 123(8), p. 684-692.

Yang, S. Q., Tan, S. K. and Lim, S. Y. (2004). "Velocity distribution and dip-phenomenon in smooth uniform open channel flows." *Journal of Hydraulic Engineering, ASCE*, 130(12), p. 1179-1186.

Yen, B. C. (2002). "Open channel flow resistance." *Journal of Hydraulic Engineering, ASCE*, 128(1), p. 20-39.

Yuen, K. W. H., (1989). "A study of boundary shear stress, flow resistance and momentum transfer in open channels with simple and compound trapezoidal cross sections." *Ph.D. Thesis*, University of Birmingham, UK.

Zeng, J., Constantinescu, G., Blanckaert, K., and Weber, L. (2008). "Flow and bathymetry in sharp open-channel bends: Experiments and predictions." *Water Resources Research*, Vol. 44, W09401,

Zheng, Y. and Jin, Y. C. (1998). "Boundary shear in rectangular ducts and channels." *Journal of Hydraulic Engineering, ASCE*, 124(1), p. 86-89.

Annexure - A

Matlab code for finding area under the curve (Division Line) and integrals.

```
% Define constants
rho = 997.0;

% Read in the data from the Line of Zero Stress Streamline
lineData = dlmread('TSW0AR2R1.txt',',');

% Get the length of the data
dataLen = length(lineData);

% Transfer the data into vectors
y = lineData(:,2);
z = lineData(:,3);
txy = lineData(:,4);
txz = lineData(:,5);
u = lineData(:,6);
v = lineData(:,7);
w = lineData(:,8);

% Find the min and max y values
yMin = min(y);
yMax = max(y);
zMax = max(z);

% Fit a splines to the data
spZ = spline(y,z);
spTxy = spline(y,txy);
spTxz = spline(y,txz);
spU = spline(y,u);
spV = spline(y,v);
spW = spline(y,w);

% Generate a list of y coordinates
yRef = yMin:0.001:yMax;

% Generate the list of z coordinates from the spline
zRef = ppval(spZ, yRef);

% Calculate the area under the streamline
area = quad(@ppval,yMin,yMax,[],[],spZ)+yMin*zMax

% Plot the spline data
subplot(2,2,1);
plot(yRef,zRef);
```

```
% Extract the breaks and coefficients of the spline
[zBreaks,zCoeffs,zL]=unmkpp(spZ);
[txyBreaks,txyCoeffs,txyL] = unmkpp(spTxy);
[txzBreaks,txzCoeffs,txzL] = unmkpp(spTxz);
[uBreaks,uCoeffs,uL] = unmkpp(spU);
[vBreaks,vCoeffs,vL] = unmkpp(spV);
[wBreaks,wCoeffs,wL] = unmkpp(spW);

% Create the coefficients of the derivative of the spline
dzdyCoeffs(:,1) = 3.0*zCoeffs(:,1);
dzdyCoeffs(:,2) = 2.0*zCoeffs(:,2);
dzdyCoeffs(:,3) = 1.0*zCoeffs(:,3);

% Construct the derivative of the spline
dzdySp=mkpp(zBreaks,dzdyCoeffs);

% Generate the points for a plot
dzdyRef = ppval(dzdySp,yRef);
subplot(2,2,2);
plot (yRef,dzdyRef);

% Construct the coefficients of the stress and secondary currents splines
for k = 1:zL
   stressCoeffs(k,:) = conv(txyCoeffs(k,:), dzdyCoeffs(k,:));
   stressCoeffs(k,3) = stressCoeffs(k,3) - txzCoeffs(k,1);
   stressCoeffs(k,4) = stressCoeffs(k,4) - txzCoeffs(k,2);
   stressCoeffs(k,5) = stressCoeffs(k,5) - txzCoeffs(k,3);
   stressCoeffs(k,6) = stressCoeffs(k,6) - txzCoeffs(k,4);
   secondaryCoeffs(k,:) = conv(vCoeffs(k,:),dzdyCoeffs(k,:));
   secondaryCoeffs(k,3) = secondaryCoeffs(k,3) - wCoeffs(k,1);
   secondaryCoeffs(k,4) = secondaryCoeffs(k,4) - wCoeffs(k,2);
   secondaryCoeffs(k,5) = secondaryCoeffs(k,5) - wCoeffs(k,3);
   secondaryCoeffs(k,6) = secondaryCoeffs(k,6) - wCoeffs(k,4);
   secondaryCoeffsFull(k,:) = rho*conv(secondaryCoeffs(k,:),uCoeffs(k,:));
end

stressFunction = mkpp(zBreaks,stressCoeffs);
stressRef=ppval(stressFunction,yRef);
stressIntegral = quad(@ppval,yMin,yMax,[],[],stressFunction)
subplot(2,2,3);
plot(yRef, stressRef);

secondaryCurrentFunction = mkpp(zBreaks, secondaryCoeffsFull);
secondaryCurrentRef = ppval(secondaryCurrentFunction,yRef);
secondaryCurrentIntegral =
quad(@ppval,yMin,yMax,[],[],secondaryCurrentFunction)
subplot(2,2,4);
plot(yRef, secondaryCurrentRef);
```

Annexure - B

Figures for comparison of wall shear with change in approach used.

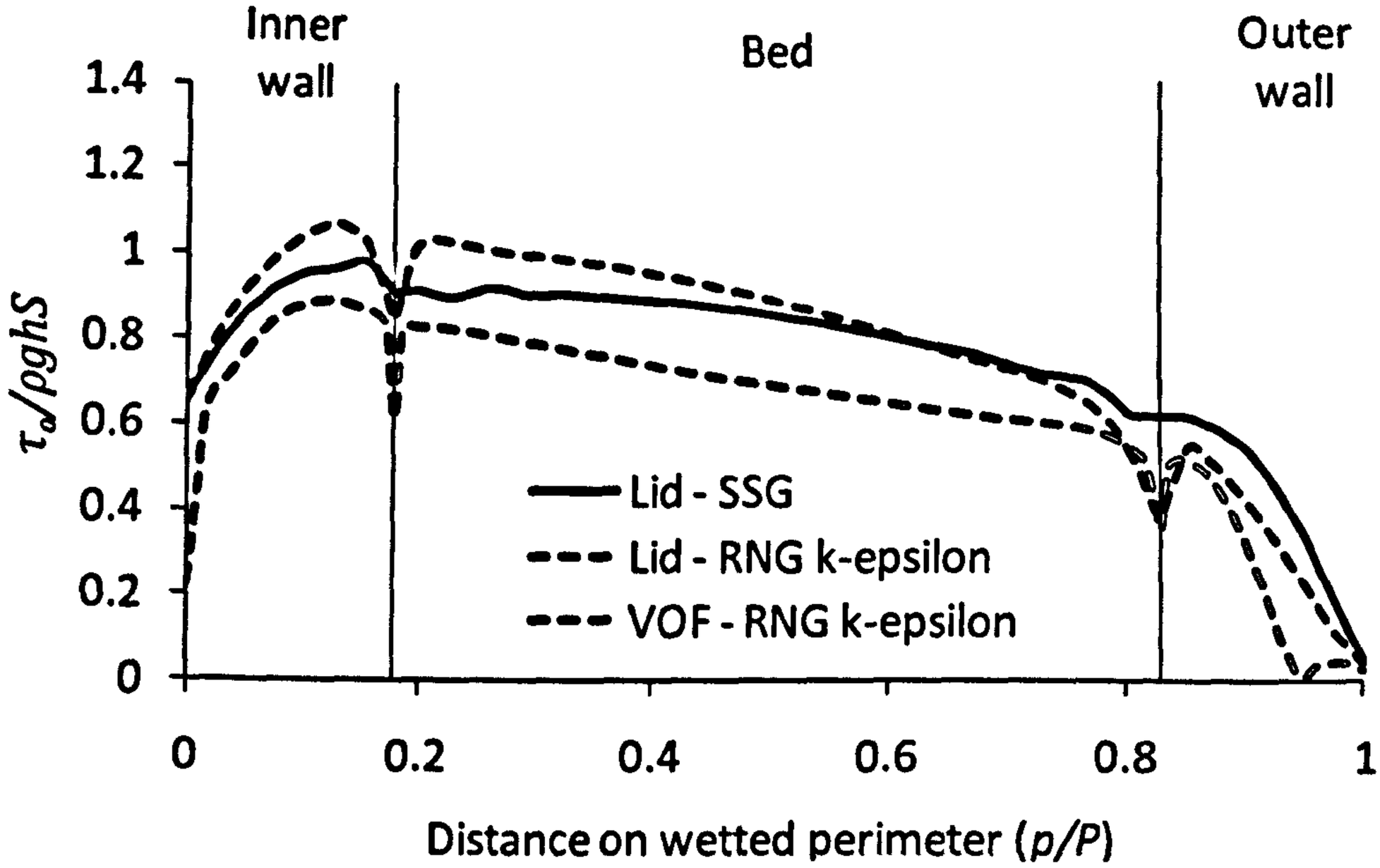

Figure B.8.1 Comparison of non-dimensionalized wall shear on the wetted perimeter at bend entry.

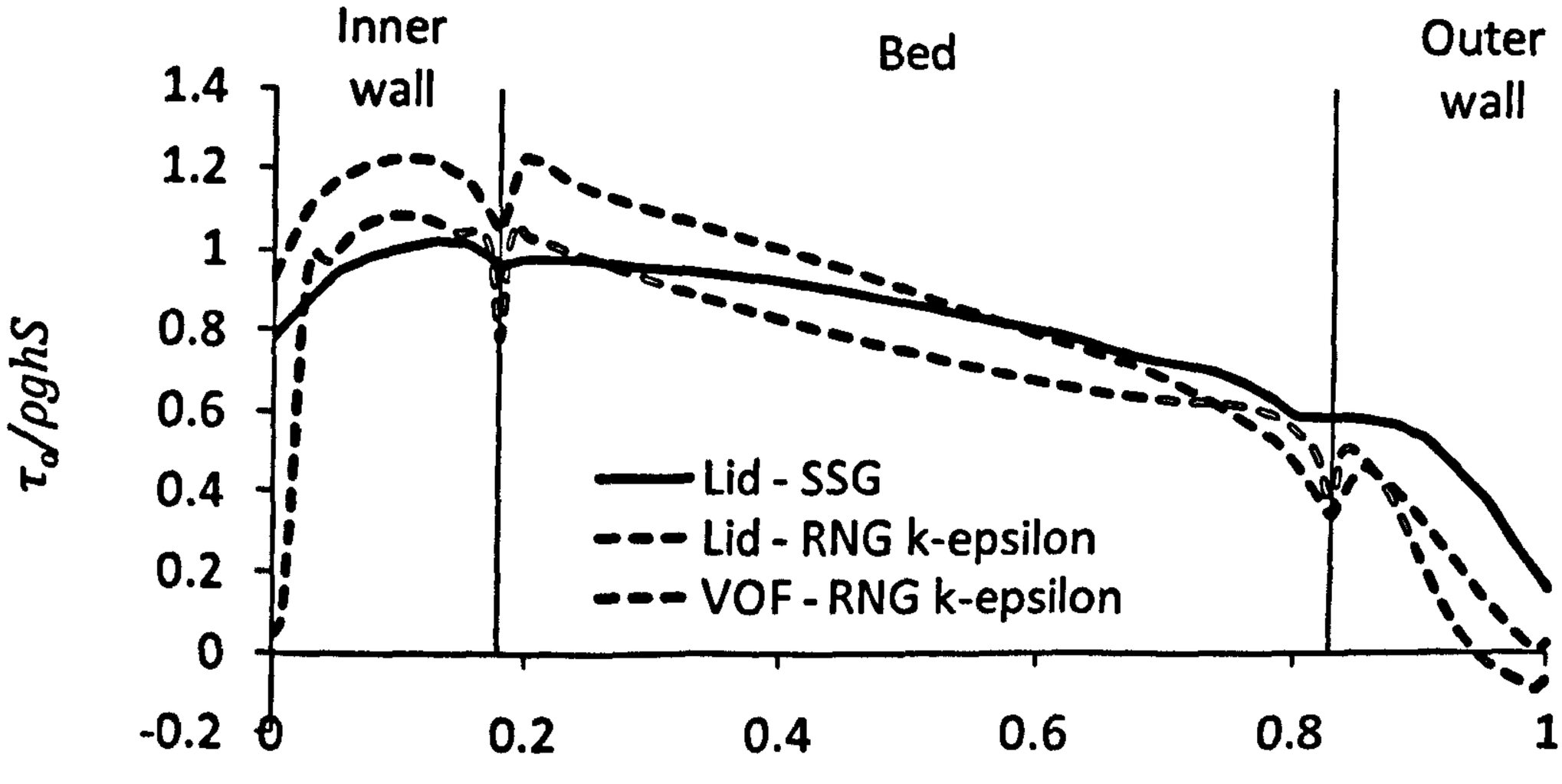

Figure B.8.2 Comparison of non-dimensionalized wall shear on the wetted perimeter at a section 15 degrees inside bend.

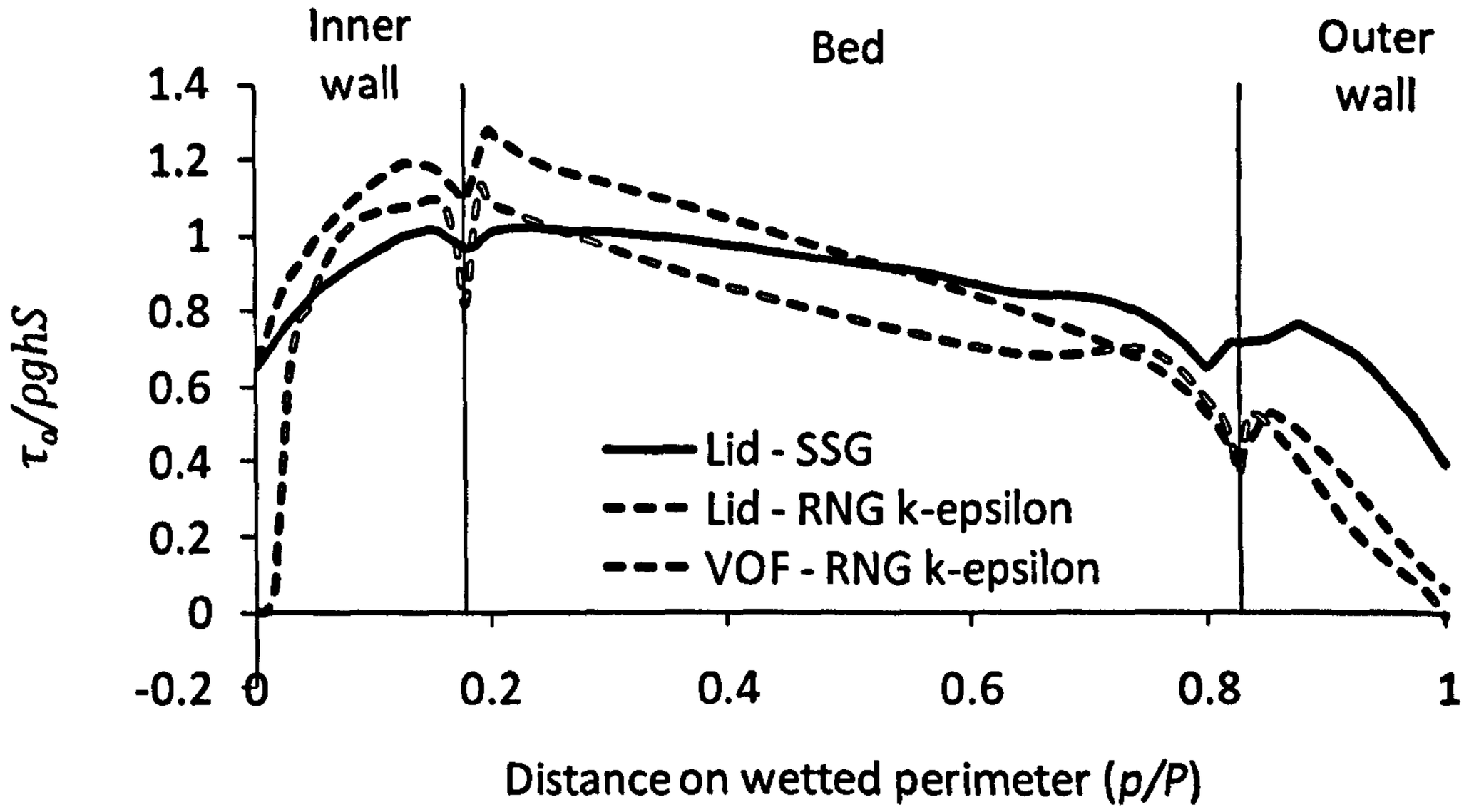

Figure B.8.3 Comparison of non-dimensionalized wall shear on the wetted perimeter at a section 30 degrees inside bend.

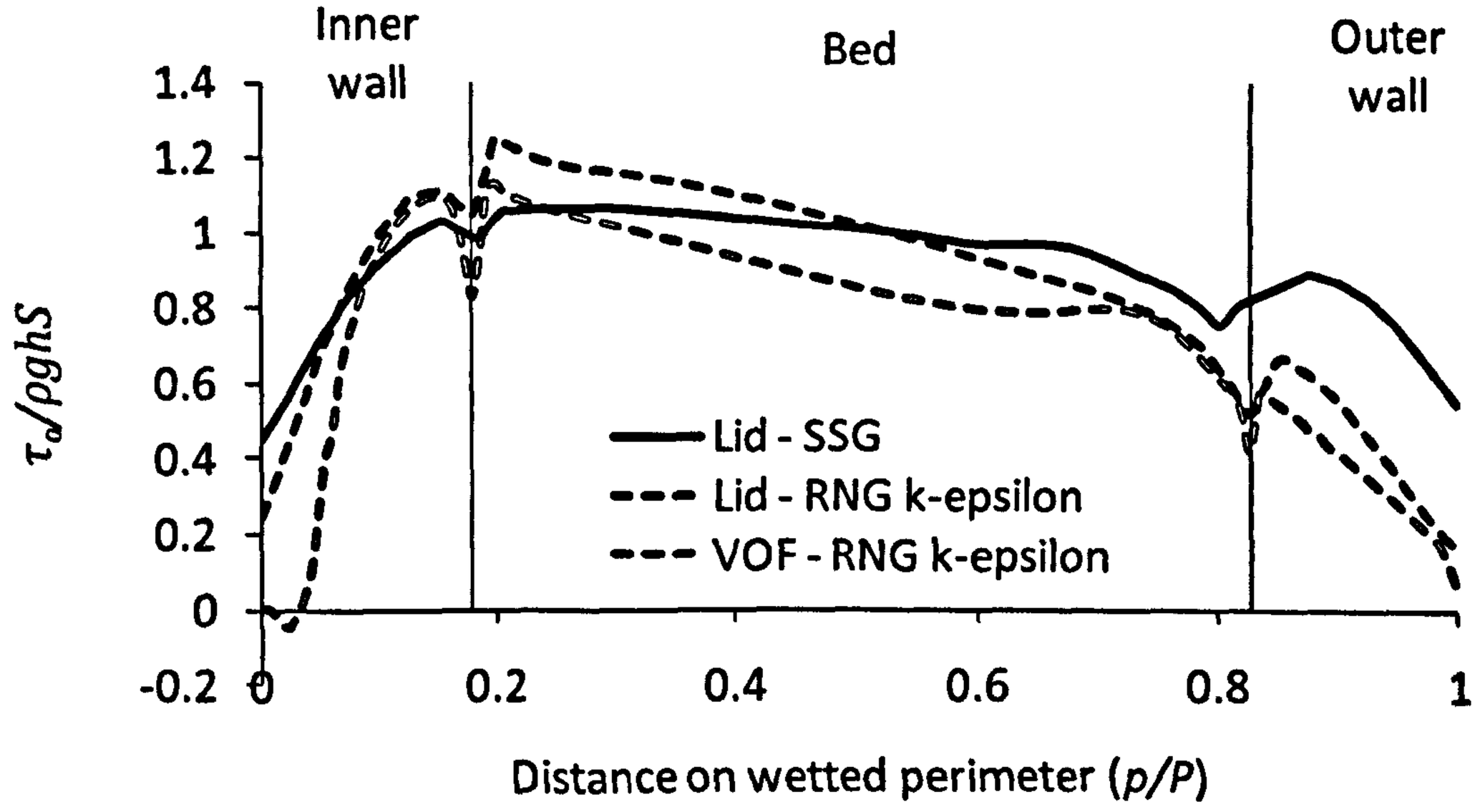

Figure B.8.4 Comparison of non-dimensionalized wall shear on the wetted perimeter at a section 45 degrees inside bend.

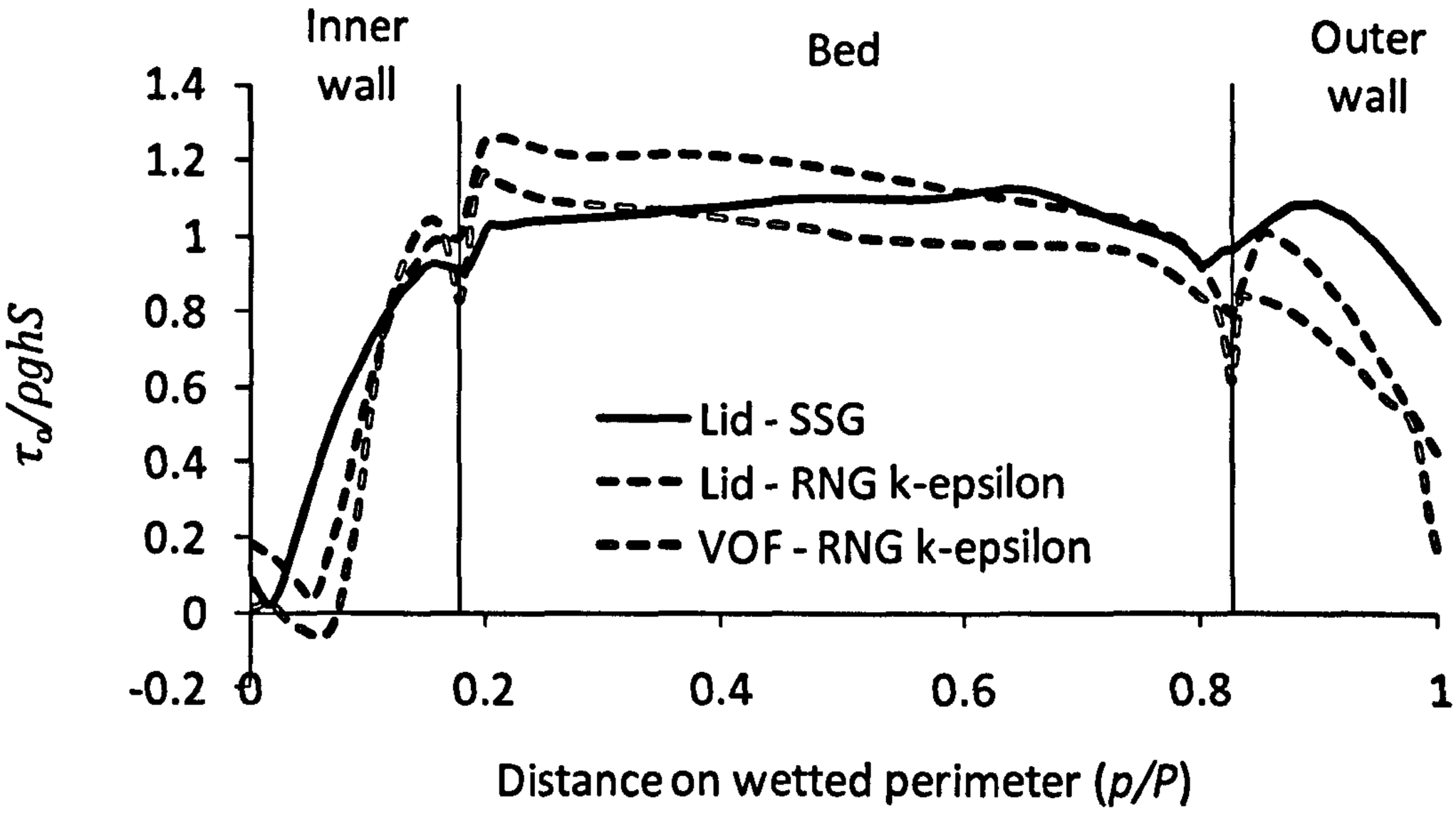

Figure B.8.5 Comparison of non-dimensionalized wall shear on the wetted perimeter at bend exit.